DISSERTATION | DOCTORAL THESIS

Titel | Title

Irreversible Electrochromic Displays for Smart Labels in Cold-chain Applications

verfasst von | submitted by

Dott. Dott. mag. Gianvito Romano

angestrebter akademischer Grad | in partial fulfilment of the requirements for the degree of

Doktor der Naturwissenschaften (Dr.rer.nat.)

Wien | Vienna, 2026

Studienkennzahl lt. Studienblatt | Degree programme code as it appears on the student record sheet:	UA 796 605 419
Dissertationsgebiet lt. Studienblatt | Field of study as it appears on the student record sheet:	Chemie
Betreut von | Supervisor:	Univ.-Prof. Davide Bonifazi PhD

The research work presented in this doctoral thesis was carried out between June 2020 and May 2023 at the University of Vienna (Austria). During this period, I completed research secondments at Etteplan Oyj in Tampere (Finland) from May to June 2022, at Ynvisible GmbH in Charneca de Caparica (Portugal) from July 2022 to February 2023, and at Ynvisible GmbH in Freiburg (Germany) from March to April 2023. All research activities were conducted under the supervision of Prof. Dr. Davide Bonifazi.

I hereby declare that this thesis was written by me and that all scientific results, analyses and interpretations presented herein are my own.

Gianvito Romano, 2026

© Copyright Gianvito Romano, University of Vienna, Austria

“A Gina”

"Curiosity is more important than knowledge."

Albert Einstein

ACKNOWLEDGMENTS

I would like to thank Prof. Dr. Davide Bonifazi for giving me the opportunity to join his research group, and Dr. Laura Maggini for her continuous support throughout these years.

My appreciation extends as well to Dr. Antoine Stopin, who accompanied me during the first and most challenging months of this journey. His guidance and his way of thinking, especially the idea of removing “I don’t know” from my vocabulary, played a meaningful role in my growth both as a researcher and as a person.

I am deeply thankful to all the PIs and PhD students involved in the CHARISMA project for welcoming me so warmly during my secondments and for integrating me into their teams from the very first day. Working with them was a formative and enriching experience that has shaped my scientific path.

I would like to express my sincere thanks to the PIs Prof. Dr. Donald Lupo, Prof. Dr. Jorge Parola, Prof. Dr. César Laia, Dr. Philippe Marrec, Prof. Davide Bonifazi and Dr. Carlos Pinheiro for their guidance, scientific input and continuous support. I am equally grateful to the Project Managers, Dr. Antoine Stopin and Dr. Polyxeni Bozatzi, for their coordination, availability and encouragement throughout the project.

My gratitude also goes to the CHARISMA PhD students, whose collaboration and friendship made the experience truly memorable. In particular, I wish to thank Hamed, Matin, Alberto, Diem, Maria, Fabio, Elin and Sunil for their support, their teamwork and the many moments shared during meetings, experiments and travels.

I would also like to thank Sanna Lahokallio, Senior Reliability Specialist at Etteplan, and Lucia Gomes, COO at Ynvisible, for their assistance, professionalism and kindness during my stays in their institutions.

A very special thank you goes to Diem, who has treated me like a true brother both inside and outside the laboratory since the very beginning. His presence, empathy and support have meant a great deal to me, and I remain sincerely grateful for this.

My thanks also extend to Marco Franceschini for his valuable contribution to our scientific work and for his patience and understanding during the more demanding days in the office.

I am deeply grateful to every member of the Group for their support, friendship and the many positive moments shared over the years. In no particular order, I would like to thank Martina,

Cristian, Terezia, Rúben, Davide, Daniele, André, Melina, Deborah, Liubov, El Czar, Lorenzo, Chiara, Nils, Miquel, Fabio, Josué, Beatrice, Vivek and Jack F. Their presence made this journey not only scientifically meaningful but also lighter, smoother and truly enjoyable.

I would also like to express my sincere thanks to SpeedPox GmbH, the company where I currently work, for supporting me during the writing of this thesis and for providing the flexibility, time and understanding necessary to complete this important work. Their trust and encouragement have been greatly appreciated.

My deepest thank goes to my parents, whose constant support has remained a source of strength throughout this journey. Even from afar, they have always made me feel their presence, reassurance and unconditional belief in my abilities.

I am also thankful to my friends from my hometown, Monopoli. Despite the distance, they have always made me feel close and connected. Their friendship and loyalty have never failed, and for this I am truly grateful.

Finally, my heartfelt gratitude goes to Antonella, the lighthouse of my journey. Her trust in me and in my decisions has meant more than words can convey. Her support has given me strength in every difficult moment and has been a constant source of motivation. I am especially thankful that we can share this new chapter of life together in Vienna, a path of discovery and growth for both of us.

TABLE OF CONTENTS

ACKNOWLEDGMENTS iv

TABLE OF CONTENTS 9

LIST OF ABBREVIATIONS 13

ABSTRACT 16

ZUSAMMENFASSUNG 18

CHAPTER 1 21

INTRODUCTION 21

1.1 The phenomenon of electrochromism 21

1.1.1 Definition and basic principles 21

1.1.2 The electrochromic display (ECD) 23

1.2 Materials for electrochromism 38

1.2.1 Inorganic electrochromic materials 39

1.2.2 Organic electrochromic materials 43

1.3 Irreversible electrochromic systems 62

1.3.1 Concept and characteristics 62

1.3.2 Potential Applications 62

1.3.3 Current irreversible technologies and limitations 64

1.4 Aim of the dissertation 66

REFERENCES 67

CHAPTER 2 81

DOPAMINE-BASED IRREVERSIBLE ELECTROCHROMIC DISPLAYS 81

INTRODUCTION 81

2.1 The molecule of dopamine 81

2.2 Toward DA oxidation to PDA formation 82

2.2.1 Spontaneous oxidation of DA 82

2.2.2 Electrochemical oxidation of DA 87

2.3 Aim of the project 89

RESULT AND DISCUSSION 90
2.4 Fabrication and activation of a DA-based *i*-ECD 90
2.5 Effect of the pH 92
2.6 Optimization of operating parameters 93
2.6.1 Study of the optimal concentration of DA for i-ECDs 93
2.6.2 Determination the activation threshold voltage of the i-ECDs 95
2.6.3 The importance of DA for the i-ECDs 96
2.7 DA self-oxidation and *i*-ECDs stability 97
2.8 *i*-ECDs characterization 101
2.8.1 Surface Morphological Characterization: SEM and AFM Analysis 102
2.8.2 XPS 104
2.9 DA electrosynthesis in solution with salt-bridge 106
2.10 DA spectroelectrochemistry in solution 108
2.11 DA cyclic voltammetry 112
2.12 *i*-ECD charge consumption and CE 116
2.13 Kinetic analysis 118
2.14 Proof of irreversibility 120
2.15 Role of the electrolyte 122
2.16 Reliability tests 125
2.16.1 i-ECDs Bendability study 126
2.16.2 i-ECDs stability under storage at low temperature 128
2.16.3 i-ECDs activation - temperature tolerance 129
2.16.4 i-ECDs stability under solar light exposition 131
2.17 DA functionalization 132
2.17.1 Methoxydopamine 133
2.17.2 Chlorodopamine 136
2.17.3 Nitrodopamine 138
2.18 *i*-ECDs design 142
2.19 Integration: CHARISMA smart label prototype for cold-chain applications 145

2.20 Integration: prototype for cold-chain and Prelonic prototype for ticket events 148

2.21 Conclusions and outlook 151

REFERENCES 153

CHAPTER 3 158

DOPAMINE-BASED INK FORMULATION FOR PRINTING TECHNOLOGY 158

INTRODUCTION 158

3.1 Current production of ECDs 158

3.1.1 Electropolymerisation 158

3.1.2 Spin coating 160

3.1.3 Inkjet and spray coating 161

3.1.4 Blade coating 164

3.1.5 Screen printing 166

3.2 Ink formulation 168

3.3 Aim of the project 171

RESULT AND DISCUSSION 172

3.4 DA ink formulation 172

3.4.1 Agar Agar 172

3.4.2 Starch 173

3.4.3 PEG 174

3.4.4 Porcine skin 175

3.5 Doctor blade ink formulation and *i*-ECD testing 176

3.5.1* P*reliminary assessment and viscosity optimization 177

3.5.2 Preparation and deposition of the DA Ink 178

3.5.3 *Testing of the formulation in i-ECDs: casting, activation and charge consumption* 180

3.5.4 i-ECDs stability 186

3.6 Screen printing ink formulations and *i*-ECD production 189

3.7 Conclusions and outlook 190

REFERENCES 192
CHAPTER 4 200
SACRIFICIAL AGENTS IN POLYTHOPHENES-BASED ECDs 200
INTRODUCTION 200
4.1 Polythiophene polymers 200
4.2 Aim of the project 203
RESULT AND DISCUSSION 204
4.3 Manufacturing and characterization of polythiophenes-based ECDs 204
4.4 Harnessing sacrificial agents to promote irreversible EC transformations 212
4.4.1 Irreversibility test - polythiophenes decolouration in solution 212
4.4.2 Irreversibility test - polythiophenes decolouration in i-ECDs 218
4.4.3 Use of sacrificial agents - study in solution 220
4.5 Conclusions 227
REFERENCES 228
CHAPTER 5 233
CONCLUSION AND OUTLOOK 233
CHAPTER 6 237
EXPERIMENTAL SECTION 237
6.1 Instrumentation 237
6.2 Chemicals and Materials 242
6.3 Methods 243
Chapter 2 243
Chapter 3 254
Chapter 4 262
6.4 Synthetic procedures 263
Appendix: ^{1}H, ^{13}C, AND HRMS SPECTRA 268

LIST OF ABBREVIATIONS

°C	Degrees Celsius
µm	Micrometer
AFM	Atomic Force Microscopy
Ag/AgCl - KCl 3M/sat.	Silver/Silver Chloride – Potassium Chloride 3 Molar/Saturated
AZO	Aluminum zinc oxide
AntiOX	Antioxidant
AZO	Aluminum-Doped Zinc Oxide
BMITFSI	1-Butyl-3-Methylimidazolium Bis(Trifluoromethanesulfonyl)imide
BuDOP	Poly(3,4-butylene-dioxy-pyrrole)
C.E.	Counter Electrode
CE	Coloration Efficiency
CHARISMA	Entrepreneuring Chemical Irreversibility To Prototype Responsive Smart Labels
ClDA	Chlorodopamine
CMR	Carcinogenic, Mutagenic, or Toxic for Reproduction
CN	Cyan
CPU	Central Processing Unit
CR	Contrast Ratio
CRT	Cathode Ray Tube
cP	Centipoise
CV	Cyclic Voltammetry
DA	Dopamine
DA+AntiOX	Dopamine 10 g/L + $Na_2S_2O_5$ 5 g/L in PBS pH 7.4
DAQ	Dopaminequinone
DAC	Dopamineaminochrome
DAL	Leucodopaminechrome
DHI	5,6-Dihydroxyindole
DSQ	Dopamine Semiquinone
DSSC	Dye-Sensitized Solar Cell
ΔT	Delta Transmittance
EC	Electrochromic
ECD	Electrochromic Display
EDG	Electron-Donor Group
EDOT	3,4-Ethylenedioxythiophene
e-Ink	Electronic Ink
ePDA	Electropolymerized Polydopamine
EtOH	Ethanol
EWG	Electron-Withdrawing Group
FTO	Fluorine tin oxide
GPC	Gel Permeation Chromatography
GZO	Gallium zinc oxide
HOMO	Highest Occupied Molecular Orbital

HRMS	High Resolution Mass Spectroscopy
HPMC	Hydroxypropyl Methylcellulose
ICPs	Intrinsically Conduction Polymers
***i*-ECD**	Irreversible Electrochromic Display
IoT	Internet of Things
ITO	Indium Tin Oxide
KCl	Potassium Chloride
KH_2PO_4	Potassium Hydrogen Phosphate
LCD	Liquid Crystal Display
LED	Light Emitting Diode
Li^+	Lithium Ion
LiTFSI	Lithium Bis(Trifluoromethanesulfonyl)imide
LUMO	Lowest Unoccupied Molecular Orbital
mA/h	Milliampere Per Hour
mC	Millicoulomb
MeProDOP	Methyl-substituted propylenedioxy-pyrrole
MOFs	Metal Organic Frameworks
mPa·s	Millipascal Second
Mp	Peak Molecular Weight
Mn	Number Average Molecular Weight
MV^{2+}	Methyl Viologen
NCS	N-Chlorosuccinimide
NFC	Near Field Communication
nm	Nanometer
NMR	Nuclear Magnetic Resonance
NO_2DA	Nitrodopamine
NPs	Nanoparticles
OD	Optical Density
OM	Optical Modulation
OMeDA	Methoxydopamine
PANI	Polyaniline
PAN	Polyacrylonitrile
PB	Prussian Blue
PBS	Phosphate Buffered Saline
PC	Propylene carbonate
PCB	Printed Circuit Board
PD	Polydispersity
PDA	Polydopamine
PEC	Polyethylene Carbonate
PEDOT:PSS	Poly(3,4-ethylenedioxythiophene):Poly(styrene Sulfonate)
PEG	Polyethylene Glycol
PEO	Polyethylene oxide
PET	Polyethylene Terephthalate

PMMA	Poly(Methyl Methacrylate)
PPy	Polypyrrole
ProDOP	Propylenedioxy-pyrrole
Pt	Platinum
PXDOT	Poly(3,4-Alkylenedioxythiophene)
PXDOP	Poly(3,4-Alkylenedioxypyrrole)
R.E.	Reference Electrode
REDOX	Reduction-Oxidation
r-ECD	Reversible Electrochromic Display
RGB	Red Green Blue
ROS	Reactive oxygen species
RH	Relative Humidity
rt	Room Temperature
s	Second
SAL	Silicon Austria Lab
SCs	Supercapacitors
SCE	Saturated calomel electrode
SEM	Scanning Electron Microscopy
t	Time
T@540 nm	Transmittance Recorded at 540 nm
T@600 nm	Transmittance Recorded at 600 nm
tOX,90%	Oxidation time to reach 90 percent of T@600 nm
tRED,90%	Reduction time to reach 90 percent of T@600 nm
THF	Tetrahydrofuran
TFT	Thin Film Transistor
TLC	Thin Layer Chromatography
TNO	Niobium-Doped Titanium Oxide
UV-Vis	Ultraviolet–Visible Spectroscopy
V	Voltage
W.E.	Working Electrode
WO_3	Tungsten Trioxide
Wt	Weight
XPS	X-ray Photoelectron Spectroscopy
XRD	X-ray Diffraction
λ	Wavelength
σ	Conductivity
Ω/sq	Sheet Resistance

ABSTRACT

The continuous growth of sensor technologies across industrial, biomedical, and consumer markets has intensified the need for reliable strategies to communicate sensor outputs in a clear, interpretable, and user-friendly manner. As sensing capabilities become increasingly embedded in mass-manufactured goods, the translation of raw sensor data into immediate visual information is essential for ensuring product safety, quality monitoring, and process traceability. Visual indicators, in particular, represent a powerful and low-barrier interface, enabling rapid information transfer without the need for external electronics or user training. Within this context, two fundamentally different types of visual signalling systems can be identified. Reversible systems capable of repeatedly switching between multiple optical states and irreversible systems that undergo a single, permanent optical transition after activation. The selection of one or the other is governed by operational requirements, environmental constraints, device longevity, and the nature of the event to be communicated.

Irreversible systems offer unique advantages when a single, time-stamped, and tamper-evident visual message is required. Chemical irreversibility, often regarded as a limitation in dynamic devices, becomes an enabling principle for designing materials whose optical state can be permanently altered through a well-defined triggering stimulus. Such materials are particularly attractive for the production of disposable smart labels because they provide unambiguous readouts, are inherently robust to environmental fluctuations after activation, and can be engineered using low-cost chemistries. These characteristics are especially valuable in temperature-sensitive supply chains, such as those for food, pharmaceuticals, vaccines, and biological samples, where deviations from the prescribed thermal range can pose serious safety and economic risks. Cost-effective irreversible chromogenic labels capable of permanently registering thermal events would significantly enhance the monitoring, safety, and sustainability of these logistics infrastructures.

This dissertation presents the development, characterization, and engineering of organic irreversible electrochromic displays (*i*-ECDs) designed to undergo a permanent optical transformation upon application of an electrical stimulus. The predominant aim is to create simple, scalable, and environmentally compatible devices that can be incorporated into cold-chain smart labels to provide an unambiguous visual signal linked to temperature-dependent triggering logic. The thesis is composed of four chapters. Chapter 1 provides a comprehensive introduction to smart-label technologies and electrochromic (EC) materials. It surveys existing thermal indicators, including mechanical, chemical, and hybrid systems, outlining their operational principles and limitations. The chapter also reviews the state of the art in reversible

and irreversible ECDs, with emphasis on organic systems, and delineates the specific advantages of irreversible EC approaches for disposable temperature-tracking applications.

Chapter 2 forms the central body of the work and details the conceptualization, fabrication, and mechanistic understanding of dopamine-based *i*-ECDs. The chapter examines the effect of key formulation and device parameters, including electrolyte pH, dopamine concentration, and operational voltage, on the activation behaviour, colour contrast, and device stability. Extensive surface characterization through SEM, AFM, and XPS is employed to uncover the structural and chemical transformations responsible for irreversibility, providing a correlation between electrochemical oxidation, polymer deposition, and optical modification. A full reliability and ageing study assesses the long-term stability of the activated optical state and quantifies the total electrical charge required for activation. Additionally, the chapter investigates various dopamine derivatives, enabling a structure–function analysis that elucidates how functional groups influence polymerization pathways and EC performance. The final section demonstrates electronic integration of the *i*-ECDs into a preliminary smart-label architecture, highlighting the feasibility of incorporating these devices into real-world cold-chain systems.

Chapter 3 expands the dopamine platform by introducing gelling agents capable of increasing the viscosity of the aqueous EC formulation, allowing for coating and printing processes. Rheological modification, printability, and film-forming behaviour are explored in detail. The impact of these modifications on activation charge, colour development, mechanical stability, and long-term robustness is studied through a direct comparison between printed systems and liquid-based devices. Fabrication of *i*-ECDs using doctor-blade deposition is demonstrated, followed by preliminary results from screen-printing trials, establishing the technical basis for scalable manufacturing.

In Chapter 4, an alternative irreversible EC approach based on polythiophene (PTs) derivatives is explored. The chapter introduces the concept of locking the oxidized state of PTs by promoting chemical reactions with sacrificial nucleophiles, permanently altering the polymer's electronic structure. Initially, controlled oxidation is used to increase solubility and partially remove the polymer layer, enabling modulation of thickness and colour intensity. Subsequently, a broad library of alcohols and amines is evaluated for their ability to react with the oxidized PTs backbone, aiming to shift the resulting bandgap outside the visible region and thus eliminate the original colour. This approach offers a second, mechanistically distinct strategy for irreversible electrochromism and demonstrates its potential for generalization beyond dopamine-based systems.

Overall, this work establishes a broad framework for designing, optimizing, and implementing organic irreversible EC systems for smart-label applications. It introduces two independent irreversible chromogenic concepts, provides mechanistic insights into their activation pathways, and demonstrates their compatibility with low-cost processing and scalable fabrication methods. The outcomes of this research underscore the potential of organic *i*-ECDs as versatile tools for next-generation temperature-monitoring technologies in cold-chain logistics and beyond.

ZUSAMMENFASSUNG

Das kontinuierliche Wachstum sensortechnologischer Anwendungen in industriellen, biomedizinischen und verbraucherorientierten Märkten hat den Bedarf an zuverlässigen Strategien verstärkt, um Sensorsignale klar, interpretierbar und nutzerfreundlich zu kommunizieren. Da Sensorkomponenten zunehmend in massenproduzierte Güter integriert werden, ist die Umwandlung von Rohsensordaten in unmittelbare visuelle Informationen entscheidend, um Produktsicherheit, Qualitätsüberwachung und Prozessrückverfolgbarkeit zu gewährleisten. Visuelle Indikatoren stellen dabei eine leistungsstarke und zugängliche Schnittstelle dar, da sie eine schnelle Informationsübertragung ermöglichen, ohne dass externe Elektronik oder Nutzerschulung erforderlich sind. In diesem Kontext lassen sich zwei grundsätzlich unterschiedliche Arten visueller Signalgebungssysteme unterscheiden, nämlich reversible Systeme, die wiederholt zwischen mehreren optischen Zuständen wechseln können, und irreversible Systeme, die nach Aktivierung einen einzigen, permanenten optischen Übergang durchlaufen. Die Auswahl zwischen beiden Ansätzen hängt von betrieblichen Anforderungen, Umweltbedingungen, Lebensdauer des Geräts sowie der Art des zu kommunizierenden Ereignisses ab.

Irreversible Systeme bieten spezifische Vorteile, wenn eine einmalige, zeitgestempelte und manipulationssichere visuelle Anzeige benötigt wird. Chemische Irreversibilität, die in dynamischen Systemen häufig als Einschränkung gilt, wird hier zu einem grundlegenden Prinzip für die Entwicklung von Materialien, deren optischer Zustand durch einen definierten Auslösereiz dauerhaft verändert wird. Solche Materialien eignen sich besonders für die Herstellung von Einweg-Smart-Labels, da sie eindeutige Anzeigen liefern, nach Aktivierung gegenüber Umweltschwankungen robust sind und auf kostengünstigen Reaktionschemien basieren können. Diese Eigenschaften sind insbesondere in temperatursensitiven Lieferketten von großem Wert, etwa bei Lebensmitteln, Pharmazeutika, Impfstoffen oder biologischen

Proben, bei denen Abweichungen vom vorgeschriebenen Temperaturbereich erhebliche Sicherheits- und wirtschaftliche Risiken darstellen können. Kosteneffiziente irreversible chromogene Labels, die thermische Ereignisse dauerhaft registrieren können, würden die Überwachung, Sicherheit und Nachhaltigkeit solcher Logistikinfrastrukturen deutlich verbessern.

Diese Dissertation präsentiert die Entwicklung, Charakterisierung und technologische Umsetzung organischer irreversibler elektrochromer Displays (*i*-ECDs), die bei Anlegen eines elektrischen Stimulus eine permanente optische Transformation durchlaufen. Das übergeordnete Ziel besteht darin, einfache, skalierbare und umweltverträgliche Geräte zu entwickeln, die in temperaturabhängige Smart-Labels integriert werden können und ein eindeutiges visuelles Signal liefern, das an eine temperaturgesteuerte Auslöselogik gekoppelt ist. Die Arbeit gliedert sich in vier Kapitel. Kapitel 1 bietet eine umfassende Einführung in Smart-Label-Technologien und elektrochrome Materialien. Es gibt einen Überblick über bestehende thermische Indikatoren, darunter mechanische, chemische und hybride Systeme, und erläutert deren Funktionsprinzipien und Grenzen. Zudem werden der Stand der Technik reversibler und irreversibler ECDs, mit besonderem Fokus auf organische Systeme, dargestellt sowie die spezifischen Vorteile irreversibler elektrochromer Ansätze für Einweg-Temperaturüberwachungssysteme dargelegt.

Kapitel 2 bildet den zentralen Kern der Arbeit und beschreibt die Konzeption, Herstellung und mechanistische Aufklärung von Dopamin-basierten *i*-ECDs. Untersucht wird der Einfluss zentraler Formulierungs- und Geräteparameter wie ElektrolytpH, Dopaminkonzentration und Betriebsspannung auf Aktivierungsverhalten, Farbkontrast und Gerätestabilität. Umfassende Oberflächenanalysen mittels SEM, AFM und XPS liefern Einblicke in die strukturellen und chemischen Transformationen, die der Irreversibilität zugrunde liegen, und ermöglichen eine Korrelation zwischen elektrochemischer Oxidation, Polymerabscheidung und optischer Modifikation. Eine vollständige Zuverlässigkeits- und Alterungsstudie bewertet die Langzeitstabilität des aktivierten optischen Zustands und quantifiziert die für die Aktivierung benötigte elektrische Gesamtladung. Darüber hinaus werden verschiedene Dopaminderivate untersucht, was eine Struktur-Funktions-Analyse ermöglicht, die den Einfluss funktioneller Gruppen auf Polymerisationspfade und elektrochrome Leistung aufzeigt. Der letzte Abschnitt des Kapitels demonstriert die elektronische Integration der *i*-ECDs in eine erste Smart-Label-Architektur und zeigt damit die Anwendbarkeit der Geräte in realen Kühlkettenumgebungen.

Kapitel 3 erweitert die Dopaminplattform, indem Geliermittel eingeführt werden, die die Viskosität der wässrigen elektrochromen Formulierung erhöhen und damit Beschichtungs-

sowie Druckprozesse ermöglichen. Rheologische Modifikation, Druckbarkeit und Filmbildungsverhalten werden detailliert untersucht. Der Einfluss dieser Anpassungen auf Aktivierungsladung, Farbentwicklung, mechanische Stabilität und Langzeitrobustheit wird durch einen direkten Vergleich zwischen gedruckten Systemen und flüssigen Geräten analysiert. Die Herstellung von *i*-ECDs mittels Rakelbeschichtung wird demonstriert, gefolgt von ersten Ergebnissen aus Siebdruckversuchen, die die technische Grundlage für eine skalierbare Fertigung legen.

In Kapitel 4 wird ein alternativer irreversibler elektrochromer Ansatz auf Basis von Polythiophen-Derivaten (PTs) untersucht. Das Kapitel führt das Konzept ein, den oxidierten Zustand von PTs durch gezielte Reaktionen mit opfernden Nukleophilen zu fixieren, wodurch die elektronische Struktur des Polymers dauerhaft verändert wird. Zunächst wird eine kontrollierte Oxidation eingesetzt, um die Löslichkeit zu erhöhen und die Polymerlage teilweise abzutragen, wodurch Schichtdicke und Farbintensität modulierbar werden. Anschließend wird eine umfangreiche Bibliothek an Alkoholen und Aminen daraufhin geprüft, inwieweit sie mit dem oxidierten PT-Rückgrat reagieren können, um die resultierende Bandlücke außerhalb des sichtbaren Spektrums zu verschieben und damit die ursprüngliche Farbe vollständig zu eliminieren. Dieser Ansatz bietet eine zweite, mechanistisch unabhängige Strategie für irreversible Elektrochromie und zeigt das Potenzial zur Übertragbarkeit über Dopamin-basierte Systeme hinaus.

Insgesamt etabliert diese Arbeit ein umfassendes Rahmenwerk zur Entwicklung, Optimierung und Implementierung organischer irreversibler elektrochromer Systeme für Smart-Label-Anwendungen. Sie führt zwei unabhängige irreversible chromogene Konzepte ein, liefert mechanistische Einblicke in deren Aktivierungswege und demonstriert deren Kompatibilität mit kostengünstigen Prozessen und skalierbaren Fertigungsmethoden. Die Ergebnisse unterstreichen das Potenzial organischer *i*-ECDs als vielseitige Werkzeuge für zukünftige Temperaturüberwachungstechnologien in Kühlketten und darüber hinaus.

CHAPTER 1

INTRODUCTION

1.1 The phenomenon of electrochromism

1.1.1 Definition and basic principles

With the rapid progression of contemporary display technologies, electrochromic (EC) displays, a type of non-emissive (passive) display, have gained significant interest.[1,2] These displays operate based on the principle of electrochromism, which refers to the reversible change in a material's colour, transmittance, absorbance, or reflectance when an electrical voltage is applied.[3] This change results from the movement of ions or electrons within the material, thereby modifying its optical properties. EC materials, which take their name from the phenomenon, exhibit a dynamic transition between states, shifting from transparent to opaque or displaying a range of colours, all driven by redox (reduction-oxidation) reactions triggered by electrical stimulation allowing the display to present content and information effectively.[4] Unlike widely commercialized active light-emitting display technologies such as cathode ray tube (CRT) displays,[5] liquid crystal (LCDs) displays[6] and light-emitting diode (LED) displays,[7] as well as established non-emissive display types like electrophoretic,[8] dielectrophoretic,[9] electrowetting,[10] and photonic crystal displays,[11] the research and development of electrochromic displays (ECDs) is still in its growing stages. In recent years, the number of scholarly articles and research papers focusing on ECDs has seen a notable increase, reflecting the growing interest in this technology. For example, as illustrated in Figure 1.1, the number of articles related to ECDs has skyrocketed, with over 800 articles published in 2020 alone, compared to fewer than 50 publications per year in the early stages of the field, highlighting the rapidly expanding research efforts and the technology's potential to significantly impact the display industry.[12]

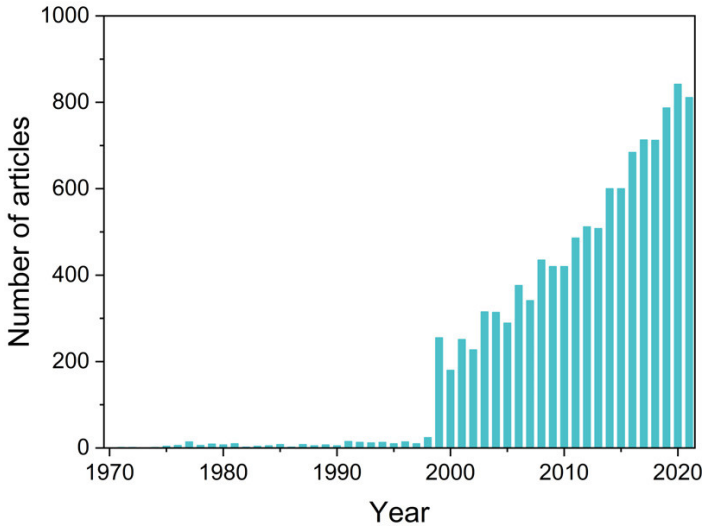


Figure 1.1. Trend in the number of articles published on electrochromic (EC) research from 1970 to 2021. The data was sourced from the Web of Science using the search terms "electrochromic" OR "electrochromism" to identify relevant publications.[12]

While high-quality ECDs products have not yet achieved commercial maturity, their distinctive advantages and significant potential, as will be discussed further in this chapter, indicate that they could emerge as a highly anticipated next-generation display technology. ECDs offer excellent outdoor readability and are gentle on the eyes, thanks to their subtractive colour mode, which relies on light absorption rather than emission.[12] Unlike traditional displays that emit light, the visuals ECDs are produced through colour changes in materials driven by electrochemical redox processes. This approach significantly reduces the risk of eye damage from intense blue light, providing a more comfortable and enjoyable reading experience, even in bright ambient light conditions.[13] Furthermore, ECDs are characterized by their flexibility, scalability, foldability, and transparency.[14,15] Many EC materials are highly compatible with a variety of substrates, including glass, metal, plastic, and even fibers and textiles, making them ideal for future portable electronics, such as wearable sensors.[16] Finally, this technology have demonstrated lower energy consumption than LCDs and OLEDs because of their optical memory effect, which enables them to retain images even when power is removed. Unlike LCDs and OLEDs, which require constant power to maintain an image, ECDs only need power when changing the display, making them more energy-efficient.

The unique properties of ECDs, such as their non-emissive nature, reduced energy consumption, and adaptability to various substrates, position them as promising candidates for a wide range of applications. Although the technology is still in its developmental stages, the potential for ECDs to revolutionize the display industry cannot be underestimated. As research continues to optimize and enhance the performance of these materials, the promise of ECDs becoming a key player in the next generation of display technologies grows ever stronger. In

the following sections, we will explore the specific applications of electrochromism, beginning with the construction of ECDs and exploring how their properties can be exploited across different fields and industries.

1.1.2 The electrochromic display (ECD)

1.1.2.1 Building structure of ECD

ECDs are a specific type of electrochemical cell. These devices typically feature a multi-layered structure in which two EC layers are separated by an electrolyte layer.[17] The operation of an ECD is controlled by an external voltage applied through conductive electrodes situated on either side of the EC layers. The fundamental architecture of an ECD mainly consists of five distinct layers, which can be either stacked on a single substrate or sandwiched between two substrates in a laminated configuration, Figure 1.2a.[18] These layers together form the final structure of the ECD, as illustrated in Figure 1.2b.[19]

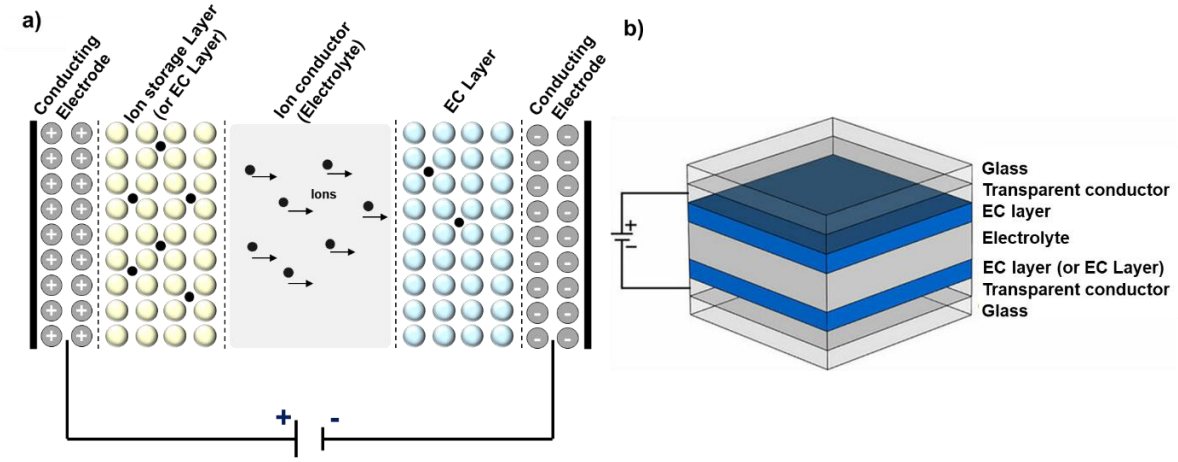


Figure 1.2. a) Cross-sectional diagram illustrating the layers in a typical laminated ECD. b) Structure of an ECD.[19]

These layers include the EC layers, the ion-storage layer, the electrolyte layer, and the transparent conductive electrodes. The EC and ion-storage layers are mixed conductors, capable of conducting both ions and electrons, and they are primarily responsible for the colour-changing properties of the display. There are many materials that exhibit EC properties, and they can be broadly categorized into inorganic and organic types. Inorganic EC materials include transition metal oxides such as tungsten oxide (WO_3), which is one of the most widely studied and used materials due to its high stability and reversible coloration.[20,21] Other examples include nickel oxide (NiO),[22,23] molybdenum oxide (MoO_3),[21] and vanadium oxide (V_2O_5),[24] each offering different optical properties and coloration efficiencies. On the organic

side, EC polymers (ECPs) such as polyaniline (PANI),[25,26] polythiophene (PT),[27–29]and poly(3,4-ethylenedioxythiophene) (PEDOT)[30,31] are commonly used. These materials are favoured for their flexibility, tunable colours, and ease of processing. Additionally, viologens, a class of organic compounds, are also utilized in EC applications, known for their distinct colour changes upon reduction. The various materials that can be employed for electrochromism will be analysed and discussed in the following paragraphs, where their properties, advantages, and potential applications in ECDs will be further explored.

The electrolyte layer, on the other hand, is a pure ion conductor that separates the two EC layers and facilitates ion movement when an external voltage is applied. Its role is crucial in maintaining the neutrality of the system and enabling the electrochemical reactions essential for the device's operation.[32] There are four main types of electrolytes used in ECDs: aqueous, organic liquid, ionic liquid, and solid polymer. Aqueous and organic liquid electrolytes are commonly utilized in EC smart glass due to their durability and ease of manufacturing. However, these electrolytes are not without drawbacks, such as potential leakage and limited chemical stability. Organic liquid electrolytes typically include propylene carbonate (PC) or ethylene carbonate, with salts like $LiClO_4$ or $NaClO_4$ added to enhance their EC properties. Ionic liquid electrolytes often contain compounds such as $EtNH_3NO_3$. The choice of salt in these electrolyte solutions directly influences the ion transport properties and overall electrochemical behaviour of the ECD. The ionic radius of the chosen ion plays a significant role in determining the electrolyte's efficiency. Ions like potassium (K^+) have a larger ionic radius (1.33 Å) compared to smaller ions such as hydrogen (H^+) with an ionic radius of only 0.29 Å, Figure 1.3. Li^+ ions, with an ionic radius of 0.68 Å, are widely used in ECDs due to their high ionic conductivity, which contributes to rapid switching speeds, high coloration efficiency, and wide optical modulation ranges. These lithium-based electrolytes, especially when dissolved in organic solvents like PC, have been a mainstay in the field due to their ability to facilitate effective ion transport across EC layers such as WO_3. However, the small size of Li^+ also means that it can be easily trapped within the host electrode over time, leading to degradation in device performance.[33,34] $NaClO_4$, another commonly employed salt, offers a cost-effective and safer alternative to lithium-based systems. Despite the larger ionic radius of Na^+ (1.01 Å), which can slow down the insertion and extraction processes within the EC materials, it is still effective in devices designed to accommodate these larger ions. Notably, Prussian Blue (PB) and its analogy are particularly well-suited for Na^+ based systems due to their open-framework structures, which can readily host larger ions. These materials, when paired with sodium-based electrolytes, exhibit excellent EC performance, including high

coloration efficiency (CE, 149.3 cm^2/C) and stability over extended cycling (10000 cycles).[35–37]

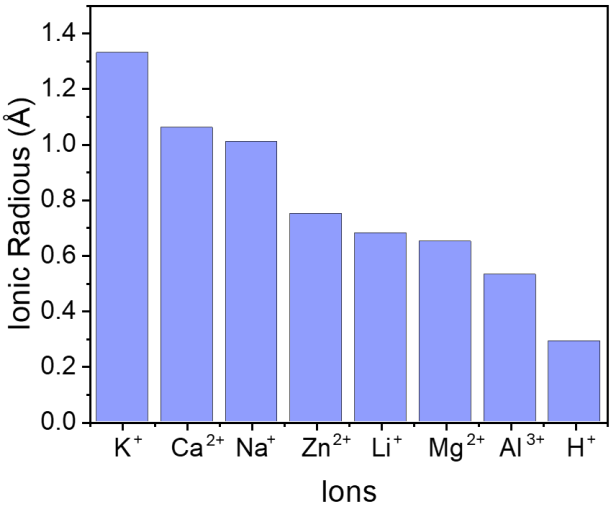


Figure 1.3. Ionic radius of K^+, Ca^{2+}, Na^+, Zn^{2+}, Li^+, Mg^{2+}, Al^{3+}, H^+. Data acquired by the work of Yilin Ding et at.[38]

Ionic liquid electrolytes are another important category, often selected for their wide electrochemical windows and thermal stability. These electrolytes are typically less volatile and more chemically stable than traditional organic solvents, reducing the risk of leakage and enhancing the longevity of ECDs. Salts such as lithium bis(trifluoromethanesulfonyl)imide (LiTFSI) are frequently used in conjunction with ionic liquids, such as 1-butyl-3-methylimidazolium bis(trifluoromethanesulfonyl)imide (BMITFSI). The combination of LiTFSI with BMITFSI has been shown to maintain high ionic conductivity, even in a low-viscosity environment, contributing to the stable performance of ionic liquid-based ECDs.[39] Solid polymer electrolytes represent a distinct approach, utilizing a polymer matrix, often in gel or solid form, to immobilize the electrolyte.[40,41] These systems typically involve a polymer such as poly(ethylene oxide) (PEO) or poly(methyl methacrylate) (PMMA), in which salts like $LiClO_4$ or LiTFSI are dissolved. The polymer matrix provides mechanical flexibility, while the dissolved salts ensure ionic conductivity. The performance of solid polymer electrolytes is heavily influenced by the interaction between the polymer and the salt. For instance, in PEO-based electrolytes, the polymer chains coordinate with lithium ions, facilitating their transport across the electrolyte.[42,43]

Finally, the transparent conductive electrodes, deposited on the substrate, typically a transparent plastic such as polyethylene terephthalate (PET) or glass, serve to complete the ECD. These electrodes are referred to as the working electrode (W.E.) and the counter electrode

(C.E.), to which the positive and negative terminals are connected. Both electrodes must be transparent to visible light, allowing the EC materials to be seen from outside. Nowadays, the most effective combination of light transmission and conductivity available is indium tin oxide (ITO). ITO is an inorganic material with a low resistance coefficient (0.0001 Ohm/cm), high visible light transmittance (over 90%), and strong infrared radiation reflection, making it suitable for various applications in devices and systems.[44–46] However, one of the drawbacks of ITO is its high cost, as indium is a rare earth element. As an alternative, other highly conductive oxides can be used, such as fluorine-doped tin oxide (SnO_2 or FTO),[47] aluminium-doped zinc oxide (ZnO or AZO),[48] gallium-doped zinc oxide (ZnO or GZO),[49] and niobium-doped titanium oxide (TiO_2 or TNO).[50] Beyond conductive oxides, organic polymers also present viable alternatives. Materials like PEDOT,[51] PANI,[52] and polypyrrole (PPY)[53] are commonly used as EC active layers within displays. However, when these polymers are applied with a thin layer, they can become transparent while maintaining their electrical conductivity. This property enables their use not only as active layers but also as transparent electrodes, effectively substituting inorganic materials in ECDs.[54]

ECDs can be built using different architectures, with two common approaches being the vertical stack and coplanar configurations. In a vertical stack, the EC materials and conductive layers are positioned on two separate substrates, typically layers of PET with an ITO coating (PET-ITO). These layers are separated by an electrolyte. The EC material is printed on both substrates, and the ions travel between these layers through the electrolyte when a voltage is applied. This structure allows for the two EC layers to overlap, which can enable more complex and detailed visual effects, though it requires precise alignment to avoid short circuits, Figure 1.4a. In contrast, coplanar structures place both the EC material on the same layer, but these are separated into different regions with distinct conductive tracks. The electrolyte facilitates the ion exchange between adjacent EC regions, and the ions move horizontally across the surface rather than vertically between layers, Figure 1.4b. The coplanar design simplifies the construction process by eliminating the need for precise layering and alignment and reducing the numbers of required layers. Nevertheless, it restricts the arrangement of visual elements since the EC layers must be placed side by side.

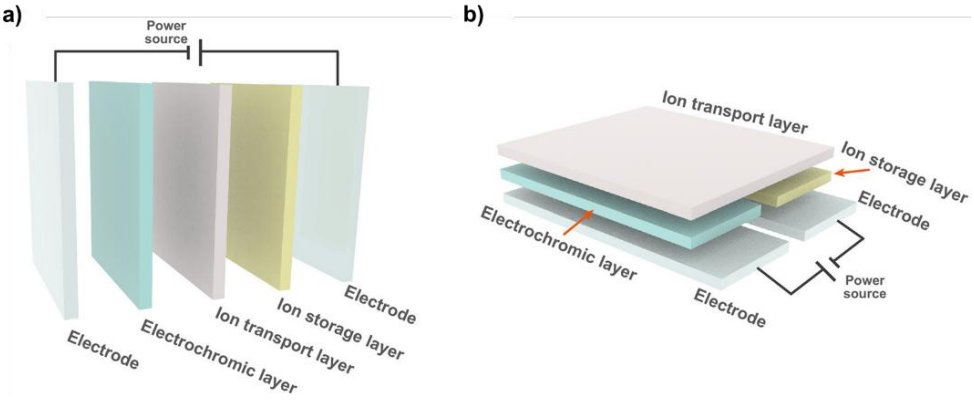


Figure 1.4. Visual graphic of and ECD in a) vertical and b) coplanar architecture.[12]

The vertical stack architecture in ECDs has a significantly higher switching speed compared to the coplanar design.[55] Liu et al. demonstrated that the switching time for a vertical ECD with a solution electrolyte is approximately 1 second, whereas the coplanar configuration requires 2 seconds to achieve full colour-switching. When using a gel electrolyte, the vertical structure maintains its fast switching time of 1 second, but the lateral design exhibits a slower response of 2-3 seconds due to the longer ion transport distance within the electrolyte.[55] Similarly, Brooke et al. reported that lateral ECDs exhibited switching times over than a minute, whereas vertical ECDs demonstrated significantly faster switching, with 1.9 seconds from the oxidized state to the reduced state and 3.3 seconds for the reverse switching.[56]

This faster switching is primarily due to how ions move to balance the charge generated by the redox reactions occurring during the voltage application. In the vertical stack configuration, the EC materials are layered one on top of the other, with a thin layer of electrolyte in between. When a voltage is applied, the ions move vertically between these two layers. The direct and short path that the ions travel is a key reason for the faster switching speed. Since the ions have a much shorter distance to cover, the electrochemical reactions, oxidation and reduction, required to change the display's colour or transparency occur more quickly. In contrast, the coplanar design places both EC materials side by side on the same layer. In this configuration, the ions must travel laterally across the surface of the display, through the electrolyte, to complete the switching process. This lateral movement involves a much longer distance, which slows down the ion transport and leads to slower switching times. The longer the path the ions must travel to balance the charges, the more time the switching process requires, which is why the coplanar structure lags behind the vertical stack in terms of speed.[57]

ECDs are also classified based on their interaction with light, operating in either transmittance or reflection mode. These modes determine whether the device controls light passing through it or light reflecting from its surface.

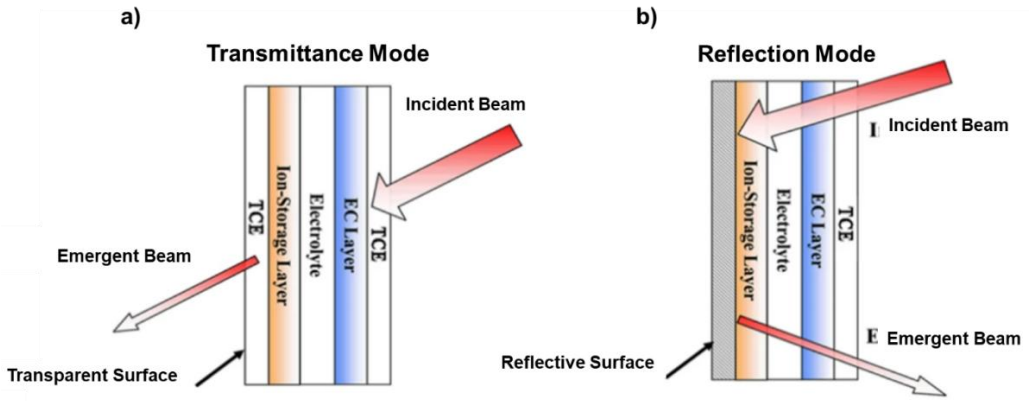


Figure 1.5. Diagram of an ECD operating in a) Transmittance and b) Reflection Mode.[58]

In transmittance mode, ECDs modulate the amount of light that passes through them, making this mode ideal for applications such as smart windows, where controlling both light and heat is critical, Figure 1.5a. Typically, the device consists of transparent conducting oxides and EC materials like WO_3.[22] When voltage is applied, ions are intercalated into the EC layer reducing its transparency. This process enables control over the amount of light passing through windows, helping to regulate heat and improve energy efficiency in buildings. In contrast, reflection mode focuses on modulating the amount of light reflected by the device, making it ideal for applications like glare-reducing rear-view mirrors and ECDs.[59] In this mode, the EC material change its reflectivity when ions are intercalated, enabling the device to control glare and ECDs to change its colours/contrast.

1.1.2.2 Performance Index

The Performance Index of an ECD involves metrics used to assess the functionality and effectiveness of EC materials and devices. These include important factors such as optical modulation (OM), contrast ratio (CR), response time, coloration efficiency (CE), durability, and lifetime, which are critical in determining display quality. These performance parameters have been widely studied and discussed over recent years, particularly in the context of display technologies.[60] In certain cases, additional factors like optical memory effect and bistability must also be considered, especially for static displays or energy storage devices. Furthermore, colour purity and tunability are crucial for full-colour displays. By evaluating these performance metrics, developers can optimize EC materials for specific uses and enhance overall display performance. We will now explore these indices, with a focus on their technical implications for ECDs.

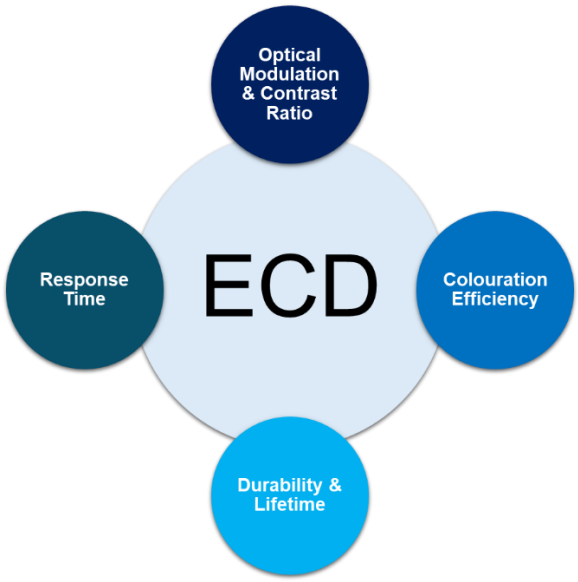


Figure 1.6. Performance Indexes of ECDs.[12]

1.1.2.2.1 Optical modulation and contrast ratio

OM serves as a parameter for assessing the colour-switching capability of an ECD. It is typically expressed as the change in absorbance or transmittance at the characteristic wavelength before and after the colour transition, as indicated in Equation 1.1. Here, $T_{coloured}$ and $T_{bleached}$ represent the transmittance in the coloured and bleached states, while $A_{coloured}$, and $A_{bleached}$ denote the corresponding absorbance values. The ΔT and ΔA quantify the OM of the ECD. In reflective displays, the change in reflectivity can similarly be used to measure OM.

Equation 1.1. $$\Delta \mathbf{T} = \mathbf{T_{bleached}} - \mathbf{T_{coloured}} \quad \text{or} \quad \Delta \mathbf{A} = \mathbf{A_{coloured}} - \mathbf{A_{bleached}}$$

In addition to OM, the CR identify the device's ability to switch between its bleached and coloured state, defined as the ratio of transmittance or reflectance in these two states, Equation 1.2.

Equation 1.2. $$\mathbf{CR} = \frac{\mathbf{T_{coloured}}}{\mathbf{T_{bleached}}} \quad \text{or} \quad \mathbf{CR} = \frac{\mathbf{A_{coloured}}}{\mathbf{A_{bleached}}}$$

A high contrast ratio, such as 80–90%, means the bright state is significantly more transmissive or reflective than the dark state, creating sharp, highly visible transitions.[61] A moderate CR around 50–60% still provides noticeable contrast but with less distinct changes.[62] In contrast, a low CR, typically below 30%, results in weak differentiation between the bright and dark states, making the display appear dull with less effective switching. This becomes particularly important in environments with strong ambient light, such as outdoor settings, where a high

CR ensures better visibility and contrast without relying on external light sources, making ECD more efficient and suitable for such conditions.

1.1.2.2.2 Response time

The response time refers to the duration it takes for the display to switch from one optical state to another (e.g., from transparent to opaque or between colours) after an electrical voltage is applied.[63] For an ECD, this is specifically measured as the time required to achieve 90% of its full OM when switching from its bleached (transparent) state to its coloured state, or vice versa.[64] This is often called the colouring or fading time. The choice of 90% as a benchmark is practical because reaching the final 10% of modulation can take disproportionately longer due to the asymptotic nature of the process. Measuring at 90% provides a balance between accuracy and efficiency, as the difference between 90% and 100% is often negligible for most practical applications, such as visual display performance.[65] In general, shorter response times are desirable for ECDs. Unlike EC materials used in smart windows or energy storage systems, where switching times of several minutes are acceptable, ECDs must switch faster, with typical ranges within seconds or even milliseconds, to meet the requirements for information refresh rates.[66]

1.1.2.2.3 Coloration efficiency

Coloration efficiency (CE) is an important parameter in ECDs. It quantifies how efficiently an EC material changes its optical properties (colouration) in response to an applied electric charge. CE is typically defined as the change in optical density (ΔOD) per unit charge density (Q), usually expressed in cm^2/C and is represented by Equation 1.3, where ΔOD is the change in optical density, which is a measure of how much light absorption changes during the coloration or bleaching process and Q is the charge density in coulombs per square centimeter (cm^2/C).

Equation 1.3.

$$\mathbf{CE} = \frac{\mathbf{\Delta OD}}{\mathbf{Q}}$$

In the context, OD refers to the material's transparency or darkness, with a higher ΔOD representing a more pronounced colour change in the ECD. According to Fabretto et al., OD values in ECDs typically range between 1.0 and 1.5, with higher values enabling greater optical contrast and more efficient modulation of light transmission.[67] Similarly, Pande et al. reported OD values in the range of 1.1–1.5 as high-performance benchmarks, particularly in ECDs

designed for smart windows and display applications.[46] The charge Q represents the amount of electric charge per unit area that triggers this colour change. The lower the value, the more efficient is the material. A higher CE means that the ECD can achieve a more substantial colour change with less electrical energy, which leads to lower power consumption. In other words, a material with higher CE requires less Q to produce the same level of OM. As a result, materials and devices with higher CE are more desirable due to their greater energy efficiency. One example of an ECD with high CE is reported by Park et al., where an advanced conducting polymer-based ECD exhibited a CE of 366.6 cm^2/C,[68] significantly higher than traditional inorganic materials, such as WO_3 films CE values ranging from 43 cm^2/C to 70 cm^2/C.[69]

1.1.2.2.4 Durability and lifetime

Durability refers to a material or device's capacity to endure harsh external conditions. A reliable ECD must function effectively under extreme conditions, such as temperatures ranging from -40 to 80 °C, humidity levels up to 80%, exposure to solar light and resistance to external mechanical forces.[70] However, organic materials often exhibit limited resistance to light, particularly when exposed to UV radiation and oxygen, leading to photodegradation and material oxidation. This degradation happens because many organic molecules absorb UV light, which provides enough energy to disrupt their molecular bonds, causing structural changes. Moreover, exposure to oxygen accelerates oxidation, further weakening the material by generating reactive oxygen species.[71] The combined impact of UV absorption and oxidation leads to the deterioration of organic materials, compromising their durability and performance. Additionally, the electrolytes in these systems are typically solvent-based, which introduces additional challenges. Water-based electrolytes, in particular, tend to freeze at temperatures below 0 °C, severely impacting the device's functionality in cold conditions. Conversely, at higher temperatures, these solvents are susceptible to rapid evaporation, causing significant performance degradation. The lifetime of an ECD refers to the period over which the device maintains its functional performance, even after multiple electro-optical switching cycles (coloration and bleaching). Ideally, an ECD should demonstrate high reversibility, enduring between 10^4 to 10^6 cycles without notable optical degradation (such as a decrease in ΔT).[23,72] The durability and lifespan of an ECD are closely tied to the materials used and the underlying EC reaction mechanisms. Moreover, these factors are heavily influenced by the quality of the manufacturing process, which plays a decisive role in determining the overall performance and longevity of the device.

1.1.2.3 Applications of ECDs

ECDs have emerged as promising technologies for a wide range of applications, particularly in the fields of energy efficiency,[73] smart building technologies,[74] and adaptive optical systems.[75] The unique ability to modulate light and heat transmission in response to electrical signals makes EC materials particularly useful in applications like smart windows,[76] refection mirrors,[77] and display technologies.[78] As the demand for energy-efficient solutions increases, EC smart windows have collected significant attention for their potential to reduce heating, cooling, and lighting costs by adjusting the amount of sunlight and heat entering buildings.

1.1.2.3.1 Smart windows

EC smart windows are advanced devices that employ EC materials to regulate the amount of transmitted light and heat that passes through them.[79] These windows are typically composed of several layers, including an EC layer, electrolyte, transparent conductive electrodes and glass substrate. The core function of these windows is based on reversible redox reactions occurring in the EC materials. By applying an electrical voltage, the windows can switch between transparent (bleached) and opaque (coloured) states, allowing users to control light transmission, reduce glare, and manage heat gain in various applications such as buildings and vehicles, Figure 1.7. The materials used in EC smart windows include transition metal oxides, organic compounds, and polymers. WO_3 is one of the most commonly used materials due to its excellent EC properties, such as high CE and durability. Other materials like NiO, viologens, and conjugated polymers are also utilized.

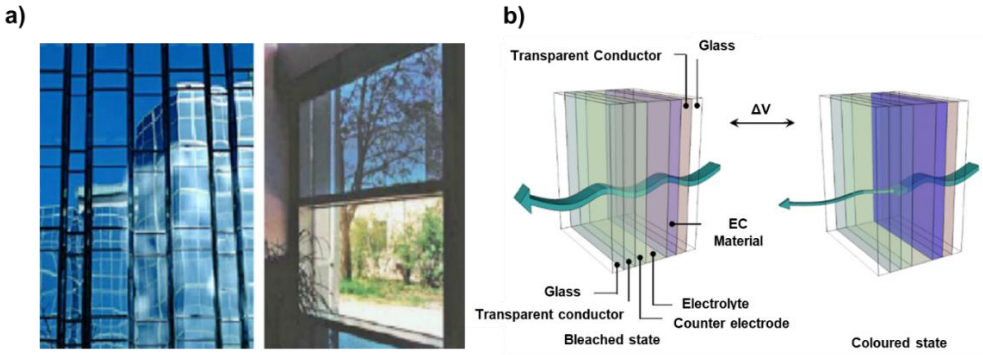


Figure 1.7. a) Real picture of an EC smart window.[80] b) Schematic representation of an EC smart window in its bleached and coloured state.[81]

The redox process is fundamental to the functioning of EC materials. In WO_3, for example, the material begins in a transparent state. When voltage is applied, positive ions such as lithium (Li^+) or hydrogen (H^+) from the ion conductor layer move into the EC layer, causing the

tungsten oxide to undergo a reduction reaction.[81] This changes its optical properties, turning the window opaque or coloured. When the voltage is reversed, the ions are extracted from the EC layer, restoring the material to its original transparent state. This ability to switch between different optical states allows EC materials to be highly effective in controlling light transmission. The detailed analysis and properties of this material will be explored in the following section.

1.1.2.3.2 Reflection mirrors

EC mirrors are reflective devices, primarily used in automotive applications, that can dynamically change their reflectivity in response to an electrical stimulus. These mirrors are particularly effective in reducing glare from headlights of vehicles behind a driver at night. By utilizing EC materials, the reflectance of the mirror can be adjusted to different levels, providing both a safety benefit and increased comfort for drivers. Similarly to smart windows, an EC mirror is built with a glass substrate, a transparent conductive layer (often ITO), and an EC layer to control light transmission. An electrolyte to facilitates ion movement, while a C.E. complements the EC layer. A reflective layer, Ag or Al, enables normal mirror function, and a protective seal ensures durability, Figure 1.8. While EC smart windows operate by modulating the amount of light transmitted through them, EC mirrors work with light reflected off their surface. However, the fundamental working principle remains the same in both cases, as both rely on the redox reactions in the EC materials to change optical properties.

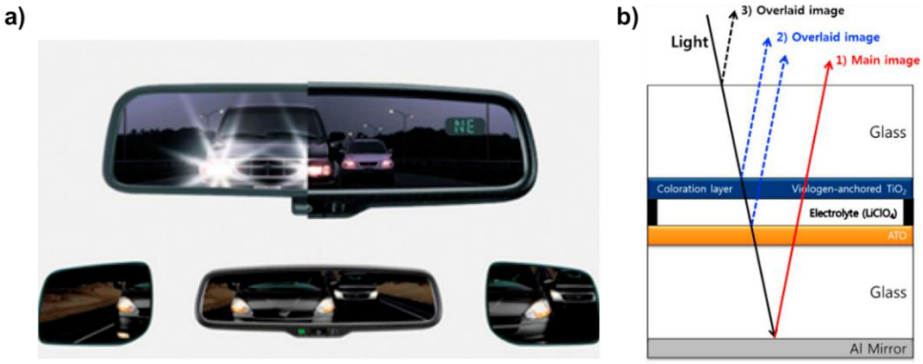


Figure 1.8. a) Real picture of an EC reflection mirror.[82] b) Schematic representation of an EC reflection mirror.[83]

The materials commonly used in EC mirrors include viologen-anchored nanoparticles, transition metal oxides like WO_3 , and NiO.[84] Viologens, in particular, are popular due to their ability to undergo fast and reversible redox reactions, which are essential for the functioning of these devices.[85]

1.1.2.3.3 Display technologies

ECDs technologies have gained significant attention due to their energy efficiency, flexibility, and ability to provide a wide range of applications, including visual indicators and information displays. There are two primary configurations: segmented and pixelated displays.

The segmented ECDs operates in a relatively straightforward way. It is designed to showcase predefined images, numbers, or letters. Additionally, this type of display is capable of dynamically changing certain content by adjusting the input electrical signals. A common example of this is the alphanumeric segmented display, Figure 1.9.[86] This type of display commonly employs a point-to-point driving system, where each display unit is individually connected to an electrode lead. EC segmented displays have recently gained significant attention because of their promising application potential in the design of intelligent displays, known for their vibrant colours and striking patterns. However, while they excel in aesthetic appeal, their capacity to adjust displayed information is more limited compared to pixelated displays.

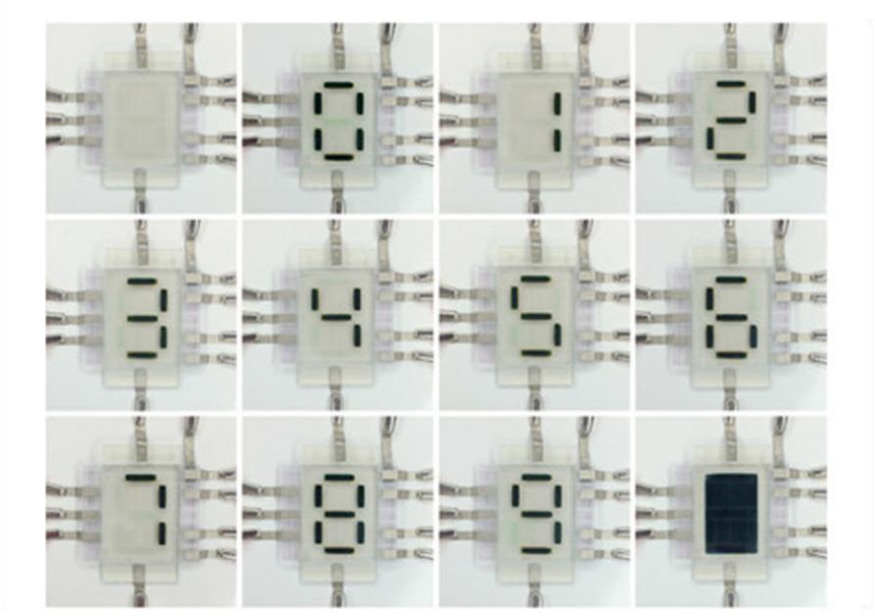


Figure 1.9. Picture of a segmented ECD.[86]

The crucial aspect of creating segmented displays lies in the fabrication of EC patterns. Based on the operating principle of ECDs, several steps must be followed, including electron transfer on the electrodes and at the interfaces between the electrode and active material, electrochemically driven redox reactions of the active materials, and ion transfer within the ECD. Furthermore, efficient patterning can be achieved through precise local spatial control, enhancing the display's overall performance and design flexibility. Many strategies and deposition techniques, such as laser etching, inkjet printing, and various coating/printing

methods, can be employed to create EC patterns. Significant attention has been dedicated to these methods in Chapter 3, exploring various approaches to optimize the deposition of the EC material and ECDs performances.

Common applications for segmented ECDs include low-power devices such as visual indicators and simple digital readouts on electronic appliances, Figure 1.10a.[87] For instance, automotive dashboards and public transport signage rely on segmented ECDs to provide essential information with low energy consumption. Additionally, electronic shelf labels in retail environments are a remarkable example, where segmented ECDs dynamically display pricing and product information, optimizing energy use while delivering clear, functional visual indicators, Figure 1.10b.[88]



Figure 1.10. a) Segmented magenta to colourless ECD.[87] b) Multicolour bistable electronic shelf labels based on EC materials.[88]

In contrast, pixelated feature take ECD technology a step further. Unlike segmented displays, which are limited to predefined segments, pixelated ECDs consist of individual pixels that can be controlled independently, Figure 1.11. This offers higher resolution and greater flexibility, enabling the dynamic display of more complex and detailed visual information.

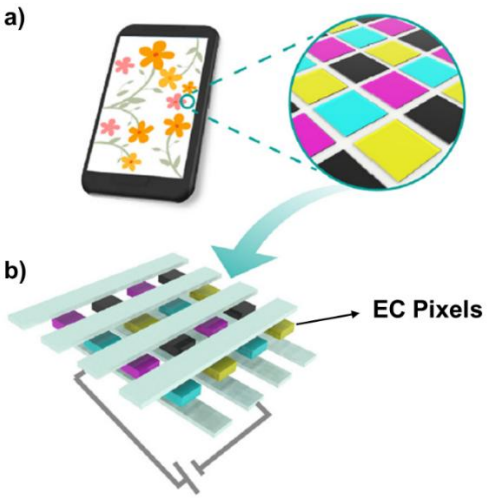


Figure 1.11. a) An EC pixel display designed for future smartphone screens utilizing EC subpixels based on CMYK printing colours. b) Structure of EC pixel displays, which consists of electrodes, EC pixels, and external circuits.[89]

By managing the "on/off" state and ratio of smart pixels, the displays can enable flexible switching and dynamic adjustment of the displayed content. However, constructing an optimal EC display that uses individually addressable EC smart pixels remains a significant challenge. Additionally, these applications demand a higher level of system coordination, involving EC pixels, electrodes, and external circuits.

An EC pixel is generally composed of one or several smaller elements, known as subpixels. The final colour of the pixel depends on how strongly each of these subpixels responds, allowing the generation of a variety of colours and intermediate shades. Because EC materials typically modify colour by absorbing specific wavelengths of light, they follow a subtractive colour mechanism. For this reason, the CMYK system (cyan, magenta, yellow, and black) is often seen as a logical design strategy. Despite this, implementing high-performing CMYK-based EC subpixels remains difficult. Therefore, even a smaller selection of colours can still be sufficient for many practical applications. As the field of EC materials continues to develop, researchers have been able to produce a wider variety of bright and distinct colours, which supports the future design of multicolour EC devices. In organic EC systems, the final colour is mainly determined by the molecular structure. For example, in viologens, the colour in the reduced state can change depending on the type of substituents, the level of conjugation, and the nature of the counter ions.[85,90] In a similar way, modifying the side chains of conjugated polymers is a common strategy to tune their colour properties.[91]

A clear example of a pixel-based EC display was demonstrated by Yohan Lee and coworkers.[92] In this case, the red, green, and blue colours were obtained by changing the thickness of WO_3 thin films. The colour change happens through a reversible electrochemical

process, where the redox state of the material is controlled. The device, represented in Figure 1.12a, was produced using photolithography and included a matrix of 789 × 463 pixels. Each pixel measured 75 μm × 75 μm and was divided into three narrow RGB sections, each about 20 μm wide. When a voltage is applied, the pixels change their optical state, moving from a transparent state to a coloured one. Another interesting approach was presented by the group of Jehyoung Koo. They developed a flexible and energy-efficient multicolour EC system, described as an artificial "skin", inspired by the way cephalopods adapt their colour. The device works at low voltage (± 3 V) and is built as an array of 8 × 8 pixels, each with an area of 0.25 cm^2. By selecting different EC polymers, they were able to produce colours like purple, orange, and green. The response time is relatively fast (around 1.5–1.75 seconds), and once the colour is reached, it can be maintained for a long time, specifically over 35000 seconds. Even under strong mechanical stress, such as bending to an 8 mm radius or stretching up to 100%, the system continues to work reliably, which is important for adaptive camouflage applications.[93]

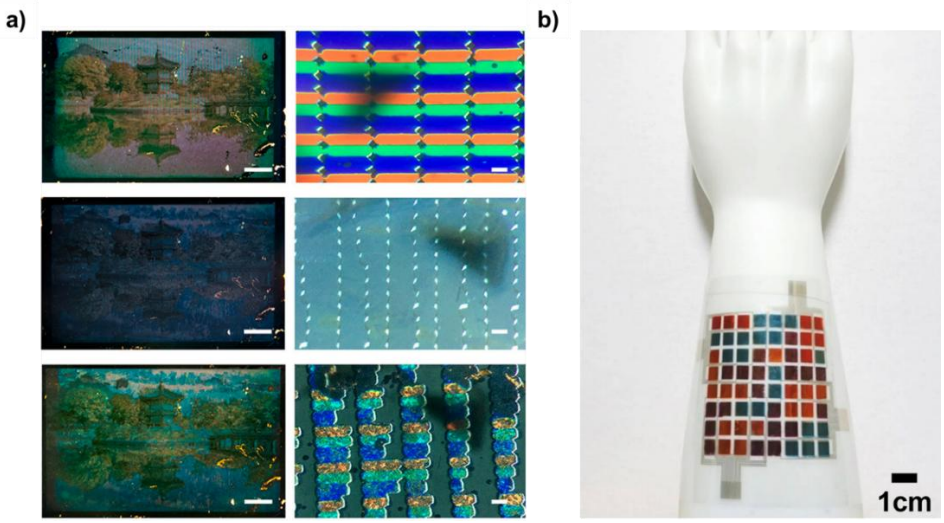


Figure 1.12. a) Images of transmission-mode pixelated ECD during electrochemically induced redox reactions, along with their corresponding microscopic photographs.[92] b) Picture of a low-power, deformable dynamic multicolour EC skin (DMECS) attached to a model hand.[93]

To explore deeper into the development and properties of EC materials, the next section will focus specifically on the materials employed in such applications, including their chemical composition, structural functionalization, redox reactions and performance enhancements. Understanding these aspects is crucial for tuning important properties of ECDs, such as colour, switching time, CE, and overall performance. By exploring the chemistry and material characteristics, the efficiency and functionality of ECDs can be optimized for a wide range of applications.

1.2 Materials for electrochromism

The discovery of EC dates back to 1815, when Jöns Jacob Berzelius observed the alteration of colour in pure WO_3 under dry hydrogen gas flow.[94] Similar findings were documented in 1824 by Friedrich Wöhler, a German chemist, through the reduction of sodium metal.[95] It wasn't until 1961 that the term "electrochromism" was coined by John Rader Platt. Platt's focus was on the colour changes induced by the molecular "Stark effect", which occurs when strong electric fields split spectral absorption lines.[96] A significant step occurred in 1969 when Satyen K. Deb, working at the American Cyanamid Company, applied an electric field to a thin WO_3 film on quartz, a method he termed "electrophotography". Deb's 1973 paper is often viewed as the starting work in EC technology, as it outlines the construction of an ECD using a WO_3 film immersed in an ion-containing electrolyte, resembling current technologies.[97] In 1984, Claes G. Granqvist and Carl M. Lampert introduced and demonstrated the idea of utilizing WO_3-based EC materials for energy-efficient smart windows.[98] This became the first major application of EC materials, drawing attention for its potential commercialization. Researchers and companies quickly focused on smart windows, recognizing their promise for widespread use in modern buildings. Meanwhile, organic EC materials have gradually gained attention, as highlighted in several key reviews. An important figure in this field is John R. Reynolds from the Georgia Institute of Technology, whose research focuses on intrinsically conducting polymers (ICPs) and their applications in EC technology.[99] Reynolds has significantly contributed to the field, particularly by studying the tunability of the bandgap in these polymers, which is essential for controlling their colour and electrical properties.[100,101]

The range of materials explored in EC research is broad, crossing from inorganic to organic and more recently, to metallorganic compounds. Inorganic EC materials are the most studied, with WO_3 being one of the earliest and most notable examples due to its robust CE and stability. Other inorganic materials of significance include MoO_3, NiO, and TiO_2, all of which exhibit varied EC properties depending on their composition and the applied stimuli. Additionally, V_2O_5 and PB have emerged as candidates for EC studies, displaying distinctive optical modulations in response to electrical inputs. Inorganic EC materials have excellent photostability, but their response speed and colour tunability are relatively limited.

Organic EC materials, on the other hand, represent a dynamic field of research, ICPs such as PANI, PPY, and PT leading the charge. These materials offer the advantage of tunable colouration and facile processing methods, making them attractive for flexible or lightweight applications. ICPs bring attractive electrical conductivities and are convenient for solution-processing methods to prepare devices, but their imperfect spectral purity remains a limiting

factor, especially in applications requiring colourful or full-colour displays. Small organic molecules, such as viologens and organic redox dyes, while offering bright colours and good colours tunability, are often hindered by thermal diffusion and poor stability in devices due to their small sizes and weights. Beyond these, metallorganic frameworks (MOFs)[102] are gaining interest for their hybrid properties, which combine the electronic flexibility of organic systems with the structural stability of inorganic matrices. These materials, exemplified by metallophthalocyanines[103] and ruthenium complexes,[104] introduce a new frontier for EC applications, offering complex electro-optical behaviours with potential in specific applications.

The exploration of EC materials crosses from robust inorganic compounds to highly tunable organic systems, with emerging interest in metallorganic frameworks that combine the strengths of both. Each class of materials presents unique properties that are being harnessed for a wide range of applications, from smart windows to flexible displays. Below, we explore deeper into these material classes highlighting their redox mechanisms, advantages, and current research trends shaping the future of EC technology.

1.2.1 Inorganic electrochromic materials

EC in inorganic materials (metal oxides) is fundamentally connected to the behaviour of the energy gap. The difference between the conduction and valence bands that determines whether a material absorbs or transmits visible light.[105] When an EC material, undergoes an electric stimulus, ions and electrons are intercalated into the material's lattice. This intercalation changes the electronic structure, narrowing or shifting the energy gap. If the energy gap shifts to fall within the visible range, the material appears coloured, typically in shades like blue for WO_3. Conversely, when the energy gap moves outside the visible range, the material becomes transparent or returns to its bleached state. This specific modulation of the energy gap via electrochemical reactions enables the reversible and tunable colour change observed in ECDs.

A key example of an inorganic EC material is WO_3, which is extensively studied for its efficient colour-changing properties under electrical stimulus. The EC working mechanism of WO_3 is based on its ability to change colour when ions (such as H^+, Li^+, or Na^+) and electrons are injected into its lattice. When a negative voltage is applied, ions and electrons are inserted into the WO_3, converting it into a reduced state, typically M_xWO_3. This causes the material to absorb visible light and turn blue. Conversely, applying a positive voltage removes the ions and electrons, returning WO_3 to its original colourless state, as described in the Scheme 1.1

below, where WO_3 is the tungsten trioxide, M^+ represents the intercalating ions, e^- is the electron transferred during the redox process and M_xWO_3 is the reduced, coloured WO_3.

Scheme 1.1. $WO_{3(\text{bleached state})} + xM^+ + xe^- \rightleftharpoons M_xWO_{3(\text{coloured state})}$

In this reaction, the ion insertion into WO_3 leads to a reduction in the tungsten atoms, causing a change in the electronic structure and optical properties. The electrochemically reduced state, M_xWO_3 absorbs visible light, making the material appear dark blue. This change is reversible, meaning that when the applied voltage is reversed, the ions are extracted from the WO_3 lattice, and the material reverts to its original transparent state, Figure 1.13.[106]

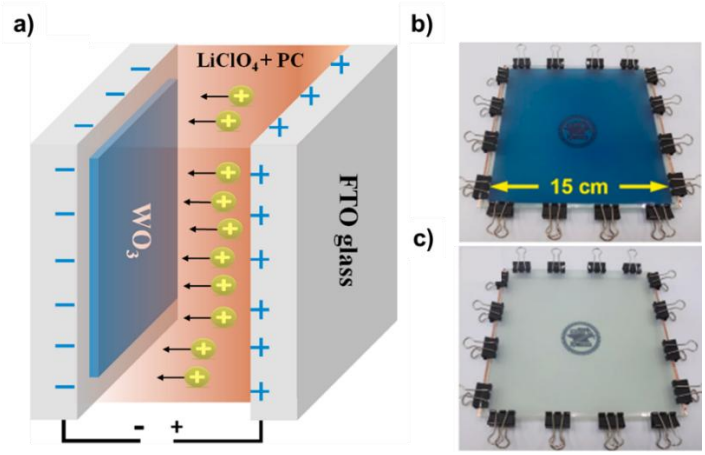


Figure 1.13. a) Schematic representation of WO_3 based ECD.[106] Digital picture of a b) coloured and c) bleached state.[107]

The EC process in WO_3 is particularly efficient due to its ability to reversibly intercalate a high concentration of ions without significant structural degradation, making it highly durable for long-term applications, such as in smart windows or displays. For instance, in the research conducted by Van-Tam Nguyen et al., a smart window retained 93.7% of its initial current density after undergoing 1000 coloration-bleaching cycles, highlighting the exceptional robustness of the EC device during repeated switching processes.[108]

The crystalline structure of WO_3 is face-centered cubic, characterized by the spatial arrangement of tungsten (W) and oxygen (O) atoms forming WO_6 octahedra, Figure 1.14. In this structure, each tungsten atom is surrounded by six oxygen atoms, creating a network of interconnected octahedral units that define the material's overall framework. This arrangement is critical for many of WO_3's physical properties, including its optical, electronic, and electrochemical behaviour. Amorphous WO_3, characterized by its disordered arrangement of WO_6 octahedrons and polygonal voids, typically shows high CE and fast response times due to its favourable ion transport properties during CE switching. However, it lacks long-term

stability because of its structural instability.[109,110] On the other hand, crystalline WO_3, which has a more ordered structure, provides much better stability during cycling due to its atomic arrangement, strong adhesion to the substrate, and slower dissolution in electrolytes.[111][112] Despite these advantages, the denser nature of crystalline WO_3 makes ion transport more difficult, leading to slower switching speeds and lower charge capacity.

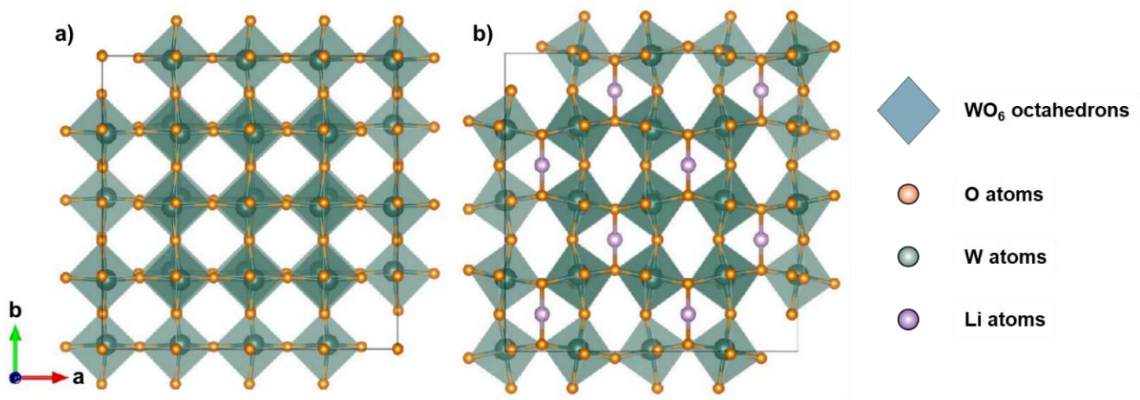


Figure 1.14. Face-centered cubic structure of pure WO_3 in its bleached state. b) Structure in its coloured Li_xWO_3 state with the insertion of the Li^+ ions inside the crystal lattice.[113]

To address these trade-offs, combining the advantages of both ordered and disordered structures has proven effective. For instance, Her et al. produced WO_3 nanorods with a crystalline core and amorphous shell, achieving a significant improvement in transmittance modulation (44% at 550 nm) and faster coloration/bleaching times (41.0/6.0 seconds) compared to purely crystalline or amorphous WO_3.[109] Similarly, Zhou et al. created WO_3 nanowire arrays with both crystalline and amorphous regions, which enhanced optical modulation (70.3% at 750 nm) and maintained good cycling durability (68.5% after 3000 cycles).[110] This approach of combining structural elements helps to optimize the EC properties of WO_3, making it a highly versatile material for energy-efficient applications such as smart windows.[114] To improve EC properties, NiO is commonly paired with WO_3. This synergy leverages the unique characteristics of both materials, leading to enhanced optical modulation, quicker switching times, and increased cycling stability in ECDs. For example, Usha and Lee demonstrated that WO_3-doped NiO thin films showed significant improvements in EC performance compared to pristine NiO. The WO_3 incorporation induced an amorphous structure in NiO, which increased the number of diffusion channels for Li^+ ions, facilitating faster ion intercalation. The optical modulation was enhanced to 66% at 550 nm, with a fast switching speed of 0.6 seconds for bleaching and 1.0 seconds for colouring. This improvement is attributed to the formation of nickel vacancies (defects) by the inclusion of WO_3, which boosted the concentration of holes and improved ion diffusion rates.[115]

NiO films also demonstrate excellent EC properties on their own. In one study, NiO thin films deposited by e-beam evaporation on ITO-coated glass showed a transmittance modulation of 66% at 630 nm for a 500 nm film. The films were able to switch between the coloured and bleached states in just 3.6 seconds and 1.4 seconds, respectively, making them highly suitable for applications in smart windows and ECD.[116] Another study explored the in situ EC efficiency of NiO films cycled in a Li^+ electrolyte, revealing that the coloration process involved the oxidation of Ni^{2+} to Ni^{3+} and Ni^{4+}. The corresponding bleaching was associated with the reduction of Ni^{4+} and Ni^{3+} back to Ni^{2+}, with long-term durability, showing potential for EC applications.[117] Similar to WO_3, the EC behaviour of NiO is characterized by a reversible colour change during redox reactions when voltage is applied as described in the Scheme 1.2.

Scheme 1.2. $Li_xNiO_{(bleached\ state)} \rightleftharpoons y(Li^+ + e^-) + Li_zNiO_{(coloured\ state)}$

The commonly accepted mechanism involves the transformation between the colourless Ni^{2+} state and the coloured Ni^{3+} state. Upon applying a negative voltage, electrons and Li^+ ions are inserted into the deposited films, reducing Ni^{3+} to Ni^{2+}, which causes the film to bleach. In contrast, applying a positive voltage leads to the de-intercalation of ions from the film, oxidizing Ni^{2+} back to Ni^{3+} and resulting in a brown coloration.[118]

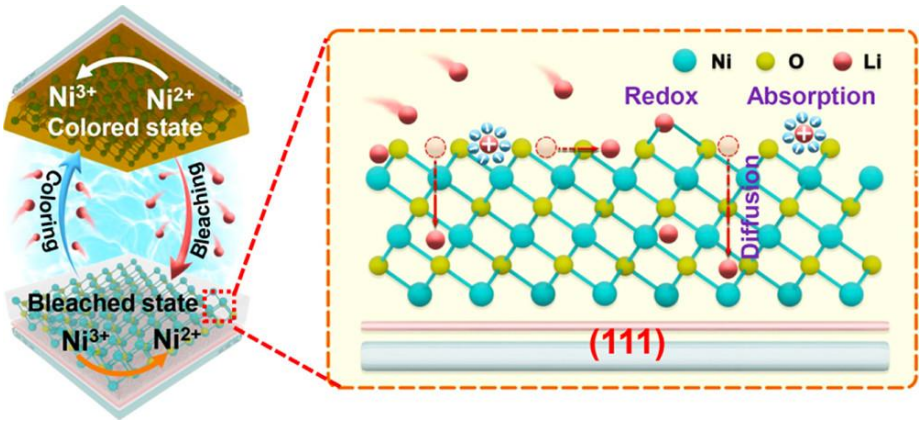


Figure 1.15. Illustrative mechanism of the bleaching and colouring phenomenon in NiO-based films.[118]

Among inorganic materials, MoO_3 also stands out as a promising EC material, sharing a similar geometry and EC mechanism with WO_3. The MoO_3 adopts a face-centered cubic structure, where molybdenum atoms are surrounded by O atoms in an octahedral configuration, Figure 1.16a. This structural similarity ensures that the EC behaviour of MoO_3 closely mirrors that of WO_3. When a negative voltage is applied, electrons and ions are injected into the MoO_3 lattice,

reducing the material and causing it to absorb visible light, typically resulting in a blue colouration. This reduced state, M_xMoO_3, is reversible which mean that applying a positive voltage removes the ions and electrons, returning the material to its bleached state, Figure 1.16b.

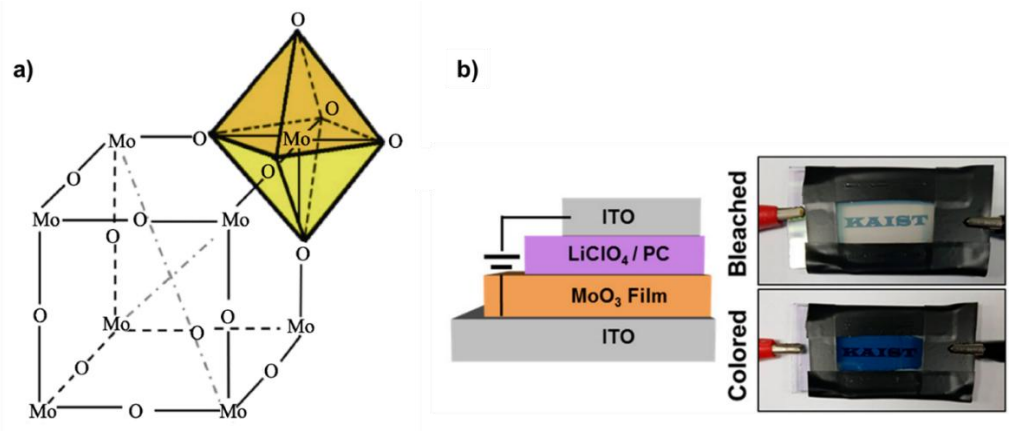


Figure 1.16. a) Face-centered cubic structure of MoO_3 and the representation of its octahedral configuration [MoO_6].[119] b) Schematic configuration of a MoO_3-based ECD with a $LiClO_4$ electrolyte in PC, along with the corresponding display image in bleached and coloured states.[120]

MoO_3 offers distinct advantages over WO_3 as an EC material, primarily due to its structural and optical properties. MoO_3, with a lower density of 4.7 g/cm^3 compared to WO_3's 7.2 g/cm^3, is lighter and more suitable for applications requiring reduced weight, like aerospace and automotive uses.[120] Its optical properties are also advantageous given that MoO_3's absorption spectrum aligns more closely with human visual sensitivity, improving visibility in ECDs.[121] In comparing MoO_3 and WO_3 for EC applications, key performance metrics reveal distinct advantages and limitations. MoO_3 nanosheets, for example, demonstrate a CE of 161.4 cm^2/C, outperforming bulk MoO_3 powder, which shows only 70.1 cm^2/C, and can approach the performance of certain WO_3 nanostructures. Switching speeds for MoO_3 are generally longer, with nanosheet films requiring approximately 11.3 seconds to bleach and 9.8 seconds to colour.[120] Although this performance is enhanced over bulk MoO_3, it remains slower than WO_3 in some configurations.

1.2.2 Organic electrochromic materials

Unlike inorganic systems, which modulate the energy gap through ionic intercalation, organic EC materials achieve comparable optical tunability via molecular conjugation, influencing the highest occupied molecular orbital (HOMO) and the lowest unoccupied molecular orbital (LUMO) gap. Among these organic materials, π-conjugated polymers have emerged as pioneering structures due to their unique structural and electronic properties. These properties

allow precise control over optical and conductive characteristics essential for advanced EC applications. The significance of π-conjugated polymers, also known as intrinsically conducting polymers (ICPs), is increasingly recognized with recent advancements in optoelectronic and photonic materials.[122] Their distinctive electrical conductivity arises from conjugated double bonds within their molecular structure, enabling superior performance in EC devices.[123]

Conjugation involves the alternating arrangement of single and multiple bonds along the polymer backbone, creating a delocalized π-electron system. This delocalization allows for enhanced electron mobility, resulting in the excellent electrical conductivity observed in conductive polymers.[124] An important development in the field occurred in 1977 when MacDiarmid, Heeger, and Shirakawa demonstrated that polyacetylene, initially an insulator, could achieve high conductivity through treatment with oxidizing or reducing agents.[125] However, widespread application of these polymers has been hindered by doping, making the polymer challenging to process. For this reason, much effort has been directed toward developing conjugated polymers that show intrinsic conductivity, meaning they can conduct electricity without doping, while still being soluble and easy to handle. A key parameter that governs their behaviour is the band gap energy (Eg), defined as the energy difference between the HOMO and LUMO. This value strongly influences both the electronic properties and the conductivity of the polymer. Therefore, the design of low Eg materials relies on the ability to tailor the HOMO–LUMO gap through structural changes.[126]

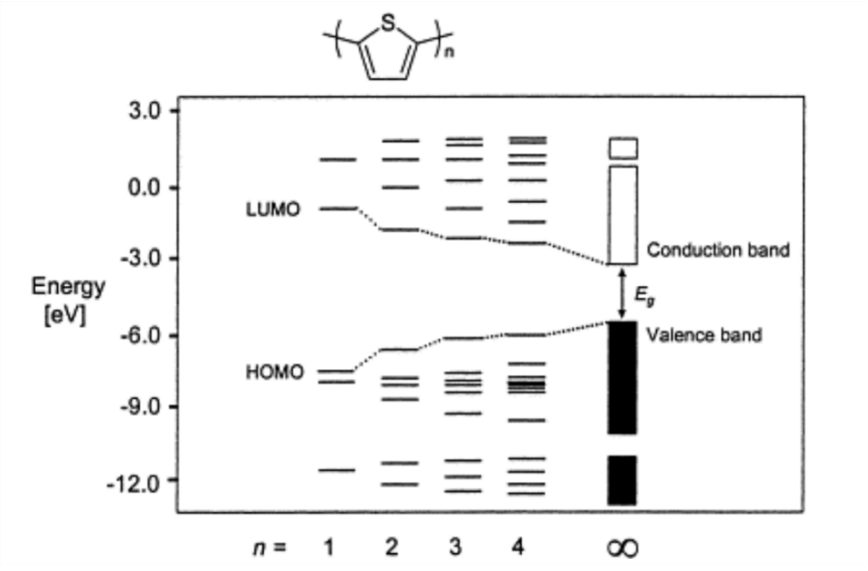


Figure 1.17. Energy gap (HUMO-LUMO distance) as a function of the conjugation chain length. The bandgap of the polymer decreases with the increase of the conjugation and vice versa.[127]

In π-conjugated polymers, the electronic and optical properties are mainly determined by the energy levels close to the HOMO and LUMO. When many monomer units are connected, these energy levels combine and form bands. The HOMO levels merge into the valence band, which is the highest occupied band, while the LUMO levels form the conduction band, which is the lowest unoccupied band. The progression of bands in a conjugated polymer with the increase of the conjugation length is reported in Figure 1.17. The polymer's Eg is determined by the separation ΔE between the HOMO and LUMO energy levels. Due to the inherent flexibility in modifying the chemical structure of π-conjugated polymers, there is continuous research interest in manipulating the band gap of these semiconductors. The exploration of "band gap engineering" is crucial in tailoring the electrical and optical properties of the polymer. The reduction of the band gap to nearly zero is anticipated to yield an intrinsically conducting polymer, highlighting the ongoing interest of desired material characteristics.[128]

1.2.2.1 Viologens

The tunability of π-conjugated polymers through structural modification has covered the way for a broader exploration of organic EC materials, where each class contributes distinct characteristics suited to specific applications. While π-conjugated polymers have demonstrated promising conductivity and optical adjustability, other organic systems bring alternative functionalities to the field. Notably, small molecules with robust redox capabilities are increasingly drawing attention.[129] One such class, viologens, exemplifies the potential of small molecules in EC applications. Known for their stable colour change upon reduction, viologens offer rapid and reversible optical transitions that are attractive for display and smart window technologies.[85]

Viologens are a class of 1,1'-disubstituted-4,4'-bipyridilium salts derived from the diquaternisation of 4,4'-bipyridyl.[130] Viologens exist in three primary redox states, with the dication being the most stable due to delocalization of the radical throughout the π system, Figure 1.18.[4] This dication state is typically colourless unless optical charge transfer with a counterion induces colour. Upon reductive electron transfer, viologen dications form radical cations, whose stability is enhanced by delocalization of the radical electron across the bipyridyl nucleus.

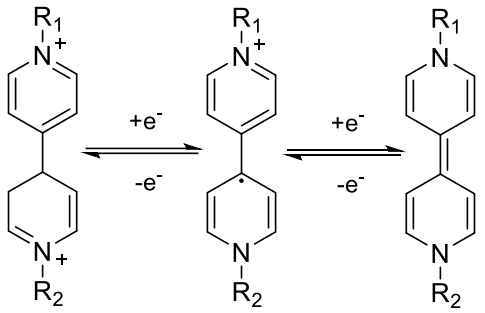


Figure 1.18. Molecular structure of typical redox states of viologens, with R_1 and R_2 representing generic substituent groups or atoms.

This delocalization imparts intense colour, with high molar absorption coefficients due to charge transfer between the (formally) +1 and neutral nitrogens.[131] By modifying the nitrogen substituents, one can tune the colour of the radical cation: simple alkyl groups yield a blue/violet hue, while aryl groups, such as 4-cyanophenyl in 1,1'-bis(4-cyanophenyl)-4,4'-bipyridilium, produce green tones.[132] In contrast, di-reduced viologens exhibit minimal colour due to the lack of optical charge transfer within visible wavelengths.[131] For instance, 1,1′-dimethyl-4,4′-bipyridilium (methyl viologen, MV^{2+}), a simple viologen, is soluble in various solvents, including water. In its dication form, MV^{2+} is colourless, while its radical cation is blue (λ_{max}~600 nm) in organic solvents and purple in water, displaying solvatochromism alongside EC behaviour, effect that occurs because the radical cation dimerizes in aqueous environments, forming a red dimer (λ_{max}~550, 900 nm) species that equilibrates with the blue monomer, resulting in a purple hue.[133,134]

The colour of viologen molecules can vary based on the nitrogen substituents ($–R_1$ and $–R_2$), which significantly affects the EC performance of ECDs, allowing these molecules to cover a broad spectrum of visible colours. For instance, extending the alkyl chain length shifts the colour of the radical cation from blue to red due to an enhanced dimerization effect.[135] In contrast, modifications like aryl substitutions can produce green tones.[136] For example, in the work of Moon et al., multi-coloured, low-power, flexible ECDs were developed using ion gels with different viologen derivatives. By combining these viologens with specific ionic liquids and polymers, the ECDs display colours (blue, green, and red) through modulation of electronic states and dimerization behaviour. Heptyl viologen (HV) in 1-butyl-3-methylimidazolium bis(trifluoromethylsulfonyl)imide [BMI][TFSI] produces a blue colour (absorption at 605 nm), while replacing [BMI][TFSI] with 1-butyl-3-methylimidazolium tetrafluoroborate [BMI][BF_4] shifts the equilibrium to a red dimer $(HV^{+}\bullet)_2$ at 540 nm, respectively Figure 1.19a,b. Meanwhile, p-cyanophenyl viologen (CN-PV) generates green upon reduction, with absorption

at 595 nm, Figure 1.19c. The ECDs show distinct EC properties with efficient colouration times (11–18 seconds) and high CE (78–155 cm^2/C).

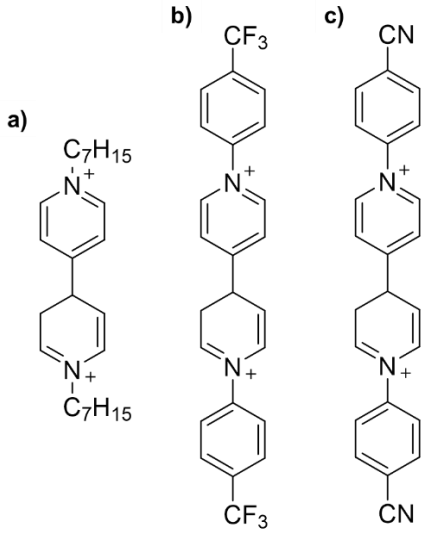


Figure 1.19. Chemical structures of viologen derivatives with varying functional groups affecting EC properties. a) Monoheptyl viologen with C_7H_{15} alkyl substituents, often resulting in a blue coloration in the radical cation state. b) Trifluoromethyl-substituted viologen with CF_3 groups, which produces a red colour. c) Dicyano-substituted viologen with CN groups, which exhibits a green colour shift.

1.2.2.2 Intrinsically conductive polymers

Intrinsically conductive polymers can be synthesized from heterocyclic aromatic compounds like thiophene, aniline, furan, pyrrole, carbazole, azulene, and indole.[137] These compounds, through chemical or electrochemical oxidation, can form various conductive polymer structures such as polypyrrole (PPy), polyaniline (PANI) and polythiophene (PT) along with functionalized forms like poly(3-methylaniline) (MEPA), poly(3-methylthiophene) (P3MTh), and poly(3-methylpyrrole) (P3MPy). Shifts between different oxidation states (oxidized, neutral, and reduced) directly influence their conductivity and colour. As the polymer's redox state changes, it moves from a conductive oxidized state to a non-conductive reduced or neutral state, impacting the visible and near-infrared absorption spectra. These changes lead to noticeable colour variations in the polymer films, with shifts in appearance between coloured (reduced) and colourless (oxidized) forms. Depending on the degree of oxidation or reduction, the polymers can display a range of hues, from yellow and orange to red, purple, dark blue, green, light blue, and black.

1.2.2.2.1 Polypyrrole

PPy is a prominent conducting polymer that exhibits excellent electroactivity, enabling reversible colour changes under applied electrical potential. PPy is particularly favoured because of its relatively low oxidation potential (~0.8 V) compared to other aromatic monomers, which facilitates both chemical and electrochemical synthesis in a variety of solvents, including aqueous environments.[138,139] The electrical conductivity of PPy and its derivatives is strongly influenced by the process of doping, which involves incorporating electron-donating or electron-accepting species into the polymer structure.[140,141] In its neutral (undoped) state, PPy functions as a semiconductor, with a relatively large energy gap of around 3.16 eV.[53]

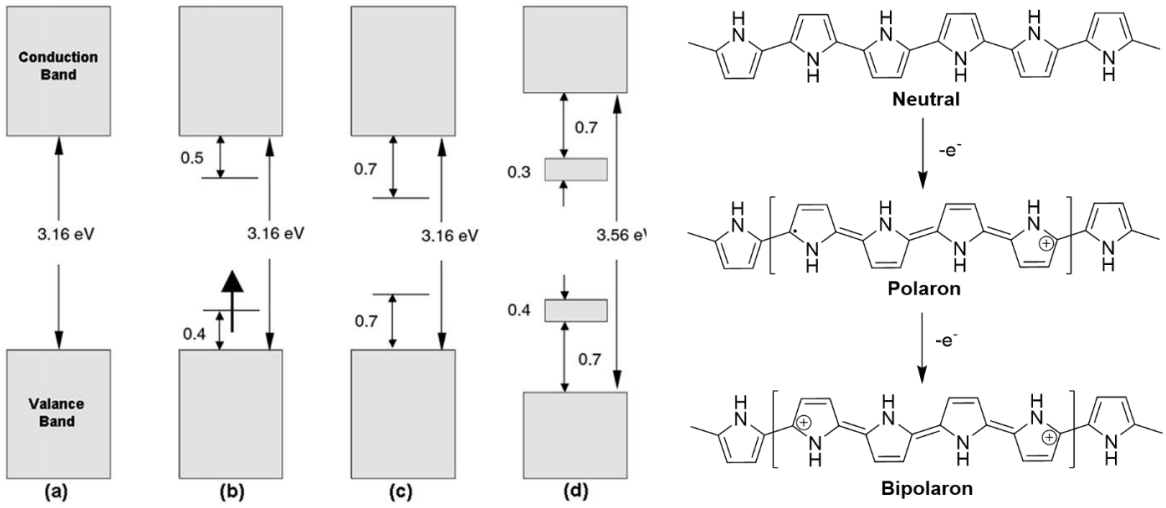


Figure 1.20. Electronic energy diagrams and molecular structures for (a) neutral polypyrrole (PPy), (b) polaron state, (c) bipolaron state, and (d) fully doped polypyrrole.[53]

When doping occurs, this energy gap is reduced as the polymer forms polarons, radical cations that arise from the oxidation process.[142] These polarons create new electronic states within the bandgap, enabling longer wavelength transitions. As the level of oxidation increases, polarons can combine to form bipolarons, which are dicationic species that further reduce the bandgap, potentially down to 1.46 eV, resulting in enhanced electrical conductivity and altered optical absorption characteristics, Figure 1.20. The structural transformations that accompany doping are significant, as PPy undergoes a shift from a benzoid-like structure to a more quinoid-like conformation.[143] This structural relaxation facilitates the formation of the polaronic states. With increased doping, the energy levels associated with bipolarons emerge, characterized by broad low-energy absorption bands due to electronic transitions from the top of the valence band. As oxidation continues, these bipolaronic states can overlap, forming intermediate band structures that further modify the polymer's optical and EC properties, allowing for tunable colour changes based on the degree of p-type doping.

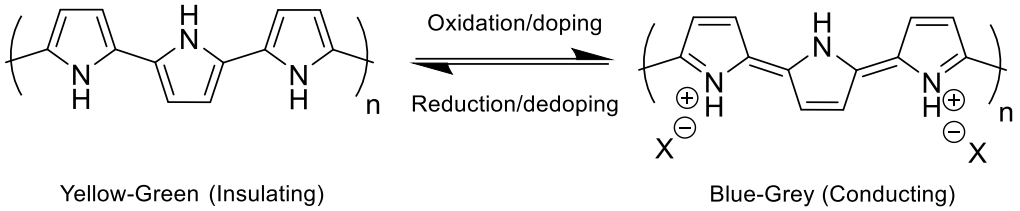


Figure 1.21. Oxidation and reduction mechanism in ppy.[53]

The band gap of PPy is approximately 3.16 eV, giving the polymer a yellow-green appearance in its neutral state and a blue-gray colour when oxidized, Figure 1.21. However, PPy tends to degrade with repeated cycling, and only very thin films can be fully de-doped. Despite this limitation, polypyrrole derivatives with enhanced EC performance can be developed by customizing the functional groups on the polymer's repeat units. The colour variations in conducting polymers are largely determined by the band gap and the distinct features of the band structure. Techniques like structural modification, copolymerization, blending, and lamination are frequently employed to fine-tune the band gap, enabling precise control over the colour properties.[144] For example, the EC properties of PPy have been notably enhanced through functionalization strategies. Ak et al. reported an enhancement by electrochemically copolymerizing pyrrole with octa(thiophenephenyl)silsesquioxane (OPS). The copolymer OPS-PPy exhibited a clear multicolour response, with colours changing between yellow, red, green-gray, and blue.[145] It also performed better than regular PPy in terms of speed and contrast. The switching time was reduced to about 0.4 seconds (compared to 1.1 seconds), and the optical contrast increased from 17% to 30% at 730 nm. These effects are mainly due to the presence of OPS units, which reduce how tightly the polymer chains are packed. As a result, ions can move more easily during redox reactions, and more active sites are available for doping. A different approach to improve PPy is to combine it with EDOT. In this case, Zhao-yang and coworkers showed that increasing the amount of EDOT shifts the π–π* absorption peak to higher wavelengths, from 462 nm to 556 nm.[146] At the same time, a reduction in the band gap was observed, with values ranging from 1.71 to 1.64 eV.

In recent years, substituting PPy structures at the 3-position has shown promise for modulating properties like bandgap control and colour, similar to what has been achieved with PT derivatives. Despite the advances, only a few studies have investigated poly(3-alkylpyrrole)s due to synthetic challenges and their air sensitivity in the neutral state.[147,148] Notable examples of these materials include poly(methyl substituted bipyrroles),[149] poly(3-hydroquinonylpyrrole)[150] and poly(3-alkylsulfonate pyrrole)s,[151] Figure 1.22. Among them,

poly(methyl substituted bipyrroles) undergoes a transmissive-yellow to gray-blue transition upon oxidation, indicating potential applications in ECDs. Expanding beyond the 3-position, substitution at both the 3- and 4-positions of pyrrole, similar to the modifications done on PTs, offers another layer of control. This type of substitution prevents the formation of undesired α–β couplings during polymerization, which can otherwise reduce conjugation length and limit solubility. Such structural adjustments allow polymerization to proceed via the 2- and 5-positions, producing polymers with fewer structural irregularities.

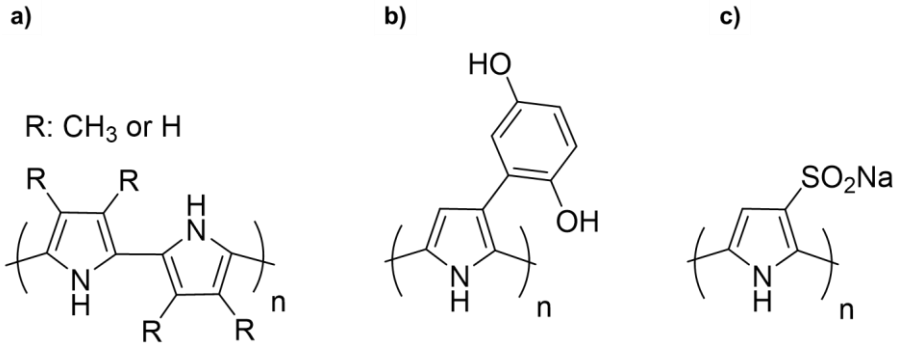


Figure 1.22. Functionalization of polypyrrole at positions 3 and 4: a) Poly(methyl-substituted bipyrroles), b) Poly(3-hydroquinonylpyrrole), c) Poly(3-alkylsulfonate pyrrole).

The 1990s marked significant advancements in the EC properties of PT derivatives, particularly with the rise of poly(3,4-alkylenedioxythiophene) (PXDOT) materials. As easily oxidizable, stable, low bandgap polymers, PXDOT derivatives originated from the pioneering work of Jonas et al., who first anodically polymerized EDOT.[152] This produced a cathodically colouring polymer with a bandgap of 1.6 eV, switching between nearly transparent with a slight blue tint to a deep blue hue. PEDOT, the most famous PXDOT derivative, achieved a bandgap of 1.1 eV, lower than that of PPy and PT, primarily due to the electron-donating nature of the oxygen atoms in the structure, which elevates the HOMO and reduces the bandgap.

The emergence of PXDOT inspired similar exploration in pyrrole-based derivatives. Introducing alkylenedioxy bridges to the 3- and 4-positions of pyrrole led to the development of poly(3,4-alkylenedioxypyrrole)s (PXDOPs), creating a family of electroactive conjugated polymers with unique properties, Figure 1.23.[153] The first member, PEDOP, demonstrated a bandgap of 2.0 eV and an OP of 59%.[154] The introduction of varying alkylenedioxy rings and substituents in the PXDOP family allowed for further customization of optoelectronic properties. For example, ProDOP, MeProDOP, Me_2ProDOP, and BuDOP all exhibited a bandgap of 2.2 eV but varied in colour states: ProDOP switched from orange (neutral) to brown (intermediate) to gray-blue (oxidized), with a maximum absorbance at 522 nm. Similarly, MeProDOP and Me_2ProDOP transitioned from orange in the neutral state to red-brown in the

intermediate state and light blue when fully oxidized, absorbing at 530 nm and 534 nm, respectively.[155] BuDOP, meanwhile, transitioned from orange to blue-gray with a maximum absorbance at 533 nm.

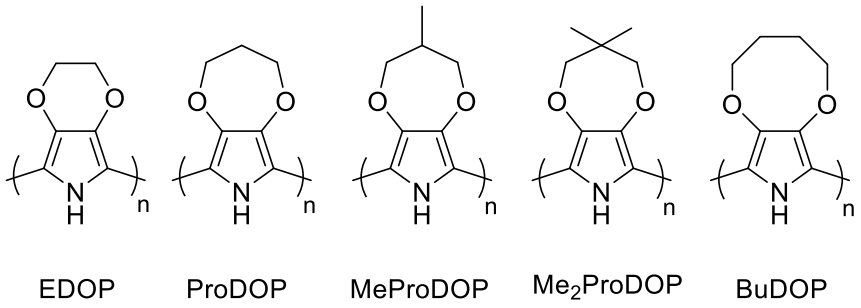


Figure 1.23. Chemical structures of various 3,4-substituted polypyrroles derivatives, including EDOP, ProDOP, MeProDOP, Me_2ProDOP, and BuDOP, commonly used in electrochemical and EC applications.[53]

In particular, Me_2PProDOP demonstrated high stability, achieving an optical contrast of 76% at 534 nm and retaining 90% of its electroactivity after 40,000 switching cycles.[156] In a similar study, PProDOP films were layered together with PEDOT and additional PProDOP to form a stacked polymer structure. This multilayer design allowed the design of dual-polymer EC films. By carefully selecting the combination of polymers and controlling each layer separately using potentiostatic techniques, a wide variety of colours could be obtained. This approach highlights the flexibility of these materials and their potential for different EC applications.[157]

1.2.2.2.2 Polyanilines

PANI has gained significant attention among conducting polymers due to its outstanding environmental stability,[158] ease of synthesis, and remarkable optical, electrochemical, and electrical properties. Recognized as a unique member of π-conjugated conducting polymers, PANI was first synthesized in 1862 and became extensively studied as a conducting material starting in the 1980s. PANI's molecular structure, featuring nitrogen atoms integrated within a phenyl ring backbone. The typical chemical oxidative copolymerization method used to synthesize PANI encounters significant limitations in processability. These challenges arise due to PANI's inherently rigid backbone and strong interchain interactions, which result in poor solubility and limited mechanical flexibility. Such properties hinder its ease of dissolution and melt-processing, restricting its broader application potential.[159,160] To mitigate these limitations and improve PANI's processability, researchers have explored various electrochemical synthesis strategies, adjusting parameters like potential, charge, reaction time, temperature, pH, ionic strength, and electrolyte composition. This electrochemical fine-tuning

allows for greater control over PANI's structural and morphological properties, thus broadening its synthetic possibilities and enhancing its applicability across diverse fields.[161]

The EC properties of PANI are defined by its ability to undergo distinct colour changes across its various oxidation states, which make it an attractive material for a range of responsive applications. In its leucoemeraldine base (LEB), the fully reduced form of PANI, the polymer appears colourless or light yellow, reflecting the absence of extensive conjugation in the polymer backbone. As it undergoes partial oxidation to the emeraldine salt (ES), PANI takes on a green colour. Upon reaching full oxidation in the pernigraniline state or emeraldine base (EB), PANI shifts to a blue or violet colour, indicating the highest oxidation level and limited electrical conductivity due to structural saturation, Figure 1.24.[162,163]

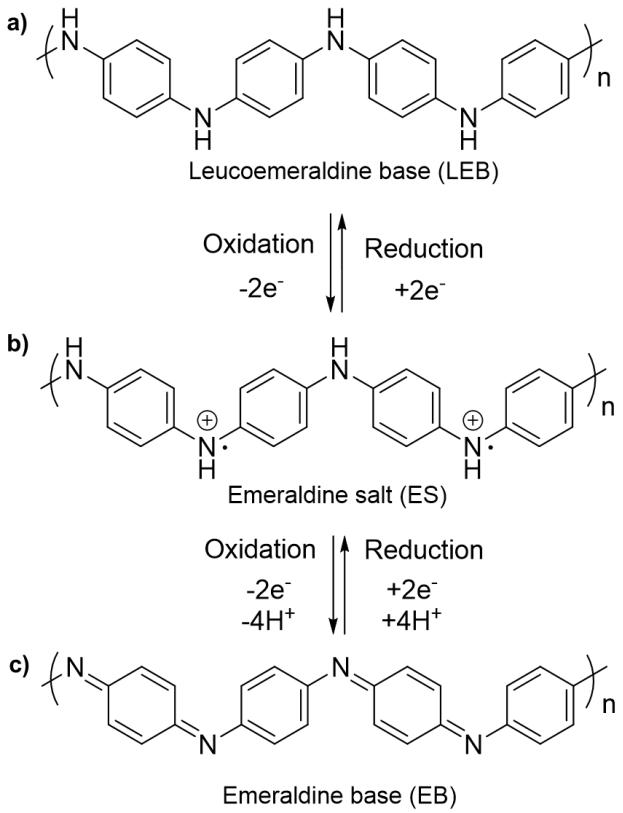


Figure 1.24. Chemical structures of PANI in different oxidation states: a) Leucoemeraldine (colourless/light yellow), b) Emeraldine salt (green), and c) Emeraldine base (blue).

PANI, like PPy, can be functionalized to enhance its properties for practical use across various fields such as electronics, optics, and energy storage. However, one of PANI's key limitations is that it is a powder that does not melt and has minimal solubility in common organic solvents, which makes it challenging to handle.[164,165] Several methods exist to modify PANI such as functionalizing the initial monomer to produce mono- or disubstituted aniline derivatives,[166,167] polymer-analogous conversion (where functional groups are added to an already-formed polymer),[168] copolymerization,[160,169] and doping.[170,171] Each approach can

impact the material's conductivity, stability, and electroactivity. Although polymer-analogous conversions are less explored due to the limited recyclability of PANI, some successful modifications have been achieved by introducing substituents directly onto PANI's aromatic ring. However, this process can result in products with uneven chain lengths and non-ideal properties if conversions are incomplete. The best strategy for modifying PANI is to functionalize the monomer by adding specific substituents, producing mono- or disubstituted aniline derivatives that are subsequently polymerized. The growing body of research highlights efforts to develop various low-molecular-weight aniline compounds designed for conversion into high-molecular-weight polymers.[166,167]

The electronic absorption spectrum of PANI features two distinct peaks. Specifically, one at approximately 330 nm, associated with the π–π* electron transition between conjugated aromatic rings, and another at around 620 nm, which corresponds to the n–π* transition occurring within the quinoid segments of the polymer.[172–174] These peaks serve as a means to evaluate the proportion of benzoid and quinoid units, offering insights into the oxidation states of PANI's macromolecular structure. PANI derivatives exhibit similar spectral characteristics, with two absorption bands analogous to the base polymer. However, the incorporation of substituents on the aromatic ring induces shifts in the absorption maxima. These shifts are attributed to the steric and electronic effects introduced by the substituents, which modify the polymer's electronic environment and geometric conformation, Figure 1.25.[175,176]

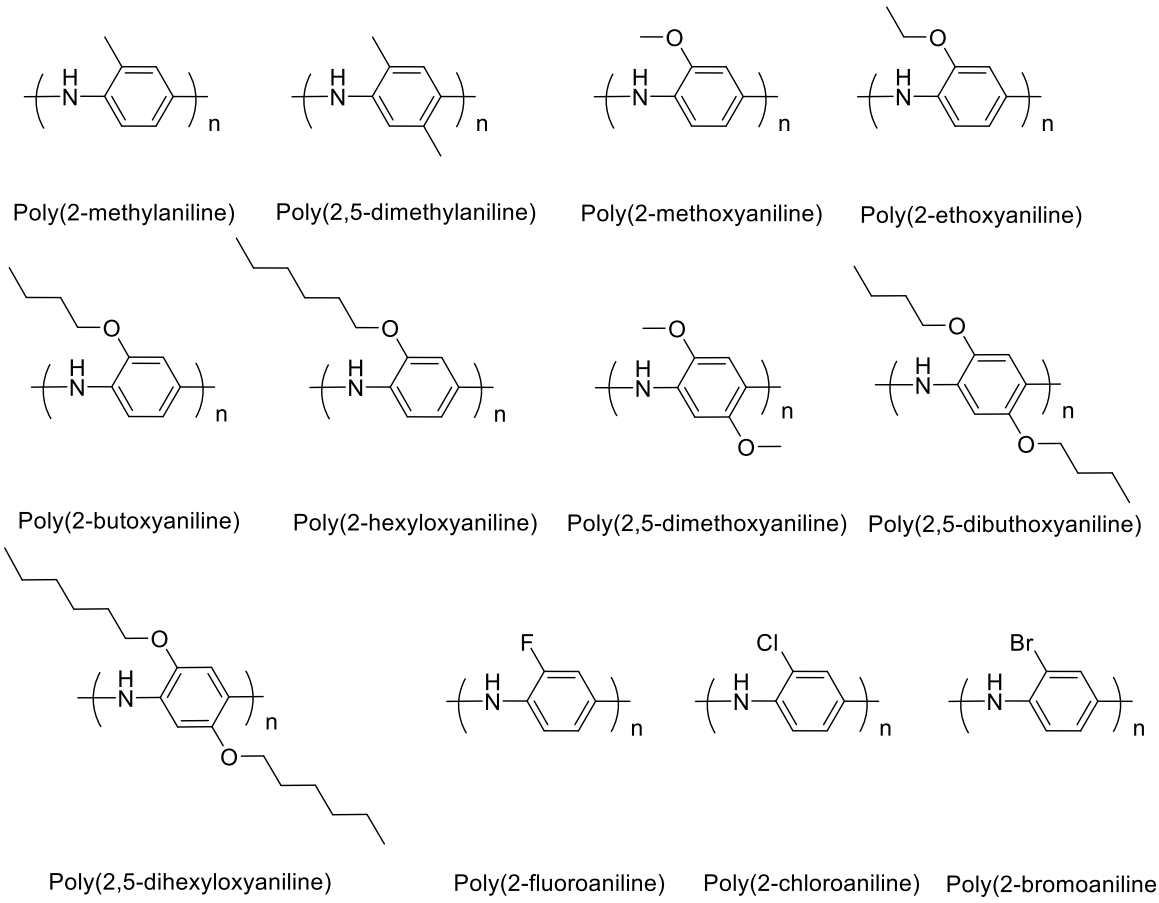


Figure 1.25. Series of polymers derived from substituted PANI along with their absorption maxima, including Poly-2-methylaniline (310 nm), Poly-2,5-dimethylaniline (308 nm), Poly-2-methoxyaniline (325 nm), Poly-2-ethoxyaniline (320 nm), Poly-2-butoxyaniline (340 nm), Poly-2-hexyloxyaniline (340 nm), Poly-2,5-dimethoxyaniline (350 nm), Poly-2,5-dibutoxyaniline (370 nm), Poly-2,5-dihexyloxyaniline (375 nm), Poly-2-fluoroaniline (289 nm), Poly-2-chloroaniline (324 nm), and Poly-2-bromoaniline (315 nm).

For instance, alkyl groups positioned ortho to the aromatic ring lead to a hypsochromic shift, reflecting a reduction in the wavelength of the absorption maxima. This phenomenon arises from increased torsion in the polymer chain, resulting in a non-planar structure. According to Wei et al., the introduction of a methyl group in poly(o-toluidine) causes a shift in the absorption maximum from 330 nm in polyaniline to 318 nm, while for poly(o-ethylaniline), the maximum further shifts to 311 nm.[177] Similarly, Andriianova et al. report that alkyl groups, particularly ortho-substituted ethyl or propyl chains, lead to a shift in oxidation potential, increasing from 0.12 V for polyaniline to 0.30 V for poly(o-ethylaniline).[178] Conversely, alkoxy groups, which attach through an oxygen atom, promote a bathochromic shift by stabilizing the planar conformation and enhancing electron donation within the polymer. The extent of the bathochromic shift is further amplified by the addition of multiple alkoxy groups or the elongation of their carbon chains, which intensifies their electron-donating properties. The introduction of a single methoxy group at the 2-position in polyaniline shifts the absorption maximum from 315 nm in polyaniline to 325 nm in poly(2-methoxyaniline) (PMOA), while

poly(2,5-dimethoxyaniline) (PDMOA) exhibits an absorption maximum at 350 nm. A similar effect is observed with poly(2,5-diethoxyaniline) (PDEOA), shifting to 355 nm, while for longer alkoxy substituents such as butoxy (-O-C_4H_9) and hexyloxy (-O-C_6H_{13}), the shift becomes more pronounced, with poly(2-butoxyaniline) (PBOA) and poly(2,5-dibutoxyaniline) (PDBOA) showing maxima at 340 nm and 370 nm, respectively.[172] This demonstrates that even small changes to the polymer's structure can significantly impact the optical and electronic properties.

1.2.2.2.3 Polythiophenes

PTs are among the most studied conducting polymers due to their superior environmental stability,[179] facile polymerization,[180] versatile optical,[181] electrochemical,[182] and electrical properties.[183] As PPy and PANI, also PTs belong to the family of π-conjugated conducting polymers, with their backbone formed by alternating single and double bonds between carbon atoms in the thiophene ring. These structural characteristics grant PTs favourable charge transport capabilities and adaptable optoelectronic properties, with an energy gap of approximately 2.0 eV, positioning this material within the semiconductor class.[184]

The most distinctive feature of PTs is their ability to exhibit EC properties. In their neutral state, PTs consist of a planar backbone of thiophene rings linked by alternating single and double bonds, forming a π-conjugated system with delocalized π-electrons, which gives them intrinsic semiconducting properties. The bandgap of PTs varies significantly depending on their structural modifications. The aromatic form of PT exhibits a bandgap of 1.83 eV, while the quinoid form, which is less stable in standard PTs, has a significantly lower bandgap of 0.47 eV. Structural modifications such as polyisothianaphthene (PITN) further reduce the bandgap to approximately 1.16 eV, approaching the infrared region and enhancing electrical conductivity.[185] This undoped state is electrically neutral, with no charges present on the polymer backbone. Upon doping, achieved by removing electrons via voltage application, the π-electron density redistributes along the chain, inducing structural distortions and transforming the polymer from a semiconductor to a conductor by reducing the bandgap and enabling charge transport. The polaronic state arises when a single electron is removed, creating a radical cation with a localized positive charge and associated electronic distortion. This state introduces two in-gap electronic states between the valence and conduction bands, facilitating charge transport.[186] The energy levels of these in-gap states have been found to be around 0.3–0.5 eV above the valence band.[143] The bipolaronic state emerges when two electrons are removed, resulting in a dication with more delocalized positive charges and

pronounced structural distortions.[187] The electronic and structural states of PTs are shown in Figure 1.26.

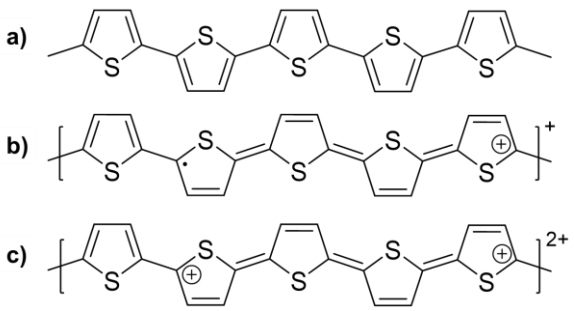


Figure 1.26. Electronic states of PTs: a) neutral, b) polaronic, and c) bipolaronic.[188]

Despite their versatile optoelectronic properties and relatively low bandgap for a polymer material, PTs exhibit significant challenges in processability. Unsubstituted PTs demonstrate poor solubility, dissolving only in highly polar solvents such as DMF, and are insoluble in common solvents like EtOH, water, and THF. Their rigid, planar π-conjugated backbone and strong interchain interactions promote aggregation, leading to a semicrystalline morphology with crystallinity as low as 7% in some modified PTs. Higher crystallinity intensifies interchain forces and reduces free volume, making dissolution more difficult, whereas lower crystallinity improves solubility by facilitating solvent penetration.[189–191] These characteristics hinder PTs' ease of dissolution and melt-processing, restricting their broader applicability. To address these limitations, functionalization of the thiophene monomer has been explored to introduce substituents that improve solubility, processability, and stability while preserving or enhancing the polymer's inherent electronic properties. Functionalization strategies frequently involve incorporating alkyl chains of different lengths or other substituents to enhance solubility, crystallinity, and processability. This approach minimizes aggregation by disrupting interchain π-π stacking interactions. Below, we discuss functionalized examples of PTs, arranged from the smallest substituent to the most complex.

One of the earliest examples is Poly(3-methylthiophene) (PMT), which incorporates a methyl group as the side chain. PMT absorbs light around 420 nm in its neutral state, which transitions to higher wavelengths upon doping, Figure 1.27a. Despite the enhanced environmental stability of the polymer, its limited solubility and processability restrict its broader use in applications.[192,193] Moving to longer alkyl substituents, Poly(3-hexylthiophene) (P3HT) stands out as one of the most widely studied PT derivatives, Figure 1.27b.[194] The addition of a hexyl chain improves solubility in common organic solvents and facilitates thin-film formation. Regio-regular P3HT exhibits an absorption maximum around 520 nm in its neutral state and transitions to a bleached or colourless state upon oxidation.[195,196] This reversible

optical property is vital for applications in organic electronics. Its regioregular structure enhances charge carrier mobility and contributes to better performance for applications in organic electronics. Poly(3-octylthiophene) (P3OT), with its longer octyl side chain, significantly improves solubility and processability compared to shorter-chain analogs, Figure 1.27c. It exhibits an absorption peak around 500 nm in its neutral state.[197,198] Upon doping, polaronic absorption bands emerge in the infrared region, indicating enhanced conductivity. Poly(3-decylthiophene) (P3DT) continues the trend of improved solubility and flexibility with longer side chains , Figure 1.27d.[199,200] P3DT absorbs light at approximately 530 nm in its neutral state, maintaining the conjugation characteristics observed in shorter alkyl-substituted PTs. For even longer side chains, Poly(3-dodecylthiophene) (P3DDT) introduces superior crystallinity and solubility, Figure 1.27e. The absorption maximum of P3DDT in its neutral state is approximately 540 nm, with films demonstrating vibronic structure indicative of strong π-π stacking.[201,202] Poly(3-(2-ethylhexyl)thiophene) (P3EHT) features a branched alkyl chain, which disrupts interchain π-π stacking to a greater extent than linear chains, Figure 1.27f. This results in slightly reduced crystallinity but improved solubility and processability. P3EHT absorbs light at around 550 nm in its neutral state, with significant red-shifting upon film formation, reflecting interchain coupling effects.[203,204] Poly(4,4'-dioctyl-2,2'-bithiophene) (PDOBT)**,** a more structurally complex polymer, is synthesized from regio-specific polymerization, Figure 1.27g. It absorbs light at *ca.* 388 nm in the neutral state, and its alternating head-to-head and tail-to-tail couplings limit conjugation length.[205]

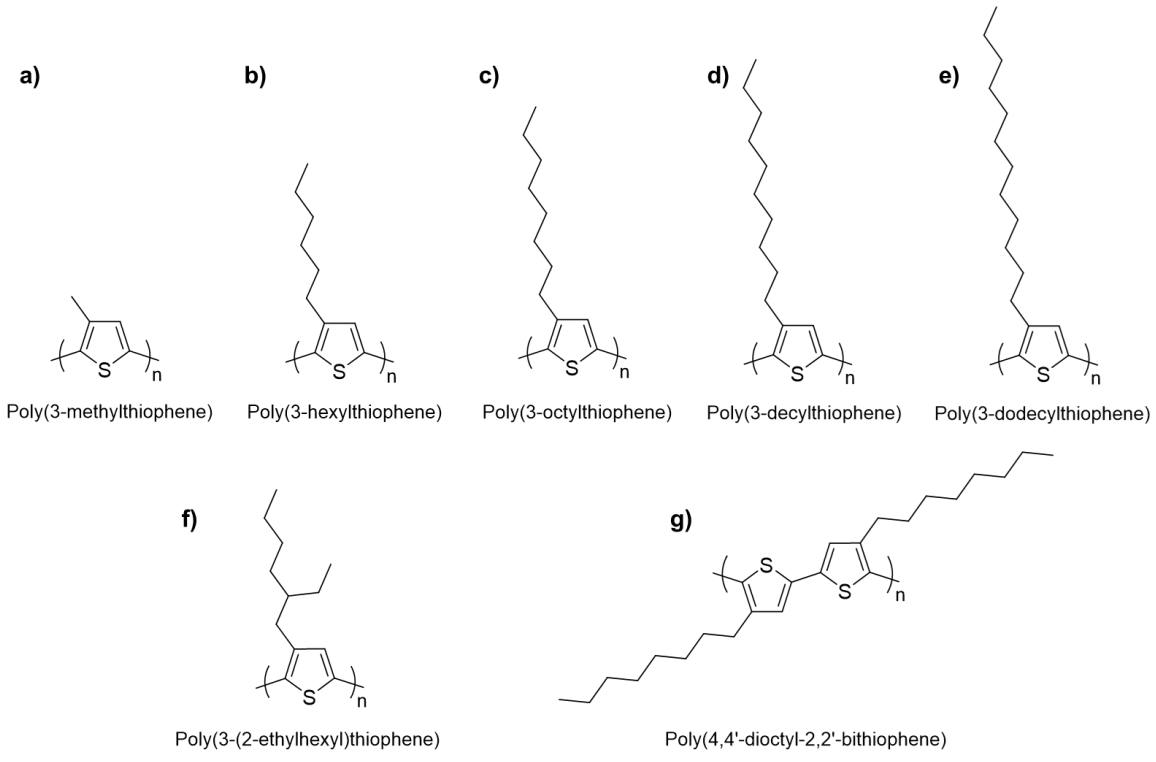


Figure 1.27. Structures of substituted PTs featuring alkyl chains at the 3-position.

Alternative substituent groups for PTs, such as aromatic, cyclic, or polar groups, significantly alter the electronic, optical, and structural properties of the resulting polymers. Unlike alkyl derivatives, which primarily enhance solubility and processability, non-alkyl substituents introduce steric hindrance or functional interactions that modulate interchain π-π stacking, thus affecting electronic behaviour and backbone rigidity. For instance, in poly(3-cyclohexylthiophene) (P3CHT), the rigid cyclohexyl side chain disrupts planar stacking of the thiophene backbone, leading to distinct mechanical and electronic properties. The tensile modulus of P3CHT at 25°C is 43.96 MPa, but it decreases to 4.80 MPa at 140°C due to increased molecular relaxation. The stress at break reaches a maximum of 24.12 MPa at 55°C, where the polymer also exhibits its highest strain at break of 206%. Furthermore, electrical conductivity is strongly dependent on molecular alignment. Doping P3CHT with iodine increases its conductivity by a factor of seven when the draw ratio is raised from 1.0 to 3.0, reaching values as high as $1.74 \cdot 10^{-3}$ S/cm. This increase is attributed to improved interchain charge transport due to mechanical stretching.[206] In comparison, poly(3-hexylthiophene) (P3HT) exhibits a bandgap reduction from 1.87 eV to approximately 1.2 eV upon doping, making it a more efficient charge transport material, Figure 1.28a.[189] Another example is poly(3-phenylthiophene) (P3PhT), where the aromatic phenyl substituent introduces a large steric hindrance, further reducing π-π interactions and crystallinity, Figure 1.28b.[207] Despite this, P3PhT retains significant conjugation length and electronic mobility, with its absorption spectrum centered around 430 nm.[208] For instance, poly(3-(methoxyethoxy)thiophene) (PMEOT) introduces a methoxyethoxy side chain, which improves solubility in polar solvents and aqueous systems while exhibiting an absorption maximum in the range of 400–430 nm, attributed to the electron-donating effects of the methoxyethoxy side chains, Figure 1.28c.[209] Similarly, Poly-(3,4-dibutoxythiophene) (PDBOT) incorporates both alkoxy and methyl substituents. This combination facilitates regioselective polymerization, yielding highly regioregular polymers, with an absorption wavelength typically in the range of 410–450 nm, reflecting its enhanced conjugation, Figure 1.28d.[210,211]

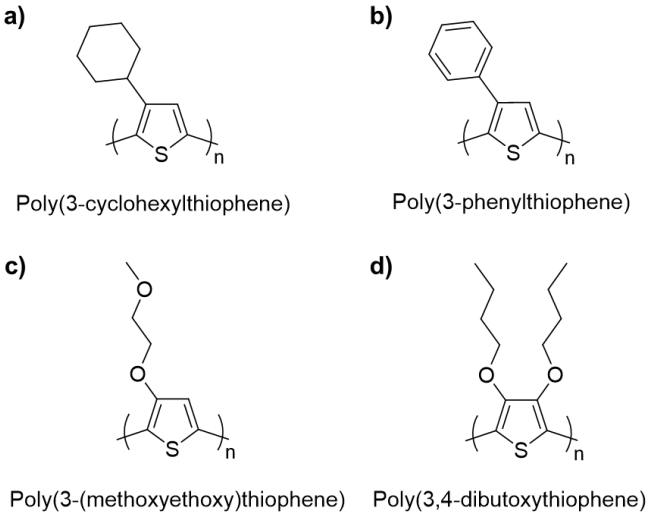


Figure 1.28. Structures of substituted PTs featuring cyclic, aromatic and methoxy/ethoxy groups in position 3,4.

To address the broader solubility challenges of PTs in polar solvents researchers have developed various water-soluble PT derivatives.[212] The first water-soluble PT derivatives were synthesized in 1987, specifically Poly(3-ethanesulfonatethiophene) and Poly(3-butanesulfonatethiophene), Figure 1.29a,b.[213] These polymers introduced sulfonate groups into the side chains of the thiophene backbone, enabling solubility in water through ionic interactions. The sulfonate groups ($-SO_3^-$) are highly polar and can form strong electrostatic interactions with water molecules. These interactions occur as the negatively charged sulfonate groups attract the partial positive charges of the hydrogen atoms in water molecules, leading to the formation of hydration shells around the polymer chains. This hydration process interrupts intermolecular interactions between polymer chains, thereby increasing their solubility in water.[214]

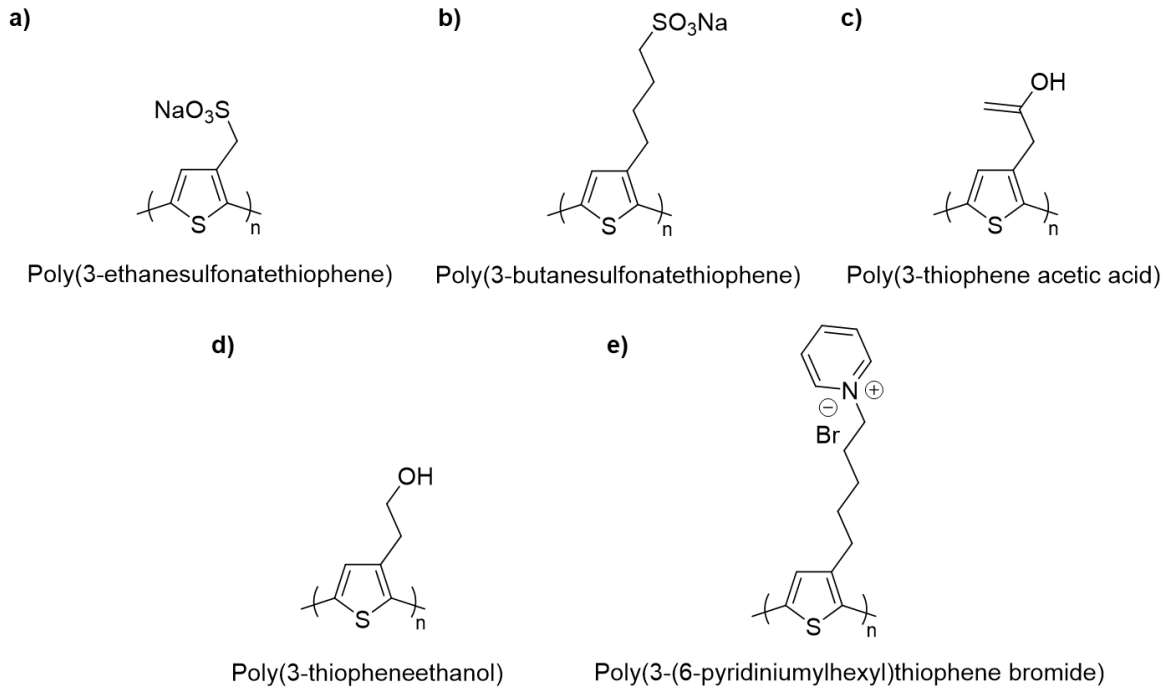


Figure 1.29. Structures of water soluble PT derivatives.

Since this initial advancement, additional water-soluble PT derivatives have been developed to further expand their applicability in aqueous environments. One significant example is poly(3-thiophene acetic acid) (PTAA), which incorporates carboxylic acid groups into the side chains of the thiophene ring, Figure 1.29c. These functional groups confer water solubility through hydrogen bonding with water molecules.[215] PTAA typically exhibits an absorption maximum of approximately 430 nm in its neutral state.[216] Similarly, poly(3-thiopheneethanol) (PTE) enhances water solubility by introducing hydroxyl groups into the side chains. These hydroxyl groups improve the hydrophilicity of the polymer, enabling compatibility with aqueous environments, Figure 1.29d.[217] The absorption maximum of PTE in its neutral state is observed around 420 nm.[218] Another example is poly(3-(6-pyrrolidiniumhexyl)thiophene bromide), a cationic polythiophene derivative in which pyrrolidinium groups are attached to the side chains, Figure 1.29e.[219] These ionic substituents make the polymer soluble in water and allow its interaction with polar solvents. The most widely studied and commercially significant example of water-soluble or better dispersible PTs is PEDOT when combined with polystyrene sulfonate (PSS), Figure 1.30.

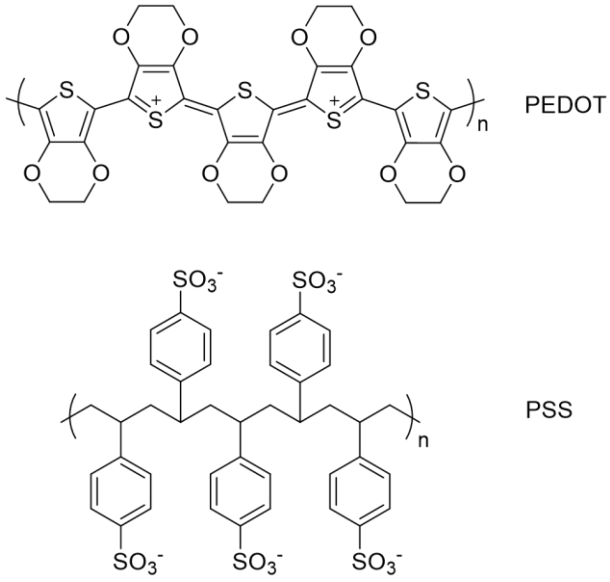


Figure 1.30. Chemical structure of PEDOT:PSS.

Generally, the PEDOT is highly regarded due to its properties, supported by quantitative data from research. It exhibits electrical conductivity up to 1000 S/cm when doped, as demonstrated in studies like those by Zhang et al.[220] Its stability during redox cycles is remarkable, retaining over 90% efficiency after 1000 cycles.[221] A paper reporting on the cycling stability of PEDOT in an ECD indicates its ability to retain 88.1% of its activity after 250000 redox cycles.[222] Additionally, PEDOT films achieve over 85% transparency in the visible spectrum, making them ideal for transparent electronic applications.[223] Polystyrene sulfonate (PSS) is added to PEDOT to enhance its solubility, processability, and performance, creating the widely used PEDOT:PSS composite. PSS provides water dispersibility to PEDOT, which is inherently insoluble, allowing for the preparation of stable aqueous dispersions.[224] PSS stabilizes the doped state of PEDOT by acting as a counterion. This stabilization occurs due to the ionic interactions between the positively charged PEDOT chains and the negatively charged sulfonate groups of PSS.[225,226] PEDOT:PSS exhibits an absorption maximum near 600 nm, which is associated with its delocalized π-conjugated system and electronic transitions involving polarons and bipolarons, the primary charge carriers in its doped state. In its oxidized, doped configuration, PEDOT displays a light blue colour due to broad absorption spanning the visible and near-infrared regions, a characteristic linked to the formation of these charged species and its high conductivity, which can reach up to 2063 S/cm.[227] Conversely, in its neutral or reduced state, PEDOT assumes a blue or gray coloration as its absorption shifts to lower energies, characterized by a sharp peak around 400 nm, reflecting significantly reduced conductivity, typically in the range of 10^{-3} to 10^{-2} S/cm.[228]

1.3 Irreversible electrochromic systems

While the adaptability and reversibility of EC materials have driven their extensive adoption in dynamic applications, the exploration of irreversible EC systems introduces broad possibilities in scenarios where permanent optical changes are advantageous. Applications such as tamper-evident seals, counterfeit detection, dosage indicators, and temperature or pressure-responsive labels benefit from the ability to create a lasting visual record of activation. These systems offer enhanced reliability and security by ensuring critical information remains visible over time, even without continuous power or monitoring.[229][230] This shift from reversibility to irreversibility opens opportunities for innovative applications, which will be explored in the following section.

1.3.1 Concept and characteristics

Although ECDs provide dynamic control of their optical characteristics, irreversible electrochromism remains a largely unknown research area. This is primarily due to the general view that EC irreversibility, caused by EC material degradation, represents a limitation and drawback for ECDs when undergoing significant redox cycles.[231–233] However, this perceived limitation of irreversibility can be transformed into a unique feature for specific applications. In scenarios where permanent colour change is desirable, such as in tamper-evident packaging or temperature indicators, the irreversible nature of electrochromism becomes an advantage rather than a drawback. By providing a permanent record of activation or exposure, irreversible electrochromic displays (*i*-ECDs) offer enhanced security and reliability, ensuring that critical information cannot be manipulated and remains visible even after extended periods. Moreover, considering that *i*-ECDs only provide visual feedback, they can be integrated with a wide array of sensors, thereby impacting numerous application fields.[234–236] Thus, while EC irreversibility may set challenges in certain perspectives, it presents unique opportunities for innovative applications where rapid and permanent feedback is essential.

1.3.2 Potential Applications

An *i*-ECD is a type of display technology where applying an electrical potential initiates an electrochemical reaction that permanently changes the colour/transmittance. Unlike reversible technologies, the change in colour in *i*-ECDs cannot be reversed, making it a one-time occurrence.[237] To achieve irreversibility in ECD, the exploitation of redox reactions could be an approach. However, typical polymers/molecules employed in ECDs tend to undergo

reversible reactions, allowing for multiple switching cycles and thus shifting colour several times, Figure 1.31a.[101,238,239] There are significant challenges in making EC polymers irreversible due to its intrinsic design for reversible electrochemical cycling, stable π-conjugation, and electrolyte interactions that favour reversibility. Inducing irreversibility requires overoxidation, structural disruption, or chemical reactions that permanently alter its redox properties, all of which demand precise control to avoid uncontrolled degradation. These complexities will be explored in detail in Chapter 4 of this dissertation. To date, the most efficient and smart approach to achieving a permanent colour change, which occurs only once and maintains stability over time, is via the electropolymerisation reactions.[237] During the study and development of an *i*-ECD, is selected a monomer capable of leading, through electropolymerisation reactions, to the formation of the corresponding polymer. The monomer therefore must have a different absorption from that of the electrosynthesized polymer in order to obtain a colour variation at the end of the process. An example is provided by EDOT, the monomeric precursor of PEDOT. The monomer absorbs in the UV and is transparent in the visible, while the polymer absorbs in the blue region.[240,241] During the application of potential, the monomer will be oxidized leading to the irreversible formation of the polymer on the anode in which during the progression of the reaction it will grow in thickness showing an increasingly intense colour over time. This will produce an irreversible colour change able to switch from transparent to dark blue in a fraction of time that relies on the monomer concentration, the electrical conductivity of the electrodes, electrolyte and applied potential, Figure 1.31b.[242–244] However, while the electropolymerisation of EDOT into PEDOT is irreversible, the resulting PEDOT itself is a reversible EC polymer, as previously discussed. This means that once formed, PEDOT can undergo reversible oxidation and reduction processes. By switching the polarity of the applied potential, PEDOT can transition between its neutral and oxidized state, transitioning from dark to light blue.

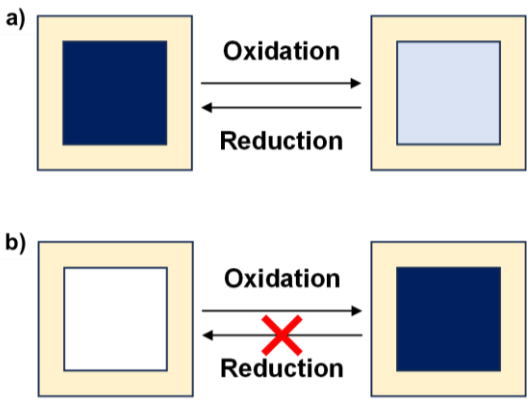


Figure 1.31. Visual representation of a) a reversible ECD where a PEDOT layer (dark blue) can be oxidized and afterwards reduced several times and b) an *i*-ECD where the EDOT monomer (transparent) can be electropolymerized forming a PEDOT layer.

To ensure the proper functionality of the *i*-ECD, the manufacturing process follows a different approach than the one used for standard reversible ECDs, Figure 1.32a. If in the reversible configuration involve two transparent electrodes positioned opposite each other, with the EC polymer deposited over, in the case of *i*-ECDs, the monomer is directly incorporated into the electrolyte situated between the electrodes, Figure 1.32b. Consequently, selecting the appropriate electrolyte, especially considering its solvent composition, is crucial to enable the dissolution of the monomer within it. Failure in solubilization inhibits the electropolymerisation reaction, thereby hindering the functionality of the *i*-ECD.

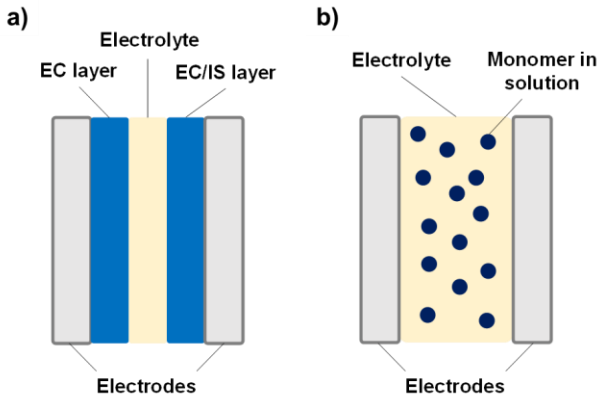


Figure 1.32. Illustration depicting a) a reversible ECD consisting of two electrodes lodging two EC layers or one EC layer along with an ion storage (IS) layer, separated by an electrolyte, and b) an irreversible configuration featuring two electrodes containing an electrolyte wherein the monomer, undergoing electropolymerisation reaction, is solubilized.

1.3.3 Current irreversible technologies and limitations

i-ECDs have significant potential due to their ability to provide irreversible and permanent optical changes in colour or transmittance. However, there are currently no commercial products based on this technology, and even scientific research on irreversible electrochromism is limited. Most studies focus on reversible ECDs, where irreversibility is typically seen as a drawback, displays lose functionality after multiple switching cycles. This perception may have prevented researchers from exploring irreversibility as a potential advantage, leaving the field largely unexplored.[34,232]

A potential exploitation of irreversible electrochromism emerged in 2015 with Chromera, Inc. which developed a bistable indicator utilizing electropolymerisation of monomers, such as thiophene based (EDOT, 2-bithiophene) or nitrogen based (aniline) by applying 4.0 V for 20 seconds and subsequently reversing the polarity to permanently block the colour, Figure 1.33.

The irreversibility occurs only if the voltage polarity is reversed after the initial switch, adding a layer of complexity to the circuit and electronic components required for the final device.

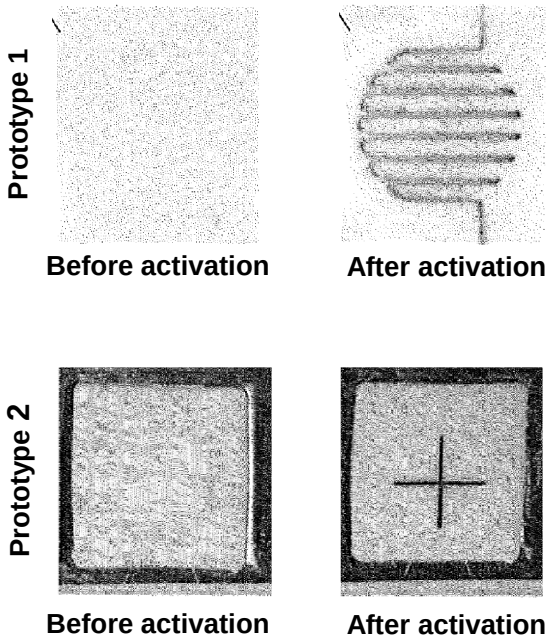


Figure 1.33. Picture of two prototypes developed by Chromera, Inc.[77]

Recent advancements in 2023 by Elin et al. in collaboration with Ynvisible mark one of the first examples of *i*-ECDs in literature. Termed "irreversible electrochemical indicators," these devices exploit the electropolymerisation of EDOT which occur inside the display forming a layer of PEDOT over the PET-ITO electrodes, Figure 1.34.[237] The monomer is directly solubilized inside an UV-curable electrolyte which require an applied potential of *ca.* 3.0 V to electropolymerize.

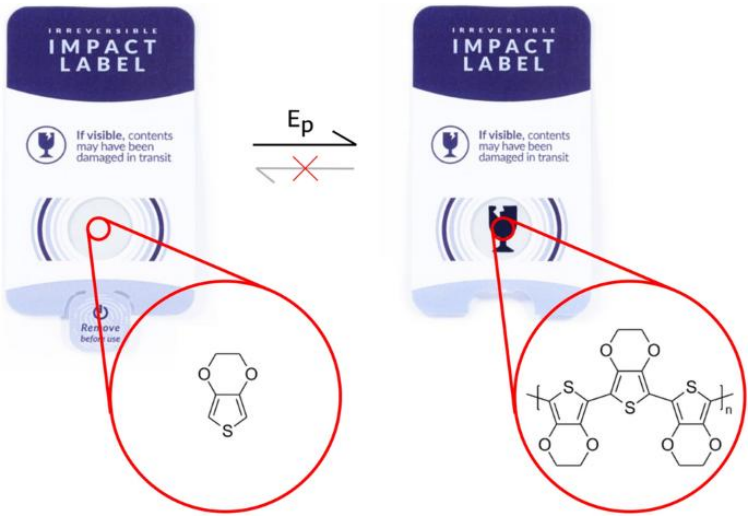


Figure 1.34. Picture of the irreversible impact label exploiting the electropolymerisation of EDOT.[237]

Concurrently, Ynvisible capitalized on this mechanism to develop "Irreversible Pixels," device designed to permanently display and record information, acting as a visual and physical memory, Figure 1.35.[245]



Figure 1.35. Pictures of two irreversible pixel displays after the process of activation through applied voltage.

Despite the potential of current irreversible EC technologies, several considerations must be addressed. One major concern is the intrinsic EC reversibility of the PEDOT layer (or any EC polymer) formed during electropolymerisation inside the *i*-ECD. Further changes in voltage polarity can generate reversible redox reactions leading to multiple colour changes and potentially compromising the technology's irreversibility and tamper-proofing capabilities. Moreover, the fact that these monomers require organic solvents for solubilization presents significant challenges, as such solvents are often restricted due to safety regulations or require strict handling protocols to mitigate health and environmental risks. This limitation complicates scalability in industrial settings and poses additional concerns for applications involving food, pharmaceuticals, or other consumables, where solvent residues must be minimized or entirely eliminated.

1.4 Aim of the dissertation

The technology developed in this dissertation aligns precisely with this objective by addressing the initial challenge of generating a colour change not produced by the formation of an EC polymer/compound avoiding the problem of reversibility. Furthermore, it eliminates the need for organic solvents, opting instead for water as a non-toxic solvent compatible with numerous applications. Additionally, the activation threshold for the irreversible and permanent colour change is significantly lowered to a minimum of 1.5 V, which reduces the space needed for batteries or capacitors to power the indicators, making it advantageous for compact designs.

This effect is achieved by exploiting the irreversible oxidative electropolymerisation of dopamine (DA) into polydopamine (PDA), a black polymer. DA is a water-soluble monomer that appears transparent in solution. Upon the application of an external voltage, DA undergoes oxidation, leading to the formation of reactive intermediates that initiate oligomerization. These oligomers further polymerize into PDA, resulting in a progressive darkening of the film. The final coloration, ranging from brown to black, depends on the polymer concentration and the thickness of the deposited layer, ensuring a stable and permanent visual change.[246]

REFERENCES

[1] P. F. Bai, R. A. Hayes, M. Jin, L. Shui, Z. C. Yi, L. Wang, X. Zhang, G. Zhou, *Prog. Electromagn. Res.* **2014**, *147*, 95–116.

[2] R. Kaçar, R. B. Serin, E. Uçar, A. Ülkü, *Mater. Today Commun.* **2023**, *35*, 105534.

[3] M. H. Chua, T. Tang, K. H. Ong, W. T. Neo, J. W. Xu, **2019**, DOI 10.1039/9781788016667-00001.

[4] R. J. Mortimer, *Annu. Rev. Mater. Res.* **2011**, *41*, 241–268.

[5] H. Roehrig, H. Blume, T.-L. Ji, M. Browne, *J. Digit. Imaging* **1990**, *3*, 134–145.

[6] B. Bahadur, *Mol. Cryst. Liq. Cryst.* **1984**, *109*, 3–93.

[7] A. A. Bergh, P. J. Dean, *Proc. IEEE* **1972**, *60*, 156–223.

[8] A. L. Dalisa, *IEEE Trans. Electron Devices* **1977**, *24*, 827–834.

[9] R. Pethig, *Biomicrofluidics* **2010**, *4*, 022811.

[10] Y. Lu, B. Tang, G. Yang, Y. Guo, L. Liu, A. Henzen, *Micromachines* **2021**, *12*, 206.

[11] A. C. Arsenault, D. P. Puzzo, A. Ghoussoub, I. Manners, G. A. Ozin, *J. Soc. Inf. Disp.* **2007**, *15*, 1095–1098.

[12] C. Gu, A.-B. Jia, Y.-M. Zhang, S. X.-A. Zhang, *Chem. Rev.* **2022**, *122*, 14679–14721.

[13] H. Fan, W. Wei, C. Hou, Q. Zhang, Y. Li, K. Li, H. Wang, *J. Mater. Chem. C* **2023**, *11*, 7183–7210.

[14] W. Wu, W. C. Poh, J. Lv, S. Chen, D. Gao, F. Yu, H. Wang, H. Fang, H. Wang, P. S. Lee, *Adv. Energy Mater.* **2023**, *13*, 2204103.

[15] J. P. Coleman, A. T. Lynch, P. Madhukar, J. H. Wagenknecht, *Sol. Energy Mater. Sol. Cells* **1999**, *56*, 395–418.

[16] M. C. Hartel, D. Lee, P. S. Weiss, J. Wang, J. Kim, *Biosens. Bioelectron.* **2022**, *215*, 114565.

[17] P. R. Somani, S. Radhakrishnan, *Mater. Chem. Phys.* **2003**, *77*, 117–133.

[18] G. Cai, J. Wang, P. S. Lee, *Acc. Chem. Res.* **2016**, *49*, 1469–1476.

[19] S. Bulja, R. Kopf, A. Tate, T. Hu, *Sci. Rep.* **2016**, *6*, 28839.

[20] Y. Zhen, B. P. Jelle, T. Gao, *Anal. Sci. Adv.* **2020**, *1*, 124–131.

[21] C.-T. Lee, S. Han, Y.-X. Zhao, Y.-C. Hung, T.-H. Hsu, H.-Y. Hsieh, K.-W. Weng, *Surf. Coat. Technol.* **2019**, *363*, 426–429.

[22] G. A. Niklasson, C. G. Granqvist, *J. Mater. Chem.* **2006**, *17*, 127–156.

[23] N. S. Pham, L. T. Nguyen, H. T. Nguyen, V. Q. Nguyen, T. B. T. Nguyen, C. D. Tran, B. N. Nguyen, A. Q. K. Nguyen, *Ceram. Int.* **2023**, *49*, 33413–33417.

[24] A. Carolin Amala, R. Vignesh, G. V. Geetha, R. Sivakumar, *Phys. Status Solidi A* **2021**, *218*, 2100282.

[25] T. Qin, L. Deng, P. Zhang, M. Tang, C. Li, H. Xie, S. Huang, X. Gao, *Nanoscale Res. Lett.* **2022**, *17*, 51.

[26] S. Zhang, G. Sun, Y. He, R. Fu, Y. Gu, S. Chen, *ACS Appl. Mater. Interfaces* **2017**, *9*, 16426–16434.

[27] A. J. C. Da Silva, F. A. Ribeiro Nogueira, J. Tonholo, A. S. Ribeiro, *Sol. Energy Mater. Sol. Cells* **2011**, *95*, 2255–2259.

[28] A. Chaudhary, D. K. Pathak, M. Tanwar, P. Yogi, P. R. Sagdeo, R. Kumar, *ACS Appl. Electron. Mater.* **2019**, *1*, 58–63.

[29] L. De Lazari Ferreira, H. D. R. Calado, *J. Solid State Electrochem.* **2018**, *22*, 1507–1515.

[30] R. Colucci, G. C. Faria, L. F. Santos, G. Gozzi, *J. Mater. Sci. Mater. Electron.* **2019**, *30*, 16864–16872.

[31] Y. Yang, H. Deng, Q. Fu, *Mater. Chem. Front.* **2020**, *4*, 3130–3152.

[32] V. A. Shakhnov, A. I. Vlasov, S. V. Tokarev, *IOP Conf. Ser. Mater. Sci. Eng.* **2016**, *151*, 012005.

[33] D. Dong, W. Wang, A. Rougier, A. Barnabé, G. Dong, F. Zhang, X. Diao, *J. Mater. Chem. C* **2018**, *6*, 9875–9889.

[34] R. Zhang, Q. Zhou, S. Huang, Y. Zhang, R.-T. Wen, *Nat. Commun.* **2024**, *15*, 2294.

[35] Y. Yang, Y. Peng, Z. Jian, Y. Qi, Y. Xiong, W. Chen, *ACS Appl. Mater. Interfaces* **2022**, *14*, 8157–8162.

[36] H.-Y. Liao, T.-C. Liao, W.-H. Chen, C.-H. Chang, L.-C. Chen, *Sol. Energy Mater. Sol. Cells* **2016**, *145*, 8–15.

[37] V. D. Ivanov, *Ionics* **2020**, *26*, 531–547.

[38] Y. Ding, M. Wang, Z. Mei, X. Diao, *Sol. Energy Mater. Sol. Cells* **2022**, *248*, 112037.

[39] H. Moulki, D. H. Park, B.-K. Min, H. Kwon, S.-J. Hwang, J.-H. Choy, T. Toupance, G. Campet, A. Rougier, *Electrochimica Acta* **2012**, *74*, 46–52.

[40] Z. Song, F. Chen, M. Martinez-Ibañez, W. Feng, M. Forsyth, Z. Zhou, M. Armand, H. Zhang, *Nat. Commun.* **2023**, *14*, 4884.

[41] J. C. Barbosa, R. Gonçalves, C. M. Costa, S. Lanceros-Méndez, *ACS Omega* **2022**, *7*, 14457–14464.

[42] Z. Xue, D. He, X. Xie, *J. Mater. Chem. A* **2015**, *3*, 19218–19253.

[43] G. Homann, L. Stolz, J. Nair, I. C. Laskovic, M. Winter, J. Kasnatscheew, *Sci. Rep.* **2020**, *10*, 4390.

[44] B. Zhang, G. Xu, S. Tan, C. Liu, *Opt. Mater.* **2020**, *101*, 109756.

[45] D. E. Shen, D. B. Iyer, A. M. Dejneka, J. R. Reynolds, A. M. Österholm, *ACS Appl. Opt. Mater.* **2023**, *1*, 906–914.

[46] G. K. Pande, J. S. Heo, J. H. Choi, Y. S. Eom, J. Kim, S. K. Park, J. S. Park, *Chem. Eng. J.* **2021**, *420*, 130446.

[47] J. Chu, J. Lan, D. Lu, J. Ma, X. Wang, B. Wu, M. Gong, R. Zhang, S. Xiong, *Micro Nano Lett.* **2016**, *11*, 749–752.

[48] M. Wang, Q. Liu, G. Dong, Y. He, X. Diao, *Electrochimica Acta* **2017**, *258*, 1336–1347.

[49] B. Zhang, L. Ma, X. Hao, Y. Zhang, Y. Tian, *Electrochimica Acta* **2023**, *467*, 143132.

[50] R. Liu, Y. Ren, J. Wang, Y. Wang, J. Jia, G. Zhao, *Ceram. Int.* **2021**, *47*, 31834–31842.

[51] J. Kawahara, P. A. Ersman, I. Engquist, M. Berggren, *Org. Electron.* **2012**, *13*, 469–474.

[52] M. K. Ram, E. Maccioni, C. Nicolini, *Thin Solid Films* **1997**, *303*, 27–33.

[53] P. Camurlu, *RSC Adv.* **2014**, *4*, 55832–55845.

[54] G. Dijk, H. J. Ruigrok, R. P. O'Connor, *Adv. Mater. Interfaces* **2020**, *7*, 2000675.

[55] G. Liu, Y. Liu, M. Zhang, Z. Yang, P. Gane, *Org. Electron.* **2020**, *81*, 105674.

[56] R. Brooke, E. Mitraka, S. Sardar, M. Sandberg, A. Sawatdee, M. Berggren, X. Crispin, M. P. Jonsson, *J. Mater. Chem. C* **2017**, *5*, 5824–5830.

[57] Q. Cai, H. Yan, R. Yao, D. Luo, M. Li, J. Zhong, Y. Yang, T. Qiu, H. Ning, J. Peng, *Membranes* **2022**, *12*, 1039.

[58] B. Sun, Y. Li, *J. Mater. Chem. C* **2022**, *10*, 388–412.

[59] T. Richardson, *Solid State Ion.* **2003**, *165*, 305–308.

[60] X. Yu, P. Guo, J. Chen, S. Li, H. Li, *Responsive Mater.* **2024**, *2*, e20240013.

[61] M. Li, A. Patra, Y. Sheynin, M. Bendikov, *Adv. Mater.* **2009**, *21*, 1707–1711.

[62] B. Sankaran, J. R. Reynolds, *Macromolecules* **1997**, *30*, 2582–2588.

[63] Y. Zhang, D. Liu, Z. Ren, W. Liu, B. Wang, S. Song, T. Hao, L. Xu, H. Ji, J. Sun, L. Zhang, Y. Li, *Chem. Eng. J.* **2024**, *499*, 155960.

[64] X. Lv, Y. Yang, L. Xu, J. Li, Z. Xu, R. Zhu, D. S. Wright, C. Zhang, *React. Funct. Polym.* **2020**, *156*, 104737.

[65] W. Wang, X. Wang, X. Xia, Z. Yao, Y. Zhong, J. Tu, *Nanoscale* **2018**, *10*, 8162–8169.

[66] S. Zhang, J. Ren, S. Chen, Y. Luo, X. Bai, L. Ye, F. Yang, Y. Cao, *J. Electroanal. Chem.* **2020**, *870*, 114248.

[67] M. Fabretto, T. Vaithianathan, C. Hall, P. Murphy, P. C. Innis, J. Mazurkiewicz, G. G. Wallace, *Electrochem. Commun.* **2007**, *9*, 2032–2036.

[68] C. Park, J. M. Kim, Y. Kim, S. Bae, M. Do, S. Im, S. Yoo, J. H. Kim, *ACS Appl. Electron. Mater.* **2021**, *3*, 4781–4792.

[69] S. J. Yoo, J. W. Lim, Y.-E. Sung, *Sol. Energy Mater. Sol. Cells* **2006**, *90*, 477–484.

[70] K. Chen, I. Song, L. You, J. Mei, *Acc. Chem. Res.* **2025**, *58*, 24–35.

[71] J. Jensen, M. V. Madsen, F. C. Krebs, *J. Mater. Chem. C* **2013**, *1*, 4826–4835.

[72] L. Wang, M. Guo, J. Zhan, X. Jiao, D. Chen, T. Wang, *J. Mater. Chem. A* **2020**, *8*, 17098–17105.

[73] C. G. Granqvist, M. A. Arvizu, İ. Bayrak Pehlivan, H.-Y. Qu, R.-T. Wen, G. A. Niklasson, *Electrochimica Acta* **2018**, *259*, 1170–1182.

[74] A. Cannavale, U. Ayr, F. Fiorito, F. Martellotta, *Energies* **2020**, *13*, 1449.

[75] J. Wang, L. Zhang, W. Zhan, J. Dong, Y. Ma, J. Li, W. Li, C. Zhang, *Chem. Eng. J.* **2024**, *483*, 149078.

[76] R. Baetens, B. P. Jelle, A. Gustavsen, *Sol. Energy Mater. Sol. Cells* **2010**, *94*, 87–105.

[77] T. Kamimori, J. Nagai, M. Mizuhashi, **n.d.**

[78] C. G. Granqvist, S. Green, G. A. Niklasson, N. R. Mlyuka, S. Von Kræmer, P. Georén, *Thin Solid Films* **2010**, *518*, 3046–3053.

[79] M. A. Macdo, L. H. Dall'Antonia, B. Valla, M. A. Aegerter, **n.d.**

[80] J. Gupta, H. Shaik, S. A. Sattar, *J. Mater. Sci. Mater. Electron.* **2024**, *35*, 1–13.

[81] B. R. Park, J. Hong, E. J. Choi, Y. J. Choi, C. Lee, J. W. Moon, *Energies* **2019**, *12*, 1181.

[82] P. Yang, P. Sun, W. Mai, *Mater. Today* **2016**, *19*, 394–402.

[83] H. N. Kim, S. M. Cho, C. S. Ah, J. Song, H. Ryu, Y. H. Kim, T.-Y. Kim, *Mater. Res. Bull.* **2016**, *82*, 16–21.

[84] F. G. K. Baucke, **n.d.**

[85] K. Madasamy, D. Velayutham, V. Suryanarayanan, M. Kathiresan, K.-C. Ho, *J. Mater. Chem. C* **2019**, *7*, 4622–4637.

[86] X. Yu, M. Chang, W. Chen, D. Liang, X. Lu, G. Zhou, *ACS Appl. Mater. Interfaces* **2020**, *12*, 39505–39514.

[87] J. Remmele, D. E. Shen, T. Mustonen, N. Fruehauf, *ACS Appl. Mater. Interfaces* **2015**, *7*, 12001–12008.

[88] Y. Wang, S. Wang, X. Wang, W. Zhang, W. Zheng, Y.-M. Zhang, S. X.-A. Zhang, *Nat. Mater.* **2019**, *18*, 1335–1342.

[89] C. Gu, A.-B. Jia, Y.-M. Zhang, S. X.-A. Zhang, *Chem. Rev.* **2022**, *122*, 14679–14721.

[90] E. C. Atayde, Y.-C. Wang, B. M. Matsagar, L.-C. Chen, K.-C. Ho, K. C.-W. Wu, *Mater. Today Sustain.* **2024**, *27*, 100878.

[91] L. Beverina, G. A. Pagani, M. Sassi, *Chem. Commun.* **2014**, *50*, 5413–5430.

[92] Y. Lee, J. Yun, M. Seo, S.-J. Kim, J. Oh, C. M. Kang, H.-J. Sun, T. D. Chung, B. Lee, *Nano Lett.* **2020**, *20*, 6084–6090.

[93] J. Koo, V. Amoli, S. Y. Kim, C. Lee, J. Kim, S.-M. Park, J. Kim, J. M. Ahn, K. J. Jung, D. H. Kim, *Nano Energy* **2020**, *78*, 105199.

[94] Y. Wang, B. F. Long, C. Y. Liu, G. A. Lin, *High Temp. Mater. Process.* **2021**, *40*, 171–177.

[95] G. Meyer, *Z. Für Anorg. Allg. Chem.* **2007**, *633*, 2537–2552.

[96] J. R. Platt, *J. Chem. Phys.* **1961**, *34*, 862–863.

[97] S. K. Deb, *Philos. Mag. J. Theor. Exp. Appl. Phys.* **1973**, *27*, 801–822.

[98] J. S. E. M. Svensson, C. G. Granqvist, *Thin Solid Films* **1985**, *126*, 31–36.

[99] P. Shi, C. M. Amb, E. P. Knott, E. J. Thompson, D. Y. Liu, J. Mei, A. L. Dyer, J. R. Reynolds, *Adv. Mater.* **2010**, *22*, 4949–4953.

[100] C. M. Amb, A. L. Dyer, J. R. Reynolds, *Chem. Mater.* **2011**, *23*, 397–415.

[101] A. A. Argun, P.-H. Aubert, B. C. Thompson, I. Schwendeman, C. L. Gaupp, J. Hwang, N. J. Pinto, D. B. Tanner, A. G. MacDiarmid, J. R. Reynolds, *Chem. Mater.* **2004**, *16*, 4401–4412.

[102] C. Tao, Y. Li, J. Wang, *Coord. Chem. Rev.* **2023**, *475*, 214891.

[103] F. Demir, Z. Bıyıklıoğlu, A. Koca, *J. Electrochem. Soc.* **2014**, *161*, G1–G6.

[104] Y. H. Qi, P. Desjardins, X. S. Meng, Z. Y. Wang, *Opt. Mater.* **2003**, *21*, 255–263.

[105] K. J. Patel, G. G. Bhatt, J. R. Ray, P. Suryavanshi, C. J. Panchal, *J. Solid State Electrochem.* **2017**, *21*, 337–347.

[106] D. Ma, T. Li, Z. Xu, L. Wang, J. Wang, *Sol. Energy Mater. Sol. Cells* **2018**, *177*, 51–56.

[107] C.-M. Chang, Y.-C. Chiang, M.-H. Cheng, S.-H. Lin, W.-B. Jian, J.-T. Chen, Y.-J. Cheng, Y.-R. Ma, K. Tsukagoshi, *Sol. Energy Mater. Sol. Cells* **2021**, *223*, 110960.

[108] V.-T. Nguyen, B. K. Min, S. K. Kim, Y. Yi, C.-G. Choi, *J. Mater. Chem. C* **2021**, *9*, 3183–3192.

[109] Y.-C. Her, C.-C. Chang, *CrystEngComm* **2014**, *16*, 5379–5386.

[110] D. Zhou, D. Xie, F. Shi, D. H. Wang, X. Ge, X. H. Xia, X. L. Wang, C. D. Gu, J. P. Tu, *J. Colloid Interface Sci.* **2015**, *460*, 200–208.

[111] R.-T. Wen, S. Malmgren, C. G. Granqvist, G. A. Niklasson, *ACS Appl. Mater. Interfaces* **2017**, *9*, 12872–12877.

[112] R.-T. Wen, C. G. Granqvist, G. A. Niklasson, *Nat. Mater.* **2015**, *14*, 996–1001.

[113] Y. Cui, Q. Wang, B. Liu, Y. Gao, **2020**, DOI 10.21203/rs.3.rs-25346/v1.

[114] Z. Xia, H. Wang, Y. Su, P. Tang, M. Dai, H. Lin, Z. Zhang, Q. Shi, *Coatings* **2020**, *10*, 577.

[115] K. S. Usha, S. Y. Lee, R. Sivakumar, C. Sanjeeviraja, *Ceram. Int.* **2024**, *50*, 36651–36665.

[116] S. Pereira, A. Gonçalves, N. Correia, J. Pinto, L. Pereira, R. Martins, E. Fortunato, *Sol. Energy Mater. Sol. Cells* **2014**, *120*, 109–115.

[117] Q. Liu, Q. Chen, Q. Zhang, Y. Xiao, X. Zhong, G. Dong, M.-P. Delplancke-Ogletree, H. Terryn, K. Baert, F. Reniers, X. Diao, *J. Mater. Chem. C* **2018**, *6*, 646–653.

[118] Z. Luo, L. Liu, X. Yang, X. Luo, P. Bi, Z. Fu, A. Pang, W. Li, Y. Yi, *ACS Appl. Mater. Interfaces* **2020**, *12*, 39098–39107.

[119] W. Jinmin, H. O. U. Lijun, M. A. Dongyun, *J. Inorg. Mater.* **2021**, *36*, 461.

[120] T. G. Novak, J. Kim, A. P. Tiwari, J. Kim, S. Lee, J. Lee, S. Jeon, *ACS Sustain. Chem. Eng.* **2020**, *8*, 11276–11282.

[121] D. Dixit, K. V. Madhuri, *Superlattices Microstruct.* **2021**, *156*, 106936.

[122] H. Lu, X. Li, Q. Lei, *Front. Chem.* **2021**, *9*, DOI 10.3389/fchem.2021.732132.

[123] J. Ouyang, *SmartMat* **2021**, *2*, 263–285.

[124] A. Ajayaghosh, *Chem. Soc. Rev.* **2003**, *32*, 181–191.

[125] H. Shirakawa, E. J. Louis, A. G. MacDiarmid, C. K. Chiang, A. J. Heeger, *J. Chem. Soc. Chem. Commun.* **1977**, 578–580.

[126] J. Roncali, *Macromol. Rapid Commun.* **2007**, *28*, 1761–1775.

[127] H. Van Mullekom, *Mater. Sci. Eng. R Rep.* **2001**, *32*, 1–40.

[128] J. Roncali, *Chem. Rev.* **1997**, *97*, 173–206.

[129] K. W. Shah, S.-X. Wang, D. X. Y. Soo, J. Xu, *Polymers* **2019**, *11*, 1839.

[130] P. M. S. Monk, R. J. Mortimer, D. R. Rosseinsky, *Electrochromism: Fundamentals and Applications*, John Wiley & Sons, **2008**.

[131] W. Wu, S. Guo, J. Bian, X. He, H. Li, J. Li, *J. Energy Chem.* **2024**, *93*, 453–470.

[132] R. G. Compton, A. M. Waller, P. M. S. Monk, D. R. Rosseinsky, *J. Chem. Soc. Faraday Trans.* **1990**, *86*, 2583–2586.

[133] P. M. S. Monk, R. D. Fairweather, M. D. Ingram, J. A. Duffy, *J. Chem. Soc. Perkin Trans. 2* **1992**, 2039–2041.

[134] R. J. Mortimer, T. S. Varley, *Chem. Mater.* **2011**, *23*, 4077–4082.

[135] Y. Alesanco, A. Viñuales, G. Cabañero, J. Rodriguez, R. Tena-Zaera, *Adv. Opt. Mater.* **2017**, *5*, 1600989.

[136] J.-W. Kim, J.-M. Myoung, *Adv. Funct. Mater.* **2019**, *29*, 1808911.

[137] A. V. Shchegolkov, S.-H. Jang, A. V. Shchegolkov, Y. V. Rodionov, A. O. Sukhova, M. S. Lipkin, *Nanomaterials* **2021**, *11*, 2376.

[138] X. Zhang, J. Zhang, W. Song, Z. Liu, *J. Phys. Chem. B* **2006**, *110*, 1158–1165.

[139] S. Bose, T. Kuila, Md. E. Uddin, N. H. Kim, A. K. T. Lau, J. H. Lee, *Polymer* **2010**, *51*, 5921–5928.

[140] T.-H. Le, Y. Kim, H. Yoon, *Polymers* **2017**, *9*, 150.

[141] T. Nezakati, A. Seifalian, A. Tan, A. M. Seifalian, *Chem. Rev.* **2018**, *118*, 6766–6843.

[142] A. O. Patil, A. J. Heeger, F. Wudl, *Chem. Rev.* **1988**, *88*, 183–200.

[143] J. L. Bredas, G. B. Street, *Acc. Chem. Res.* **1985**, *18*, 309–315.

[144] I. D. Brotherston, D. S. K. Mudigonda, J. M. Osborn, J. Belk, J. Chen, D. C. Loveday, J. L. Boehme, J. P. Ferraris, D. L. Meeker, *Electrochimica Acta* **1999**, *44*, 2993–3004.

[145] M. Ak, B. Gacal, B. Kiskan, Y. Yagci, L. Toppare, *Polymer* **2008**, *49*, 2202–2210.

[146] Z. Zhao-yang, T. Yi-jie, X. Xiao-qian, Z. Yong-jiang, C. Hai-feng, Z. Wen-wei, *J. Appl. Polym. Sci.* **2013**, *129*, 1506–1512.

[147] M. Bayat, H. Izadan, S. Santiago, F. Estrany, M. Dinari, D. Semnani, C. Alemán, G. Guirado, *J. Electroanal. Chem.* **2021**, *886*, 115113.

[148] K. Kaeriyama, M. Sato, K. Hamada, *Makromol. Chem. Rapid Commun.* **1989**, *10*, 171–175.

[149] T. Benincori, E. Brenna, F. Sannicolò, G. Zotti, S. Zecchin, G. Schiavon, C. Gatti, G. Frigerio, *Chem. Mater.* **2000**, *12*, 1480–1489.

[150] A. B. Kon, J. S. Foos, T. L. Rose, *Chem. Mater.* **1992**, *4*, 416–424.

[151] E. E. Havinga, W. Ten Hoeve, E. W. Meijer, H. Wynberg, *Chem. Mater.* **1989**, *1*, 650–659.

[152] D. M. Welsh, A. Kumar, E. W. Meijer, J. R. Reynolds, *Adv. Mater.* **1999**, *11*, 1379–1382.

[153] R. M. Walczak, J. R. Reynolds, *Adv. Mater.* **2006**, *18*, 1121–1131.

[154] C. L. Gaupp, K. Zong, P. Schottland, B. C. Thompson, C. A. Thomas, J. R. Reynolds, *Macromolecules* **2000**, *33*, 1132–1133.

[155] P. Schottland, K. Zong, C. L. Gaupp, B. C. Thompson, C. A. Thomas, I. Giurgiu, R. Hickman, K. A. Abboud, J. R. Reynolds, *Macromolecules* **2000**, *33*, 7051–7061.

[156] E. Unur, J.-H. Jung, R. J. Mortimer, J. R. Reynolds, *Chem. Mater.* **2008**, *20*, 2328–2334.

[157] O. Olsson, M. Gugole, A. Dahlin, *Nanophotonics* **2023**, *12*, 1591–1599.

[158] D. E. Stilwell, S.-M. Park, *J. Electrochem. Soc.* **1988**, *135*, 2254.

[159] N. Gospodinova, L. Terlemezyan, *Prog. Polym. Sci.* **1998**, *23*, 1443–1484.

[160] M. Jaymand, *Prog. Polym. Sci.* **2013**, *38*, 1287–1306.

[161] S. Kumar, R. Prakash, P. Maiti, *Sol. Energy* **2022**, *231*, 985–1001.

[162] A. Saraswat, S. Kumar, *Eur. Polym. J.* **2023**, *182*, 111714.

[163] A. H. Majeed, L. A. Mohammed, O. G. Hammoodi, S. Sehgal, M. A. Alheety, K. K. Saxena, S. A. Dadoosh, I. K. Mohammed, M. M. Jasim, N. U. Salmaan, *Int. J. Polym. Sci.* **2022**, *2022*, 9047554.

[164] N. Su, *Nanoscale Res. Lett.* **2015**, *10*, 301.

[165] M. Beygisangchin, S. Abdul Rashid, S. Shafie, A. R. Sadrolhosseini, H. N. Lim, *Polymers* **2021**, *13*, 2003.

[166] S. Lakard, J. Husson, S. Monney, C. C. Buron, B. Lakard, *Prog. Org. Coat.* **2016**, *99*, 429–436.

[167] A. Watanabe, K. Mori, A. Iwabuchi, Y. Iwasaki, Y. Nakamura, O. Ito, *Macromolecules* **1989**, *22*, 3521–3525.

[168] C. Barbero, H. J. Salavagione, D. F. Acevedo, D. E. Grumelli, F. Garay, G. A. Planes, G. M. Morales, M. C. Miras, *Electrochimica Acta* **2004**, *49*, 3671–3686.

[169] M. Heydari, P. Najafi Moghadam, A. R. Fareghi, M. Bahram, N. Movagharnezhad, *Polym. Adv. Technol.* **2015**, *26*, 250–254.

[170] K. Khamngoen, N. Paradee, A. Sirivat, *J. Polym. Res.* **2016**, *23*, 172.

[171] C.-W. Kuo, S.-J. Chen, P.-R. Chen, T.-Y. Wu, W.-T. Tsai, C.-G. Tseng, *J. Taiwan Inst. Chem. Eng.* **2013**, *44*, 497–504.

[172] G. D'Aprano, M. Leclerc, G. Zotti, G. Schiavon, *Chem. Mater.* **1995**, *7*, 33–42.

[173] J. Stejskal, P. Kratochvíl, N. Radhakrishnan, *Synth. Met.* **1993**, *61*, 225–231.

[174] J. Petrova, J. Romanova, G. Madjarova, A. Ivanova, A. Tadjer, *J. Phys. Chem. B* **2012**, *116*, 6543–6552.

[175] E. Ortega, F. Armijo, I. Jessop, M. A. Del Valle, F. R. Diaz, *J. Chil. Chem. Soc.* **2013**, *58*, 1959–1962.

[176] A. N. Andriianova, Y. N. Biglova, A. G. Mustafin, *RSC Adv.* **2020**, *10*, 7468.

[177] Y. Wei, W. W. Focke, G. E. Wnek, A. Ray, A. G. MacDiarmid, *J. Phys. Chem.* **1989**, *93*, 495–499.

[178] S. I. C. de Torresi, A. N. Bassetto, B. C. Trasferetti, *J. Solid State Electrochem.* **1998**, *2*, 24–29.

[179] U. Mehmood, A. Al-Ahmed, I. A. Hussein, *Renew. Sustain. Energy Rev.* **2016**, *57*, 550–561.

[180] S. S. Jeon, S. J. Yang, K.-J. Lee, S. S. Im, *Polymer* **2010**, *51*, 4069–4076.

[181] B. M. W. Langeveld-Voss, R. A. J. Janssen, E. W. Meijer, *J. Mol. Struct.* **2000**.

[182] M. Kabasakaloglu, T. Kiyak, H. Toprak, M. L. Aksu, *Appl. Surf. Sci.* **1999**, *152*, 115–125.

[183] P. Pascariu, D. Vernardou, M. P. Suchea, A. Airinei, L. Ursu, S. Bucur, I. V. Tudose, O. N. Ionescu, E. Koudoumas, *Mater. Des.* **2019**, *182*, 108027.

[184] Si. M. Bouzzine, G. Salgado-Morán, M. Hamidi, M. Bouachrine, A. G. Pacheco, D. Glossman-Mitnik, *J. Chem.* **2015**, *2015*, 1–12.

[185] S. Wang, W. Zhu, I. E. Jacobs, W. A. Wood, Z. Wang, S. Manikandan, J. W. Andreasen, H.-I. Un, S. Ursel, S. Peralta, S. Guan, J.-C. Grivel, S. Longuemart, H. Sirringhaus, *Adv. Mater.* **2024**, *36*, 2314062.

[186] S. Ghosh, V. Gueskine, M. Berggren, I. V. Zozoulenko, *J. Phys. Chem. C* **2019**, *123*, 15467–15476.

[187] R. K. Khanna, Y. M. Jiang, B. Srinivas, C. B. Smithhart, D. L. Wertz, *Chem. Mater.* **1993**, *5*, 1792–1798.

[188] T. P. Kaloni, P. K. Giesbrecht, G. Schreckenbach, M. S. Freund, *Chem. Mater.* **2017**, *29*, 10248–10283.

[189] H.-J. Wang, C.-P. Chen, R.-J. Jeng, *Materials* **2014**, *7*, 2411.

[190] Y. Lu, S. Wang, C. Xiong, G.-H. Hu, *Synth. Met.* **2020**, *270*, 116603.

[191] M. Jaymand, M. Hatamzadeh, Y. Omidi, *Prog. Polym. Sci.* **2015**, *47*, 26–69.

[192] J. Roncali, A. Yassar, F. Garnier, *J. Chem. Soc. Chem. Commun.* **1988**, 581–582.

[193] G. Tourillon, A. M. Flank, P. Lagarde, *J. Phys. Chem.* **1988**, *92*, 4397–4400.

[194] S. Kesornsit, C. Direksilp, K. Phasuksom, N. Thummarungsan, P. Sakunpongpitiporn, K. Rotjanasuworapong, A. Sirivat, S. Niamlang, *Polymers* **2022**, *14*, 3860.

[195] I. Osaka, R. D. McCullough, *Acc. Chem. Res.* **2008**, *41*, 1202–1214.

[196] L.-M. Gao, Y.-Y. Hu, Z.-P. Yu, N. Liu, J. Yin, Y.-Y. Zhu, Y. Ding, Z.-Q. Wu, *Macromolecules* **2014**, *47*, 5010–5018.

[197] T. Kodaira, A. Watanabe, O. Ito, M. Watanabe, H. Saito, M. Koishi, *J. Phys. Chem.* **1996**, *100*, 15309–15313.

[198] J. Cerón Solís, E. De La Rosa, E. Peña Cabrera, *Opt. Mater.* **2006**, *29*, 167–172.

[199] N. Takeda, J. R. Miller, *J. Phys. Chem. B* **2012**, *116*, 14715–14723.

[200] A. Matsuse, S. Takeuchi, K. Yoshino, T. Kobayashi, **1998**.

[201] I. Musselman, *J. Membr. Sci.* **1999**, *152*, 1–18.

[202] J. Wang, *Polym. Degrad. Stab.* **2005**, *89*, 15–20.

[203] R. Hou, B. Zhao, F. Wu, G. Wang, T. Shen, H. Guo, J. Zhang, H. Chen, S. Tan, *Org. Electron.* **2015**, *20*, 142–149.

[204] Z. Fei, P. Boufflet, S. Wood, J. Wade, J. Moriarty, E. Gann, E. L. Ratcliff, C. R. McNeill, H. Sirringhaus, J.-S. Kim, M. Heeney, *J. Am. Chem. Soc.* **2015**, *137*, 6866–6879.

[205] R. D. McCullough, *Adv. Mater.* **1998**, *10*, 93–116.

[206] N. Somanathan, G. Wegner, *Polymer* **1996**, *37*, 1891–1895.

[207] K. E. Aasmundtveit, E. J. Samuelsen, W. Mammo, M. Svensson, M. R. Andersson, L. A. A. Pettersson, O. Inganäs, *Macromolecules* **2000**, *33*, 5481–5489.

[208] J. He, Z. Su, B. Yan, L. Xiang, Y. Wang, *J. Macromol. Sci. Part A* **2007**, *44*, 989–993.

[209] S. A. Chen, C. C. Tsai, *Macromolecules* **1993**, *26*, 2234–2239.

[210] K. Faid, R. Cloutier, M. Leclerc, *Macromolecules* **1993**, *26*, 2501–2507.

[211] C. L. Callender, C. A. Carere, G. Daoust, M. Leclerc, *Thin Solid Films* **1991**, *204*, 451–457.

[212] C. Li, G. Shi, *ACS Appl. Mater. Interfaces* **2013**, *5*, 4503–4510.

[213] A. O. Patil, Y. Ikenoue, F. Wudl, A. J. Heeger, *J. Am. Chem. Soc.* **1987**, *109*, 1858–1859.

[214] X. Li, H. Zhang, C. Lin, R. Tian, P. Zheng, C. Hu, *Polymers* **2022**, *14*, 5499.

[215] D.-J. Liaw, B.-Y. Liaw, J.-P. Gong, Y. Osada, **1999**.

[216] T. Wu, L. Wang, Y. Zhang, S. Du, W. Guo, M. Pei, *RSC Adv.* **2015**, *5*, 16684–16690.

[217] H. Goktas, X. Wang, N. D. Boscher, S. Torosian, K. K. Gleason, *J. Mater. Chem. C* **2016**, *4*, 3403–3414.

[218] M. R. A. Alves, H. D. R. Calado, C. L. Donnici, T. Matencio, *Synth. Met.* **2010**, *160*, 22–27.

[219] D. A. Rider, B. J. Worfolk, K. D. Harris, A. Lalany, K. Shahbazi, M. D. Fleischauer, M. J. Brett, J. M. Buriak, *Adv. Funct. Mater.* **2010**, *20*, 2404–2415.

[220] J. Zhang, Y. Dong, J. Xie, Z. Li, *Small* **n.d.**, *n/a*, 2407256.

[221] J. Lee, M. S. Kim, W. Jang, D. H. Wang, *ACS Appl. Mater. Interfaces* **2024**, *16*, 38310–38323.

[222] L. Cao, W. Zhang, B. Lu, C. Du, J. Zhang, W. Zhou, L. Zhao, X. Cheng, Y. Zhang, L. Zhang, G. Zhang, J. Xu, **2024**, DOI 10.2139/ssrn.4930397.

[223] J. Yi, J. Chen, Z. Wang, J. Zhu, X. Li, *ACS Appl. Mater. Interfaces* **2024**, *16*, 59268–59279.

[224] N. Terasawa, M. Tanaka, *Sens. Actuators Phys.* **2023**, *362*, 114609.

[225] H. Yousefian, A. Babaei-Ghazvini, A. A. Isari, S. A. Hashemi, B. Acharya, A. Ghaffarkhah, M. Arjmand, *Surf. Interfaces* **2024**, *51*, 104481.

[226] C. Jeong, D. Kim, F. S. Kim, *Mater. Chem. Phys.* **2022**, *284*, 126062.

[227] L. Zhang, J. Luo, F. Cai, L. Liu, G. Suo, Y. Wu, Y. Yang, *Carbon* **2025**, *235*, 120074.

[228] Y.-Y. Deng, X.-L. Shi, T. Wu, H. Wu, Y.-M. Liu, M. Zhu, W.-D. Liu, M. Li, P. Huang, Q. Liu, Z.-G. Chen, *Chem. Eng. J.* **2024**, *502*, 158104.

[229] K. Muthamma, D. Sunil, P. Shetty, *Mater. Today Chem.* **2020**, *18*, 100361.

[230] P. P. Mondal, M. Neem, R. Chand, A. Pandit, S. Neogi, *Chem. Mater.* **2024**, *36*, 10451–10473.

[231] M. Takayanagi, T. Tsuchiya, S. Ueda, T. Higuchi, K. Terabe, *Appl. Surf. Sci.* **2021**, *568*, 150898.

[232] D. Dong, W. Wang, A. Rougier, A. Barnabé, G. Dong, F. Zhang, X. Diao, *J. Mater. Chem. C* **2018**, *6*, 9875–9889.

[233] T. A. Welsh, E. R. Draper, *RSC Adv.* **2021**, *11*, 5245–5264.

[234] W. Wu, P. S. Lee, *Soft Sci.* **2024**, *4*, N/A-N/A.

[235] X. Chen, L. Luo, Z. Zeng, J. Jiao, M. Shehzad, G. Yuan, H. Luo, Y. Wang, *J. Materiomics* **2020**, *6*, 643–650.

[236] H. Seok, S. Son, J. Cho, S. Choi, K. Park, C. Kim, N. Jeon, T. Kim, H.-U. Kim, *Sensors* **2022**, *22*, 4288.

[237] E. L. Howard, C. A. T. Laia, C. Pinheiro, A. J. Parola, *J. Appl. Electrochem.* **2024**, *54*, 547–557.

[238] T. Abidin, Q. Zhang, K.-L. Wang, D.-J. Liaw, *Polymer* **2014**, *55*, 5293–5304.

[239] R. J. Mortimer, A. L. Dyer, J. R. Reynolds, *Displays* **2006**, *27*, 2–18.

[240] H. Chen, W. Wang, J. Zhu, Y. Han, J. Liu, *Polymer* **2022**, *240*, 124485.

[241] V. S. Vasantha, R. Thangamuthu, S.-M. Chen, *Electroanalysis* **2008**, *20*, 1754–1759.

[242] K. C. (Nee Włodarczyk), J. Karczewski, P. Jasiński, *Electrochimica Acta* **2015**, *176*, 156–161.

[243] A. I. Melato, M. H. Mendonça, L. M. Abrantes, *J. Solid State Electrochem.* **2009**, *13*, 417–426.

[244] H. J. N. P. D. Mello, M. Mulato, *Synth. Met.* **2018**, *239*, 66–70.

[245] "Irreversible Pixel is a new display technology by Ynvisible," can be found under https://www.ynvisible.com/news-inspiration/irreversible-pixel-by-ynvisible, **n.d.**

[246] J. Szewczyk, M. Pochylski, K. Szutkowski, M. Kempiński, R. Mrówczyński, I. Iatsunskyi, J. Gapiński, E. Coy, *Mater. Today Chem.* **2022**, *24*, 100935.

CHAPTER 2

DOPAMINE-BASED IRREVERSIBLE ELECTROCHROMIC DISPLAYS

INTRODUCTION

2.1 The molecule of dopamine

Dopamine (DA) is a catecholaminergic neurotransmitter central to both biological signalling and redox chemistry.[1] Structurally, dopamine is composed of a catechol ring (1,2-dihydroxybenzene) linked to an ethylamine side chain, giving it the molecular formula $C_8H_{11}NO_2$, Figure 2.1. Functionally, dopamine plays an essential role in regulating movement, reward processing, mood, and cognition. These effects are mediated through a family of G-protein-coupled dopamine receptors, expressed throughout key brain regions.[2,3]

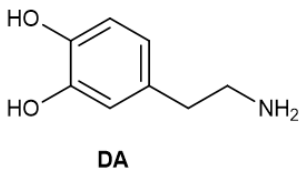


Figure 2.1. Chemical structure of dopamine.

Beyond its classical neurotransmitter role, DA catechol structure renders it chemically reactive and prone to oxidation. Under physiological conditions, DA can undergo auto-oxidation, producing dopamine-o-quinone and reactive oxygen species (ROS) such as superoxide and hydrogen peroxide.[4] When not properly isolated in synaptic vesicles, this oxidative pathway is cytotoxic and contributes directly to neurodegenerative processes. In Parkinson's disease (PD), dopaminergic neurons of the substantia nigra pars compacta are particularly vulnerable to oxidative damage caused by dopamine-derived quinones and the accumulation of neuromelanin, which impairs mitochondrial function and promotes α-synuclein aggregation.[5,6] The redox cycling of DA, exacerbated by environmental or genetic deficits in antioxidant defenses, is a well-established contributor to selective neuronal degeneration in PD.[7]

However, this oxidative reactivity, while pathological in vivo, can be strategically exploited in engineered systems. Under controlled electrochemical conditions, numerous studies have shown that dopamine undergoes a two-electron, two-proton electrooxidation to form dopamine-o-quinone, which subsequently undergoes intramolecular cyclization and polymerization, ultimately yielding polydopamine (PDA). PDA is a melanin-like polymer with

broad adhesive, conductive, and optical properties.[8–10] This transformation enables DA to serve not only as a neurotransmitter but also as an electroactive monomer in functional materials design, inspiring applications across optoelectronics, biointerfaces, and photonic systems. For instance, Ambrico et al.[11] developed hybrid metal-insulator-semiconductor devices using polydopamine thin films, exploiting its eumelanin-like semiconductive properties and dark coloration to realize next-generation bioelectronic interfaces. The study highlights how oxidation-triggered polymerization of DA yields uniform, functional coatings with tunable conductivity and light absorption ideal for bioinspired electronics. In another study, Zhang et al.[12] used DA to synthesize monodispersed PDA black nanoparticles for scalable structural colour films, showing strong angle-independent optical effects due to PDA's broadband light absorption, enabling pigment-free display and coating applications. Moreover, Deng et al.[13] highlighted the versatility of PDA-based colloidal materials in incorporating functional nanomaterials, attributing this to PDA's intrinsic redox activity and strong adhesion properties, which make it particularly effective as an interlayer in optoelectronic devices such as conductive inks and flexible displays. In this way, DA's molecular nature connects biological function with technological innovation. Its dual identity, as a central neuromodulator and a redox-active precursor to functional materials, places it at a unique crossroads between neurobiology, pathology, and electronic device engineering.

2.2 Toward DA oxidation to PDA formation

To fully exploit the functional versatility of DA in materials science and bioengineering, it is essential to understand its chemical behaviour under oxidative conditions. The transformation of DA into PDA hinges on a complex and environment-sensitive oxidation pathway that dictates not only the efficiency of polymerization but also the properties of the resulting material. Let us now examine in detail the oxidation mechanism of DA, focusing on how different physicochemical environments, particularly pH, modulate the formation of key intermediates and drive the transition toward PDA.

2.2.1 Spontaneous oxidation of DA

Under mildly alkaline aqueous conditions (pH ~8.5) and in the presence of dissolved oxygen, DA undergoes spontaneous oxidation, following the pathway illustrated in Figure 2.3. The monomer is more prone to self-oxidation under alkaline conditions because high pH facilitates deprotonation of the catechol hydroxyl groups, increasing the electron density and making the

molecule more susceptible to oxidation.[14] Under these conditions, the presence of molecular oxygen plays a central role as the primary oxidizing agent. As DA is deprotonated, it becomes more nucleophilic and readily donates electrons to dissolved O_2, which acts as the terminal electron acceptor in the redox process. This results in the formation of dopaminequinone (DAQ) and reactive oxygen species like hydrogen peroxide.[15–17] In the absence of oxygen, such as in nitrogen-purged environments, this oxidative process does not proceed, and DA remains in its reduced, colourless form. This effect can be visually demonstrated by comparing DA solutions exposed to air versus nitrogen. The former turns brown over time due to oxidation and polymerization, while the latter remains clear. Such differences are often used as qualitative indicators of oxidative progression in solution-based systems, see Figure 2.2.

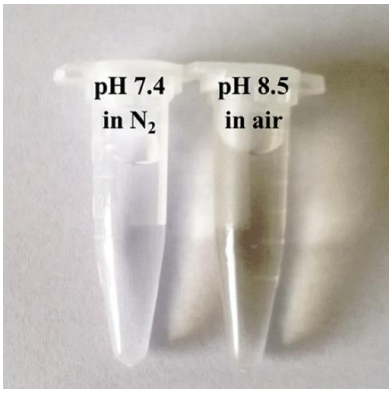


Figure 2.2. Visual comparison of DA solutions after 3 hours. On the left, a solution subjected to electropolymerisation at pH 7.4 under a nitrogen atmosphere remains clear and colourless due to the absence of oxidative conditions. On the right, a solution undergoing spontaneous self-polymerization at pH 8.5 in the presence of air exhibits a dark brown colour, indicating extensive oxidation and polymer formation.[16]

Once oxidation is initiated by molecular oxygen, the process proceeds through the gradual conversion of DA to DAQ via a two-electron, two-proton transfer mechanism. This intermediate is quickly transformed by a Michael-type intramolecular cycloaddition reaction to produce leucodopaminechrome (DAL). Further oxidation of DAL produce the dopamineaminochrome (DAC) that after molecular rearrangement leads to the production of 5,6-dihydroxyindole (DHI).[18]

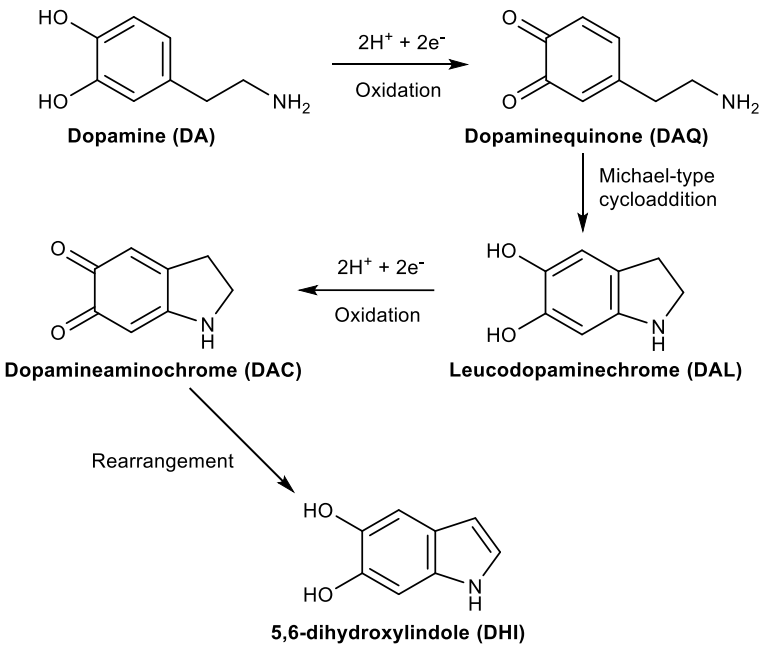


Figure 2.3. DA self-oxidation pathway.

At this point, the reaction branches into two parallel but intertwined mechanisms as reported in Figure 2.4. The first involves (A) covalent oxidative polymerization where DHI can be further oxidized to its quinonoid form. These indole derivatives undergo covalent coupling reactions, forming oligomers such as DHI-DHI dimers and more complex trimeric conjugates incorporating DA and DHI units. These species progressively build the covalent backbone of PDA, leading to an amorphous polymer structure rich in catechol, amine, and indole moieties. Simultaneously, (B) non-covalent self-assembly contributes to PDA formation. In this specific pathway DA, DHI, and other intermediates before aforementioned can form supramolecular aggregates through π–π stacking, hydrogen bonding, and electrostatic interactions. One such assembly is the $(Dopamine)_2$/DHI physical trimer, which is stabilized by non-covalent forces and integrates into the forming PDA network. These physical assemblies, although not covalently bound, play a role in determining PDA's morphology and mechanical properties.[19]

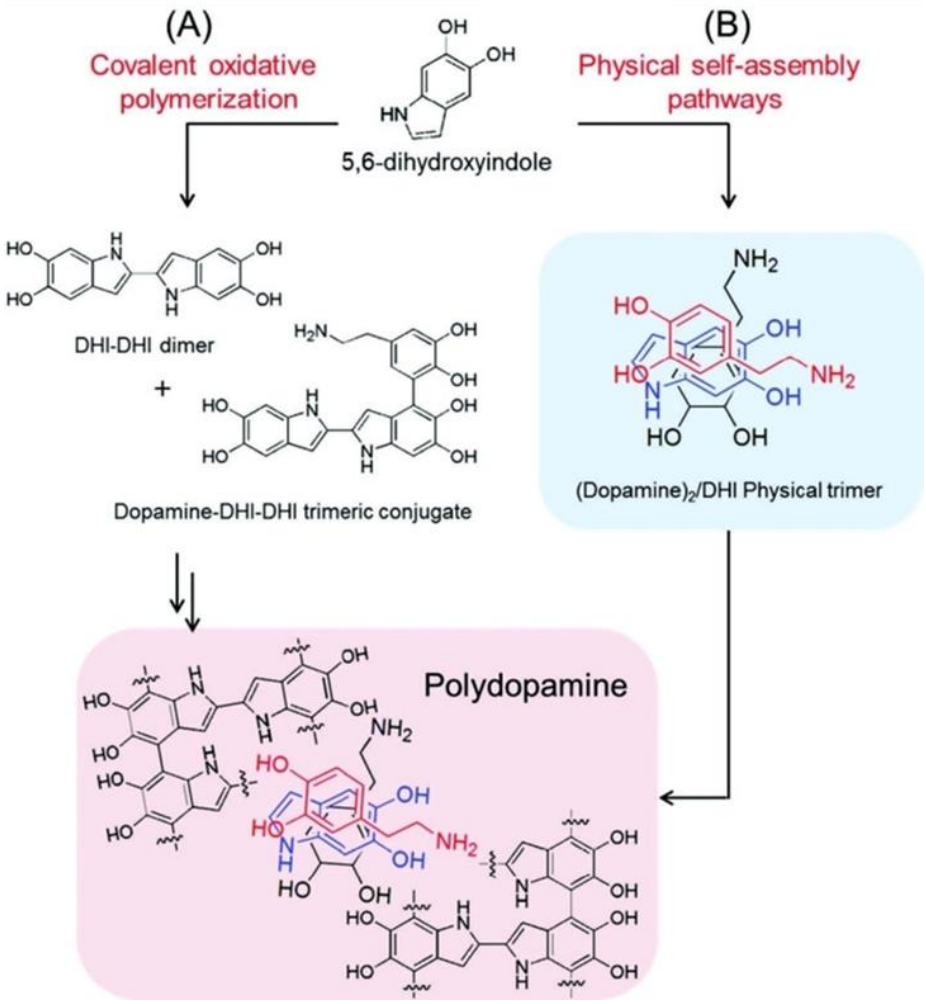


Figure 2.4. Different pathway for the formation of PDA. (A) oxidative polymerization involving covalent bond formation and (B) non-covalent self-assembly process between DA and DHI.[19]

Although the initial oxidative steps leading from DA to DHI are well-characterized and widely accepted, the final structure of PDA remains an open and actively debated question. Rather than a single, well-defined polymeric configuration, PDA is better understood as a heterogeneous ensemble of oligomeric and supramolecular species. Several structural proposals have been advanced over the years to describe the complexity of this material. Among the most significant contributions are those coordinated from Marco d'Ischia. Specifically Alfieri and coworkers explored the nature of PDA.[20] Their investigations revealed that PDA does not follow the classical eumelanin model, based only on polymerized DHI units. For instance, their mass spectrometry data consistently show a dominant signal at m/z 402, suggesting the presence of a trimeric structure that includes both cyclized and uncyclized building blocks, possibly a hybrid assembly of DA and DHI derivatives. These findings cast doubt on the idea that PDA is primarily composed of linear or cyclic DHI oligomers. Although dimeric species such as the 2,4′- and 2,7′-linked DHI units, highlighted in Figure 2.5, were previously proposed as fundamental intermediates, experimental evidence

indicates that these structures are either only minor constituents or lack the stability required to serve as the main framework of PDA.

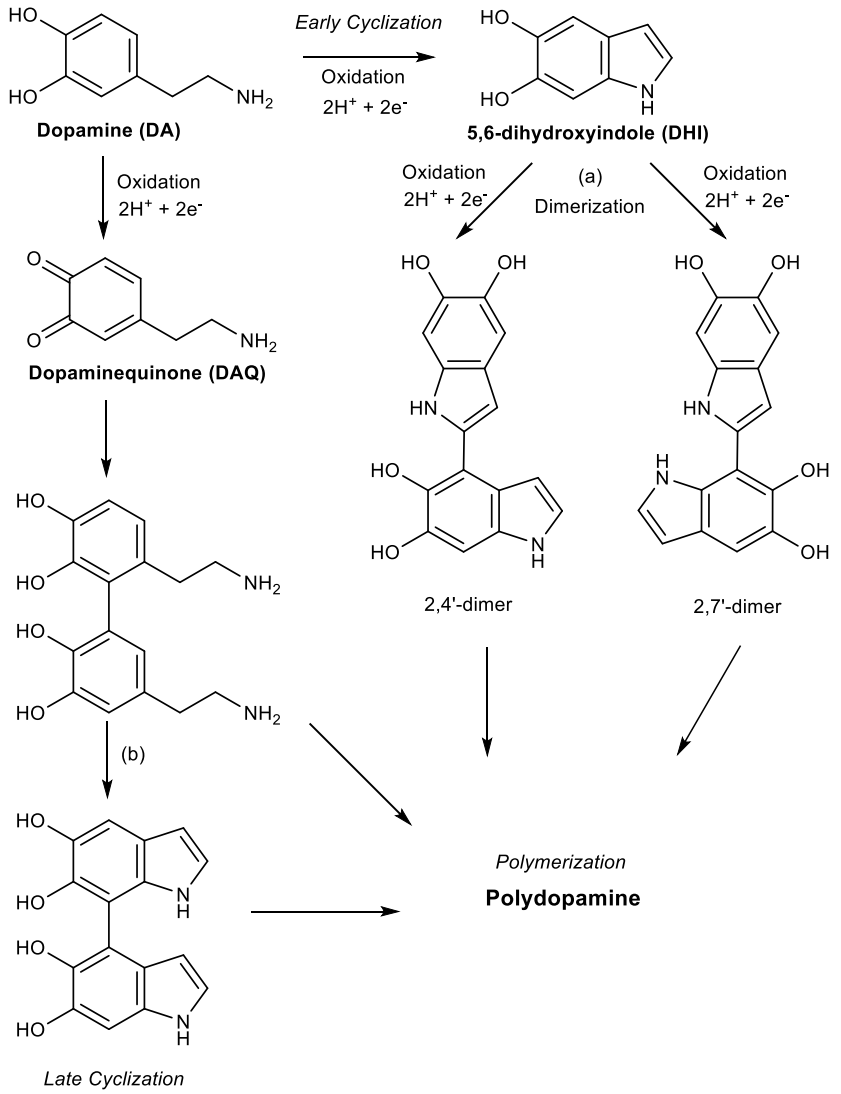


Figure 2.5. (a) Oxidative coupling of 5,6-dihydroxyindole (DHI), yielding two primary dimeric structures: the 2,4′-biindolyl and the 2,7′-biindolyl; (b) potential formation of indole-based oligomers through late-stage coupling and cyclization pathways, originating from early-cyclized intermediates.[20]

The oxidation of DA to PDA becomes particularly relevant when examining how this pathway contributes to film formation on surfaces. In this context, a study by Alfieri et al. provides important insights into the dynamics of PDA film formation, distinguishing between two intertwined yet distinct processes identified as film deposition and film growth.[21] These processes are governed by the interplay between DA concentration, the presence of quinonoid intermediates, and external additives such as amines and oxidants. Under standard conditions (pH 9.0 in carbonate buffer), PDA film formation is strongly dependent on DA concentration. At low concentrations (≤1 mM, ≤0.2 g/L), DA fails to form detectable films. This is attributed to the prevalence of the intramolecular cyclization pathway, which leads to non-adhesive DHI

units and eventual aggregation into insoluble eumelanin-like particles. Conversely, at higher concentrations (≥10 mM, ≥2 g/L), film deposition is readily observed, particularly in the early phases of DA oxidation. This correlates with the transient presence of reactive DAQ species, which engage in intermolecular coupling, yielding adhesive oligomers with uncyclized amine groups critical for cross-linking and surface adhesion.

Moreover, experimental studies confirm that the initial oxidation pathway of DA remains consistent even in environments closer to physiological conditions (pH 5.8–7.4), supporting the formation of semiquinone intermediates as the first critical step in PDA formation.[22] In this pH range, DA predominantly exists in its fully protonated form, where both phenolic groups remain undissociated and the primary amine is present as an ammonium ion. Despite the protonated state, DA is still oxidizable, indicating that proton abstraction and electron transfer are closely coupled processes even in mildly acidic conditions. However, lowering the pH significantly affects the subsequent reaction kinetics. At pH 5.8, the transformation of DA into coloured polymeric products proceeds much more slowly than at pH 7.4 or above. This is due to the suppression of key follow-up reactions such as dimerization, cyclization, and further oxidation steps, which depend on the availability of deprotonated species. The high proton concentration at lower pH hinders the dissociation of hydroxyl groups and slows down the conversion of semiquinone radicals into downstream oligomeric or polymeric species.[22,23] Consequently, the intermediates generated in the early stages of oxidation accumulate without progressing efficiently toward PDA formation. In contrast, at neutral pH *(e.g.*, pH 7.4), these reactions accelerate noticeably. The reduced proton activity facilitates the deprotonation of OH groups, enabling more rapid electron delocalization and subsequent chemical transformations such as Michael-type additions and ring closure reactions. As a result, the rate of PDA formation increases, and the buildup of insoluble, brown-black polymeric material becomes more pronounced.

2.2.2 Electrochemical oxidation of DA

In addition to the well-documented spontaneous oxidation of DA under alkaline conditions, DA can also be oxidized via an electrochemical pathway by applying a suitable potential.[22] While both mechanisms initiate with the oxidation of DA to DAQ through a two-electron, two-proton transfer, the electrochemical route introduces a level of reversibility not accessible in spontaneous oxidation, Figure 2.6. This reversible control, which characterizes the electrochemical steps E_1 (DA/DAQ), E_2 (DAL/DAC), and E_3 (DHI/IQ), allows for dynamic modulation of intermediate redox states. Nevertheless, the overall pathway is not entirely

reversible. Critical chemical transformations such as the intramolecular cyclization of DAQ to DAL, denoted as C_1, and the rearrangement of DAC to form DHI, labelled C_2, are both irreversible steps.[16] These chemical reactions proceed spontaneously once their respective intermediates are formed and cannot be reversed electrochemically. From cyclic voltammetry (CV) studies carried out by Wang and coworkers,[16] the DA/DAQ redox couple (E_1) typically occurs around +0.18 V vs. SCE, while the DAC/DAL redox couple (E_2) is seen around −0.21 V, and DHI/IQ (E_3) can appear near +0.2 to +0.3 V depending on pH and electrode conditions. These potentials can shift with solution composition, electrode surface, and scan rates. Each of these redox steps corresponds to distinct chromophores that absorb in the visible range. The same study showed that DAQ presents a yellow colouration (λ_{max} ~395 nm), DAC appears reddish (λ_{max} ~480 nm), and IQ has a brown hue. These spectral features were confirmed in colorimetric oxidation studies performed by Palladino et at.[24] using hypochlorous acid (HOCl), where DA oxidation to DAQ was immediate and proportional to oxidant concentration, reinforcing DAQ's diagnostic utility via its visible absorption signature.

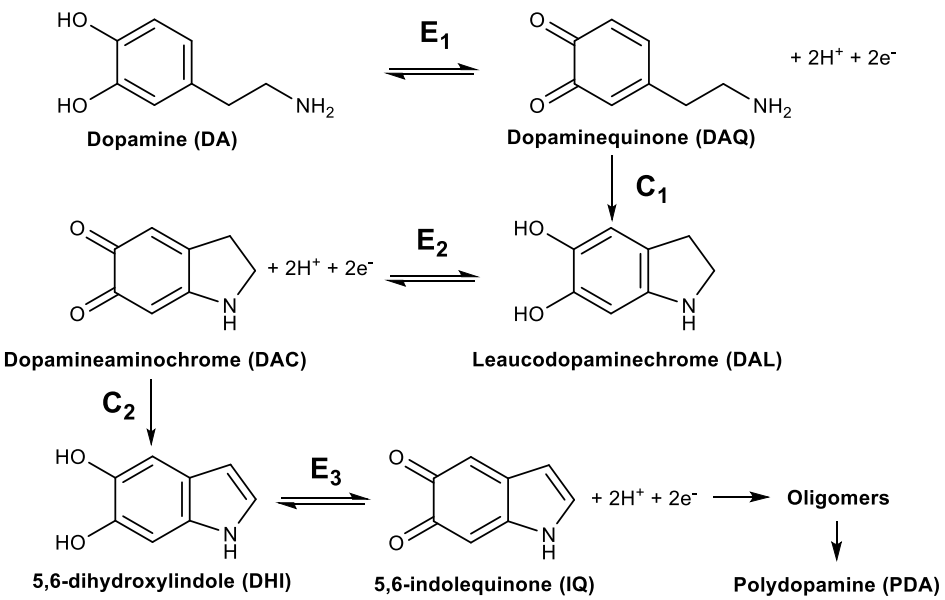


Figure 2.6. Chemical pathway of electrochemical oxidation of DA for the formation of ePDA. $E_{1,2,3}$ are identified as electrochemical driven reactions while $C_{1,2}$ as chemical reactions.

Comparing the two principal methods of PDA formation, spontaneous self-polymerization under alkaline conditions versus electrochemical polymerization, reveals fundamental differences in efficiency, morphology, and application potential. Under alkaline self-oxidation (at pH 8.5 in Tris buffer), DA oxidizes in the bulk solution through exposure to molecular oxygen. This process leads to the formation of dispersed PDA aggregates and non-uniform coatings. Wang et al.[16] quantified this inefficiency, reporting that more than 10 hours were required to deposit a 20 nm-thick PDA layer using a 2 g/L DA solution in alkaline conditions.

Moreover, a significant amount of DA is consumed in forming unwanted nano/microparticles in solution, which do not contribute to the coating and actually increase surface roughness. In contrast, electropolymerisation confines DA oxidation to the vicinity of the electrode surface, typically using CV in a potential range of −0.5 to +0.5 V vs. SCE in deoxygenated, neutral Tris-buffered saline (pH 7.4). This method produces dense, smooth, and conformal ePDA films. According to the same study, ePDA coatings reached a thickness of approximately 35 nm within just 30 minutes of CV, with further deposition leading to films exceeding 100 nm. Notably, the deposition rate for ePDA was consistently higher than that observed for self-polymerized films over equivalent time periods. Ellipsometry measurements revealed that the thickness of ePDA coatings was nearly double that of self-polymerized PDA after 1 hour under comparable conditions.

Building upon this foundational understanding, the following section outlines the specific objectives and experimental strategies developed to harness dopamine's redox chemistry for functional device applications.

2.3 Aim of the project

According to the introductory overview, DA monomers possess the capability to undergo self-oxidation, leading to their polymerization into PDA. Furthermore, studies have also demonstrated that this polymer can be synthesized electrochemically by applying an external potential to induce oxidation when DA is in an aqueous solution. Initially, a DA solution appears transparent within the visible spectrum. However, as it undergoes polymerization into PDA, its coloration shifts from light brown to deep black. The final colour depends on the degree of polymerization and the thickness of the resulting film, with greater polymer accumulation leading to a darker appearance.[25]

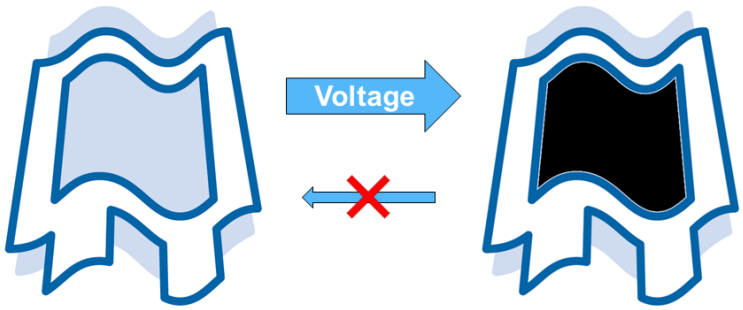


Figure 2.7. Schematic representation of an *i*-ECD before (left) and after (right) the application of a potential difference.

The primary aim of this chapter is to harness and regulate this chemical transformation to enable the development of irreversible electrochromic displays (*i*-ECDs), capable of transitioning from a transparent state to a black hue upon the application of voltage, Figure 2.7. The chapter includes a range of investigations, experiments, and parameter optimizations, including pH levels, solution concentrations, and applied voltages. Rigorous reliability and durability assessments, such as resistance to bending, exposure to varying temperatures, and UV radiations, are conducted on the *i*-ECD. The study concludes by subjecting the *i*-ECDs to integration tests involving electronic components like temperature sensors, batteries, and NFC antennas, which aim to develop smart labels designed for monitoring the cold chain showing their ability to respond to stimuli in real-life applications.

RESULT AND DISCUSSION

2.4 Fabrication and activation of a DA-based *i*-ECD

Building upon the introduced concepts, we harnessed the phenomenon of DA electro-oxidation as the fundamental process for the manufacturing of *i*-ECDs. In leveraging the potential-initiated colour change for the development of *i*-ECDs, the research initially focussed on defining specific conditions (*e.g.*, concentration, pH, voltage). The aim was to exercise complete control over the process activation and achieve optimal visual contrast. Our first objective in establishing key parameters for an efficient DA-based *i*-ECD was to identify the optimal electrolyte. We selected PBS for its capability to readily dissolve DA and facilitate ionic conductivity, a widely recognized trait utilized in various studies involving DA.[26] Considering pH selection, as detailed in the chapter's introduction, literature suggests a preference for DA oxidation in basic pH environments, while acidic conditions hinder this process.

In conducting our tests, we aimed to develop an EC solution that would prompt a rapid colour response (within 60 seconds) upon activation via applied potential. Concurrently, our goal was to avoid premature DA self-oxidation that could occur before the application of a potential pulse. To meet these objectives, our initial experiments guided us to select a pH 7.4, striking a balance between achieving a swift colour response and preventing self-oxidation phenomena prior to activation.

After settling the electrolyte choice (*i.e.*, PBS; pH of 7.4), we proceeded to test DA solutions of varying concentrations and pH in flexible *i*-ECDs, with different potentials, to identify the most effective operating conditions for achieving a distinct colour change on demand. Our

flexible *i*-ECDs, were manufactured using a vertical stack architecture, employing two flexible, conductive PET (125 µm thick) - ITO (200 nm thick, 35-40 Ω/sq) electrodes placed face to face with an adhesive Nitto spacer in between. This spacer created a chamber filled with the DA solution, prepared simply by dissolving the molecule in PBS (Figure 2.8a,b). The resulting *i*-ECD had a total thickness of approximately 400 µm and an active area of 1 cm^2 whose structure is reported in Figure 2.8c.

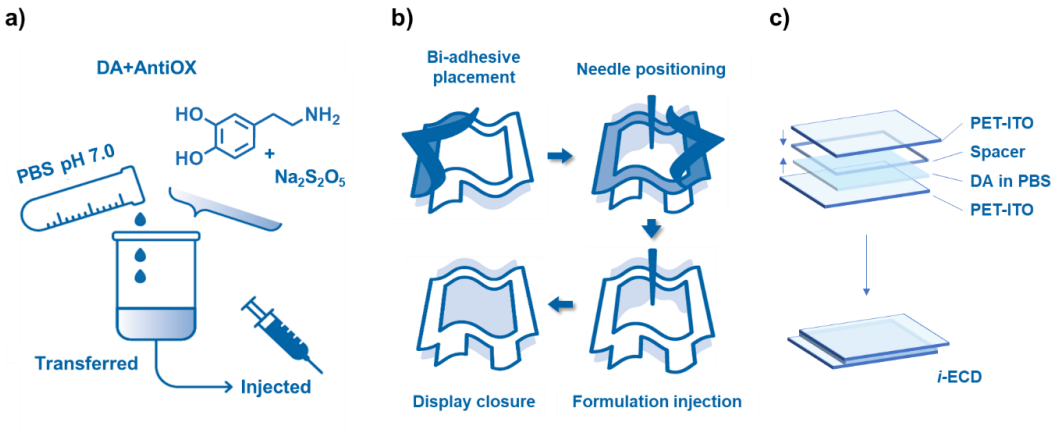


Figure 2.8. a) Required steps for the preparation of the DA based formulation. b) Essential stages for the manufacturing of the DA based *i*-ECD. c) Exploded 3D view of the *i*-ECD.

Then, the manufactured *i*-ECD was subjected for the first time to an applied potential of 1.5 V for 600 seconds constantly monitoring its transmittance at a single wavelength of 600 nm (T@600 nm). To quantitatively track device darkening, we opted to monitor the variation in transmittance at a single wavelength. The deliberate selection T@600 nm as the investigative wavelength aimed to align with the peak absorption point for human vision.[27] Figure 2.9 shows the result of the voltage application. The *i*-ECD underwent a massive drop in transmittance passing from transparent to black registering a final $\Delta T > 80\%$. Over a thorough analysis of the spectrum, can observe how a significant portion of transmittance decrease within the first 60 seconds of voltage application, characterized by a sharp curve slope. This phase marks the occurrence of the entire colour change. In the following minutes, the slope notably reduces, signifying a reduction in reaction speed attributable to a decrease in electrode conductivity.

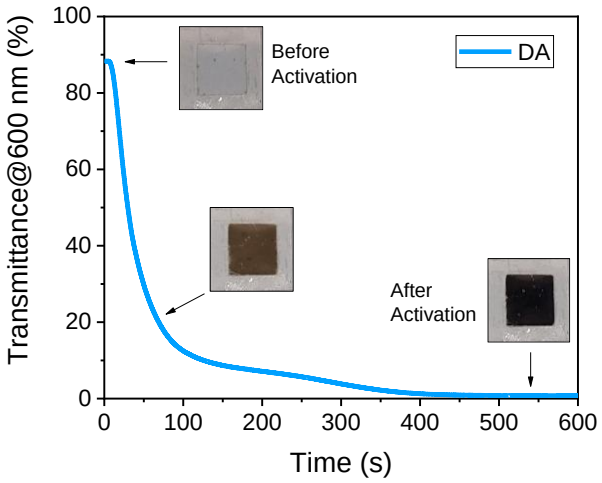


Figure 2.9. T@600 nm of a DA-based *i*-ECD recorded during the application of 1.5 V for 600 s.

2.5 Effect of the pH

Oxidation of DA is a process by which electrons and protons of the two OH groups are removed from the structure of the molecule.[28] This occurs in aqueous solution and is greatly facilitated in the presence of oxygen.[29] The pH of the medium in which DA is dissolved is also fundamental for the oxidation reaction. In particular, it is known from the literature that DA oxidation is facilitated at basic pH, while acidic environments tend to hinder the process.[30] The pH value plays a critical role in ensuring the production of a stable and voltage reactive *i*-ECD. As a result, it was necessary to carry out a pH optimization investigation, involving both acidic and alkaline conditions.

The initial tests, conducted without the application of voltage, involved just the preparation of four solutions of DA of PBS at pH 1.5, 4.5 (acidified with HCl), 9.8, and 12 (basified using NaOH). The result after 1 hour of rest, visible in Figure 2.10a, confirms literature research. Lower pH levels impede the spontaneous oxidation of DA, leading to a transparent solution. As the pH increases, the self-oxidation of DA intensifies, displaying a brownish tint at pH 4.5 and evolving into an intense black hue at pH 9.8 and pH 12 where the process accelerates rapidly forming oligomers leading to black PDA formation. This observation already underscores that opting for a basic pH, while it promotes the oxidation reactions essential for the colour change, is not a viable choice. This is because it would cause the premature spontaneous consumption of DA even before the manufacturing of *i*-ECD. Therefore, an acidic pH is the preferred choice. However, to fully understand the challenges associated with low pH values, it is essential to construct an *i*-ECD using these solutions and apply voltage to verify

the colour transformation. Therefore, four *i*-ECDs, prepared with these solutions underwent activation at 1.5 V for 600 seconds. Before activation, a bare *i*-ECD exhibited T@600 nm of approximately 80%. Figure 2.10b displays the pictures of the *i*-ECDs, each corresponding to a different pH, captured after the voltage application. In the highly acidic environment (pH 1.5) known to decelerate DA oxidation, *i*-ECDs exhibited no transmittance variation (T@600 nm 77.1%; Figure 2.10c). Conversely, at pH > 10, rapid self-oxidation of DA significantly reduced the available monomer concentration for the reaction upon voltage application, leading to a much lower ΔT (pH 12, T@600 nm 45.9%). The *i*-ECDs prepared with pH values ranging from 6 to 10, highlighted in the cyan area of the graph, exhibited the highest ΔT upon voltage activation (pH 9.8, T@600 nm 17.9% and pH 7.4, T@600 nm 6.5%).

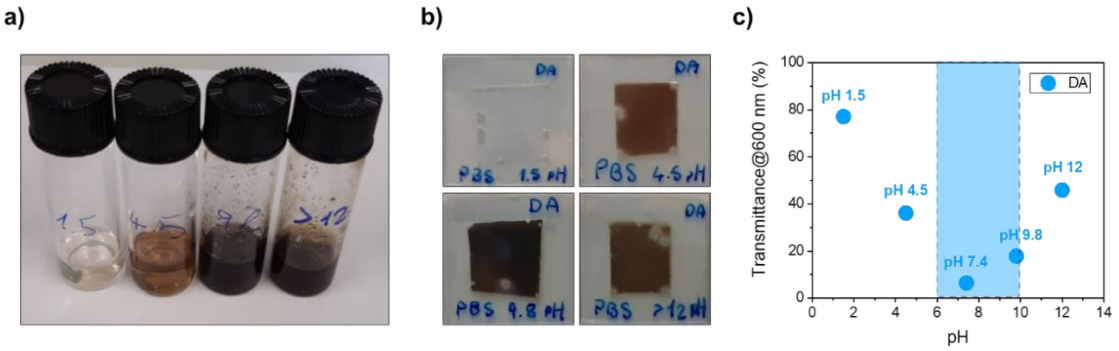


Figure 2.10. a) Pictures taken 1 hour after preparing four solutions, each containing 10 mg of DA and 1 mL of PBS at pH 1.5, 4.5, 9.8, and 12. b) Pictures of four *i*-ECDs at the end of the activation process carried out at 1.5 V for 600 s. The *i*-ECDs were prepared employing the mentioned solutions fresh, as soon as prepared. c) T@600 nm recorded after activation process via 1.5 V for 600 s of four *i*-ECDs prepared with DA 10g/L in PBS pH 1.5, 4.5, 9.8 and 12. The analysis include one *i*-ECDs prepared with DA 10 g/L in PBS pH 7.4.

2.6 Optimization of operating parameters

Maximizing the *i*-ECDs ΔT and colour transition rate upon voltage activation while minimizing DA consumption and voltage requirements is essential for improving efficiency and reducing both manufacturing and energy costs. To achieve this, a series of experiments were conducted to determine the best DA concentration and voltage parameters for the *i*-ECD. The following sections present the findings and their impact on device performance.

2.6.1 Study of the optimal concentration of DA for i-ECDs

The concentration of DA in PBS was investigated, being strictly related to the maximum ΔT achievable upon display activation. The analysis involved assembling eight *i*-ECDs with varying DA concentrations (ranging from 0 to 100 g/L) in PBS at pH 7.4. These were subjected

to a consistent 1.5 V voltage for 600 seconds, a choice made to align with the objective of integrating the *i*-ECD into a smart label powered by a printed battery capable of providing a minimum of 1.5 V.

The first data point at 0 g/L in Figure 2.11a indicates that no ΔT is observed in the absence of DA (T@600 nm 78.3%). The first *i*-ECD picture in Figure 2.11b confirms that, without monomer, oxidation cannot take place, and consequently, no colour change is observed. At a concentration of 1 g/L, a light brown colour hue is observed, as visible in the second *i*-ECDs image (T@600 nm 31.1%). This is due to the limited DA availability, which is fully consumed during voltage application before a sufficiently thick layer can form to produce a deep black contrast. At concentration of 5 g/L, a further drop in transmittance is observed (T@600 nm 3.8%), reaching its lowest value at 10 g/L (T@600 nm 1.8%), resulting in fully black *i*-ECD. Increasing the DA concentration beyond 10 g/L does not further reduce transmittance, as the i-ECD already appears fully black (T@600 nm 1.8%). Any additional DA beyond this point is excessive, leading only to material waste. Moreover, at higher monomer concentrations (*e.g.*, 100 g/L), a slight increase in T@600 nm (up to 15%) is observed, indicating that an excess of DA may hinder performance. This effect can be attributed to the high DA concentration, which reduces the relative proportion of the electrolyte salt in the solution. As more DA is added, the electrolyte salt to DA ratio decreases, limiting the availability of ions for the electrochemical oxidation of the monomer. This reduction in ion mobility slows down reaction kinetics, affecting the efficiency of the process.

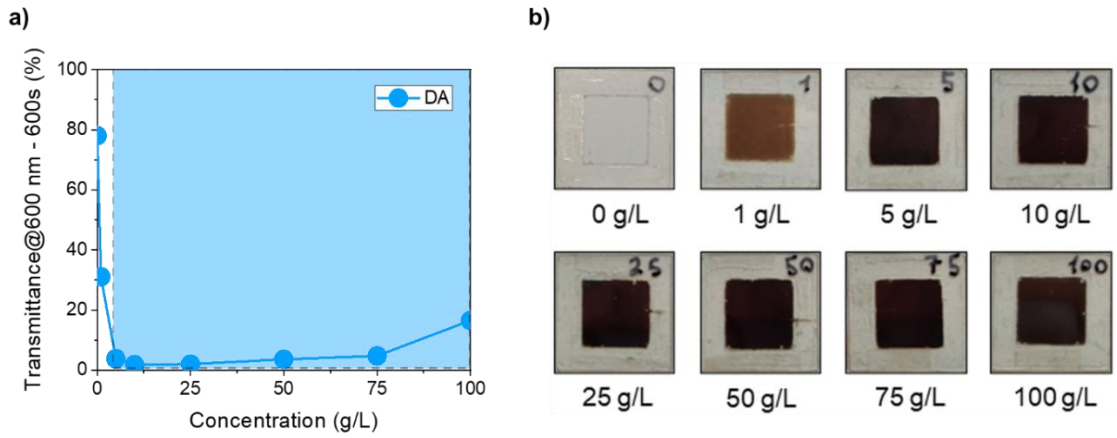


Figure 2.11. a) T@600 nm recorded after activation by applying 1.5 V for 600 s of eight *i*-ECDs prepared employing DA in PBS pH 7.4 at concentration, expressed in g/L, of 0, 1, 5, 10, 25, 50, 75, 100 (0 g/L: no DA, only PBS). The highlighted light blue region denotes the level of DA concentration capable of causing a ΔT sufficient for the naked eye to perceive an intense black colour. b) Images of the eight *i*-ECDs manufactured employing different concentrations of DA in PBS pH 7.4, after their activation via applied potential of a 1.5 V.

To conduct all further tests under consistent conditions, it was necessary to select a fixed DA concentration. We established 10 g/L as the standard, as it provides the highest ΔT. Although 5 g/L yielded the similar ΔT values, a higher concentration was chosen to compensate for the gradual consumption of DA due to self-oxidation over time. This approach helps maintain consistent performance and extends the shelf life of the *i*-ECDs, as discussed further in the following sections.

2.6.2 Determination the activation threshold voltage of the i-ECDs

The effect of the voltage on the colouration of the *i*-ECD was investigated. The analysis was performed by assembling eleven *i*-ECDs, prepared with DA 10 g/L in PBS pH 7.4, subjected to a voltage ramp (0.5–3.0 V) for 600 seconds. Figure 2.12a illustrates that applied potential of 1.0 V or lower failed to activate the *i*-ECDs, resulting in no ΔT. As a result, there is no observable change in colour, which is clearly demonstrated by the transparent pictures of the *i*-ECDs post activation shown in Figure 2.12b. At 1.25 V, the *i*-ECD exhibits a black coloration, corresponding to a T@600 nm of 45.7% (ΔT of *ca.* 35%). Above 1.5 V, all the *i*-ECDs turn black, forming a uniform layer, consistent with observations from the concentration experiment.

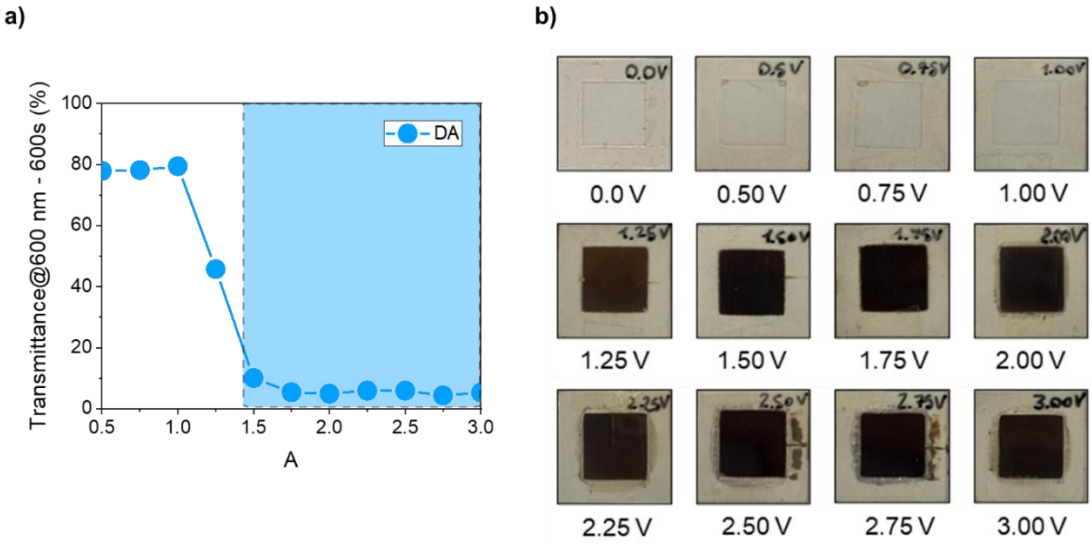


Figure 2.12. a) T@600 nm recorded after activation by applying a voltage ramp for 600 s on eleven *i*-ECDs prepared with DA 10 g/L in PBS pH 7.4. The optimal operating parameters for an *i*-ECD are indicated in the highlighted light blue area. b) Images of the eleven *i*-ECDs manufactured employing constant concentration of DA 10 g/L in PBS pH 7.4, after their activation via a ramp (0.5V–3.0V) of applied potential.

Higher voltages primarily influence the rate of colour change, accelerating the visual response. As shown in Figure 2.13, two *i*-ECDs activated at 1.5 V and 3.0 V exhibit different switching

speeds. At 1.5 V, a T@600 nm of approximately 20% is reached in about 60 seconds, whereas the same value is attained within just 10 seconds at 3.0 V, making the process six times faster.

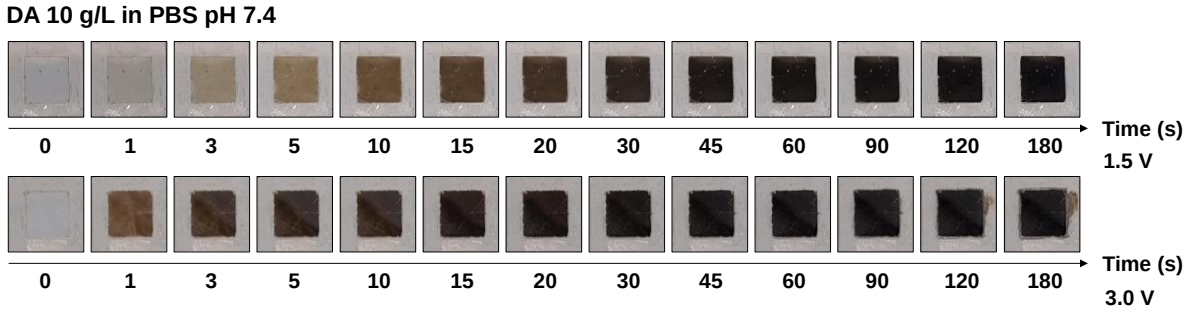


Figure 2.13. Frames extracted from a video recording depicting two *i*-ECDs, manufactured employing DA 10 g/L in PBS pH 7.4. These frames capture the activation process, conducted at both 1.5 V and 3.0 V.

2.6.3 The importance of DA for the i-ECDs

After optimizing the operational parameters for *i*-ECD fabrication and activation, we aimed to assess the importance of DA in enabling colour change upon voltage application. To illustrate this, we compared the performance of *i*-ECDs prepared with DA in PBS against those containing only PBS, highlighting the necessity of the monomer for electrochemical oxidation and subsequent coloration.

The analysis involved two sets of five *i*-ECDs prepared employing DA in PBS at pH 7.4 and five *i*-ECDs prepared using only PBS at pH 7.4. The graph in Figure 2.14a illustrates that for both *i*-ECDs no ΔT was registered upon the application of 1.0 V (T@600nm 80%), as confirmed through the transparent pictures of the *i*-ECDs acquired post activation, Figure 2.14b. At higher voltages, specifically 2.0 V and 3.0 V, the DA-based *i*-ECDs experienced a drop in T@600nm reaching 2.4% and 3.5%, whereas the PBS-only *i*-ECDs remained unresponsive. An important decrease of T@600nm to 43.2% and 21.9% occurred only at potentials of 4.0 V and 5.0 V. However, even at these higher voltages, the T@600 nm values remained significantly higher than those of the DA-based *i*-ECDs. Additionally, the PBS-only *i*-ECDs displayed a distinct brownish hue rather than the uniform black coloration achieved with DA. These results highlight the critical role of the monomer in reducing the voltage threshold required for activation while also ensuring a homogeneous and deep black coloration, which is unachievable with PBS alone.

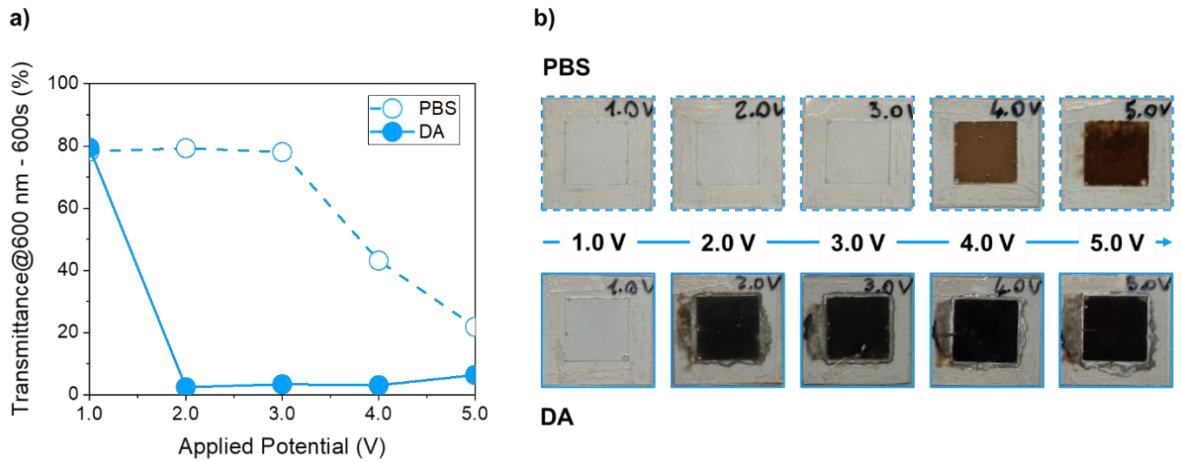


Figure 2.14. a) T@600 nm recorded after activation by applying a voltage ramp for 600 s on five + five *i*-ECDs prepared with respectively only PBS pH 7.4 (dashed line) and DA 10 g/L in PBS pH 7.4. b) Images of the ten *i*-ECDs after their activation via a ramp of applied potential.

2.7 DA self-oxidation and *i*-ECDs stability

In an oxygen-rich aqueous environment, DA naturally undergoes self-oxidation, following the mechanism previously described. While this oxidation is the very process that enables colour change in *i*-ECDs, its spontaneous occurrence must be strictly controlled. The goal is to ensure that colouration occurs exclusively in response to an applied voltage, preventing unwanted activation. To illustrate the impact of uncontrolled oxidation, a DA solution in PBS at pH 7.4 was left exposed to air for 12 hours, allowing spontaneous oxidation to take place. Figure 2.15 illustrates the outcome of the experiment, depicting as expected the colour change in the solution due to the formation of PDA inside the vial and along the edges.

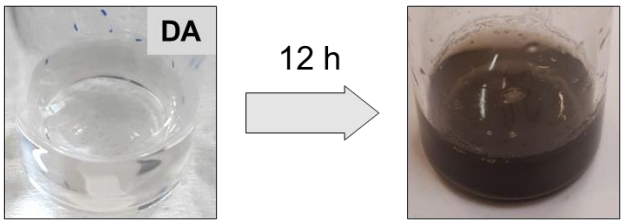


Figure 2.15. Picture of a 10 g/L DA solution in PBS pH 7.4 in vials before (transparent) and after (black) 12 hours.

The self-oxidation process poses an undesirable issue in the development of *i*-ECDs, as it changes their colour spontaneously without the application of the voltage, thereby affecting the technology's proper functioning. To understand the impact of self-oxidation, a DA-based *i*-ECD was prepared, and its transmittance changes continuously monitored over a 27-day period without applying voltage. In accordance with the experiment in solution, Figure 2.15a report

self-oxidation effect showing an important decrease in T@600 nm of *ca.* 30% due to spontaneous PDA formation on the *i*-ECDs electrodes which drastically change their colour, Figure 2.15b.

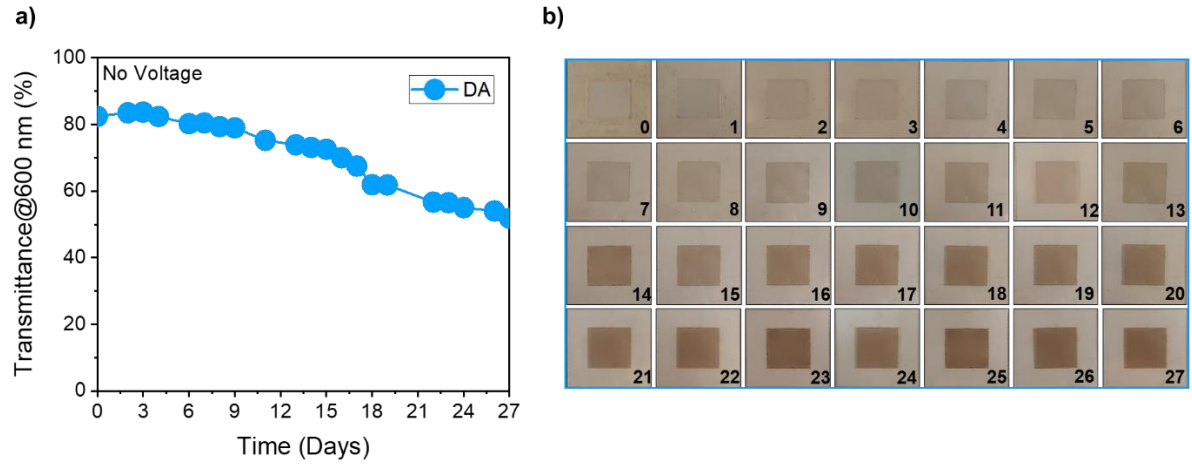


Figure 2.16. a) T@600 nm recorded every day for a single *i*-ECD prepared employing a solution of DA 10 g/L in PBS pH 7.4. b) Pictures of the same *i*-ECD acquired daily.

To address the problem, an antioxidant was added to the solution. The selected compound, sodium metabisulfite ($Na_2S_2O_5$), functions as an oxygen scavenger. It reacts with dissolved oxygen molecules, thereby preventing the spontaneous oxidation of DA.[31] To evaluate its effectiveness, the experiment was repeated with a twin solution, now supplemented with $Na_2S_2O_5$ 0.5:1 mol ratio (= to weight ratio) to DA, DA+AntiOX. The outcome depicted in Figure 2.17, after 12 hours of exposition, reveals no colour variations.

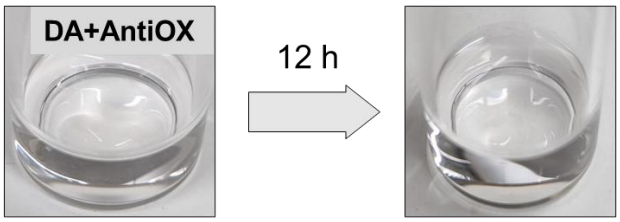


Figure 2.17. Picture of a 10 g/L DA solution in PBS pH 7.4 with the employment of $Na_2S_2O_5$.

The antioxidant effectively prevented the self-oxidation of DA, maintaining the solution's transparency and preserving the monomer concentration over time. By inhibiting spontaneous oxidation, it ensured that DA was not gradually consumed, thereby keeping its concentration stable. The introduction of the antioxidant prevents the spontaneous colour change of *i*-ECDs. This was experimentally verified by conducting the same monitoring using an *i*-ECD prepared with DA+AntiOX. Accordingly, Figure 2.18a shows that T@600 nm remains consistent

throughout the entire monitoring period. The outcome is a fully transparent *i*-ECD, identical to its condition on day 0 when it was manufactured, Figure 2.18b.

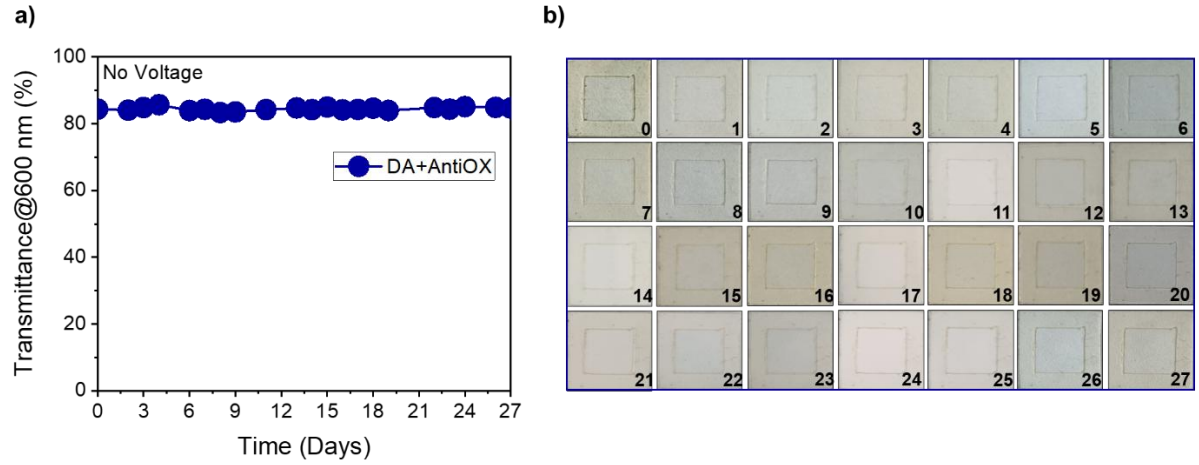


Figure 2.18. a) T@600 nm recorded every day for a single *i*-ECD prepared employing a solution of DA 10 g/L in PBS pH 7.4 with $Na_2S_2O_5$ 5 g/L, DA+AntiOX. b) Pictures of the same *i*-ECD acquired daily.

The $Na_2S_2O_5$ concentration at a 0.5:1 mol ratio to DA, employed in the DA+AntiOX solution, exhibited remarkable stability against spontaneous oxidation. The monitoring of the *i*-ECD prepared with this solution consistently registered an unchanged T@600 nm over 100 days, Figure 2.19. Thanks to its remarkable stability, this 0.5:1 mol ratio between DA and $Na_2S_2O_5$ was selected as standard solution for the manufacturing of *i*-ECDs.

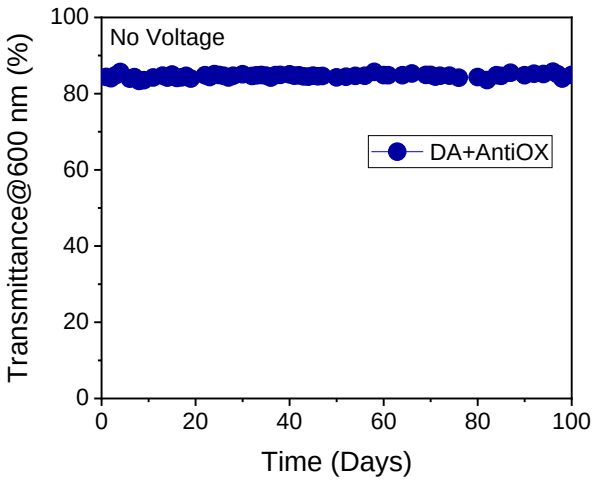


Figure 2.19. T@600 nm recorded every day for a single *i*-ECD prepared employing a solution of DA+AntiOX over 100 days.

Therefore, integrating an antioxidant into the *i*-ECD solution is crucial to preventing self-oxidation, which would otherwise lead to the gradual consumption of DA. Over time, this monomer drop would progressively reduce the achievable ΔT upon activation, severely

affecting the maximum ΔT achievable upon activation. This phenomenon is illustrated in Figure 2.20a, which presents the evolution of T@600 nm following a 600-second activation at 1.5 V over a 10-day period, comparing two sets of nine *i*-ECDs, one prepared with DA alone and the other with DA combined with an antioxidant (DA+AntiOX). During the first 2 days, both sets exhibit similar T@600 nm values. However, from day 3 onward, in the absence of the antioxidant, the self-oxidation of DA becomes significant, leading to a marked increase in maximum T@600 nm reachable upon activation. Specifically, on day 3, the DA-based *i*-ECDs reach 43.8% T@600 nm, while those containing DA+AntiOX exhibit a remarkable 8.8%. This gap widen overtime, peaking on day 8, when the DA-only *i*-ECDs no longer respond to applied voltages, displaying a T@600 nm of 71.4% compared to 17.3% for the antioxidant-stabilized ones. As a result, the activated *i*-ECDs progressively develop a lighter brown colour, which becomes increasingly pronounced from day 7 onward, Figure 2.20b. This colouration is no longer driven by an EC response but only arises from the self-oxidation of DA. This observation is consistent with previous findings and confirms that, in the absence of antioxidant protection, DA is gradually consumed over time, resulting in irreversible PDA layer formation which affects the *i*-ECDs' functionality.

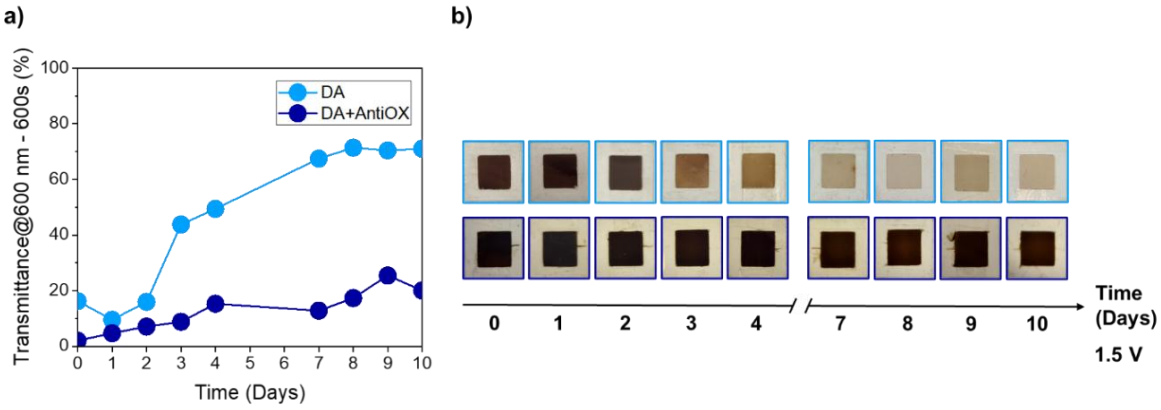


Figure 2.20. a) T@600 nm recorded after the application of 1.5 V for 600 s each 24 hours of nine *i*-ECDs prepared with (DA, light blue) and nine *i*-ECDs with (DA+AntiOX, dark blue). b) Pictures of the *i*-ECDs subjected to the analysis after the activation process carried out at 1.5 V for 600 s.

After the effective colour-switching functionality upon voltage activation in the presence of the antioxidant was confirmed, the long-term performance was evaluated. The colour change capability of DA+AntiOX-based *i*-ECDs was therefore assessed over a period of approximately 3 months. A total of nine *i*-ECDs were prepared and regularly activated over 80 days using 1.5 V for 600 seconds. As shown in Figure 2.21a, even after 80 days, the T@600 nm following activation increased by only about 20% compared to day 0, indicating that the EC response remains largely preserved. Furthermore, Figure 2.21b demonstrates that applying a higher voltage of 3.0 V further enhances the colouration, resulting in T@600 nm values approximately

10% lower than those achieved with 1.5 V. These findings confirm that the inclusion of an antioxidant effectively maintains the colour change capability of *i*-ECDs over extended periods.

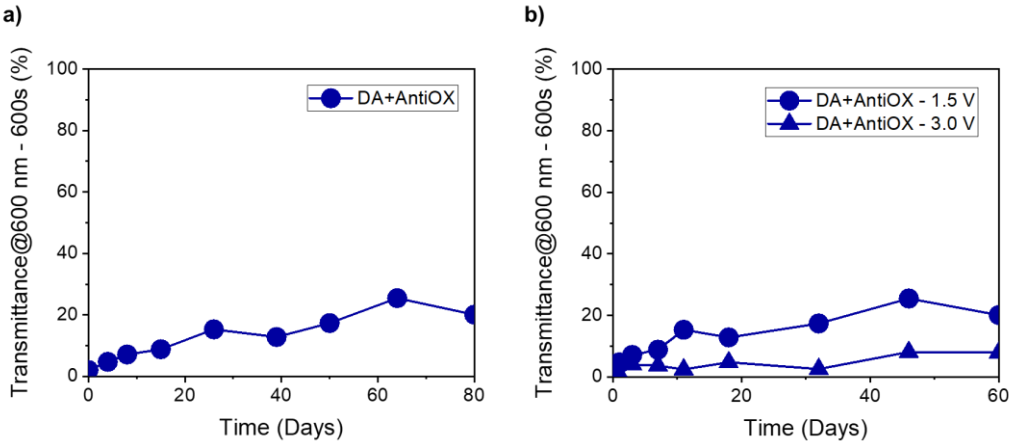


Figure 2.21. a) Single transmittance wavelength at 600 nm recorded after the application of 1.5 V for 600 s of nine *i*-ECDs prepared with DA+AntiOX over a timeframe of 80 days. b) Single transmittance wavelength at 600 nm recorded after the application of 1.5 V and 3.0 V for 600 s of eight + eight *i*-ECDs prepared with DA+AntiOX over a timeframe of 60 days.

2.8 *i*-ECDs characterization

Upon disassembling the *i*-ECD voltage activation, an unexpected phenomenon that challenged our initial assumptions was encountered. Contrary to what is reported in the literature, the black PDA film did not form on the working electrode (W.E.), where DA oxidation typically occurs. Instead, the counter electrode (C.E.), which is usually expected to remain transparent, had turned black, while the W.E. remained mostly clear with only a faint orange hue, Figure 2.22. This unexpected result led us to investigate the underlying processes in more detail.

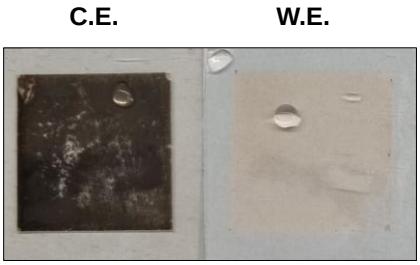


Figure 2.22. Front view of an open *i*-ECD prepared with DA 10 g/L in PBS pH 7.4 after activation process carried out with 1.5 V for 600 s. On left, the C.E., while on right the W.E.

To elucidate the reactions occurring within the *i*-ECD and to understand the composition and formation mechanism of the black film, we carried out a comprehensive set of surface

characterization analyses. These included Scanning Electron Microscopy (SEM), Atomic Force Microscopy (AFM), and X-ray Photoelectron Spectroscopy (XPS). To explain why the black layer appeared on the opposite electrode, our initial hypothesis was that positively charged DA oxidation products, formed over W.E. during electro-oxidation, might migrate toward the negatively charged C.E. during voltage application, where they could deposit and form ePDA. However, the experimental data revealed a different scenario. SEM analysis of the black C.E. revealed the presence of surface-bound nanoparticles (NPs), which were further confirmed by AFM. XPS analysis then clarified the film's composition. The black layer observed on the C.E. is not composed of ePDA but rather consists of metallic indium (In) and tin (Sn) NPs. These originate from the electrochemical reduction of the ITO substrate. The black coloration is due to their strong absorption of visible light, which explains why the black layer appears specifically on the C.E.[32] In contrast, the W.E. displays a light orange patina, which serves as evidence of DA oxidation occurring at that site. This coloration is characteristic of DA oxidation products that absorb in the visible spectrum[24] and will be further confirmed through spectroelectrochemical analysis in the following section.

2.8.1 Surface Morphological Characterization: SEM and AFM Analysis

To highlight the surface changes induced by voltage application, we compared two ITO layers, a pristine reference and the C.E. of an *i*-ECD after activation. This comparison clearly reveals significant morphological differences. As shown in Figure 2.23a, the pristine ITO surface appears clean, with only grain boundaries visible, which are typical of films obtained via sputtering.[33,34] In contrast, the C.E. surface after activation shows an important change, with a dense layer of metallic NPs indicating significant surface modification, Figure 2.23b. For this analysis, an *i*-ECD prepared with DA+AntiOX was activated by applying 1.5 V for 600 seconds. After the activation, the device was carefully disassembled, and the C.E. was subjected to SEM analysis. The observed NPs are the result of the electrochemical reduction of the native metal oxides (In_2O_3 and SnO_2) that compose the ITO, confirming the occurrence of redox processes and the formation of metallic In/Sn at the C.E. upon voltage application.

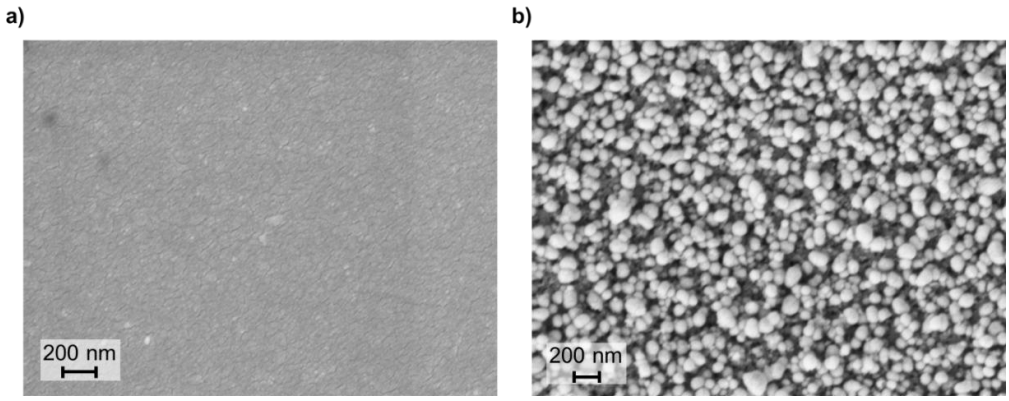


Figure 2.23. a) SEM images of pristine ITO. b) SEM images of the C.E. of an *i*-ECD prepared with DA+AntiOX after application of 1.5 V for 600 s.

The extent of ITO reduction, and thus the formation of metallic NPs, is directly influenced by the duration of voltage application. Prolonged activation results in higher ITO reduction, leading to an increased formation of metallic NPs on the C.E. surface. This correlation is shown in Figure 2.24, which presents SEM images of four C.E.s from *i*-ECDs prepared with DA+AntiOX, each activated at 1.5 V for different time intervals: (a) 0 s, (b) 30 s, (c) 60 s, and (d) 120 s. As the activation time increases, a greater number of NPs form on the electrode surface, progressively darkening it until the entire surface is covered, resulting in a black contrast. These morphological changes are in agreement with the corresponding pictures of the C.E.s (top left corner of each SEM images), which exhibit a gradual darkening of the surface.

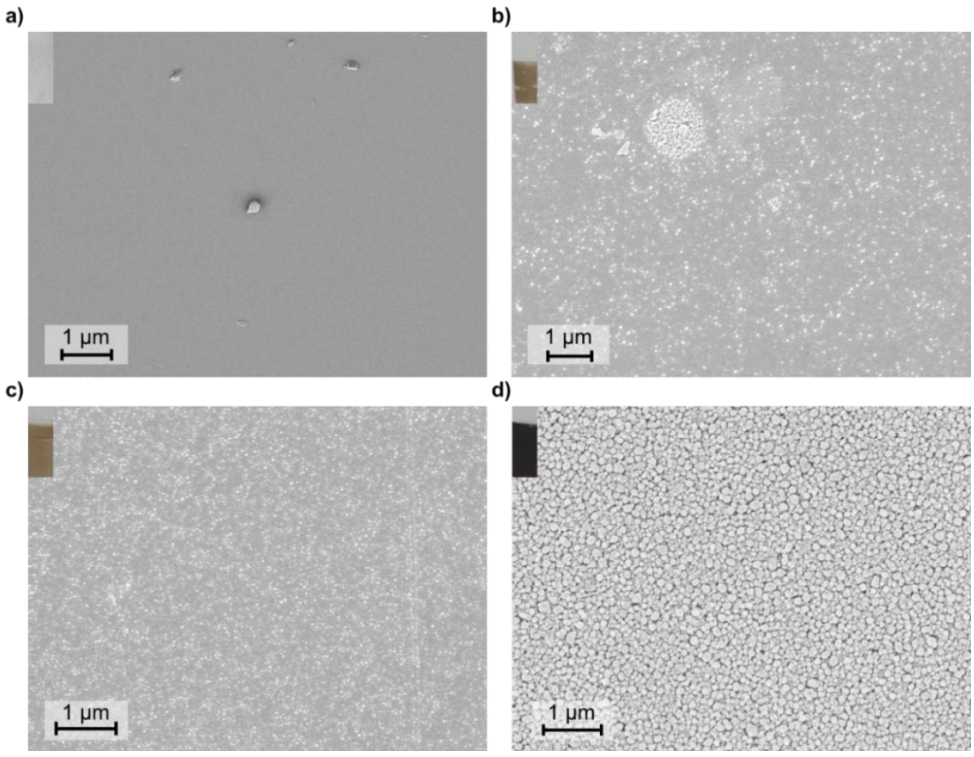


Figure 2.24. SEM images of the C.E. *i*-ECDs prepared with DA+AntiOX after activation at 1.5 V at a) 0 s, b) 30 s, c) 60 s and d) 120 s.

AFM measurements further confirm the morphological changes observed via SEM. The topography of the pristine ITO (Figure 2.25a) displays a remarkable smooth surface, whereas the AFM image of the C.E. after activation (Figure 2.25b) shows a pronounced increase in surface roughness. This roughness is consistent with the presence of metallic NPs formed during ITO reduction and supports the conclusion of significant surface restructuring upon voltage application.

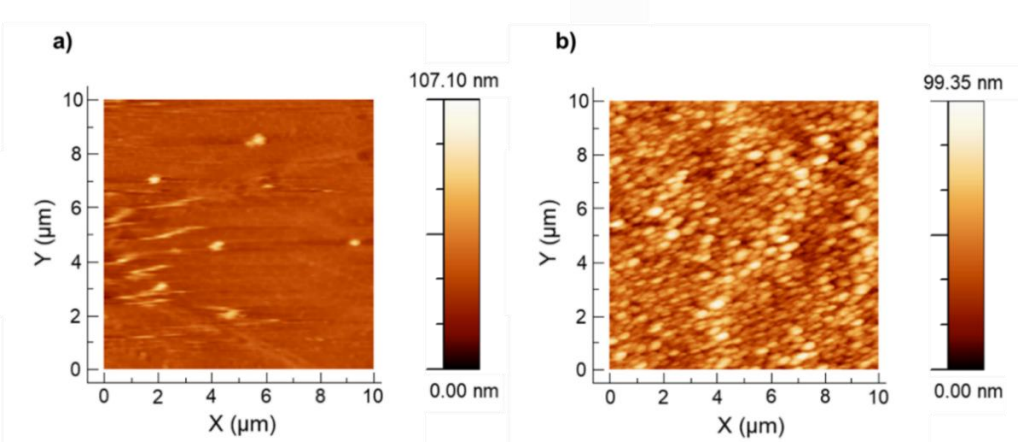


Figure 2.25. a) AFM images of pristine ITO. b) AFM images of the C.E. of an *i*-ECD prepared with DA+AntiOX activated with 1.5 V for 600 s.

2.8.2 XPS

XPS analyses were performed on three DA+AntiOX *i*-ECDs. After being activated for 600 seconds at 1.5 V, the displays were disassembled, rinsed with distilled water, and the surfaces of both the C.E. and the W.E. were analysed by XPS, Table 2.1.

Sample	**C1s (%)**	**O1s (%)**	**In3d (%)**	**Sn3d (%)**	**N1s (%)**	**P2p (%)**
ITO pristine	40.59 ± 0.94	40.26 ± 0.52	17.22 ± 0.69	1.67 ± 0.07	N.D.	N.D.
C.E.	35.20 ± 0.71	42.70 ± 0.36	14.11 ± 0.35	1.24 ± 0.03	1.16 ± 0.17	4.60 ± 0.25
W.E.	70.26 ± 0.30	20.32 ± 0.30	0.54 ± 0.05	N.D.	7.32 ± 0.31	1.05 ± 0.14

Table 2.1. Surface elemental percentage obtained through XPS of the reference substrate, pristine ITO, the black film (C.E.), and the W.E. obtained opening an *i*-ECD prepared with DA activated with 1.5 V for 600s. Data obtained by average of three measurements for each element. N.D.= Not detected.

The elemental analysis of C.E. reveals a composition closely matching that of pristine ITO. Carbon (C 1s) and oxygen (O 1s) are present at 35.20 ± 0.71% and 42.70 ± 0.36%, respectively, while indium (In 3d) and tin (Sn 3d) are detected at 14.11 ± 0.35% and 1.24 ± 0.03%. Minor

amounts of nitrogen (N 1s, 1.16 ± 0.17%) and phosphorus (P 2p, 4.60 ± 0.25%) are also observed, likely originating from residual PBS electrolyte. The absence of elevated C and N signals suggests that no DA-related organic species are present on the C.E. surface.

In contrast, W.E. exhibits a markedly different elemental profile. A strong enrichment in carbon (C 1s, 70.26 ± 0.30%) and nitrogen (N 1s, 7.32 ± 0.31%) is observed, while signals from indium (In 3d, 0.54 ± 0.05%) are considerably reduced and tin (Sn 3d) is not detected. Oxygen (O 1s) is also significantly reduced to 20.32 ± 0.30%. This composition is consistent with the presence of a DA-derived organic layer on the W.E. surface, effectively suppressing the characteristic signals of the underlying ITO (Figure 2.26). Moreover, the distinct orange colouration observed on W.E. (Figure 2.22) matches the hues of known DA oxidation products, such as DAQ and DAC,[35] further confirming selective DA oxidation and deposition of an organic film at W.E.

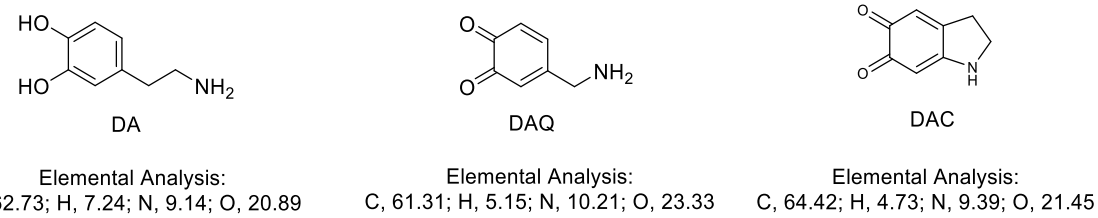


Figure 2.26. Theoretical elemental composition of DA, DAQ and DAC.

High-resolution XPS analysis (Figure 2.27a) provides strong evidence for ITO reduction at 1.5 V. In addition to the main peak at 486.6 eV, characteristic of SnO_2 and consistent with pristine ITO, a distinct shoulder appears at 485.2 eV. This lower binding energy feature is a clear signature of metallic tin Sn(0), confirming the electrochemical reduction of ITO under the applied potential. In contrast no signal attributable to metallic indium In(0) is observed. According to literature,[32] In(0) is prone to rapid oxidation, readily transforming into In_2O_3 upon exposure to air or aqueous environments. As a result, the high-resolution XPS spectrum (Figure 2.27b) displays only a peak at 444.0 eV, attributed to In_2O_3, which is consistent with pristine ITO.

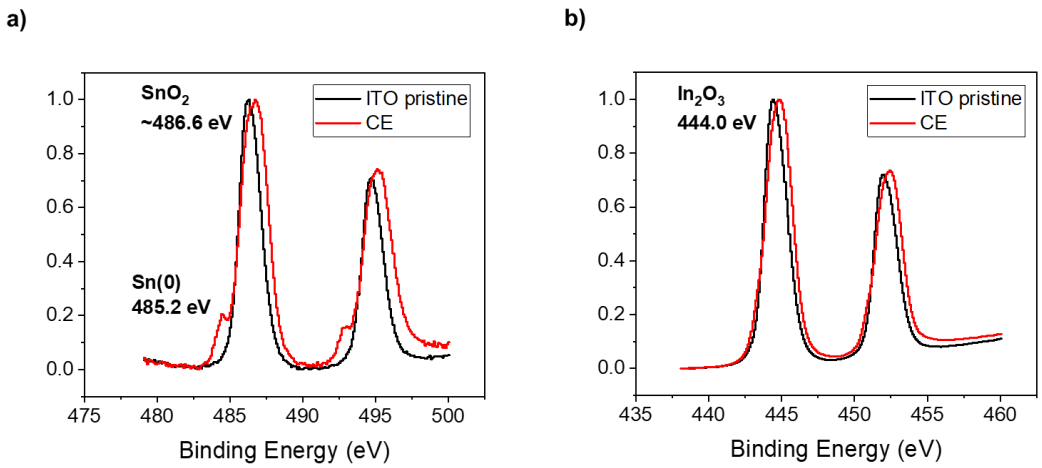


Figure 2.27. a) High-resolution Sn spectra related to the pristine ITO and C.E. of the black layer. b) High-resolution In spectra related to the pristine ITO and C.E. of the black layer.

2.9 DA electrosynthesis in solution with salt-bridge

To further confirm that the formation of the black film was not due to any organic compounds derived from DA, but rather exclusively from the electrochemical reduction of ITO, an activation experiment was conducted by physically separating the two ITO electrodes constituting the *i*-ECD. In this setup, the W.E. was immersed in a solution of DA in phosphate-buffered saline PBS, while the C.E. was placed in a separate compartment containing only PBS. As illustrated in the graphic reported in Figure 2.28a, a salt bridge was incorporated between the two compartments to maintain electrochemical continuity by enabling ionic conduction. This prevents charge buildup in either compartment and preserves electroneutrality, ensuring the sustained flow of current and correct progression of the redox processes. A constant potential of 1.5 V was applied across the electrochemical cell for 600 seconds.

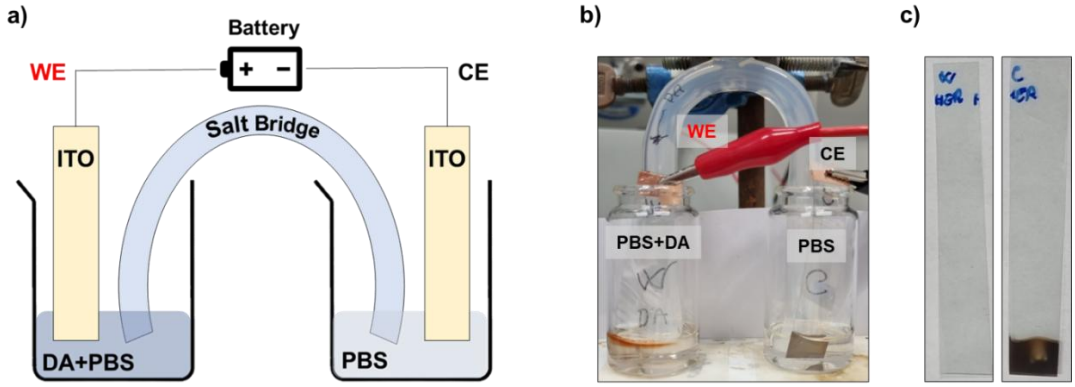


Figure 2.28. a) Graphic illustration depicts the experimental setup featuring a salt bridge. Within this setup, the W.E. is immersed in a solution comprised of DA in PBS pH 7.4, while the C.E. resides in a PBS pH 7.4 alone. The electrodes are connected to a potentiostat providing 1.5 V applied for 600 s. The salt bridge maintains charge neutrality and is made with an Agar Agar gel and 3M KCl. b) Real picture of the experimental setup. c) Pictures of the ITO electrodes at the end of the process.

Figure 2.28b shows a photograph of the experimental setup at the end of the voltage application. During this stage, two main simultaneous electrochemical processes occur within the *i*-ECD. The electro-oxidation of DA at the W.E. and the electrochemical reduction of ITO at the C.E. The orange layer observed on the W.E. is attributed to the oxidation of DA, consistent with literature studies.[24] In parallel, a dark layer forms on the C.E. as a result of ITO reduction, consistent with both our previous experiments and reports in the scientific literature.[32] Figure 2.28c shows that the W.E. does not retain the orange coloration after removal from the electrolyte, indicating that the oxidation products of DA are not strongly bound to the electrode surface and are instead dispersed into the electrolyte solution. In contrast, the C.E. retains its darkened appearance, as the reduction involves the ITO electrode itself.

This experiment clarifies two fundamental aspects of the electrochemical behaviour within the *i*-ECD system. The observation that the W.E., where DA oxidation occurs, remains largely transparent at the end of the voltage application strongly suggests that the visible colour change in the *i*-ECD mainly originates from the reduction of ITO at the C.E., rather than from oxidation of DA derivatives. Additionally, the absence of DA in the vial containing the C.E. demonstrates that ITO reduction does not rely on the physical presence or direct interaction of DA or derivatives over the ITO surface. The process is driven by an electrochemical redox balance, where ITO is reduced at the C.E., while DA is oxidized over the W.E.

2.10 DA spectroelectrochemistry in solution

The oxidation of DA, as previously discussed, can proceed either spontaneously in solution or be induced by the application of an external potential. In this paragraph, we focus specifically on the electro-oxidation process, with the aim of elucidating the chemical species formed upon voltage application. This investigation was prompted by previous observations, specifically the formation of a faint orange hue on the W.E. after opening the *i*-ECD following activation, Figure 2.22, and the formation of an orange layer over the W.E. surface during DA electrosynthesis in solution using a salt bridge setup, Figure 2.28b.

To investigate the processes, DA was electro-oxidized in solution to enable the acquisition of its UV-Vis absorption spectrum. Spectroelectrochemical characterization was conducted in a cuvette containing a DA solution in PBS at pH 7.4. During the experiment, a constant potential of 1.5 V was applied while recording the absorbance from 300 to 600 nm. The setup employed a three-electrode system consisting of an Ag/AgCl (R.E.), a platinum grid (W.E.), and a platinum wire (C.E.). The progressive increase in absorbance observed in the UV–Vis spectra, Figure 2.29a, is attributable to the formation of DAC as the result of the electrochemical oxidation of DA over time. DAC exhibits a characteristic absorption peak at 480 nm, which intensifies gradually, indicating its continuous accumulation in solution. Notably, the absence of detectable signals corresponding to DAQ, a known precursor of DAC, can be rationalized by its rapid conversion. The molecule of DAQ once formed rapid undergoes Michael-type intramolecular cycloaddition,[36] forming DAL which is further electrochemically oxidized, leading directly to DAC.[37] This interpretation is supported by Palladino et al.[35] who observed a similar absorption at 480 nm during the oxidation of DA in solution. Additionally, Bisaglia et al.[36] reported the formation of an orange-coloured compound, identified as DAC, with distinct UV–Vis absorption features at 475 nm, further supporting this mechanism. This absorption peak corresponds to the orange coloration observed in the cuvette (Figure 2.29b), further confirming its association with DAC.

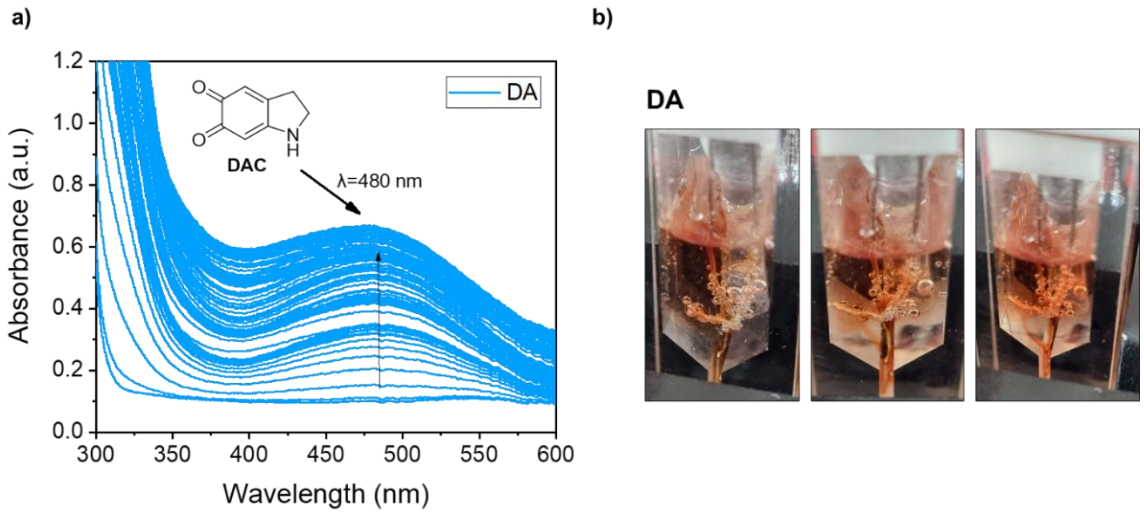


Figure 2.29. a) Absorbance in the visible spectrum as a function of wavelength over time registered during the application of an applied potential of 1.5 V for 600 s for a solution of DA in PBS pH 7.4. b) Pictures of the cuvette with the solution during the application of voltage.

The experiment was repeated with the antioxidant added to the solution, as previous observations, both during the electrosynthesis of DA+AntiOX in PBS and in *i*-ECDs prepared with the same formulation, had shown that no orange colouration developed upon voltage application. It was then hypothesized that the antioxidant might inhibit the formation of DAC, which is responsible for the characteristic colour. Thus, employing the same working setup, a solution consisting of DA+AntiOX in PBS pH 7.4 was subjected to 1.5 V for 600 seconds. As shown in Figure 2.30a, the UV–Vis spectra display a blue shift with the presence of an absorption peak at 395 nm, which is attributable to the formation of DAQ, the first oxidative product of DA. This observation is also consistent with the findings of Palladino et al,[35] and Bisaglia et al.[36], who both reported a maximum absorption at 395 nm, corresponding to the formation of a yellow compound during the oxidation of the monomer. The absorption peak falls in the yellow region as shown in the cuvette pictures acquired during the experiment, Figure 2.30b.

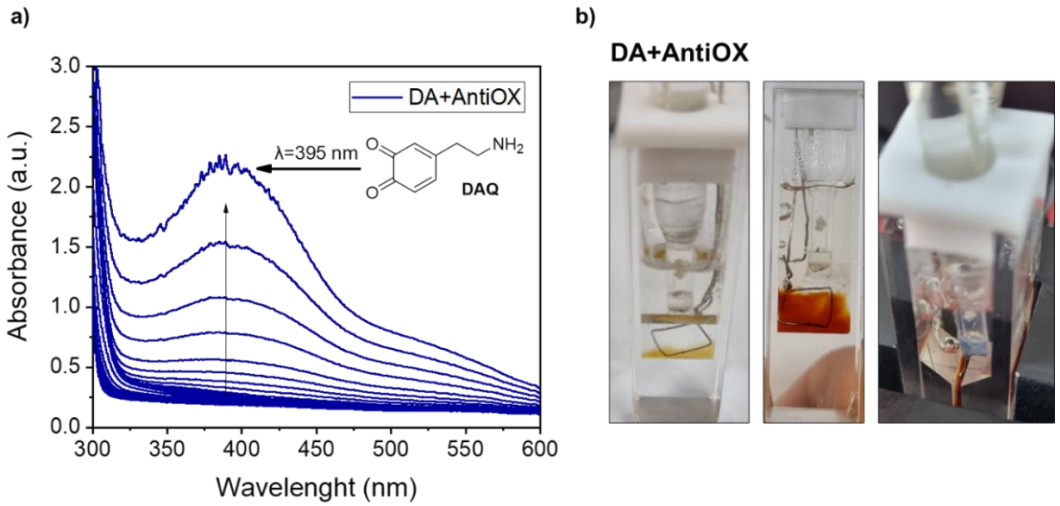


Figure 2.30. a) Absorbance in the visible spectrum as a function of wavelength over time registered during the application of an applied potential of 1.5 V for 600 s for a solution of DA+AntiOX in PBS pH 7.4. b) Pictures of the cuvette with the solution during the application of voltage.

Based on our experimental observations, we hypothesize the following mechanism. During the electro-oxidation of DA in the absence of antioxidants, the dominant visible product is DAC, evidenced by the appearance of an orange colouration and a characteristic absorbance peak around 480 nm. This result may seem counterintuitive, as DAC is generally formed only after DA is first oxidized to DAQ, which then undergoes chemical cyclization to form DAL, the direct precursor of DAC. According to this established pathway reported in literature,[38–40] DAC formation requires a sequential process: DA → DAQ → DAL → DAC. In our experiments, DAC appears to form directly upon voltage application, without any visible presence of DAQ. This can be explained by the spontaneous self-oxidation of DA in solution, which generates DAQ and leads to DAL formation even before electrochemical stimulation. When voltage is applied, the pre-formed DAL is readily oxidized to DAC. This process accounts for the immediate appearance of the orange colour associated with DAC in the absence of antioxidant, which otherwise would inhibit this spontaneous pre-oxidation. Conversely, when an antioxidant is introduced into the system, the spontaneous oxidation of DA is suppressed, thereby reducing the concentration of available DAL in solution. As a result, under electrochemical stimulation, the main visible event becomes the direct oxidation of DA to DAQ, associated with an absorbance of around 395 nm and a yellow colour. These conclusions are drawn from the evolution of the UV–Vis absorption spectra and visual colour changes, in line with previously reported studies by Palladino et al., and should be interpreted as plausible hypotheses based on spectroscopic evidence and reaction behaviour under our specific experimental conditions. Importantly, in both cases, whether the DA-based *i*-ECDs are prepared with the presence or not of antioxidant in PBS at pH 7.4, activation consistently results

in the reduction of the ITO electrode. This is because, regardless of the specific oxidation pathway, DA is oxidized at the W.E., losing electrons. These electrons flow through the external circuit and are consumed at the ITO which undergoes electrochemical reduction.

The critical aspect of this process is the occurrence of an oxidation reaction at the W.E. The ITO itself is not selective toward the specific compound undergoing oxidation. Based on this, we hypothesise that any electroactive compound capable of undergoing oxidation at the W.E. could, in principle, induce the reduction of the ITO electrode. To experimentally validate this concept, a new set of tests was conducted using catechol, a molecule structurally similar to DA but lacking the amine functional group. Catechol was selected firstly from its chemical similarity to DA and also due to its known electrochemical behaviour. It undergoes oxidation to form quinone, exhibiting an oxidation peak around 0.4 V,[41] which is comparable to the oxidation peak observed in the DA → DAQ reaction, which will be deeply discussed in the following section.

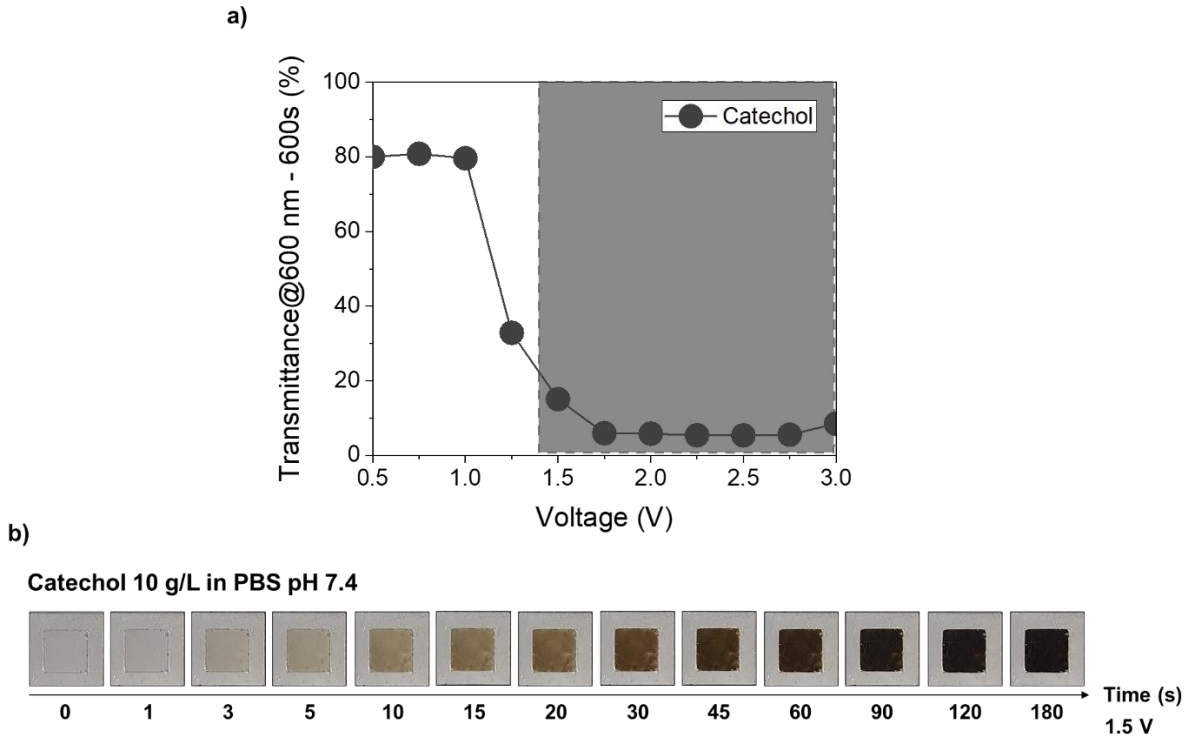


Figure 2.31. a) T@600 nm recorded after activation by applying a voltage ramp for 600 s on eleven *i*-ECDs prepared with catechol 10 g/L in PBS pH 7.4. The optimal operating parameters for an *i*-ECD are indicated in the highlighted dark grey area. b) Frames extracted from a video recording depicting an *i*-ECD, manufactured employing catechol 10 g/L in PBS pH 7.4. These frames capture the activation process, conducted at 1.5 V.

To test the hypothesis, eleven *i*-ECDs were fabricated using a 10 g/L catechol solution in PBS at pH 7.4. These displays were activated by applying a voltage ramp (0.5–3.0 V) for 600 seconds. The experimental outcomes, reported in Figure 2.31a, show a response highly consistent with that obtained for DA-based *i*-ECDs. Specifically, at voltages below 1.0 V, no

measurable change in transmittance at 600 nm (T@600 nm) was detected. At 1.25 V, a T@600 nm of 32.8% was recorded, and at 1.5 V, the transmittance dropped to 15.08%. These values are closely similar to those collected with DA (T@600 nm of 45.7% at 1.25 V and 10.07% at 1.5 V), further confirming the comparable EC behaviour. Moreover, the kinetics of the colour change, shown in Figure 2.31b, reflect those observed in DA-based *i*-ECDs, illustrating a consistent evolution of optical contrast over time. These findings underscore that the essential parameter governing ITO reduction is not the identity of the oxidised species, but rather the occurrence of the oxidation during the voltage application.

2.11 DA cyclic voltammetry

To elucidate the electrochemical reactions occurring during voltage application within the *i*-ECD, CV was selected as a suitable characterization technique. This method enables the investigation of the redox behaviour of DA and the verification of whether the observed mechanism corresponds to that reported in the literature. Measurements were conducted in a standard PBS electrolyte at pH 7.4, a condition specifically chosen to replicate the operational environment of the *i*-ECD. A potential window of ±1.0 V was applied at a scan rate of 100 mV/s, carefully selected to remain within the electrochemical stability window of water and to avoid parasitic side reactions. Figure 2.32a presents the cyclic voltammogram of DA recorded in PBS at pH 7.4, with a scan rate of 100 mV/s. The voltammogram exhibits four distinct redox peaks, two anodic (peaks 1 and 4) and two cathodic (peaks 2 and 3), which correspond to sequential oxidation and reduction events occurring during the applied potential sweep. These features are characteristic of the multi-step redox mechanism of DA and are consistent with previously reported literature on its electrochemical behaviour, Figure 2.32b.[38,39]

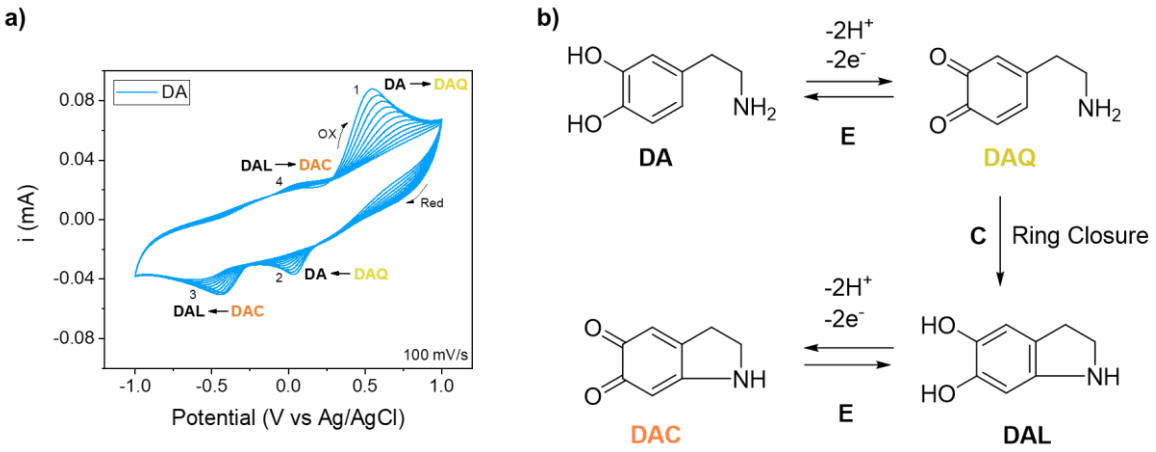


Figure 2.32. a) Cyclic voltammetry carried out in a solution of DA 10 g/L in PBS pH 7.4 between ±1.0 V with a scan rate of 100 mV/s. b) Schematic representation of the first four compounds resulting from the oxidation of DA. E: electrochemical reaction; C: chemical reaction.

The anodic peak 1, located at approximately +0.6 V (vs Ag/AgCl), corresponds to the two-electron, two-proton oxidation of DA to DAQ. This is a reversible electrochemical (E) process. The formation of DAQ can occur either via direct electrochemical oxidation or through spontaneous oxidation in aqueous solution in presence of oxygen.[42] Supporting evidence for the spontaneous oxidation pathway is provided by the gradual decrease in the UV absorbance peak at 280 nm,[43] indicative of DA consumption in the absence of any applied voltage, as shown in Figure 2.33. This figure presents the UV-Vis kinetic analysis of a 0.1 g/L DA solution in PBS at pH 7.4, where spectra were recorded over a 2-hour period with one scan every 12 minutes. The continuous drop in absorbance over time confirms the progressive, voltage-independent degradation of DA, attributed to its slow spontaneous in aqueous environment under oxygen.[44]

On the reverse scan, cathodic peak 2, observed around 0.0 V, represents the reduction of DAQ back to DA via a reversible two-electron process, completing the first redox couple. Cathodic peak 3, located near −0.4 V, corresponds to the reduction of DAC to DAL. This transformation also proceeds via a reversible two-electron process. In contrast to these electrochemical steps, the formation of DAL itself does not involve electron transfer but instead proceeds through an irreversible chemical transformation. Specifically, this is a Michael-type intramolecular cyclization reaction that occurs following the formation of DAQ. In this process, the amine side chain of DAQ acts as a nucleophile and attacks the electrophilic β-carbon of the quinone ring (at position 5), leading to the formation of a new C–N bond. This nucleophilic addition results in the closure of the ring system and the formation of DAL, a key intermediate in the electrochemical oxidation pathway of DA. Finally, anodic peak 4, appearing near +0.1 V, reflects the electrochemical oxidation of DAL back to DAC, again through a reversible two-electron process, forming the second redox couple in the system.

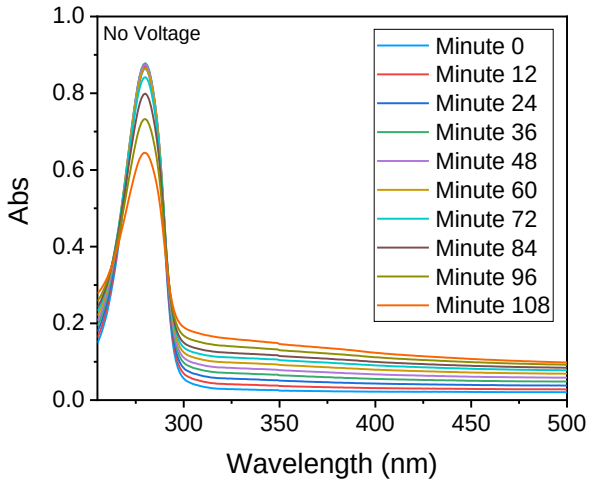


Figure 2.33. Kinetics analysis of a 0.1 g/L DA in PBS pH 7.4 where the UV-Vis absorbance was registered over 2-hour timeframes, each scan every 12 minutes. No voltage application.

Overall, this behaviour follows a well-established ECE (electrochemical–chemical–electrochemical) mechanism. The gradual decrease in peak current intensities over successive cycles further indicates DA depletion at the working electrode surface, driven both by electro-oxidation and subsequent irreversible chemical transformations. The reaction pathway shown in Figure 2.32b summarizes the redox and chemical transformations involved, including the reversible DA/DAQ and DAL/DAC couples, and the irreversible ring-closure step leading to DAL formation.

The voltammetric analysis shown in Figure 2.32a begins with the application of potential from 0.0 V. Interestingly, the first oxidation peak observed is peak 4, appearing around +0.1 V, which corresponds to the electrochemical oxidation of DAL to DAC. This observation might appear contradictory at first look, since according to the reaction mechanism, DAL is formed only after DA is first oxidized to DAQ, a process that occurs at the higher potential of approximately +0.6 V, peak 1. This apparent inconsistency is explained by the spontaneous oxidation of DA in solution. As previously discussed, when DA is dissolved in PBS at pH 7.4 and exposed to molecular oxygen, it undergoes a slow, non-electrochemical oxidation. This process leads to the formation of DAQ, which then undergoes irreversible intramolecular cyclization to form DAL. As a result, even before the application of any external voltage, a fraction of DAL is already present in solution. Therefore, when the CV scan is initiated from 0.0 V, the system already contains DAL, which can immediately undergo electrochemical oxidation to DAC, giving rise to peak 4 at +0.1 V.

To visually confirm the presence of DAL in solution, a constant potential of +0.3 V was applied to a DA solution in PBS (pH 7.4). This potential was intentionally chosen to be above the

oxidation threshold required to convert DAL into DAC, as determined from previous CV results, but below the +0.6 V required for the electrochemical formation of DAQ. This precaution ensures that only the DAL → DAC conversion occurs, without triggering the oxidation of DA to DAQ, which would compromise the specificity of the observation. Figure 2.34 presents the experimental setup, where the emergence of a distinct orange coloration on the glassy carbon W.E. surface serves as a visual confirmation of DAC formation. This colour change is consistent with both our own spectroelectrochemical data and literature reports, reinforcing the conclusion that DAL is already present in the system due to spontaneous DA oxidation, and is subsequently oxidized via applied voltage forming DAC.

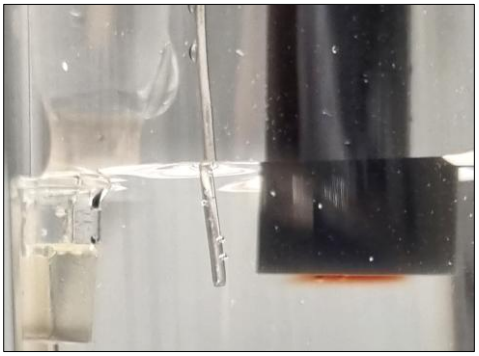


Figure 2.34. Image capturing the three-electrode configuration during the application of a constant potential of +0.3 V for 600 s to a DA solution in PBS pH 7.4.

Definitive evidence supporting the presence of DAL in solution, formed via DA self-oxidation, is presented in Figure 2.35a and Figure 2.35b. CV was performed on three PBS (pH 7.4) solutions, one containing DA under ambient conditions, one under oxygen-depleted conditions ($DA_{O_2,free}$), and the last with the antioxidant (DA+AntiOX). The corresponding absorption spectra in the visible range were recorded to identify the species formed in each case. Figure 2.30a shows that the DA solution under ambient conditions (light blue line) exhibits a clear absorption peak at 480 nm, which is characteristic of DAC, the oxidation product of DAL. This spectroscopic evidence is supported visually by Figure 2.30b, where the formation of an orange layer on the W.E. surface confirms the presence of the compound. In contrast, both the oxygen-depleted (red line) and antioxidant-treated (dark blue line) PBS show a significant reduction in the 480 nm absorption peak and no visible orange colouration on the electrode.

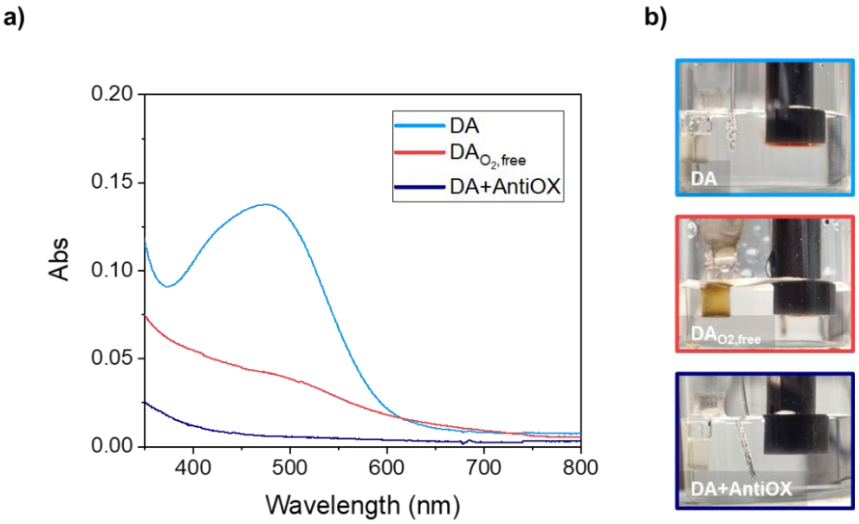


Figure 2.35. a) Absorption in the visible range of three solutions in PBS pH 7.4 based on 10 g/L of DA, $DA_{O2,free}$ and DA+AntiOX subjected to CV between ± 1.0 V for 10 cycles with 100 mV/s as scan rate. b) Pictures of three-electrodes setup of the three solutions acquired at the last voltammetric cycle.

These findings confirm that the spontaneous oxidation of DA is strongly inhibited under these conditions, preventing the formation of the first oxidation product DAQ and its downstream products DAL and DAC. A faint orange hue may still be observed in the oxygen-depleted sample due to trace amounts of residual O_2, which is difficult to remove completely, allowing minimal DA oxidation. Overall, these results confirm that in the presence of oxygen and in the absence of antioxidant protection, DA undergoes spontaneous oxidation to DAQ, which subsequently undergoes chemical cyclization to form DAL. This compound is then electrochemically oxidized to DAC during the experiment. The suppression of DAC formation under oxygen-free or antioxidant conditions provides a strong final validation of the oxidation pathway.

2.12 *i*-ECD charge consumption and CE

In the context of *i*-ECDs, the activation process refers to the application of a potential difference across the display, which triggers the colour change by inducing the reduction of the ITO electrode. The total charge consumed during this process, obtained by integrating the current over time, is a key parameter as it quantifies the energy required for the switching which is directly linked to the electrochemical efficiency. This parameter is essential for *i*-ECDs integration in smart labels or low-power systems, where the power supply (*e.g.*, a battery or supercapacitor) must deliver sufficient charge to reliably activate at least one or multiple *i*-ECDs. If the total charge required by the *i*-ECD exceeds the capacity of the power source, the switching process will remain incomplete, resulting in reduced optical contrast. Knowing the

charge consumption allows for accurate sizing of the energy source and ensures compatibility with plug-and-play configurations.

The charge consumption was evaluated by averaging the results from seven *i*-ECDs prepared using a DA+AntiOX formulation in PBS at pH 7.4. Each display was activated by applying 1.5 V for 600 seconds. Figure 2.36a shows the evolution of optical transmittance during the activation process, with the average T@600 nm reaching approximately 3% at the end of the *i*-ECDs switching. As the activation progresses, the transmittance steadily decreases, indicating the ongoing electrochemical oxidation of DA and reduction of the ITO electrode. During this process, the internal electrical resistance of the *i*-ECD gradually increases. This leads to a progressive increase in internal resistance, which in turn reduces the current flow. As shown in Figure 2.36b, this is manifested as a gradual decrease in the measured current, ultimately reaching a point where the resistance is sufficiently high that the applied potential can no longer sustain any current through the *i*-ECD electrodes. At this stage, no further redox reactions can occur, and the transmittance drop stops, marking the end of the activation process. The *i*-ECD becomes electrochemically unresponsive, having reached its final switched state.

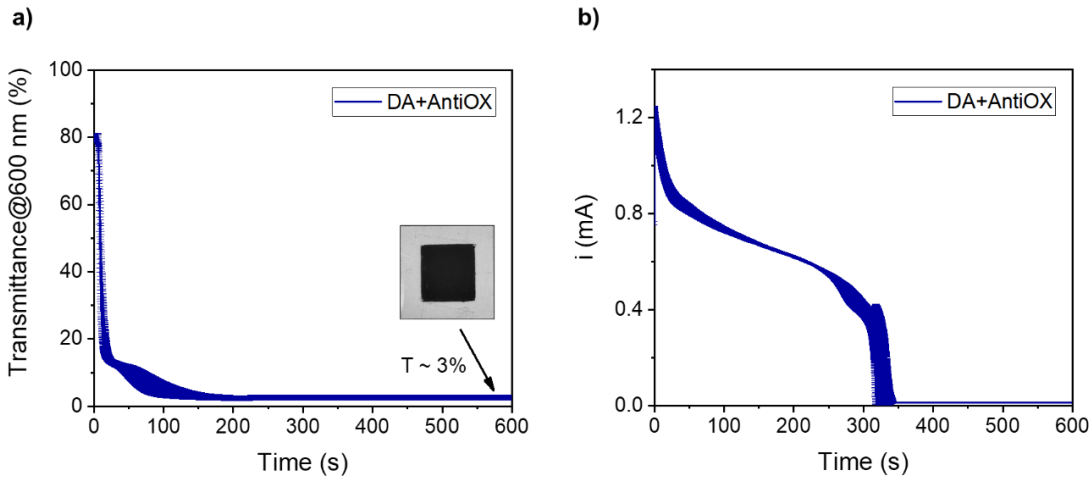


Figure 2.36. a) Average value of T@600 nm recorded during the activation at 1.5 V for 600 s of seven *i*-ECDs prepared with DA+AntiOX. b) Average value of current registered during the activation process of the seven *i*-ECDs.

By integrating the current over time, the average charge required for full activation was calculated to be 247.3 ± 22.2 mC, with a corresponding CE of 6.02 cm^2/C. To put this in perspective, a standard AAA battery (1.5 V, 1000 mAh) could theoretically deliver enough energy to fully activate more than 10000 *i*-ECDs, emphasizing the low energy requirements and high scalability of the system for integration into battery-powered smart devices.

Moreover, given that the majority of the colour change occurs within the first few seconds of voltage application, the total charge consumption can be significantly reduced by shortening

the activation time. Figure 2.37a shows that an average T@600 nm of approximately 9%, corresponding to the same visually dark contrast achieved with longer activation, is reached by applying 1.5 V for just 60 seconds. Under these conditions, the current response shown in Figure 2.37b confirms a remarkably lower charge consumption of 54.9 ± 4.9 mC, corresponding to an important improved CE of 17.65 cm^2/C. Additionally, reducing the active area of the *i*-ECD further decreases the absolute charge required. For example, an *i*-ECD with an active area of 0.25 cm^2 consumes only around 15 mC during a 60-second activation at 1.5 V, yielding a CE of 70.62 cm^2/C. This demonstrates the scalability and adaptability of the system for ultra-low-power applications, where display dimensions and power constraints are connected.

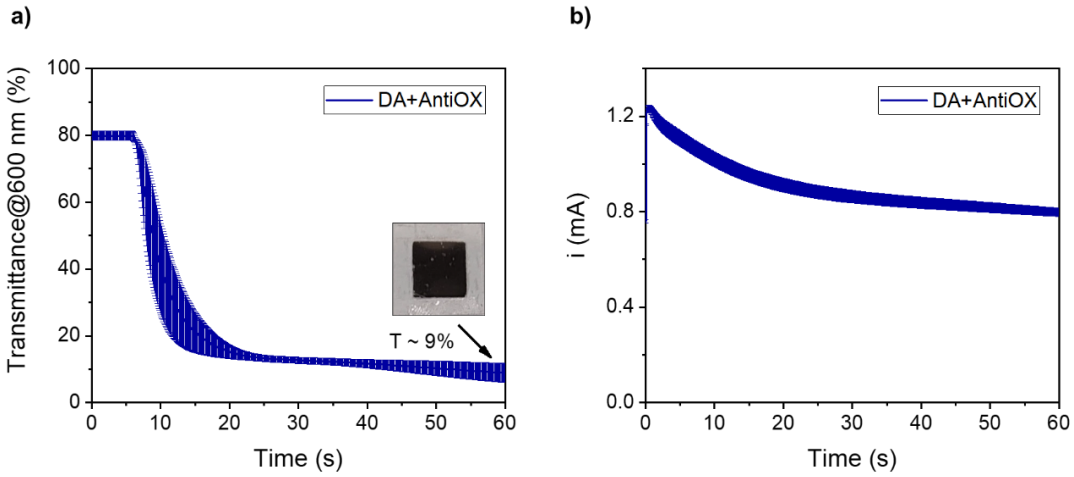


Figure 2.37. a) Average value of T@600 nm recorded during the activation at 1.5 V for 60 s of seven *i*-ECDs prepared with DA+AntiOX. b) Average value of current registered during the activation process of the seven *i*-ECDs.

2.13 Kinetic analysis

The kinetic analysis of *i*-ECD activation is an important tool to formulate hypotheses about the sequence of processes responsible for the observed trends in transmittance and current during voltage application. In this study, the behaviour of a DA-based *i*-ECD in PBS at pH 7.4 was investigated under a constant voltage of 1.5 V applied for 600 seconds. By simultaneously monitoring the transmittance (T@600 nm) and the current, we propose a four-phase mechanism that may account for the trends observed in Figure 2.38. While we cannot directly confirm the individual processes involved, this interpretation is consistent with the optical and electrical responses recorded during the experiment.

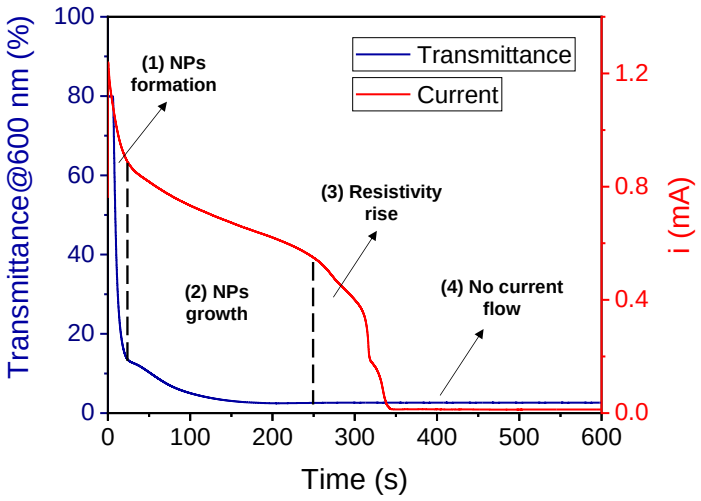


Figure 2.38. Overlap between T@600 nm of a DA-based *i*-ECDs and its registered current during the application of 1.5 V for 600 s. Occurring steps: (1) formation of superficial NPs on the ITO electrode, (2) growth of these NPs, (3) increase of ITO resistivity, (4) the current is not able to flow anymore through the *i*-ECD.

In the first phase (1), which we attribute to the formation of nanoparticles (NPs), a sharp drop in T@600 nm is accompanied by a rapid decrease in current. We hypothesize that this behaviour is due to the nucleation of metallic In and Sn NPs on the C.E. surface. As the deposition progresses and more of the surface becomes covered, a change in the slope of both the transmittance and current curves suggests the transition to a new regime. The second phase (2), which we describe as NPs growth, is likely characterized by saturation of the electrode surface with nanoparticles, limiting new nucleation events. At this stage, we speculate that existing particles either grow in size or develop into multilayered structures. This continued structural change produces a small reduction in T@600 nm, finally approaching a minimum. The third phase (3), which we refer to as resistivity rise, begins when T@600 nm nears zero and the current exhibits a sharper decline. Our hypothesis is that the ongoing reduction of In_2O_3 and SnO_2 disrupts the ITO lattice by forming metallic NPs, thereby compromising the material's ability to conduct electrons.[45,46] The proposed mechanism involves a loss of conductivity typically sustained by electron donation through oxygen vacancies within the ITO layer. In the final phase (4), identified as no current flow, the system appears to reach a point where the electrode resistivity becomes too high for the applied potential to drive further electron transport. Consequently, the current drops to zero and the *i*-ECD becomes unresponsive to continued voltage application. While further studies are needed to confirm the exact nature of these transitions, the proposed four-step sequence offers a plausible framework for interpreting the observed electro-optical behaviour during *i*-ECD activation.

2.14 Proof of irreversibility

After analysing and understanding the mechanism underlying the colour change in each *i*-ECD upon voltage application, this paragraph focuses on demonstrating and proving the irreversibility of this process. This was achieved through both electrochemical and spectroscopic analyses, which were carried out not only on *i*-ECDs but also on reversible systems. Such a comparison is essential, as understanding how an *i*-ECD undergoes an irreversible colour change requires knowledge of the structural and functional differences between a reversible EC display (*r*-ECD) and an *i*-ECD. The origin of irreversibility also lies in their different construction architecture.

In *r*-ECDs, the active EC materials, typically redox-reversible polymers, are deposited onto both electrodes, which are placed face to face and separated by an electrolyte, Figure 2.39a. Upon each reversal of the voltage polarity, the polymer films on the electrodes can be oxidized and reduced multiple times, allowing for reversible switching between coloured and bleached states. In contrast, in our *i*-ECD, the EC compound is not deposited on the electrodes but instead incorporated directly into the electrolyte, Figure 2.39b. When a potential difference is applied, the compound is oxidized at the W.E., while the C.E., which is the ITO, is simultaneously reduced. Reversing the voltage polarity swaps the roles of the electrodes, causing DA oxidation and ITO reduction to occur on the opposite sides with the consequent formation of NPs also on this electrode. Our experimental finding proved that the formation of NPs via ITO reduction is an irreversible process. This permanent deposition prevents the system from returning to its original optical state, confirming that the process is electrochemically irreversible.

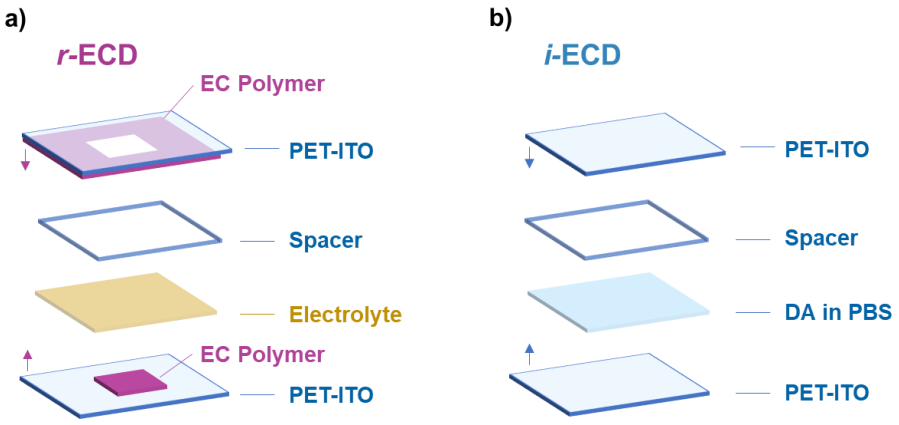


Figure 2.39. a) Illustration of an ECD with a reversible architecture, *r*-ECD. b) Illustration of an ECD with an irreversible architecture, *i*-ECD.

To experimentally validate the irreversible behaviour of *i*-ECD, a direct comparison was made with *r*-ECD. Both displays were subjected to the same voltage protocol, consisting of continuous polarity inversion between ±1.5 V over time, as shown in Figure 2.40a. In the case of the *r*-ECD, this voltage cycling induces a sequence of reversible redox reactions within the EC polymer layers deposited on both electrodes. As a result, the display exhibits a dynamic and repeatable modulation in optical transmittance in response to the alternating voltage, as illustrated by the purple line in Figure 2.40b. Conversely, in the case of the *i*-ECD, the same voltage program induces DA oxidation over the W.E and simultaneous ITO reduction at the C.E. When the voltage polarity is reversed, the processes are inverted. The electrode that previously oxidized DA now drives ITO reduction, while the electrode where ITO was previously reduced now facilitates DA oxidation. However, unlike the reversible redox reactions in *r*-ECDs, the reduction of ITO in *i*-ECDs is an irreversible process. Once reduced, the ITO layer undergoes a permanent structural and optical transformation. Consequently, with each voltage cycle, the system accumulates irreversible changes, leading to a progressive and unidirectional decrease in transmittance, as shown by the black line in Figure 2.40b. This response occurs regardless of the polarity applied, confirming the non-reversible nature of the switching mechanism in *i*-ECDs.

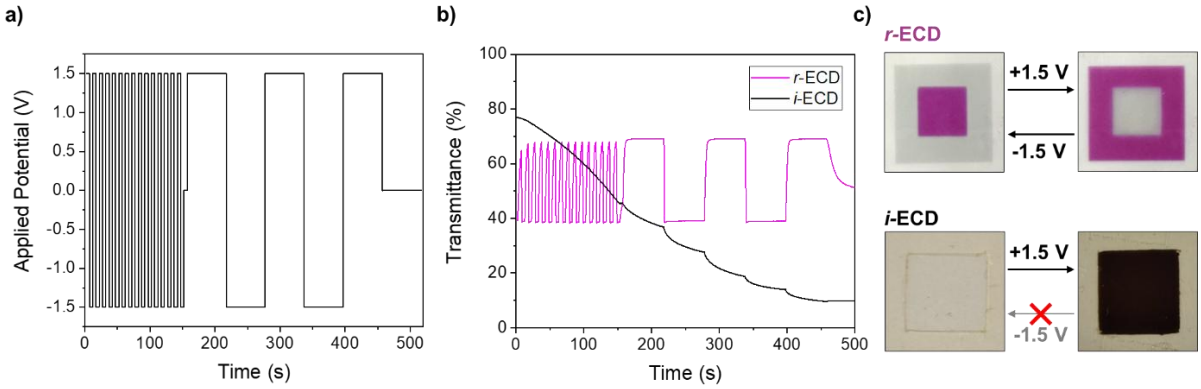


Figure 2.40. a) Applied voltage as function of time expressed in seconds. Alternation between ± 1.5 V for 30 5-seconds switches and 5 60-seconds switches applied on both *r*-ECD and *i*-ECD. b) Single wavelength transmittance measured versus the time as a response to the applied potential of *r*-ECD and *i*-ECD. c) Picture of the *r*-ECD and *i*-ECD during the application of ± 1.5 V.

Electrochemical reversibility was further assessed by performing CV analysis within a ±1.5 V potential window on both *r*-ECD and *i*-ECD. In the case of the *r*-ECD, the CV profile exhibits two well-defined and symmetric peaks in each cycle, corresponding to the reversible redox transitions of the EC polymer, as shown in Figure 2.41a. The consistent appearance of these peaks during consecutive cycles, along with their near-symmetric shape and comparable peak currents, indicates a stable and reversible redox process. In contrast, the CV response of the *i*-

ECD reveals a fundamentally different electrochemical behaviour. As shown in Figure 2.41b, distinct peaks around ±0.6 V correspond to the oxidation of DA to DAQ. In line with what was explained earlier, this arises from the symmetric two-electrode configuration, where the applied voltage is continuously inverted. As a result, the two electrodes alternate roles between working and counter throughout the scan. Since the solution containing DA is present on both electrodes, the oxidation process appears in both anodic and cathodic regions of the voltammogram. At potentials beyond approximately ±1.3 V, a sharp increase in current is observed, which is attributed to the electrochemical reduction of the ITO electrode. This reaction progressively degrades the ITO surface, significantly increasing its resistivity cycle by cycle. Consequently, the electron flow is hindered, leading to a significant drop in current over successive cycles. Finally, the current nearly vanishes as the electrode becomes highly resistive. This irreversible degradation behaviour contrasts with the *r*-ECD, where the redox processes remain reversible and stable over multiple cycles, as demonstrated by the consistent and symmetric peak profiles.

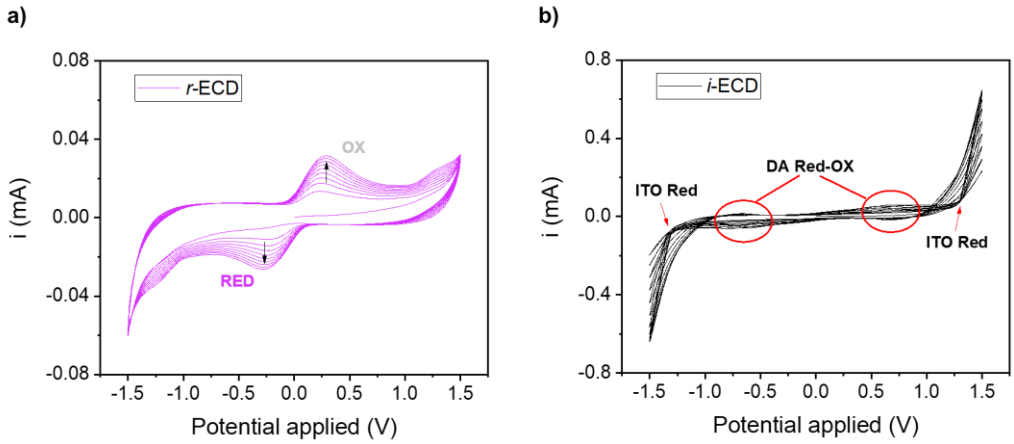


Figure 2.41. Cyclic voltammetry carried out between ±1.5 V at 100 mV/s for the a) *r*-ECD and b) *i*-ECD.

2.15 Role of the electrolyte

An electrolyte typically consists of two primary constituents. The salt, which enables ionic conduction essential for electrochemical processes, and the solvent, responsible for dissolving the salt. In the *i*-ECDs, this function is fulfilled by the PBS, comprising four distinct components, two chlorinated salts (NaCl and KCl) and two phosphate-based buffers (Na_2HPO_4 and KH_2PO_4), along with H_2O, which is essential for the dissolution of DA. The effective operation of ECDs relies significantly on ionic conductivity, which is closely tied to the choice of salt used. Until now, the *i*-ECDs activated via applied voltage were always prepared employing PBS as electrolyte. Nevertheless, in order to better understand the influence of

different salts on the ITO reduction potential, four electrolyte solutions were tested, each prepared with a concentration of 0.1 M in H_2O. Thus, four *i*-ECDs prepared with a DA-based of each solution were subjected to a voltage ramp from 0 to 3.0 V measuring the current to determine the threshold voltage for ITO reduction, highlighted by the swift increase measured current. Figure 2.42a illustrates the results, indicating that NaCl (dark blue line) and KCl (red line) exhibited the highest activation thresholds, recording 1.57 V and 1.59 V, respectively. In contrast, Na_2HPO_4 (green line) demonstrated the lowest threshold at 1.22 V, aligning with the PBS, reference in the graph (light blue line), and followed by KH_2PO_4 (purple line) at 1.42 V. From the data collected, it is clear that the lower ITO reduction potentials observed in the presence of phosphate salts are due to the presence in the electrolyte of the monohydrogen and dihydrogen phosphate anions.

As described by Hotchkiss and coworkers,[47] phosphonic acid groups, such as phosphate anions, can strongly interact with the surface of ITO via several mechanisms, including covalent bonding, electrostatic interactions, and hydrogen bonding. These interactions primarily involve the surface hydroxyl (–OH) groups and metal cations (In^{3+}, Sn^{4+}) present on the polar, hydroxyl-rich ITO surface. Covalent binding occurs through condensation reactions between the phosphonic acid and surface–OH groups, typically forming mono-, bi-, or tridentate metal–oxygen–phosphorus linkages. Electrostatic interactions may occur when negatively charged phosphate groups are attracted to positively charged surface sites on ITO, especially under acidic conditions where the surface may be protonated. Additionally, hydrogen bonds can form between the –OH groups of the ITO and non-bound phosphoryl oxygen atoms, stabilizing the monolayer structure.

These interactions not only promote the formation of a dense, well-ordered monolayer on ITO but also significantly modify its electronic properties. Upon binding, phosphate-containing molecules can induce a charge transfer process, which in this context refers to the redistribution of electrons between the adsorbed species and the ITO surface. Specifically, the lone pairs on the oxygen atoms of the phosphate may interact with empty or partially filled electronic states of the metal cations (In or Sn), leading to a partial delocalization of electrons into or out of the surface. This interfacial charge transfer alters the local electronic structure of ITO, potentially introducing new energy levels (trap states) within its band gap. As a result, the adsorption of phosphate groups can shift the Fermi level and modify the effective work function of ITO, thereby affecting its redox behaviour and shifting the reduction potential. Therefore, the lower reduction potentials observed in the presence of phosphate-containing electrolytes arise from these strong interfacial interactions and charge transfer processes, which tailor the electronic structure of ITO, making it more susceptible to reduction at lower applied voltages.

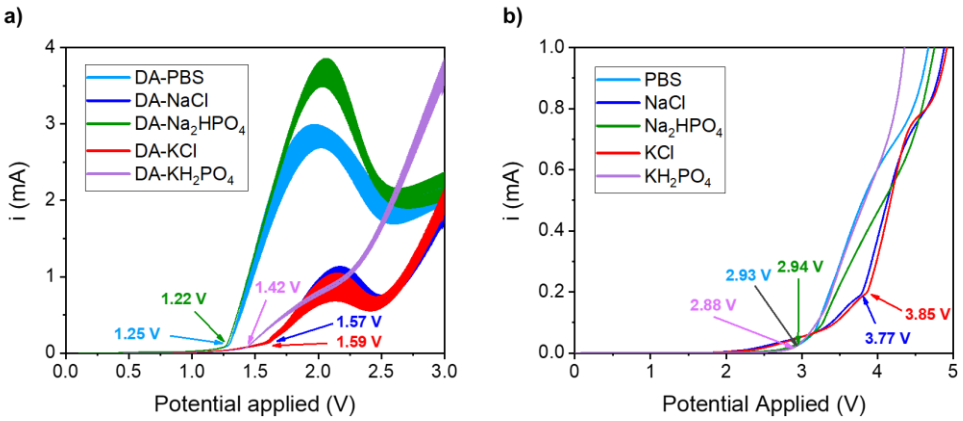


Figure 2.42. a) Registered current as function of potential applied from 0 to 3.0 V with scan rate of 100 mV/s for five *i*-ECDs prepared employing 10 g/L of DA in PBS pH 7.4 and 0.1 M of NaCl, Na_2HPO_4, KCl and KH_2PO_4. b) Registered current as function of potential applied from 0 to 5.0 V with scan rate of 100 mV/s for five *i*-ECDs prepared employing PBS pH 7.4 and 0.1 M of NaCl, Na_2HPO_4, KCl and KH_2PO_4 without the use of DA.

To further confirm the role of the DA in lowering the ITO reduction potential, a control experiment was conducted using *i*-ECDs assembled with all the electrolytes alone, without the monomer. As shown in Figure 2.42b, the absence of DA leads to a marked increase in the voltage required to initiate ITO reduction. In particular, the threshold voltage for ITO reduction in PBS alone rises to 2.93 V, more than double the value recorded in the presence of DA (1.25 V, Figure 2.42a). This outcome highlights the critical contribution of DA in facilitating charge transfer and promoting earlier onset of ITO reduction. This trend holds across all electrolyte systems. Without DA, the threshold voltages are significantly higher. NaCl reaches 3.77 V, KCl peaks at 3.85 V, KH_2PO_4 reduces slightly to 2.88 V, and Na_2HPO_4 registers 2.94 V. Despite the absence of DA, phosphate-based electrolytes still exhibit the lowest ITO reduction potentials, consistent with their strong interaction with the ITO surface via covalent bonding, electrostatic attraction, and hydrogen bonding.

The ~20 mV discrepancy observed between Na_2HPO_4 and KH_2PO_4 can be attributed to their pH difference. Under identical conditions, with the same salt concentration and DA content in water, KH_2PO_4 exhibits a significantly more acidic pH (4.31), while Na_2HPO_4 is more basic (pH 8.08), as shown in Table 2.2. As highlighted in the introduction, alkaline conditions promote the electrochemical oxidation of DA, which in turn facilitates the reduction of ITO. Conversely, acidic environments hinder DA oxidation, thereby increasing the voltage threshold required for ITO reduction. The separation of phosphate salts from the buffered PBS alters the solution's pH, making it crucial to monitor the acidity or alkalinity of each electrolyte. Table 2.2 presents the pH values recorded before and after DA solubilization. All electrolytes, except KH_2PO_4, exhibited neutral to basic pH values initially, with Na_2HPO_4 reaching 9.19. Upon addition of DA, stabilized in hydrochloric acid, the pH decreased in all solutions except PBS,

which maintained a stable value due to its buffering capability. For example, NaCl dropped from 8.18 to 6.36, KCl from 8.14 to 6.34, Na_2HPO_4 to 8.08, and KH_2PO_4 to 4.30.

Electrolyte	**pH**	**pH + DA**
PBS	7.40	7.40
NaCl	8.18	6.36
Na_2HPO_4	9.19	8.08
KCl	8.14	6.34
KH_2PO_4	4.50	4.30

Table 2.2. pH of the electrolyte solution prepared employing PBS and 0.1 M in distilled H_2O of NaCl, Na_2HPO_4, KCl and KH_2PO_4 in the first column. The second column show the pH values of the electrolytes with the addition of DA 10 g/L.

The direct consequence of this pH difference can be visually observed in Figure 2.43, where each electrolyte solution containing DA was left exposed to air for 12 hours. A clear correlation emerges, darker solutions correspond to basic pHs, indicating more advanced spontaneous oxidation of DA into its oligomeric and polymeric forms such as polydopamine. In contrast, the acidic environment of KH_2PO_4 preserves DA in its reduced form and prevents visible darkening. Meanwhile, Na_2HPO_4, with its more basic pH, shows substantial colour development due to enhanced DA auto-oxidation. These results reinforce that pH is a critical parameter in controlling DA oxidation kinetics, and consequently, the reduction of ITO. Alkaline pH environments facilitate DA oxidation which results in a higher ITO reduction rate and lower voltage threshold.

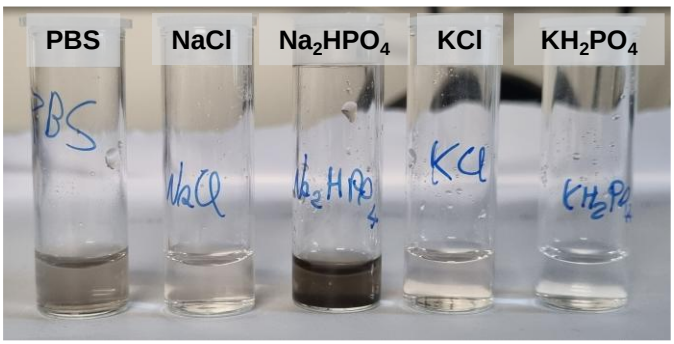


Figure 2.43. Picture of the five electrolyte solutions from left to right: PBS, and 0.1 M of NaCl, Na_2HPO_4, KCl, KH_2PO_4 prepared with the employment of DA 10 g/L, after the self-oxidation in air obtained in 12 hours.

2.16 Reliability tests

i-ECDs planned to be used for monitoring in cold-chain applications must demonstrate consistent functionality under real-world environmental conditions, which often involve

fluctuations in temperature and humidity, mechanical stress during transport, and exposure to sunlight. These displays are designed to play a critical role in monitoring the integrity of sensitive goods such as perishable foods (*e.g.*, dairy), pharmaceuticals, and biological specimens (*e.g.*, blood), where failures in performance can compromise product safety and quality. To assess their suitability, *i*-ECDs were subjected to a series of reliability tests simulating the range of conditions typically encountered in cold-chain logistics. Thermal performance was evaluated across a temperature range from −5 °C to +60°C to verify operational stability under both freezing and elevated ambient temperatures. Key parameters such as ΔT and switching speed were measured to identify any thermal degradation effects or performance drift. Given that packaging in cold-chain distribution is frequently subjected to bending, shock, and compression, mechanical flexibility was also tested. Displays were repeatedly bent with a radius of 5 mm for up to 4000 cycles to ensure that the *i*-ECDs maintained structural and functional integrity during mechanical stress. Moreover, sunlight resistance was evaluated to ensure the stability of the *i*-ECDs in case of brief, unintended exposure. While products for the cold chain are not meant to be exposed to direct sunlight, the *i*-ECDs were tested under simulated sunlight (1000 W/m^2) for 8 hours to confirm a basic level of stability under such conditions.

2.16.1 i-ECDs Bendability study

To assess mechanical durability, *i*-ECDs were subjected to controlled cyclic deformation using a custom-built dynamic 3-point bending tester, as shown in Figure 2.44a. The bending was performed before electrochemical activation, while the *i*-ECDs were still in their initial transparent state. Each display was fixed at both ends, while a central piston imposed repeated mechanical stress with a 5 mm bending radius at 1 Hz. Four *i*-ECDs prepared with DA+AntiOX underwent 250, 500, 1000, and 4000 bending cycles, respectively. Throughout these tests, no significant change in optical transmittance (T@600 nm) was observed, even after 4000 cycles, indicating that the mechanical deformation alone did not compromise optical transparency pre-activation. However, post-activation behaviour revealed evidence of mechanical damage. After applying 1.5 V for 600 seconds to initiate colouration, a distinct vertical line appeared at the site of repeated bending, as shown in Figure 2.44b. This localized feature corresponds to microcracks in the ITO layer induced by *i*-ECDs bending. ITO, while widely used as a transparent conductor, is intrinsically brittle and prone to crack formation under repeated tensile or compressive stress. As demonstrated in the study by Tran et al.[48], such mechanical stress can lead to interfacial and buckling-like delamination, especially under cyclic or

combined loading, which in turn results in increased electrical resistance and disrupted conductivity pathways. In the case of *i*-ECDs, the cracks that formed during bending introduced localized disruption in the conductive ITO layer. Upon activation, this resulted in uneven current distribution and non-uniform EC switching, as evidenced by the uneven colouration observed.

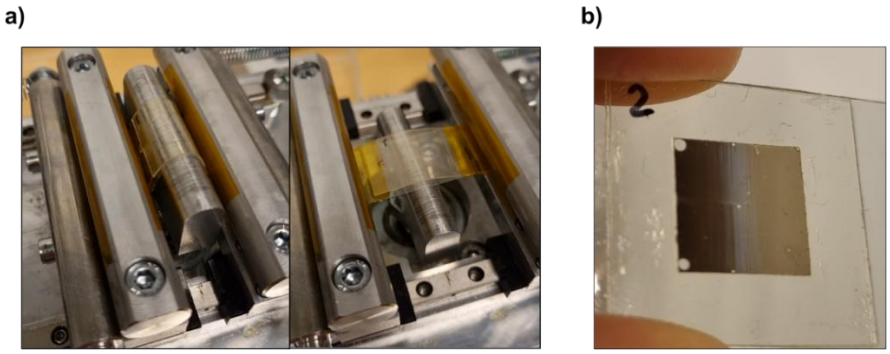


Figure 2.44. a) Pictures of the dynamic 3-point bending machine used to test four *i*-ECDs before activation. Each device underwent 250, 500, 1000, and 4000 bending cycles at a frequency of 1 Hz. b) Picture of the *i*-ECD subjected to 1000 bends after the activation via 1.5 V for 600 s. Vertical rupture lines visible in the region where the bending occurred.

These effects were further confirmed in post-activation optical analysis. As shown in Figure 2.45a, all *i*-ECDs exhibited successful colouration regardless of the number of bends, suggesting that the displays maintained EC functionality even after 4000 cycles. Nonetheless, no clear trend was observed between the number of bending cycles and the ΔT, reinforcing that the EC response was not fully compromised. However, closer inspection of the minimum T@600 nm values revealed deviations from standard behaviour. The T@600 nm post-activation did not exhibit values <10%, as is typical for pristine *i*-ECDs. Instead, the final T@600 nm plateaued around 25%, suggesting incomplete colouration due to compromised electrode performance. Figure 2.45b provides visual confirmation of this effect, showing non-uniform colouration patterns localized around the bending axis, consistent with the mechanical damage previously observed.

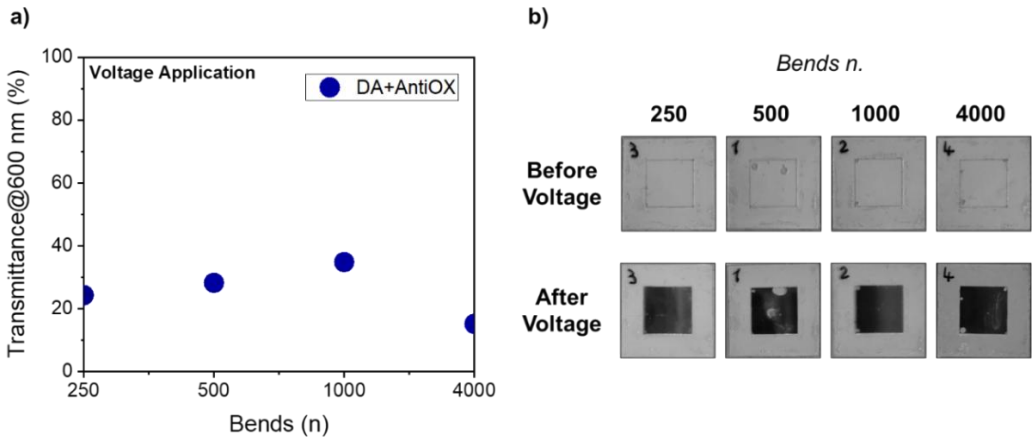


Figure 2.45. a) T@600 nm as a function of the bend number for four *i*-ECDs subjected respectively to 250, 500, 1000 and 4000 bends with the dynamic 3-point bending machine and activated via 1.5 V for 600 s. b) Pictures of the related *i*-ECDs subjected to the bending test. On top, the *i*-ECDs after the bending process while on the bottom the same *i*-ECDs after the activation via 1.5 V for 600 s.

2.16.2 i-ECDs stability under storage at low temperature

Temperature stability tests were conducted in a calibrated thermal chamber capable of maintaining tightly controlled environmental conditions. A total of fifteen *i*-ECDs, prepared using the DA+AntiOX formulation, were placed in the chamber set to 5 °C and 10% relative humidity (RH) for a continuous period of 168 hours. These parameters were selected to replicate cold-chain logistics environments and to evaluate the displays' resilience under prolonged exposure to low temperatures and dry conditions. The experimental setup, including the chamber and the *i*-ECD arrangement, is shown in Figure 2.46. To quantify the effect of storage conditions, the optical transmittance (T@600 nm) of each *i*-ECD was measured both before and after the low-temperature exposure. As illustrated in Figure 2.47a, the average T@600 nm remained unchanged across all fifteen samples, confirming that the *i*-ECDs maintained their optical state and did not undergo spontaneous activation or degradation under these cold conditions.

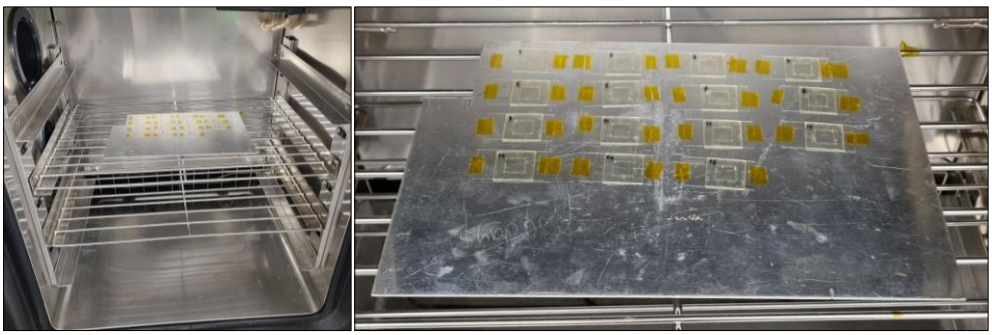


Figure 2.46. Pictures of the temperature and humidity chamber where the fifteen *i*-ECDs prepared with DA+AntiOX were stored for 168 hours at 5°C/10% RH before activation via 1.5 V for 600 s.

Furthermore, to verify that their EC functionality remained entirely functional, the *i*-ECDs were activated at 1.5 V for 600 seconds. The resulting minimum T@600 nm averaged 1.3%, consistent with the expected performance for complete black-state colouration. This demonstrates not only the stability of the *i*-ECDs during storage but also their preserved responsiveness to voltage activation. Visual evidence of uniform colouration and display integrity post-activation is presented in Figure 2.47b, further confirming the robustness of the *i*-ECDs in simulated cold-chain environments.

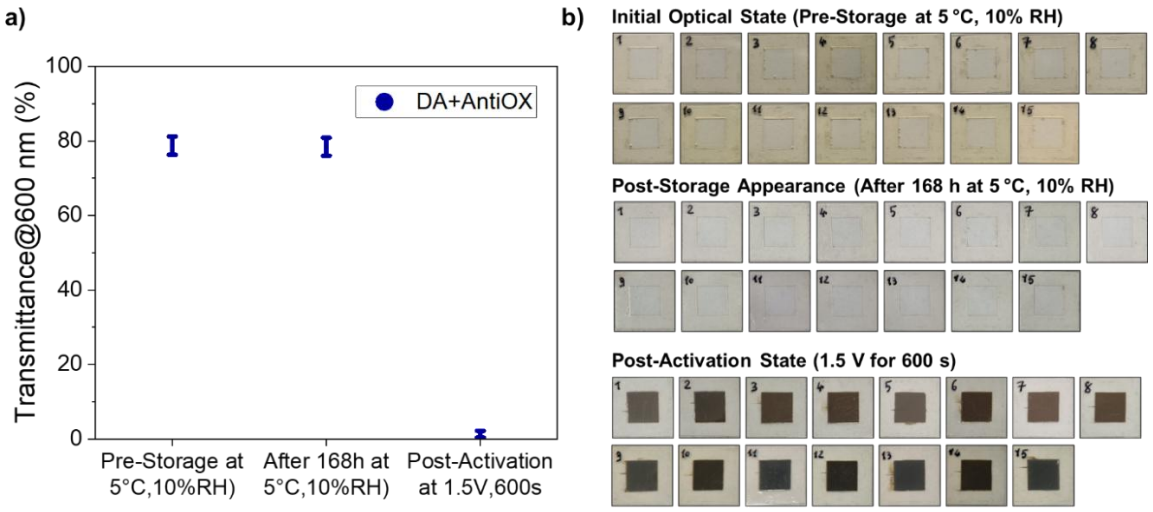


Figure 2.47. a) T@600 nm expressed as the average of fifteen *i*-ECDs before and after the storage inside the temperature and humidity chamber for 168 hours at 5°C/10% RH, empty dots, and after activation via 1.5 V for 600 s, full dot. b) Picture of the related *i*-ECDs before and after the storage and after activation.

2.16.3 i-ECDs activation - temperature tolerance

The thermal stability and activation performance of the DA+AntiOX-based *i*-ECDs were evaluated across a temperature range spanning from -5 °C to 60 °C (-5, 0, 10, 20, 40, and 60 °C). This range was selected to simulate both sub-zero and elevated ambient conditions relevant to real-world applications. The inclusion of -5 °C served to confirm that the formulation does not freeze or exhibit functional degradation below 0 °C. Temperatures of 0 °C and 10 °C were specifically chosen to reflect typical cold-chain environments, supporting the suitability of the displays for refrigerated logistics. Meanwhile, 20 °C, 40 °C, and 60 °C were used to demonstrate the operational versatility of the *i*-ECDs under moderate to high ambient conditions.

Therefore, six groups of three DA+AntiOX-based *i*-ECDs were prepared and each group was exposed to one of the selected temperatures for 1 hour in a temperature-controlled chamber. Following thermal exposure, the displays were activated in situ using an applied voltage of

1.5 V for 600 seconds, while their optical response (T@600 nm) was continuously monitored via optical fiber. As shown in Figure 2.48c, all *i*-ECDs underwent successful switching to the dark state upon activation, regardless of prior temperature exposure. The optical contrast achieved was consistently high, with the transmittance at T@600 nm in the coloured state ranging between 10% and 20%, as reported in Figure 2.48a, confirming robust EC performance across the full temperature range. However, generally, lower ΔT values were detected at temperatures below 0 °C. This phenomenon is closely associated with the ionic conductivity of the electrolyte, which is strongly temperature-dependent. At lower temperatures, both the mobility of ions and the segmental motions of polymer chains are significantly reduced due to stronger interactions between the salt and the polymer matrix. These interactions hinder ion transport, thereby limiting the efficiency of the redox reactions that drive the EC switching. As temperature increases, ionic conductivity improves because these associations weaken, allowing for greater ion mobility and more dynamic polymer chain movement, ultimately enhancing switching performance.[49] The relation between temperature and ionic conductivity is explicated in Figure 2.48b where the T@600 nm of the *i*-ECDs, measured over the activation time, clearly change based on the temperature. The higher the temperature, the faster the drop of T@600 nm.

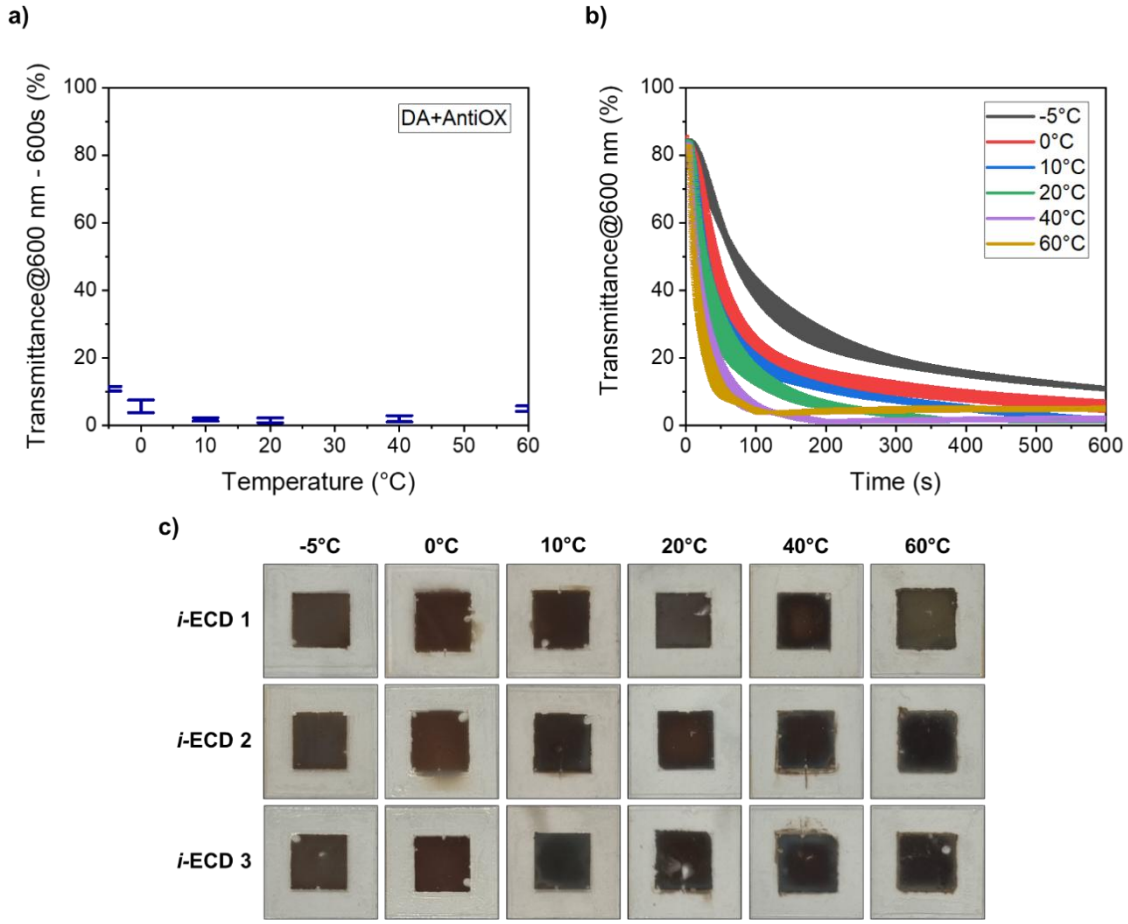


Figure 2.48. a) T@600 nm as a function of the temperature at the end of the activation process for eighteen *i*-ECDs via 1.5 V for 600 s at -5, 0, 10, 20, 40 and 60 °C. b) Single transmittance wavelength evolution as a function of time averaged for three *i*-ECDs for each activation temperature. c) Pictures of the related *i*-ECDs activated via 1.5 V for 600 s at each specific temperature at the end of the process.

2.16.4 i-ECDs stability under solar light exposition

Evaluating the stability of *i*-ECDs under solar radiation is essential for ensuring their reliability during storage, handling, or accidental exposure to ambient light. Solar light contains UV wavelengths capable of being absorbed by DA. This raises a critical concern about whether UV exposure could prematurely oxidize DA, consuming the monomer or triggering unwanted side reactions that degrade the molecule and compromise the EC functionality of the display. To investigate this, five DA+AntiOX-based *i*-ECDs were exposed to simulated sunlight (1000 W/m^2) for 8 hours. As shown in Figure 2.49, T@600 nm was measured before and after exposure. The results revealed no significant variation in the optical state of the *i*-ECDs, indicating that solar irradiation did not trigger spontaneous DA oxidation or visible degradation of the EC layer. Subsequently, the same displays were activated at 1.5 V for 600 seconds. All *i*-ECDs exhibited a strong and consistent switching response, reaching a minimum T@600 nm close to 0%, corresponding to a ΔT of approximately 80%. These findings confirm the stability

of DA even after extended solar exposure, and that the formulation demonstrates excellent UV resistance.

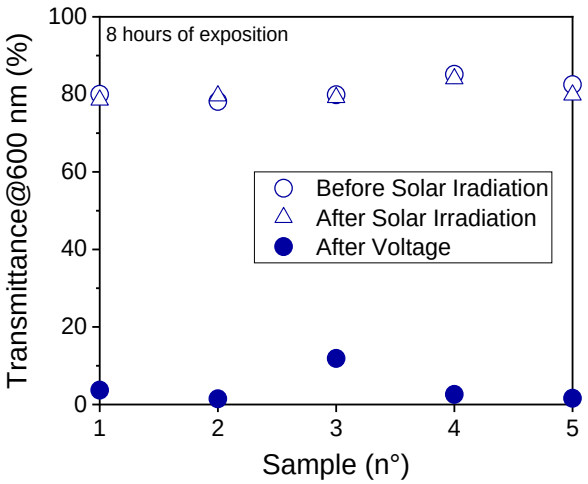


Figure 2.49. T@600 nm recorded for five *i*-ECDs prepared with DA+AntiOX before and after 8 hours irradiation with a solar lamp and after the application of 1.5 V for 600 s.

2.17 DA functionalization

To explore ways to control how quickly the *i*-ECD activates, how much voltage it needs to switch, and what initial colour it displays, we decided to chemically modify DA by attaching different functional groups to its aromatic ring. The idea was to see how changing the electronic properties of the monomer would affect the overall behaviour of the *i*-ECD. We focused on adding either electron-donating groups (EDGs), like a methoxy group ($-OCH_3$), or electron-withdrawing groups (EWGs), such as nitro ($-NO_2$) or chloro ($-Cl$) groups. These modifications are known to influence how easily DA can be oxidized. EDGs push electron density toward the aromatic ring, which can stabilize the positive charge formed upon oxidation, making the oxidation process energetically more favourable and thus lowering the oxidation potential. In contrast, EWGs pull electron density away from the ring, making the oxidized species less stable and requiring a higher potential to achieve oxidation.[50–52]

Since the oxidation of DA is directly linked to the reduction of the ITO electrode in our system, shifting the oxidation potential of the monomer should also influence the reduction potential of the ITO, and therefore when the display switches colour. Based on the behaviour of unmodified DA, we hypothesized that functionalizing it with EDGs would lower its oxidation potential, making it easier to oxidize and thus allowing ITO to reduce at lower applied voltages. On the other hand, EWGs would raise DA oxidation potential, making it harder to oxidize and

requiring higher voltages to activate the *i*-ECD. To test this, we synthesized and characterized three modified DA molecules, specifically methoxydopamine (OMeDA),[53] chlorodopamine (ClDA),[54] and nitrodopamine (NO_2DA).[55] We then analysed their electrochemical and optical behaviour using spectroelectrochemical methods to understand how these modifications influence the performance of the *i*-ECDs.

2.17.1 Methoxydopamine

The first functionalization step involved the synthesis of OMeDA, whose chemical structure is shown in Figure 2.50. This molecule was obtained through a three-step synthetic route (detailed in Scheme S3–S5), yielding a whitish powder that, like DA, forms a transparent solution in PBS at pH 7.4. The synthesis involved a copper-catalysed hydroxylation of 5-bromovanillin under basic aqueous conditions and microwave heating, affording the catechol derivative (1) in 66% yield. This intermediate was then subjected to a one-pot reaction. First, the phenolic hydroxyl groups were protected via benzylation using benzyl bromide and potassium carbonate in DMF. Subsequently, the nitrovinyl chain was introduced via condensation with nitromethane in acetic acid, yielding compound (2) in 50% overall yield for the two steps. Finally, catalytic hydrogenation of compound (2) under a hydrogen atmosphere in the presence of Pd/C and HCl reduced the nitro group to a primary amine and simultaneously removed the benzyl protecting groups, giving the target molecule OMeDA in 21% yield after purification by HPLC.

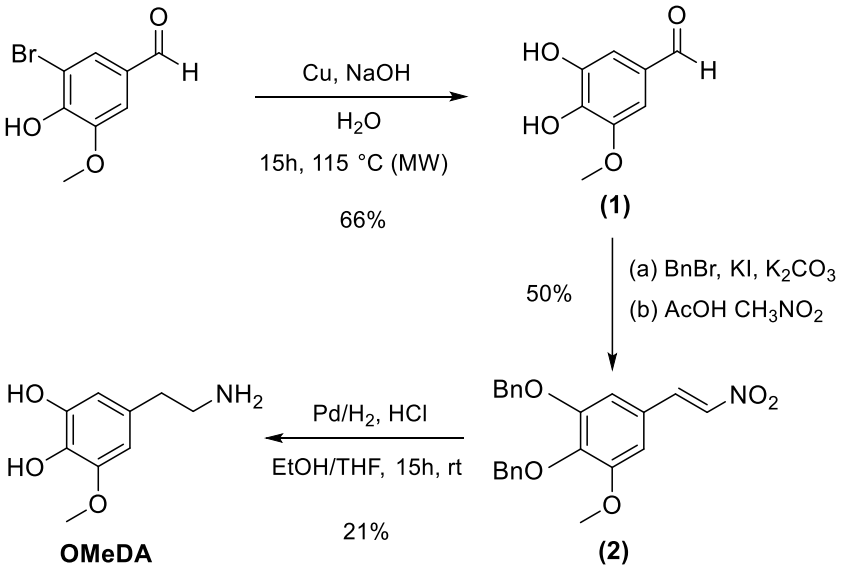


Figure 2.50. Synthesis of OMeDA.

To test the hypothesis that introducing a methoxy group could lower the oxidation potential, a CV was performed on a 10 g/L solution of OMeDA in PBS at pH 7.4. The resulting

voltammogram, shown in Figure 2.51a, displays an oxidation peak at 0.36 V, corresponding to the formation of quinone species. In comparison, the voltammogram of DA (Figure 2.51b) shows the oxidation peaks with higher potential (>0.40) V. This difference in oxidation potential confirms the expected effect of the methoxy substitution. As aforementioned, the methoxy group (–OCH_3) is known to act as EDG, which modifies the electronic distribution on the aromatic ring. Through both inductive and resonance effects, it donates electron density to the catechol system, increasing the electron richness of the ring. This higher electron density facilitates the oxidation process by stabilizing the intermediate radical cation and lowering the energy barrier for electron subtraction. In particular, the carbon atoms adjacent to the –OCH_3 group become less electron-deficient, making oxidation more favourable.[56–58] Consequently, OMeDA exhibits a lower oxidation potential than DA, as predicted.

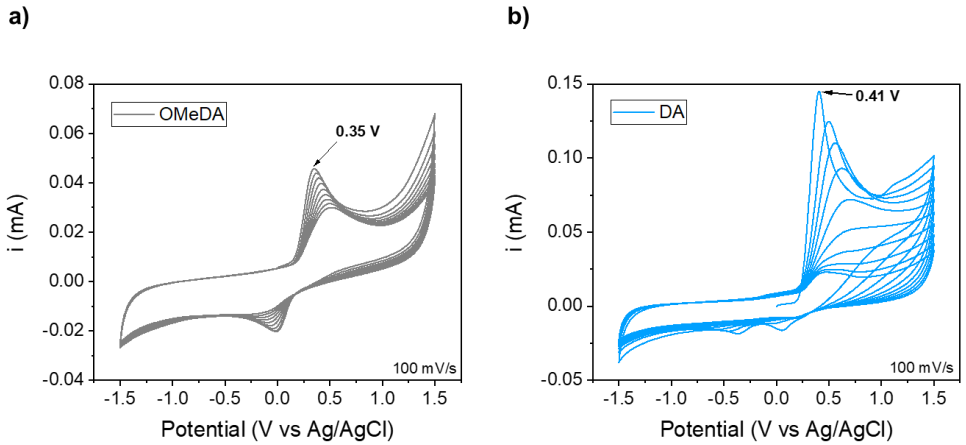


Figure 2.51. Cyclic voltammetry carried out between ±1.5 V at 100 mV/s for a solution of a) OMeDA 10 g/L, b) DA 10 g/L in PBS pH 7.4 with three-electrodes setup.

To further investigate whether the observed reduction in oxidation potential of the OMeDA correlates with a lower reduction potential of the ITO electrode, a voltage-triggered test on *i*-ECDs was conducted. Specifically, six displays were fabricated, each containing 10 g/L of OMeDA in PBS at pH 7.4, and subjected to a voltage ramp from 0.5 to 3.0 V over 600 seconds. As shown in Figure 2.52a, no significant decrease in T@600 nm was observed for voltages below 1.0 V, consistent with previous findings using DA. However, for voltages above 1.25 V, a marked drop in transmittance was detected. Importantly, at the end of the activation process, the OMeDA-based *i*-ECD exhibited a T@600 nm of just 11.7%, whereas the DA-based display, under the same conditions, reached 45.7%. This substantial difference is attributable to the lower oxidation potential of OMeDA which as consequent drops the ITO reduction potential.

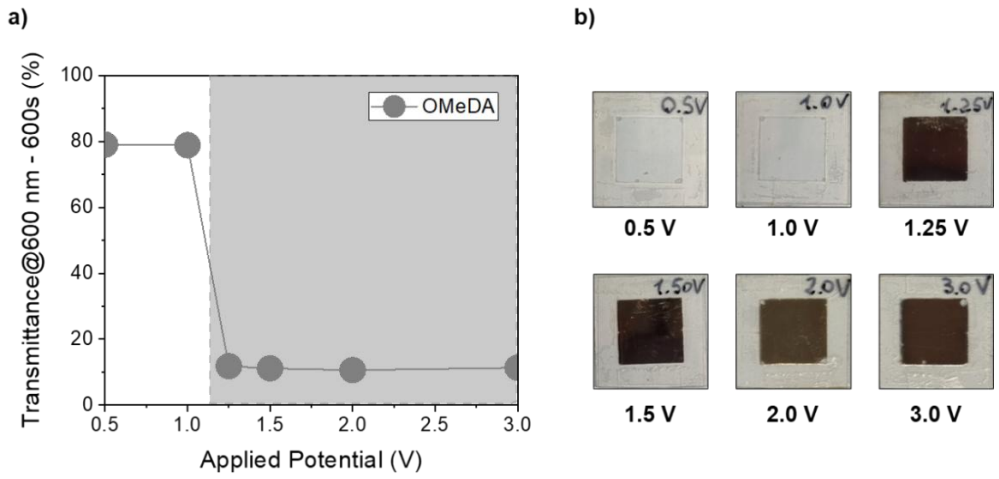


Figure 2.52. a) T@600 nm recorded after activation by applying a voltage ramp for 600 s on six *i*-ECDs prepared with OMeDA 10 g/L in PBS pH 7.4. The optimal operating parameters for an *i*-ECD are indicated in the highlighted grey area. b) Images of the *i*-ECDs after their activation via a ramp of applied potential.

Given the lower oxidation potential of OMeDA compared to DA, it was of particular interest to determine whether this would lead to a faster darkening of the *i*-ECD during activation. To explore this, two *i*-ECDs containing OMeDA at a concentration of 10 g/L in PBS pH 7.4 were prepared and activated at constant voltages of 1.5 V and 3.0 V for 180 seconds. During the activation process, photographs were taken at specific time intervals to monitor the progression of the EC response, as shown in Figure 2.53.

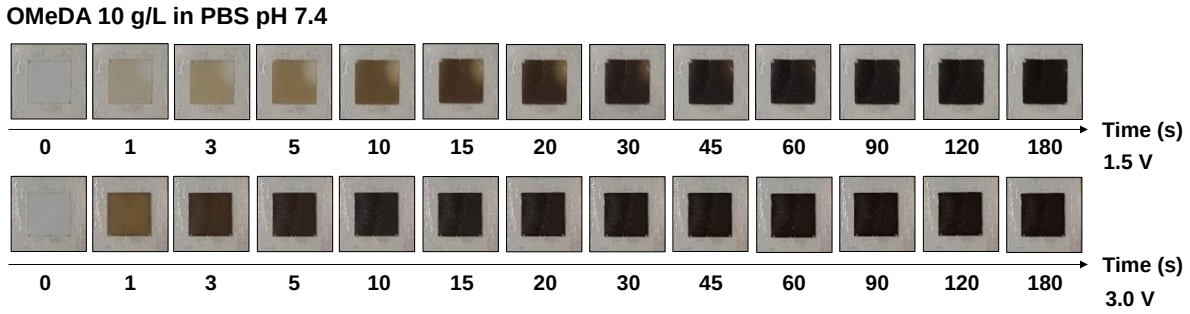


Figure 2.53. Frames extracted from a video recording depicting two *i*-ECDs, manufactured employing OMeDA 10 g/L in PBS pH 7.4. These frames capture the activation process, conducted at both 1.5 V and 3.0 V.

The overall trend in colour change is comparable to that observed in DA-based systems. Both OMeDA displays show a gradual decrease in transmittance over time, progressively darkening as the voltage is applied. As with DA, applying a higher voltage (3.0 V vs 1.5 V) results in faster ITO reduction and more rapid darkening of the display. However, based on the previously discussed results at 1.25 V, where OMeDA reached a T@600 nm of just 11.7%, compared to 45.7% for DA, the data strongly suggest that OMeDA allows for a more efficient EC response. This indicates that, even if the visual kinetics appear similar, OMeDA-based *i*-

ECDs may achieve higher contrast quickly, particularly when operating near threshold voltages.

2.17.2 Chlorodopamine

The second functionalization step introduced a chlorine substituent, yielding ClDA, as shown in Figure 2.54. This compound was synthesized via a one-step electrophilic aromatic substitution (see Scheme S2 for detailed conditions). The reaction was performed by adding N-chlorosuccinimide (NCS) to a solution of dopamine hydrochloride (DAHCl) in trifluoroacetic acid (TFA). After stirring at room temperature for 15 hours, the mixture was concentrated under a stream of argon to give a crude oily residue. Purification by flash chromatography afforded ClDA as its trifluoroacetate salt in 29% yield. The pale yellow solid was readily soluble in PBS at pH 7.4, forming a clear solution.

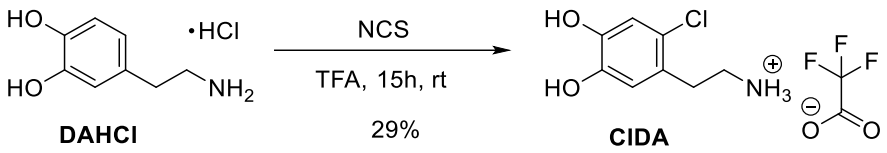


Figure 2.54. Synthesis of ClDA.

Electrochemical analysis was performed on a 10 g/L solution of ClDA in PBS pH 7.4, and the resulting cyclic voltammogram is shown in Figure 2.55. An oxidation peak associated with the formation of quinone species appears at 0.42 V. This value is nearly comparable to the oxidation potential of DA (approximately 0.41 V), yet notably higher than that observed for OMeDA (0.36 V). The shift toward a higher oxidation potential in ClDA is attributed to the presence of the chlorine atom, which acts as an EWG. These substituents are known to exercise an inductive effect that pulls electron density away from the ring system. This reduction in electron density makes the oxidation process, specifically the removal of electrons from the catechol moiety, less favourable, thereby increasing the energy required for oxidation and shifting the oxidation potential to higher voltages.

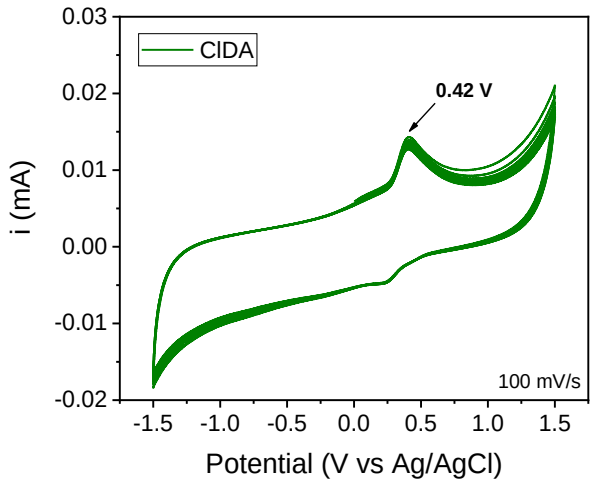


Figure 2.55. Cyclic voltammetry carried out between ±1.5 V at 100 mV/s for a solution of ClDA 10 g/L in PBS pH 7.4 with three-electrodes setup.

To evaluate the effect of chlorine functionalization on the reduction potential of the ITO electrode, a threshold voltage test was performed using eleven *i*-ECDs containing ClDA at 10 g/L in PBS pH 7.4. Each device was subjected to a voltage ramp ranging from 0.5 to 3.0 V for 600 seconds. As shown in Figure 2.56a, no significant change in T@600 nm was observed for voltages below 1.0 V, consistent with the behaviour previously reported for both DA- and OMeDA-based *i*-ECDs. When a voltage of 1.25 V was applied, the ClDA-based *i*-ECDs exhibited a T@600 nm drop reaching a minimum value of 20.9% by the end of the activation process. This transmittance is notably higher than the 11.7% recorded for OMeDA under the same conditions, but still lower than the 45.7% observed for DA. These results suggest that the presence of the chlorine substituent slightly facilitates oxidation compared to unsubstituted DA, resulting in a more significant degree of ITO reduction and thus a higher display contrast.

The observed trend can be rationalised by considering the electronic effects of the chlorine atom. As a halogen, chlorine exercises a strong inductive electron-withdrawing effect due to its high electronegativity, which tends to stabilise the oxidised form of the molecule. At the same time, chlorine can participate in resonance donation through its lone pairs when attached to an aromatic ring, partially compensating the inductive withdrawal.[59,60] The combination of these opposing effects results in a net moderate electron-donating influence, which slightly increases the molecule's electron density compared to DA, making oxidation slightly more favourable. However, chlorine's resonance donation is considerably weaker than the effect provided by the methoxy group in OMeDA, which explains why ClDA-based *i*-ECDs do not reach the same level of contrast. Figure 2.56b further confirms that, at voltages above 1.5 V,

the ClDA-based displays achieve full darkening with optical contrast and colouration similar to those observed in previous systems.

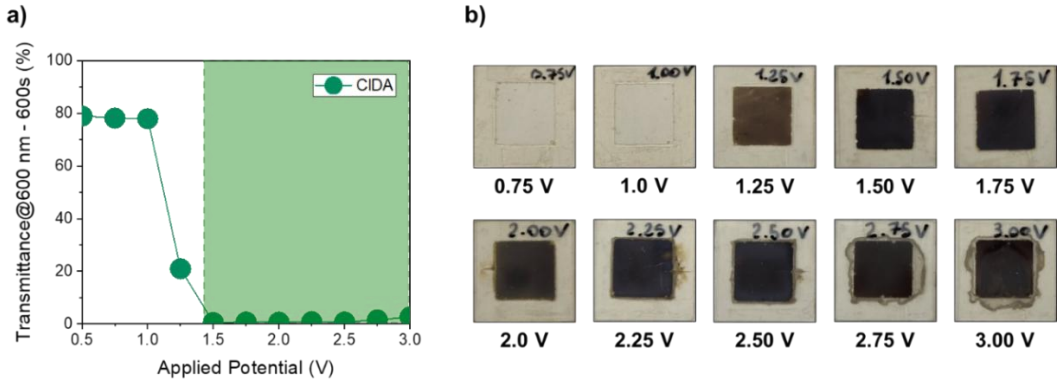


Figure 2.56. T@600 nm recorded after activation by applying a voltage ramp for 600 s on eleven *i*-ECDs prepared with ClDA 10 g/L in PBS pH 7.4. The optimal operating parameters for an *i*-ECD are indicated in the highlighted green area. b) Images of the *i*-ECDs after their activation via a ramp of applied potential.

Additionally, the colour change kinetics further support the previously discussed observations. As shown in Figure 2.57, analysis of the time-lapse frames shows no noticeable differences in the rate of colour evolution among *i*-ECDs based on DA, ClDA, and OMeDA. Although ClDA exhibits a slightly lower oxidation potential than DA, this does not result in a visibly faster reduction of the ITO electrode.

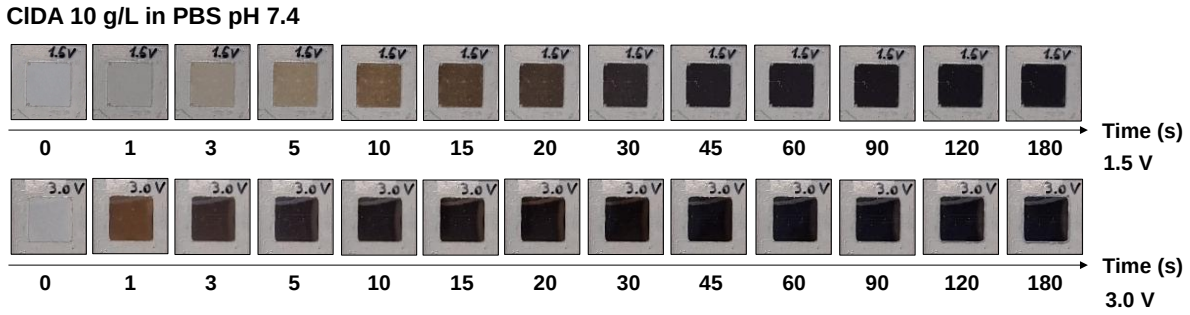


Figure 2.57. Frames extracted from a video recording depicting two *i*-ECDs, manufactured employing ClDA 10 g/L in PBS pH 7.4. These frames capture the activation process, conducted at both 1.5 V and 3.0 V.

2.17.3 Nitrodopamine

NO_2DA concludes the series of functionalization tests and, like ClDA, was synthesised starting from DAHCl. In this case, the target compound was obtained via a one-step nitration reaction, as outlined in Figure 2.58. The process yielded a yellow powder that required no further purification. When dissolved in PBS at pH 7.4, NO_2DA forms a distinctly yellow solution, imparting a characteristic tint to the resulting *i*-ECDs. However, its solubility in PBS is limited

due to the formation of sulfonate-containing salts during nitration, which can lead to insoluble complexes and lower the effective concentration. The synthesis involved dissolving DAHCl and sodium nitrite in water, followed by the slow addition of concentrated sulfuric acid under cooling (0–5 °C). A yellow precipitate formed within 20 minutes, which was collected by filtration, washed with cold water and methanol, and dried under reduced pressure. The crude product was used directly, affording NO_2DA as its sulfonate salt in 81% yield.

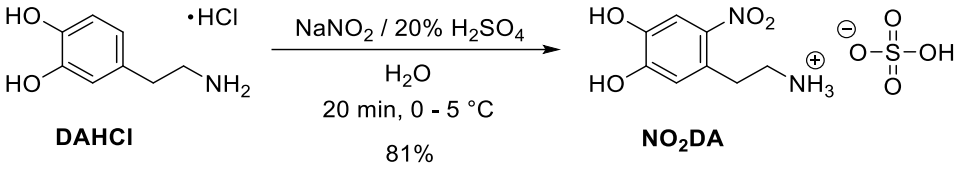


Figure 2.58. Synthesis of NO_2DA.

The electrochemical characterization of NO_2DA was carried out using CV at a concentration of 1 g/L in PBS (pH 7.4). The resulting voltammogram, shown in Figure 2.59, reveals a clear anodic peak at 0.52 V, which is shifted to a higher potential compared to the oxidation peaks of DA and its functionalized derivatives. This shift is consistent with the strong electron-withdrawing effect of the nitro group (–NO_2), which reduces the electron density on the aromatic ring and makes the oxidation process less favourable. Consequently, a higher potential is required to form the corresponding quinone species, confirming the expected influence of EWGs on the redox behaviour. The voltammogram also shows that the redox process is not reversible, as no well-defined reduction peak is observed. Additionally, a minor feature near 0.1 V, similar to that observed in the voltammogram of DA, may arise from residual monomer or related electroactive impurities, as NO_2DA was obtained via a direct nitration process without chromatographic purification.

The limited solubility of NO_2DA in PBS arises from a combination of structural and electronic factors. One key reason is the formation of the sulfonate salt during the nitration process. The reaction yields a protonated amine paired with a bisulfate counterion (HSO_4^-). This salt dissociates poorly in PBS, a buffer already rich in ions such as Na^+ and Cl^-, thereby reducing its ability to dissolve effectively in the aqueous medium. Furthermore, although the nitro group (–NO_2) is a strong EWG substituent and significantly affects redox behaviour, its associated species, the nitronium ion (NO_2^+), is structurally nonpolar. This nonpolarity arises from its linear geometry and symmetric bonding. The two N=O bonds have a small electronegativity difference (approximately 0.4), and the molecular symmetry causes the dipole moments of the bonds to cancel each other out, resulting in no overall dipole moment.[61,62] Together, the poor dissociation of the sulfonate salt and the nonpolar character of the NO_2^+ substituent reduce the

overall hydrophilicity of NO_2DA, leading to significantly lower solubility in PBS compared to DA, ClDA, and OMeDA, all of which exhibit good aqueous solubility due to their smaller and polar structures.

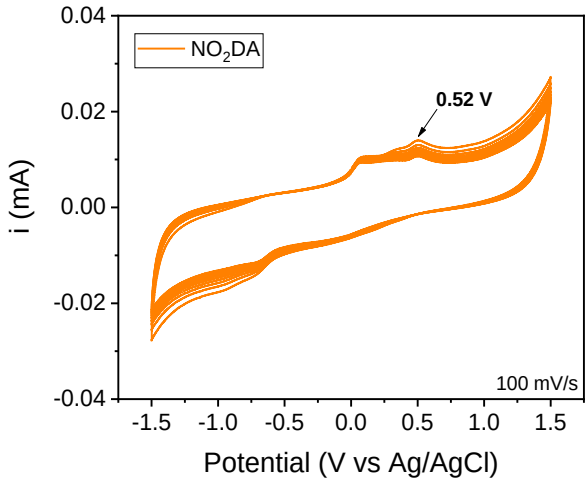


Figure 2.59. Cyclic voltammetry carried out between ±1.5 V at 100 mV/s for a solution of NO_2DA 1 g/L in PBS pH 7.4 with three-electrodes setup.

To evaluate the influence of NO_2 functionalization on ITO reduction, a threshold voltage test was conducted on eight *i*-ECDs containing NO_2DA at 1 g/L in PBS. The displays were subjected to a voltage ramp from 1.5 V to 5.0 V for 600 seconds. As shown in Figure 2.60a, no significant change in T@600 nm was observed for voltages between 1.5 V and 3.0 V, indicating a complete absence of EC activation within this range. This behaviour stands in contrast to DA-, ClDA-, and OMeDA-based *i*-ECDs, which readily switch under a 1.5 V reaching a T@600 nm very close to 0%. Interestingly, at voltages ≥3.5 V, a gradual decrease in T@600 nm is observed, becoming more pronounced at 4.5 V (T@600 nm = 46.6%) and 5.0 V (T@600 nm = 19.5%). However, this colour change, associated with the reduction of the ITO, would have occurred even in the absence of NO_2DA. This was clearly demonstrated by the control experiment using *i*-ECDs containing only PBS, which exhibited the same trend, Figure 2.14. No response at low voltages, in contrast to the immediate and significant optical response seen with DA-based *i*-ECDs. In the PBS-only system, colour change begins only at voltages above 4.0 V, where the applied potential becomes sufficient to reduce ITO even without the presence of an electroactive species which could oxidize, balancing the reduction.

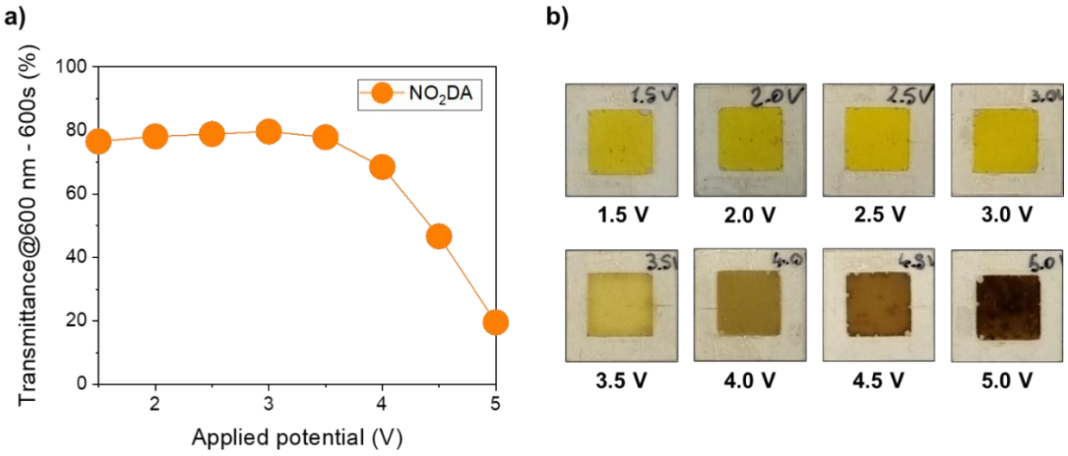


Figure 2.60. a) T@600 nm recorded after activation by applying a voltage ramp for 600 s on eight *i*-ECDs prepared with NO_2DA 1 g/L in PBS pH 7.4. b) Images of the *i*-ECDs after their activation via a ramp of applied potential.

This interpretation is further supported by the visual appearance of the activated *i*-ECDs, shown in Figure 2.60b. The resulting displays exhibit a brownish hue with low contrast, markedly different from the deep black achieved with DA, ClDA, or OMeDA. The poor optical modulation confirms that, while ITO undergoes reduction at high voltages, the NO_2DA molecule cannot effectively participate in the redox cycle. These results confirm, as speculated, that the insertion of the $-NO_2$ strongly inhibits the activation of *i*-ECDs hindering the oxidation process of NO_2DA which drastically increase the reduction potential of the ITO.

Table 2.3 summarizes the results obtained from the substitutions made to the DA molecule. Although the trend is not entirely linear or unambiguous, it is possible to observe that EWGs tend to increase the oxidation potential of DA, whereas EDGs decrease it, in accordance with our hypothesis.

Molecule	**Substituent**	**Type of Group**	**E_{pa} (V vs Ag/AgCl)**
DA	-	Reference	+0.41
OMeDA	$-OCH_3$	Electron-donating (+M)	+0.35
ClDA	–Cl	Moderate electron-donating (-*I*,+M)	+0.42
NO_2DA	$-NO_2$	Electron-withdrawing (-M)	+0.52

Table 2.3. Recap table summarizing substituents, their electronic effects, and anodic peak potentials (E_{pa}) vs Ag/AgCl, where +M: Mesomeric (resonance) donating effect; –I: Inductive withdrawing effect.

This trend can be visualised in the threshold voltage required to reduce the ITO for each substituted monomer. Specifically, Figure 2.61a shows the current response recorded during the activation of the *i*-ECDs. The onset of the ITO reduction process is indicated by a sharp increase in current, signalling the beginning of the redox process. Among the tested molecules,

OMeDA exhibits the lowest reduction threshold for the ITO at 1.30 V, in line with previous experimental observations. DA and ClDA follow closely, with very similar ITO threshold voltages of 1.35 V and 1.37 V respectively, reflecting their comparable oxidation potentials. This correspondence is also visually confirmed by the black contrast of the *i*-ECDs at the end of the potential scan (from 0 to 5 V) shown in Figure 2.61b. Finally, NO_2DA requires a significantly higher onset voltage for ITO reduction, observed at approximately 3.95 V. While this behaviour is attributed to the strong electron-withdrawing effect of the nitro group, which makes the oxidation of the monomer more difficult, a considerable contributing factor is the lower concentration of NO_2DA in the electrolyte solution in comparison to the other monomers. As previously discussed, the poor solubility of NO_2DA in PBS, due to the formation of sulfonate salts and the limited polarity of the nitro group, results in a lower availability of active species within the *i*-ECDs.

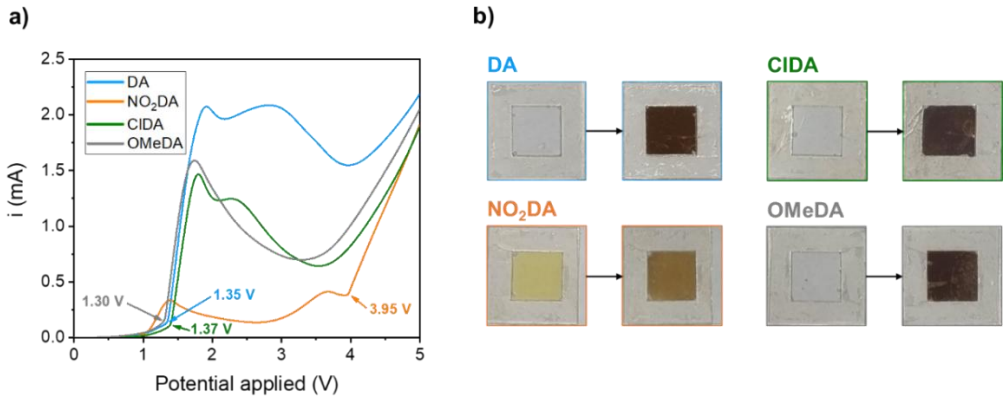


Figure 2.61. a) Registered current as function of potential applied from 0 to 5.0 V with scan rate of 100 mV/s for four *i*-ECDs prepared employing 10 g/L of DA, 1 g/L of NO_2DA, 10 g/L of ClDA and 10 g/L of OMeDA in PBS pH 7.4. b) Images of the *i*-ECDs after their activation via a ramp of applied potential.

2.18 *i*-ECDs design

Following the chemical development of the EC compounds, attention was directed toward the design and external customization of displays to broaden their practical applications. The ability to tailor the visual appearance of *i*-ECDs is critical across multiple fields, improving aesthetic value and functional utility. In sectors such as monitoring and diagnostics, integrating specific, intuitive designs into displays allows for faster and more accessible interpretation of information, thereby improving operational efficiency.

Thanks to the flexibility of the current *i*-ECD production process, design customization can be readily implemented to meet specific application requirements. This is achieved by pre-cutting NITTO double-sided tape into desired shapes using a precision cutting machine. After cutting, the standard assembly procedure described earlier in this chapter is followed to complete the *i*-ECD. Figure 2.62 showcases several examples. Design 1 illustrates a bunch of grapes intended for wine monitoring, Design 2 features a simple cross, and Design 3 depicts a blood bag design tailored for blood monitoring. An alternative and innovative customization method is presented in Design 4, which displays the logo of our research group. In this approach, the NITTO tape maintains its conventional square format, and the desired pattern is instead cut onto a sticker mask. This sticker mask is applied onto the ITO electrode, and a transparent, non-conductive material, nail polish in the specific case, is sprayed over the surface. After spraying, the sticker mask is carefully removed, exposing an uncoated region beneath. The *i*-ECD is then closed following the usual protocol. Upon applying voltage, it is essential to correctly set the polarity by selecting the ITO electrode with the planned design as the C.E. In this way, the reduction of ITO, responsible for the colour change, will occur only in the intended areas, revealing the design.

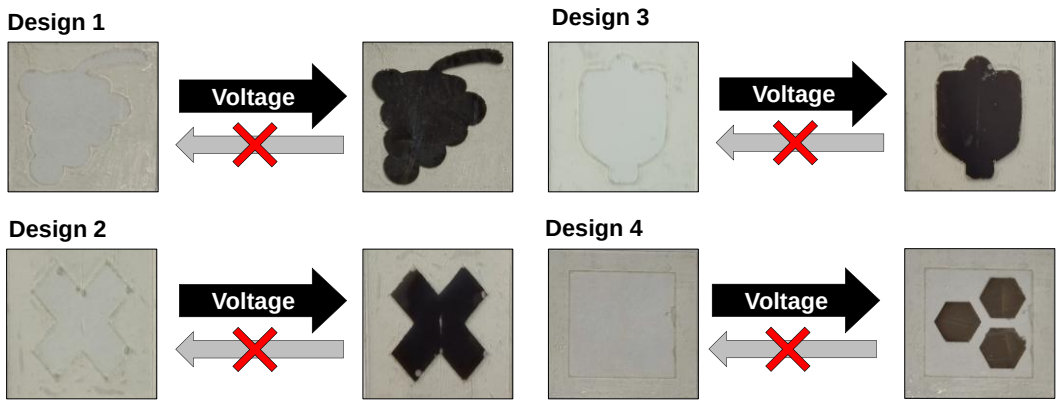


Figure 2.62. *i*-ECDs featuring various design.

The concept behind Design 5, which enables the temporary display of codes that disappear, offers significant potential for applications requiring secure and time-sensitive information, Figure 2.63. This technology can be particularly useful for generating temporary access codes, time-limited authentication tokens, or any situation where controlled, transient visibility of information is the key. The ability to reveal and then hide codes on demand provides a versatile solution for enhancing privacy and access control. The working principle is similar to that of Design 4, with a essential change. During assembly, the C.E., where the code is designed, must be positioned at the bottom, behind the W.E. This configuration ensures that upon application of a positive voltage, the code becomes visible as the C.E. undergoes reduction everywhere

except where the electrode was passivated with the specific code design. Subsequently, by inverting the polarity, the electrode on top of the *i*-ECD, can be reduced permanently hiding the code.



Figure 2.63. *i*-ECD featuring a hidden design of a numerical code that appears only once and permanently disappears once the voltage polarity is reversed.

Finally, in Design 6 a QR code appears upon the application of voltage, Figure 2.64. The working principle is the same of the previous *i*-ECD with the remarkable distinction that this particular prototype showcases an extended area exceeding 100 cm^2, significantly higher than earlier *i*-ECDs. This not only highlights the adaptability of the technology to complex designs but also underscores the flexibility to tailor *i*-ECD size based on specific applications, proving that standard dimensions beyond the 1-10 cm^2 displays areas pose no limitations.

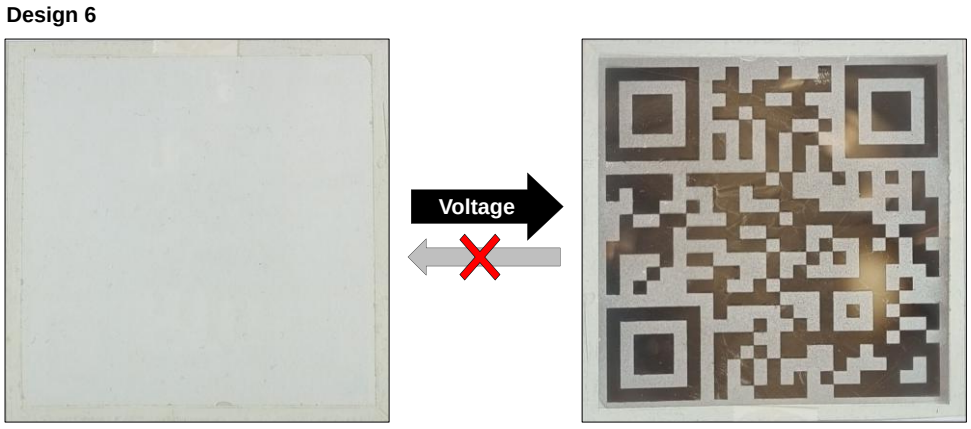


Figure 2.64. *i*-ECD featuring a hidden design of a QR code that appears through voltage application.

2.19 Integration: CHARISMA smart label prototype for cold-chain applications

The integration of our *i*-ECDs into smart labels has consistently held a prominent position on the task list since the start of the study. Real-world working tests play a crucial role in validating the functionality of the *i*-ECDs when interfaced with other electronic components. This step is fundamental in bringing our prototype closer to real market applications in the field of smart labels, particularly those employed in cold chain monitoring. To this end, a series of integration tests were conducted, ranging from preliminary assessments to the comprehensive linkage of essential components for smart label manufacturing. This innovation extends beyond conventional labelling by incorporating Internet of Things (IoT) capabilities.[63]

The first integration was performed independently completely relying on commercial devices and is illustrated in Figure 2.65. Specifically, the *i*-ECD was linked to the output pins of Arduino, serving as the CPU, which, in turn, was connected to a temperature sensor. The entire system was enclosed within a thermal chamber and connected to the power supply via a cable. A C++ code was written to set the threshold temperature at 26 °C. Upon surpassing this threshold read through the temperature sensor (T-sensor), the CPU delivered *ca.* 5.0 V to the *i*-ECDs prompting a quick colour transition from transparent to black. This demonstration showcased the feasibility of activation not only through laboratory potentiostat but also through compact devices suitable for integration into smart labels.

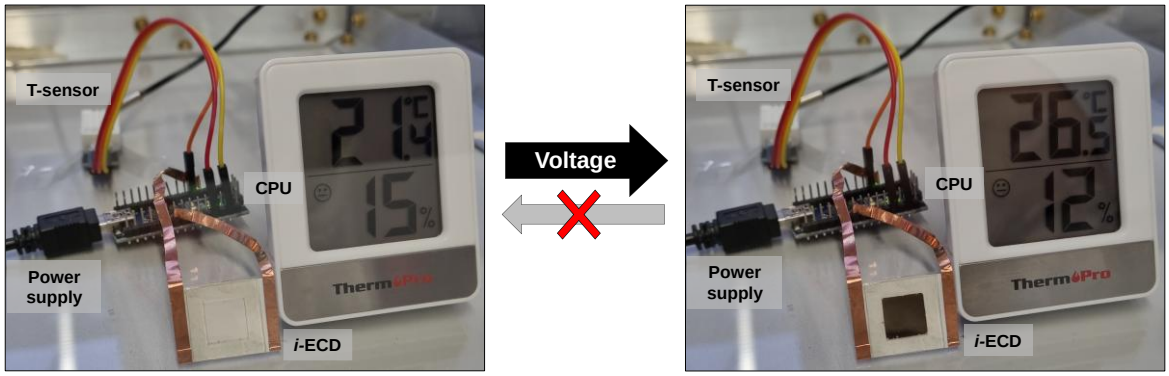


Figure 2.65. Rough smart label rough prototype assembled with the *i*-ECD, a CPU (Arduino nano), a temperature sensor and the power supply before and after *i*-ECD activation. Temperature threshold for *i*-ECD activation set to 26 °C.

In contrast to the first configuration, the second integration utilized prototype components developed within the CHARISMA project. The supercapacitors (SCs) and system connection were realized by Hamed Pourkheirollah, while the temperature sensor was developed by Sunil Kumar Behera. Figure 2.66 illustrates the sequential connection of the *i*-ECD to three SCs, which act as the power source, along with a non-electronic temperature sensor. A key feature of this setup is the complete absence of a CPU for triggering. Activation occurs directly through

a physical change at a specific, tunable temperature. This not only simplifies the system but also represents a significant advantage in terms of cost reduction and manufacturing simplicity for the smart label. Additionally, in recent years, the demand for CPUs has skyrocketed, resulting in limited availability, making this CPU-free solution even more valuable.[64] In this configuration, the three SCs, composed of two aluminium plates coated with PET, can deliver a maximum output of 1.2 V each, a limitation dictated by the water-based electrolytes employed. Nevertheless, the SCs are rechargeable, allowing for multiple uses. Similarly, the T-sensor is reusable, allowing the system to be reset and operated multiple times. It consists of two PET-ITO electrodes filled with a mixture of carbon nanotubes and hexadecanol in hexadecane. Upon freezing, this mixture undergoes a conductivity drop, enabling current flow and thereby activating the *i*-ECD connected in series.

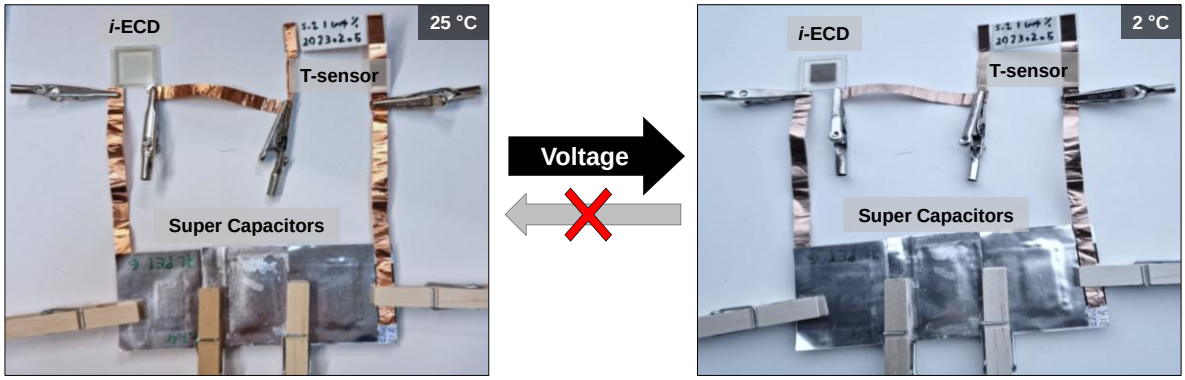


Figure 2.66. Rough CHARISMA smart label prototype assembled connecting the *i*-ECD, the temperature sensor and three super capacitors connected in series before and after *i*-ECD activation.

Figure 2.67 shows the evolution of the electrical resistance of the T-sensor as a function of time, highlighting three distinct regions. The red "OFF state" area is observed at temperatures above approximately 10 °C, where no current can flow in the circuit due to the high electrical resistance, around $10^8\ \Omega$. In this region, the electrical resistance is too high and, with the potential difference applied by the three SCs (approximately 3.6 V), the current cannot flow through the system. As a result, the *i*-ECD cannot turn colour and it will remain transparent. As the temperature decreases, the system enters the blue "Transition state." In this region, the electrical resistance shows a significant drop, reaching values around 10 °C in the range of 10^7–$10^6\ \Omega$. This decrease allows the current to start flowing through the system. When the temperature further drops to approximately 5 °C, the system transitions into the green "ON state," where the resistance reaches its minimum value (around $10^5\ \Omega$). This low resistance enables sufficient current flow through the circuit, allowing the *i*-ECD to switch colour. At the current research stage, the entire smart label is significantly constrained by the T-sensor, with its ON and OFF states highly dependent on the specific materials used, particularly the solvents.

Additionally, the sensor's resistance decreases and permits current flow only during cooling, not heating. Further investigation will be required to reverse this behaviour and enable the sensor to detect temperature increases, making it suitable for cold-chain monitoring applications.

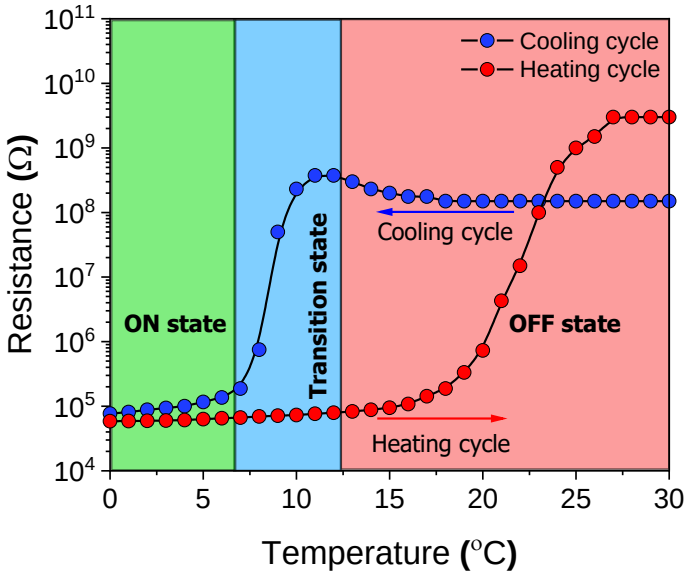


Figure 2.67. Electrical resistance as function of temperature of the T-sensor integrated into the CHARISMA smart label for a heating and cooling cycle from 0 to 30 °C (2.5 °C/min).

Following that, in collaboration with Ynvisible GmbH, the components were interconnected using printed silver traces and fully encapsulated between PET sheets, as shown in Figure 2.68. This lamination ensures mechanical stability, environmental protection, and preserves the label's flexibility and transparency, resulting in a compact and robust smart device.

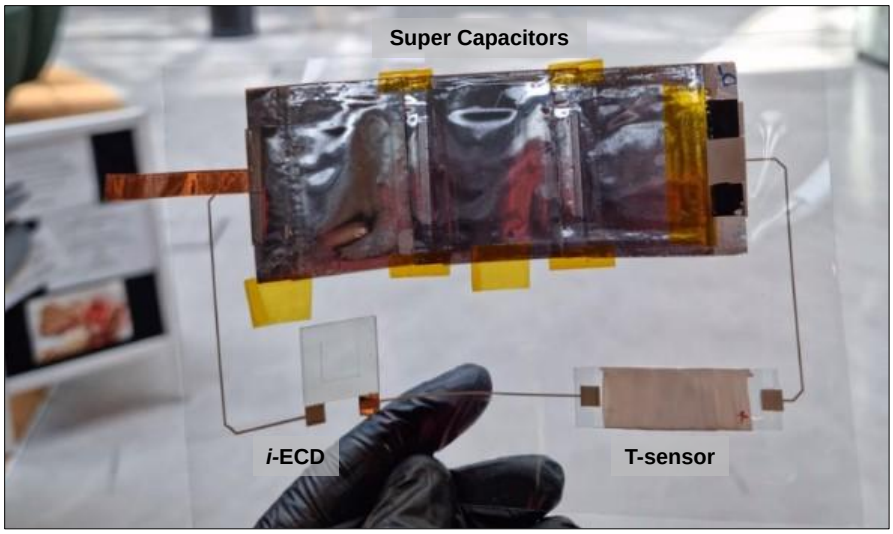


Figure 2.68. CHARISMA smart label prototype assembled integrating and sealing the *i*-ECD, the temperature sensors and three super capacitors connected in series.

In conclusion, the integration process was finalized with the addition of a front design and the incorporation of a reversible thermochromic display developed within the CHARISMA consortium. The final prototype of the smart label is shown in Figure 2.69. This complete integration demonstrates the feasibility of a low-cost, CPU-free, and fully flexible smart label for cold-chain monitoring.

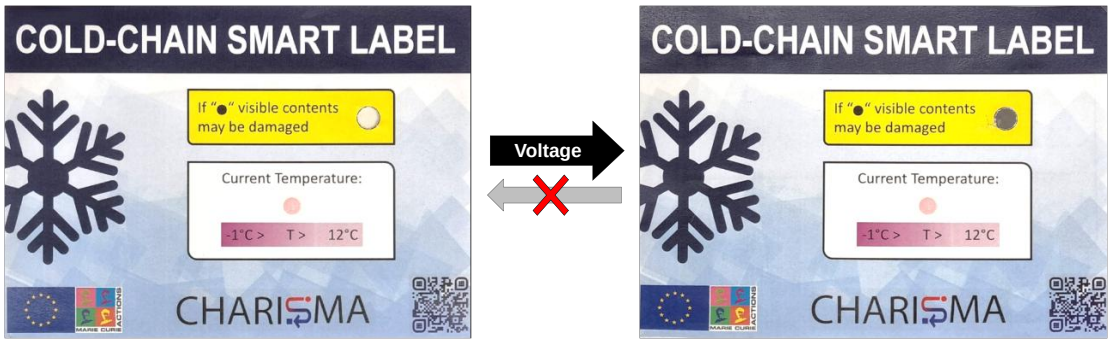


Figure 2.69. Front view of the final CHARISMA smart label including design and a reversible thermochromic display (*r*-TCD) before and after *i*-ECD activation.

2.20 Integration: prototype for cold-chain and Prelonic prototype for ticket events

In parallel with the development of the CHARISMA smart label, our innovative *i*-ECDs have been applied in a range of emerging use cases. In collaboration with Silicon Austria Labs (SAL) in Graz, we integrated *i*-ECD technology into a custom-designed printed circuit board (PCB) incorporating a CPU, temperature sensor, and NFC antenna (Figure 2.70a). The PCB also features dedicated connectors for plug-and-play compatibility, allowing for the rapid and reliable replacement of *i*-ECDs through a streamlined interface optimized for seamless integration. A tamperproof prototype, shown in Figure 2.70b, was specifically developed for individual milk carton monitoring. This approach addresses a key limitation of conventional cold-chain monitoring systems, which typically assess conditions at the batch level, thereby enabling more precise, item-level control.

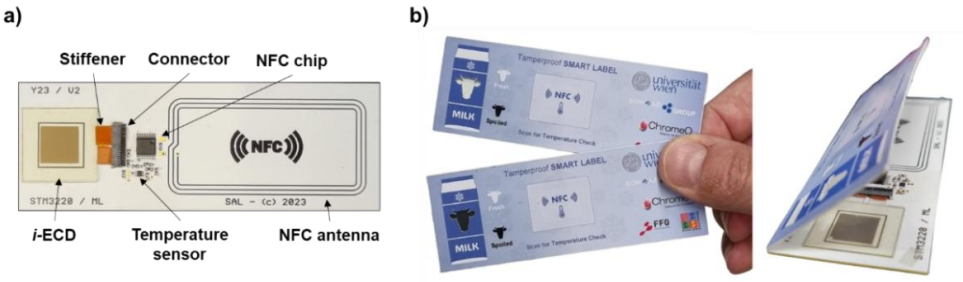


Figure 2.70. a) Back part below the main design. PCB developed by SAL equipped with a temperature sensor, an NFC chip and antenna, an integrated circuit featuring connectors two stiffeners and our *i*-ECD. b) Tamperproof smart label design for cold-chain applications before in white and after in black *i*-ECD activation and respective side view.

Figure 2.71 presents an illustrative example of the smart label affixed to a milk carton. Exploiting the embedded NFC antenna, the tamperproof smart label can communicate with a smartphone via a dedicated application. The app interface, shown in Figure 2.72, allows users to configure temperature thresholds according to product-specific requirements, providing a user-friendly and flexible tool for real-time cold-chain management.



Figure 2.71. Smart label prototype test on a carton milk, *i*-ECD activation with NFC and dedicated smartphone app.

The temperature history is automatically logged on the smartphone, offering continuous accessibility and enabling a comprehensive review of the thermal profile over time. In addition to facilitating data communication, the NFC technology also powers the entire smart label, supporting temperature sensing and voltage output when required, ensuring a self-sufficient and efficient monitoring solution.

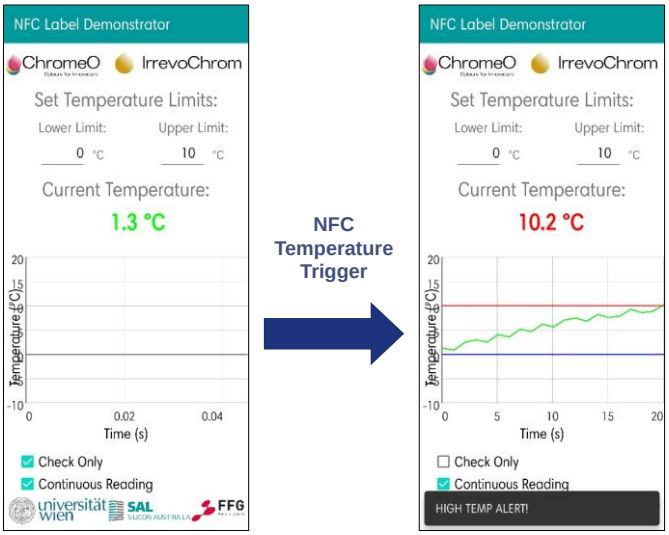


Figure 2.72. NFC app demonstrator for smartphone.

To validate the functionality and reliability of the tamperproof smart label, a demonstration was conducted using three *i*-ECDs with an upper temperature limit set at 10 °C. This value was selected as an indicative threshold for the demo. The milk carton, equipped with the smart label, was first placed in a refrigerator at approximately 1 °C for one hour. It was then exposed to room temperature until the 10 °C threshold was exceeded ("Upper Limit" in Figure 2.72), triggering the delivery of a fixed voltage output of 2.6 V. The voltage was applied for a duration of 60 seconds to ensure complete activation of the *i*-ECDs. The T@600 nm before and after activation is shown in Figure 2.73a. Each *i*-ECD exhibited final transmittance values below 5%, corresponding to an average ΔT@600 nm of approximately 77.2%, indicating a full black contrast, as depicted in Figure 2.73b.

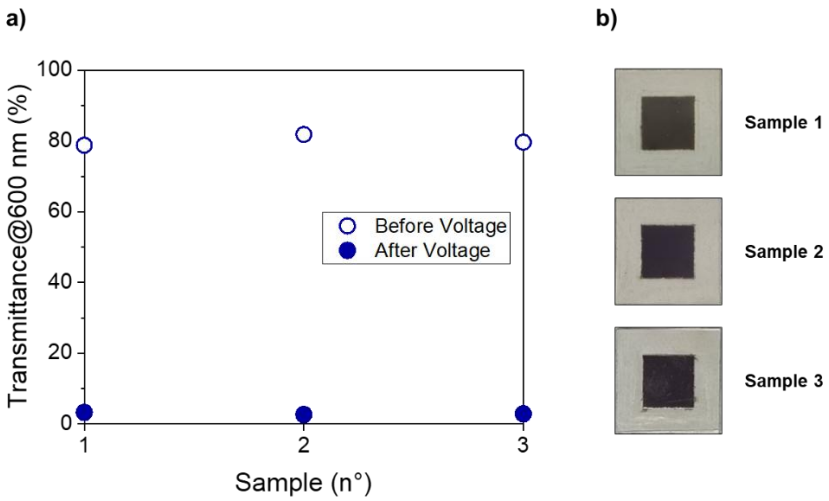


Figure 2.73. a) T@600 nm of three *i*-ECDs before (empty dots) and after (full dots) the application of voltage though the SAL PCB. b) Pictures of the relate *i*-ECDs acquired at the end of the activation process.

Currently, the tamperproof smart label does not operate fully autonomously, as it lacks an integrated power source. This demonstration was conducted to validate the integration and functionality of the *i*-ECD in combination with the electronic components of the PCB, moving beyond activation through laboratory potentiostat and approaching real-world application conditions. The experiment served as a proof-of-concept to show that the *i*-ECD can be reliably triggered within a complete electronic system. The next development phase will focus on incorporating a dedicated battery to provide continuous power to the smart label, enabling fully autonomous operation. In this configuration, the smartphone would be used exclusively for setting temperature thresholds and tracking the temperature history, further advancing the system toward practical deployment.

In parallel, in collaboration with Prelonic from Linz, *i*-ECDs were employed as visual indicators for intelligent event tickets, leveraging NFC technology. In this application, the PCB (Figure 2.74a) is equipped with an NFC antenna and adhesive connectors, enabling straightforward plug-and-play integration of the *i*-ECDs. Once connected, the PCB is positioned behind the ticket design to complete the prototype (Figure 2.74b). These smart event tickets operate without the need for a continuous power supply and therefore do not require batteries. Activation of the *i*-ECD occurs when the ticket is placed into close proximity with an NFC reader, which supplies a voltage pulse to validate the ticket permanently.

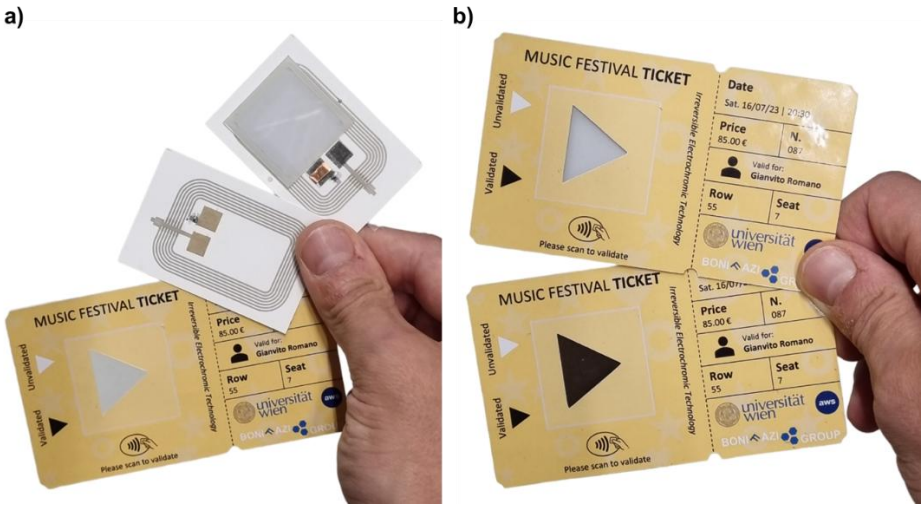


Figure 2.74. a) Prototype ticket equipped with an NFC antenna and adhesive conductive pins for *i*-ECDs connection. b) Design realized for a prototype ticket intended for a music festival.

2.21 Conclusions and outlook

This chapter comprehensively demonstrates the development, optimization, and characterization of *i*-ECDs based on DA oxidation, culminating in a system capable of

producing a remarkable and permanent colour change in response to electrical stimuli. The core innovation lies in the use of a non-toxic, water-based electrolyte system, composed of PBS at pH 7.4, DA, and sodium metabisulfite as an antioxidant. Upon application of a low voltage (≤ 1.5 V), these *i*-ECDs exhibit a rapid transition (< 60 seconds) from a transparent state to an intense black, with a ΔT of approximately 80%, confirming a high-contrast optical response. The irreversible blackening is not driven by the deposition of ePDA as initially hypothesized, but rather by the electrochemical reduction of the ITO as C.E., leading to the formation of metallic In and Sn NPs. This reduction occurs at low voltages, below 1.5 V, due to the electro-oxidation of DA at W.E. The oxidation of DA proceeds through well-defined redox pathways involving DAQ, DAL, and DAC, and plays a crucial role in lowering the threshold voltage required for ITO reduction. The reduction of ITO potential is not unique to DA, as similar effects have been observed with other electro-oxidizable compounds like catechol. Thus, the key factor enabling ITO reduction at potential ≤ 1.5 V is the presence of a compound which can be electro-oxidized at the W.E., within the window voltage applied for the process. Furthermore, the use of antioxidant has proven effective in suppressing spontaneous oxidation, previously responsible for consuming the DA monomer and hindering the long-term functionality of *i*-ECDs, significantly enhancing their shelf life and reliability, with demonstrated stability exceeding 100 days.

Extensive parameter optimization revealed the importance of key factors such as DA concentration (optimal at 10 g/L), electrolyte pH (optimal at an approximately neutral, physiologically relevant value of 7.4), and activation voltage (threshold at 1.25–1.5 V). Additionally, phosphate-containing electrolytes were found to lower the ITO reduction potential, an effect attributed to specific interfacial interactions and electronic modulation of the ITO surface by phosphate anions. The *i*-ECDs showed moderate durability under mechanical stress, temperature variation, and UV exposure, making them suitable for cold-chain applications and integration into smart labels. Furthermore, spectroelectrochemical and CV analyses confirmed the electrochemical irreversibility of the colour change, grounded in the structural transformation of the ITO electrode, rather than in a DA transformation. Importantly, the study also provided evidence that similar redox-active molecules, such as catechol, can produce comparable behaviour, indicating that the *i*-ECD architecture is modular and adaptable, capable of integrating other oxidizable compounds. This opens a promising path toward the development of a new class of electrochemically-triggered, irreversible indicators, with tunable activation thresholds, visual outputs, and storage stability.

Moreover, this work advanced the practical integration of *i*-ECDs into smart labels designed for cold-chain and traceability applications. Initial trials using commercial electronics

demonstrated the successful activation of *i*-ECDs through compact systems such as Arduino boards, underscoring their feasibility in real-world scenarios. Further integration efforts, supported by the CHARISMA research team, involved the development of miniaturized, energy-efficient modules tailored for low-voltage operation. Collaborations with industrial partners such as SAL and Prelonic further validated the versatility of *i*-ECDs. With SAL, a tamper-proof smart label was created for real-time, unit-level temperature monitoring of milk cartons, addressing a major limitation in batch-level tracking. The incorporation of NFC modules enabled interaction with smartphones, enhancing user accessibility and data transparency. Meanwhile, the partnership with Prelonic demonstrated the application of *i*-ECDs in intelligent ticketing systems, reinforcing their adaptability across diverse fields. While these integration milestones affirm the technology level of *i*-ECDs, several challenges remain, primary among them the need for improved temperature sensors and autonomous power systems. Addressing these limitations will be critical for achieving fully self-sufficient, disposable smart labels. Ongoing and future research will thus focus on resolving these bottlenecks, aiming to deliver robust, energy-efficient solutions for intelligent packaging, logistics monitoring, and authentication technologies. These findings not only lay the groundwork for market-ready applications but also position *i*-ECDs as a transformative, low-cost, and user-friendly technology in the growing field of intelligent and responsive materials. Their simple architecture, minimal energy requirements, and irreversible, high-contrast optical response make them an ideal solution for scalable, disposable monitoring systems, offering a combination of affordability, reliability, and functional adaptability.

REFERENCES

[1] S. Basu, P. S. Dasgupta, *J. Neuroimmunol.* **2000**, *102*, 113–124.

[2] C. Missale, S. R. Nash, S. W. Robinson, M. Jaber, M. G. Caron, *Physiol. Rev.* **1998**, *78*, 189–225.

[3] J. W. Kebabian, D. B. Calne, *Nature* **1979**, *277*, 93–96.

[4] L. Zecca, D. Tampellini, M. Gerlach, P. Riederer, R. G. Fariello, D. Sulzer, **n.d.**

[5] P. Manini, L. Panzella, I. Tedesco, F. Petitto, G. L. Russo, A. Napolitano, A. Palumbo, M. d'Ischia, *Chem. Res. Toxicol.* **2004**, *17*, 1190–1198.

[6] N. Chen, M. E. A. Reith, *Eur. J. Pharmacol.* **2000**, *405*, 329–339.

[7] J. D. Elsworth, R. H. Roth, *Exp. Neurol.* **1997**, *144*, 4–9.

[8] H. Lee, S. M. Dellatore, W. M. Miller, P. B. Messersmith, *Science* **2007**, *318*, 426–430.

[9] Y. Liu, K. Ai, L. Lu, *Chem. Rev.* **2014**, *114*, 5057–5115.

[10] L. C. Almeida, R. D. Correia, A. Marta, G. Squillaci, A. Morana, F. La Cara, J. P. Correia, A. S. Viana, *Appl. Surf. Sci.* **2019**, *480*, 979–989.

[11] M. Ambrico, P. F. Ambrico, A. Cardone, N. F. D. Vecchia, T. Ligonzo, S. R. Cicco, M. M. Talamo, A. Napolitano, V. Augelli, G. M. Farinola, M. d'Ischia, *J. Mater. Chem. C* **2013**, *1*, 1018–1028.

[12] C. Zhang, B.-H. Wu, Y. Du, M.-Q. Ma, Z.-K. Xu, *J. Mater. Chem. C* **2017**, *5*, 3898–3902.

[13] Z. Deng, B. Shang, B. Peng, *Chem. Rec.* **2018**, *18*, 410–432.

[14] Q. Wei, F. Zhang, J. Li, B. Li, C. Zhao, *Polym. Chem.* **2010**, *1*, 1430.

[15] G. Gkogkos, L. Panariello, E. Grammenou, M. A. Cornwell, A. Afrashtehpour, A. J. MacRobert, I. P. Parkin, A. Gavriilidis, *Chem. Eng. J.* **2023**, *467*, 143350.

[16] J. Wang, B. Li, Z. Li, K. Ren, L. Jin, S. Zhang, H. Chang, Y. Sun, J. Ji, *Biomaterials* **2014**, *35*, 7679–7689.

[17] T.-F. Wu, J.-D. Hong, *Sens. Actuators B Chem.* **2016**, *224*, 178–184.

[18] R. Lakshminarayanan, S. Madhavi, C. P. C. Sim, in *Dopamine - Health Dis.* (Ed.: S.C. Yenisetti), InTech, **2018**.

[19] S. Hong, Y. S. Na, S. Choi, I. T. Song, W. Y. Kim, H. Lee, *Adv. Funct. Mater.* **2012**, *22*, 4711–4717.

[20] M. L. Alfieri, R. Micillo, L. Panzella, O. Crescenzi, S. L. Oscurato, P. Maddalena, A. Napolitano, V. Ball, M. d'Ischia, *ACS Appl. Mater. Interfaces* **2018**, *10*, 7670–7680.

[21] M. L. Alfieri, L. Panzella, S. L. Oscurato, M. Salvatore, R. Avolio, M. E. Errico, P. Maddalena, A. Napolitano, M. D'Ischia, *Biomimetics* **2018**, *3*, 26.

[22] S. Schindler, T. Bechtold, *J. Electroanal. Chem.* **2019**, *836*, 94–101.

[23] H. L. Bui, S.-D. Huang, B. P. Lee, M.-Y. Lan, C.-J. Huang, *Colloids Surf. B Biointerfaces* **2022**, *220*, 112879.

[24] P. Palladino, F. Torrini, S. Scarano, M. Minunni, *J. Pharm. Biomed. Anal.* **2020**, *179*, 113016.

[25] A. Telli, S. Arabaci, *Text. Res. J.* **2024**, 00405175241274763.

[26] J. K. Shashikumara, B. E. K. Swamy, *Sens. Int.* **2020**, *1*, 100008.

[27] A. Delgado-Bonal, J. Martín-Torres, *Sci. Rep.* **2016**, *6*, 36038.

[28] M. Salomäki, L. Marttila, H. Kivelä, T. Ouvinen, J. Lukkari, *J. Phys. Chem. B* **2018**, *122*, 6314–6327.

[29] P. Muñoz, S. Huenchuguala, I. Paris, J. Segura-Aguilar, *Park. Dis.* **2012**, *2012*, e920953.

[30] W. Zheng, H. Fan, L. Wang, Z. Jin, *Langmuir* **2015**, *31*, 11671–11677.

[31] K. Alef, S. Iglauer, A. Barifcani, *J. Chem. Eng. Data* **2018**, *63*, 1821–1826.

[32] L. Liu, S. Yellinek, I. Valdinger, A. Donval, D. Mandler, *Electrochimica Acta* **2015**, *176*, 1374–1381.

[33] J. H. Lee, Y. H. Kim, S. J. Ahn, T. H. Ha, H. S. Kim, *Mater. Sci. Eng. B* **2015**, *199*, 37–41.

[34] C. Guillén, J. Herrero, *J. Appl. Phys.* **2007**, *101*, 073514.

[35] P. Palladino, F. Torrini, S. Scarano, M. Minunni, *J. Pharm. Biomed. Anal.* **2020**, *179*, 113016.

[36] M. Bisaglia, S. Mammi, L. Bubacco, *J. Biol. Chem.* **2007**, *282*, 15597–15605.

[37] **N.d.**

[38] R. P. Bacil, L. Chen, S. H. P. Serrano, R. G. Compton, *Phys. Chem. Chem. Phys.* **2020**, *22*, 607–614.

[39] G. Balkourani, A. Brouzgou, C. L. Vecchio, A. S. Aricò, V. Baglio, P. Tsiakaras, *Electrochimica Acta* **2022**, *409*, 139943.

[40] J. Breczko, M. E. Plonska-Brzezinska, L. Echegoyen, *Electrochimica Acta* **2012**, *72*, 61–67.

[41] D. Nematollahi, M. Alimoradi, S. W. Husain, *Electroanalysis* **2004**, *16*, 1359–1365.

[42] Y. Sun, A. N. Pham, T. D. Waite, *Environ. Sci. Process. Impacts* **2018**, *20*, 232–244.

[43] A. Falamaş, A. Petran, A.-M. Hada, A. Bende, *Int. J. Mol. Sci.* **2022**, *23*, 5483.

[44] J.-H. Lin, C.-J. Yu, Y.-C. Yang, W.-L. Tseng, *Phys. Chem. Chem. Phys.* **2015**, *17*, 15124–15130.

[45] S. Bhagwat, R. P. Howson, *Surf. Coat. Technol.* **1999**, *111*, 163–171.

[46] N. Farid, A. Sharif, R. K. Vijayaraghavan, M. Wang, H. Chan, A. Brunton, P. J. McNally, K. L. Choy, G. M. O'Connor, *J. Phys. Appl. Phys.* **2021**, *54*, 185103.

[47] P. J. Hotchkiss, S. C. Jones, S. A. Paniagua, A. Sharma, B. Kippelen, N. R. Armstrong, S. R. Marder, *Acc. Chem. Res.* **2012**, *45*, 337–346.

[48] D.-P. Tran, H.-I. Lu, C.-K. Lin, *Surf. Coat. Technol.* **2015**, *283*, 298–310.

[49] M. S. Khan, A. Shakoor, *J. Chem.* **2015**, *2015*, e695930.

[50] H. Szatylowicz, A. Jezuita, T. M. Krygowski, *Struct. Chem.* **2019**, *30*, 1529–1548.

[51] S. Rayati, A. Ghaemi, N. Sadeghzadeh, *Catal. Commun.* **2010**, *11*, 792–796.

[52] N. G. S. Mateyise, M. M. Conradie, J. Conradie, *J. Electroanal. Chem.* **2023**, *947*, 117807.

[53] J. Zhang, Y. S. Cheah, S. Santhanakrishnan, K. G. Neoh, C. L. L. Chai, *Polymer* **2017**, *116*, 5–15.

[54] L. García-Fernández, J. Cui, C. Serrano, Z. Shafiq, R. A. Gropeanu, V. S. Miguel, J. I. Ramos, M. Wang, G. K. Auernhammer, S. Ritz, A. A. Golriz, R. Berger, M. Wagner, A. Del Campo, *Adv. Mater.* **2013**, *25*, 529–533.

[55] X. Xiong, L. Xue, J. Cui, *ACS Macro Lett.* **2018**, *7*, 239–243.

[56] L. J. Kettle, S. P. Bates, A. R. Mount, *Phys. Chem. Chem. Phys.* **2000**, *2*, 195–201.

[57] R. S. Assary, F. R. Brushett, L. A. Curtiss, *RSC Adv.* **2014**, *4*, 57442–57451.

[58] M. Ren, S. Sun, Y. Wu, Y. Shi, Z. Wang, H. Cao, Y. Xie, *Chemosphere* **2022**, *296*, 134071.

[59] R. P. Smith, H. Eyring, *J. Am. Chem. Soc.* **1953**, *75*, 5183–5186.

[60] K. Inami, Y. Iizuka, M. Furukawa, I. Nakanishi, K. Ohkubo, K. Fukuhara, S. Fukuzumi, M. Mochizuki, *Bioorg. Med. Chem.* **2012**, *20*, 4049–4055.

[61] S. J. Kuhn, *Can. J. Chem.* **1962**, *40*, 1660–1663.

[62] S. S. Batsanov, *Molecules* **2022**, *27*, 8215.

[63] S. C. Mukhopadhyay, N. K. Suryadevara, in *Internet Things* (Ed.: S.C. Mukhopadhyay), Springer, Springer Nature, Switzerland, **2014**, pp. 1–17.

[64] T. Kempf, V. Bobek, T. Horvat, *Int. J. Econ. Finance* **2021**, *13*, 62.

CHAPTER 3

DOPAMINE-BASED INK FORMULATION FOR PRINTING TECHNOLOGY

INTRODUCTION

3.1 Current production of ECDs

The development of ECDs has progressed significantly in recent years, driven by advancements in materials and manufacturing techniques.[1] The current production of ECDs must fulfil several essential criteria: cost-efficiency, scalability, precision, and versatility. To meet the growing demand for ECDs in various applications such as smart windows,[2] wearables,[3] and electronic displays/visual indicators,[1,4] the production methods must consistently produce high volumes of displays with uniform quality. Techniques such as electropolymerisation,[5] spin coating,[6] inkjet/spray coating,[7] and blade coating[8] are highly effective for research and small-scale production due to their precision and adaptability. However, for industrial production and large-scale applications, scalable methods like screen printing,[9,10] which additionally has the potential to be expanded in sheet-to-sheet and roll-to-roll printing, are preferred.[11] These scalable techniques significantly enhance production efficiency and reduce costs, making ECDs technology more accessible for commercial applications. To better understand limitations and benefits of these various production techniques, the following sections provide a detailed examination of each method.

3.1.1 Electropolymerisation

Electropolymerisation is a precise technique employed in the fabrication of EC films, involving the electrochemical polymerization of monomers directly onto a substrate by applying an electric potential. This method allows for exact control over the thickness of the film and morphology, producing uniform and adherent films even on substrates with complex geometries. The versatility of this approach permits the creation of films ranging from a few nanometers to several micrometers in thickness, achieving nanoscale-level uniformity.[12,13] This technique is specifically applicable to conductive substrates, as the electrons must reach the monomers to facilitate the polymerization reactions. Upon completion, the film is attached to the electrode, which will be used in the manufacturing of the ECD. Furthermore, it is crucial

that the resultant polymeric film is electrically conductive to allow electron flow, thereby enabling the redox reactions responsible for the colour/transmittance change in the ECD.

The electropolymerisation process can be conducted within a three-electrode electrochemical cell (Figure 3.1a)[14] or directly within an ECD (Figure 3.1b).[15] In both setups, the fundamental component is the monomer, which undergoes electropolymerisation on the surface of the working electrode (W.E.) through oxidative polymerization. The monomer must be soluble in the electrolyte to allow the monomers to surround the electrodes dipped into the solution. The electrolyte provides ionic conductivity, allowing electron transfer from the source to the electrodes. In the three-electrode setup, the presence of the reference electrode (R.E.) allows for more accurate control of the potential applied to the W.E. After the electropolymerisation reaction is complete, the W.E., now coated with a polymer layer, is extracted from the electrolyte solution and finally used to prepare an ECD. In the two-electrode setup, only the W.E. and the counter electrode (C.E.) are present. Once the monomer is dissolved in the electrolyte, the solution is introduced between the two electrodes forming the ECD. Upon applying a voltage, the electropolymerisation reaction occurs directly within the display, forming the polymer layer on the W.E. This process accelerates the fabrication of an ECD but does not ensure the complete consumption of the monomer. Indeed, any remaining monomer molecules within the display may continue to polymerize on both ECD electrodes depending on the voltage polarity, which could compromise its proper functioning.

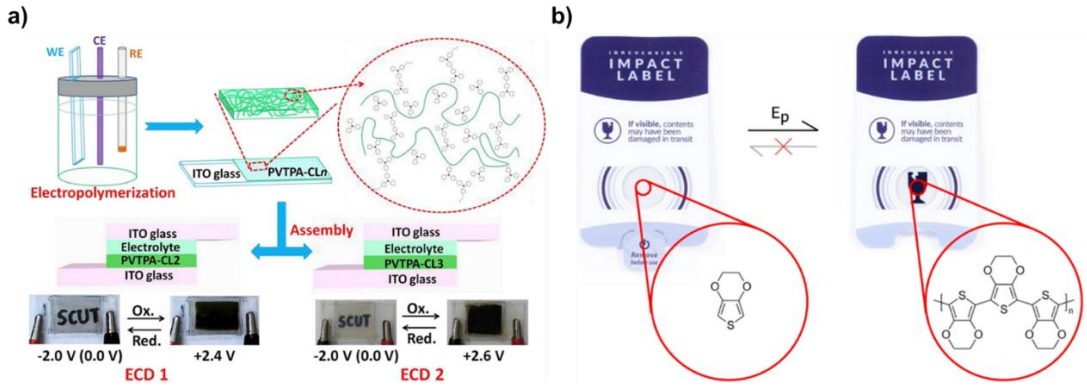


Figure 3.1. a) Experimental setup utilizing a three-electrode system for the electropolymerisation of Poly(4-vinyltriphenylamine) on the W.E. and subsequent fabrication of ECDs.[14,15] b) Irreversible EC indicator integrated into a smart impact label.

An illustrative example of this deposition technique come from the research conducted by Elena Poverenov and her team. During their study on the electropolymerisation of Poly(3,4-ethylenedioxythiophene) (PEDOT) in various solvents measuring films with a thickness average of 1 µm.[16] Further research includes the work by Fu et al. on electropolymerizing donor–acceptor–donor (D–A–D) type monomers. Their study demonstrated high optical

contrast up to 70%, short response times of less than 3 seconds, and a high coloration efficiency (CE) over 200 cm^2/C, showcasing the efficiency and versatility of this method.[17]

Electropolymerisation is a powerful technique for fabricating EC films, especially due to its precision in controlling film thickness and morphology. This enables the formation of highly uniform and adherent films on conductive substrates, improving the performance and durability of ECDs. While the process is well-established at the laboratory scale, challenges remain for industrial-scale implementation, primarily due to the need for electrochemical cells and slower deposition rates in thicker films. Nevertheless, its compatibility with scalable manufacturing methods, such as roll-to-roll processing and patterned deposition, makes electropolymerisation a promising candidate for future large-area production.

3.1.2 Spin coating

In contrast to electropolymerisation, which requires conductive substrates and electrochemical setups, spin coating offers a simpler and more versatile approach for depositing EC films. This technique involves applying a liquid solution of the EC material onto a substrate, which is then rapidly rotated to spread the solution uniformly via centrifugal force. The process steps are illustrated in Figure 3.2. The procedure begins with the deposition of a liquid formulation onto a substrate held in place by a vacuum. Once the substrate is fully covered, the spin coater accelerates to a set rotational speed and maintains it for a defined time. During spinning, the film thins out due to radial flow and solvent evaporation, ultimately forming a uniform thin film. Depending on the material system, additional steps such as thermal annealing or UV curing may be required to solidify or crosslink the film.[6] One of the key advantages of spin coating is the fine control over film thickness, which is typically governed by the viscosity of the solution, spin speed, and duration. Experimental studies consistently show that increasing the spin speed or duration typically results in thinner films, due to greater centrifugal force and extended time for film thinning via solvent evaporation and radial spreading.[18] For instance, in a study by Santonicola et al.,[19] carbon-based nanocomposite films were fabricated via spin coating at a fixed spin time of 10 seconds. Their experiments demonstrated that when the solution viscosity increased from 40 mPa·s to 160 mPa·s, and the spin speed ranged from 1000 to 5000 rpm, the film thicknesses varied from approximately 150 nm to 350 nm. The data showed that at a low viscosity of 40 mPa·s and a high spin speed of 5000 rpm, the resulting film was around 150 nm thick, whereas under higher viscosity (160 mPa·s) and lower spin speed (1000 rpm), films reached up to 350 nm thickness. These results affirm the inverse correlation between spin speed and film thickness and the direct effect of viscosity. Another

analysis was conducted by Pai et al.,[20] focusing on conjugated polymers. Their spin-coating trials used polymer solutions with viscosities ranging from 40 to 400 mPa·s. At a spin speed of 2000 rpm for 60 seconds, a low-viscosity solution (around 40 mPa·s) yielded a film thickness of approximately 100 nm. In contrast, increasing the viscosity to 400 mPa·s under the same spin conditions resulted in a much thicker film of ~480 nm.

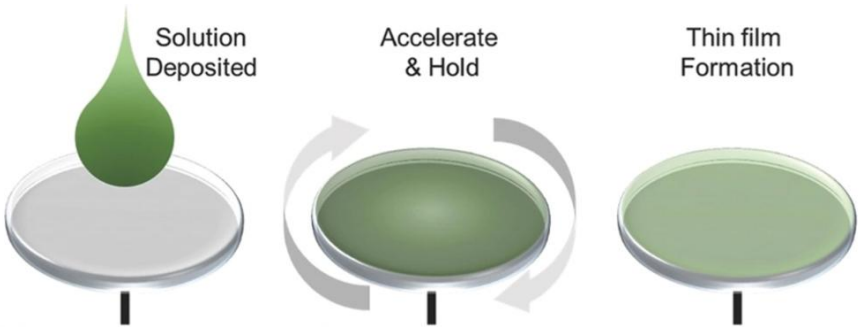


Figure 3.2. Procedure for applying a formulation through spin coating to create a thin film.[21]

This method is simple, cost-effective, and capable of producing homogeneous thin films over large areas, ranging from 10 nm to several µm in thickness, with consistent uniformity even across large substrates like 300 mm wafers.[22] In recent studies, spin coating has been effectively utilized for producing EC films, especially with WO_3-based materials. For example, Khan et al. achieved a high CE of 193.25 cm^2/C with WO_3/TiO_2 composite films, demonstrating the potential of these materials for practical EC applications.[23]

Despite the successful application of spin coating for producing high-quality EC films with excellent uniformity, a significant limitation remains in its scalability for mass production. The inherent constraints of the technique make it challenging to deposit films on large surfaces, which is a critical requirement for the commercial production of ECDs. These limitations arise from technical aspects of the method, such as the difficulty in maintaining uniform film thickness over extended areas. Consequently, while spin coating is highly effective for laboratory-scale research and small-scale applications, it is not well-suited for high-volume manufacturing. This makes it more appropriate as a research tool rather than a practical method for industrial-scale production of ECDs.

3.1.3 Inkjet and spray coating

Inkjet and spray coating are versatile techniques widely used for depositing thin films in the fabrication of ECDs.[7] These methods offer precise control over the deposition process, enabling the creation of uniform and well-defined patterns on various substrates. Inkjet coating

involves the ejection of tiny droplets of a solution containing the EC material onto a substrate.[24] The droplets are typically in the range of picoliters, allowing for high-resolution patterns. The printing process involves the use of a print head equipped with numerous nozzles that dispense the ink onto the substrate, Figure 3.3a. The droplet size, ejection frequency, and the distance between the print head and substrate, typically around 1–2 mm, are carefully controlled to achieve the desired film thickness and uniformity.[25]

In contrast, spray coating involves atomizing a liquid solution into a fine mist and then spraying it onto a substrate.[7] The process can cover large areas efficiently and is adaptable to substrates with complex geometries. A spray nozzle or atomizer is used to create the mist, and the size of the droplets can be controlled by adjusting the nozzle design and the pressure of the carrier gas, typically air or inert such as nitrogen or agon. The distance from the nozzle to the substrate is a critical parameter in inkjet and spray coating deposition processes, typically ranging between 5 cm to 30 cm, and significantly influences the film thickness and uniformity. For instance, Aziz and coworkers observed that at a nozzle-to-substrate distance of 20 cm, spray-coated films exhibited better uniformity compared to shorter distances.[26] Similarly, Habibi and coworkers reported that distances below 10 cm often result in thicker but less uniform films due to increased droplet coalescence and splash-back, while distances around 15–20 cm yield smoother and thinner layers with enhanced uniformity.[27] For ultrasonic spray coating, Silvano and coworkers demonstrated that reducing the distance from 15 cm to 10 cm increased the film thickness from ~200 nm to ~400 nm, confirming a direct correlation between shorter distances and higher material deposition.[28] This technique is thoroughly examined in Chapter 4, where it is exploited for the deposition of an EC polythiophene-based polymer film. A key advantage of spray coating lies in its ability to heat the substrate during deposition. Maintaining the substrate at an elevated temperature accelerates solvent evaporation, effectively minimizing solvent accumulation and reducing the risk of pooling. This controlled evaporation process promotes the formation of uniform films with smooth surfaces, an essential requirement for high-performance ECDs. The substrate temperature can be finely tuned based on the solvent's volatility, allowing for precise control over drying dynamics and film morphology.[29]

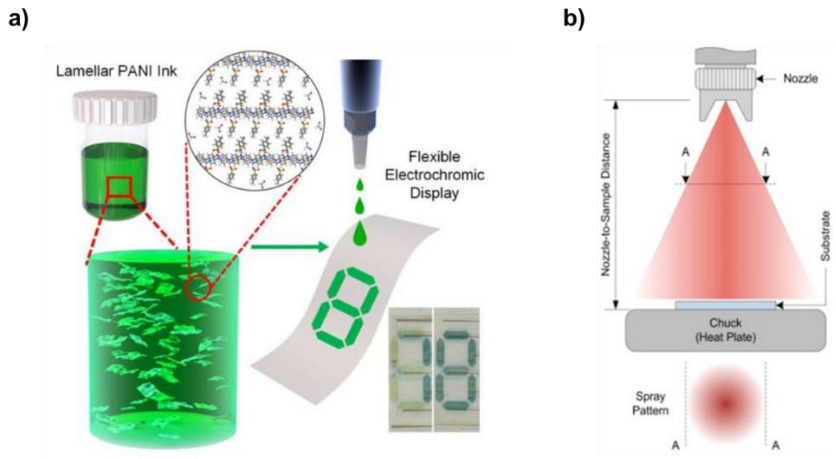


Figure 3.3. a) Illustration scheme of the inkjet printing process of polyaniline (PANI) over a flexible substrate for the development of an ECD.[24] b) Illustrative diagram of the spray coating technique with vertical alignment between the nozzle and substrate.[30]

Despite their advantages, inkjet and spray coating techniques face notable challenges in high-scale production. The primary limitations include difficulty in achieving uniformity over large areas, inconsistency in film thickness, and scalability issues. For example, Neo and coworkers highlight that these methods often struggle to maintain uniform deposition on large surfaces, which is essential for high-volume manufacturing.[31] Additionally, Dawo and coworkers observe that while these techniques can be adapted for flexible electronics, their current inefficiencies in scaling up hinder their potential for mass production.[32] These limitations highlight the need for alternative methods or significant advancements in existing technologies to meet the demands of large-scale fabrication ECDs.

Numerous studies in the literature have utilized these techniques for depositing EC layers. A notable example is the work by Huang and coworkers, as illustrated in the Figure 3.3a, where the inkjet printing technique was employed to fabricate an ECD with a polyaniline (PANI) layer. This device demonstrated an optical contrast of 76%, a CE of 259.1 cm^2/C, and a REDOX switching time of approximately 2 seconds.[24] The same technology was exploited by Chang-Jian and coworkers demonstrating the manufacturing of ECDs with remarkable features, including a ΔT of 54.1%, a rapid response time of 1.1 seconds, and a CE of 83.9 cm^2/C.[33] Similarly, spray coating has been effectively utilized in several studies for depositing EC films. For instance, the research work carried out by Choi and coworkers created spray-coated ECDs with a redox potential of -1.5 V, fast switching under 10 seconds, and stability for 90000 seconds with initial transmittance losses of less than 5%.[34] In another study by Zhang and coworkers, the spray coating technique was used to deposit a large-sized EC polymeric layer of PANI (6.0 × 7.0 cm^2). This layer exhibited high optical contrast (71.6% at

600 nm) and rapid response times (*ca.* 0.5 seconds for both colouring and bleaching), showcasing the potential of this technique for producing large-area ECDs.[35]

3.1.4 Blade coating

Blade coating, also known as doctor blade coating, is a relatively simple process that does not require specialized equipment for solvent vaporization, making it a cost-effective and accessible option for various thin-film fabrication applications. This technique involves using a blade or knife to spread a thin layer of EC material ink across a substrate,[36] producing uniform films with thicknesses ranging from 100 nm to several µm and in large-scale areas.[37] The work of Dinh and coworkers exemplifies the potential of blade coating, as they successfully created a film based on an electrolyte gel and EC material with a CE of 33.7 cm^2/C, a thickness of approximately 600 nm, and a surface area of 6×10 cm^2, demonstrating the technique's ability to produce functional films on a significantly larger scale than typical EC indicators, which are often only a few cm^2 in size.[8] A study of Mjejrin and coworkers also highlighted the fabrication of double-sided ECDs using the doctor blade method, emphasizing its capability in producing reliable and high-performance films.[38] Additionally, the inks developed for doctor blade coating often possess viscosities in the range of 500 to 5000 mPa·s, which is comparable to the typical screen printing ink viscosity range of 1000 to 10000 mPa·s. This alignment facilitates a smoother transition from laboratory-scale prototyping to industrial-scale roll-to-roll or screen printing processes, thereby enhancing manufacturing scalability without the need for substantial reformulation of the ink composition.[39,40]

The process begins with the preparation of an ink formulation, which typically includes a solvent, binder, and the desired material, Figure 3.4.[41] This formulation is then deposited onto a moving substrate. A blade, positioned at a fixed height above the substrate, spreads the formulation evenly, controlling the thickness of the film. Finally, the coated film undergoes post-treatment, which can involve drying to evaporate the solvent or exposure to UV light to cure the material.[42] Additionally, in some cases, the solvents are intentionally retained within the formulation, or other post-treatment methods such as heat application are used to achieve desired film properties.

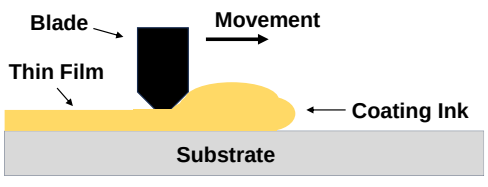


Figure 3.4. Diagram of the manufacturing process for doctor blade.

This technique is versatile and can be used to deposit various types of layers, including ceramic layers for capacitors and fuel cells,[43] polymer films for electronic applications,[44] composite layers for energy storage devices, and nanomaterial coatings for photovoltaic cells.[45] Doctor blade casting can handle inks with viscosities ranging from 1 to 10000 mPa·s, and it can produce films with thicknesses ranging from a few micrometers to several millimeters.[46] The method allows for the fabrication of films with thicknesses ranging from a few micrometers up to approximately 300 μm, depending on factors such as blade height, ink rheology, and substrate translation speed, as demonstrated in the scalable coating of oxide-based electrodes for battery applications.[47] This precise control over film thickness is one of the key advantages of the doctor blade method, particularly for applications that demand highly uniform coatings. In ECDs and dye-sensitized solar cells (DSSCs), TiO_2 films with controlled thicknesses in the range of 10–20 μm have been shown to enhance charge transport and overall device efficiency, as demonstrated in the study by Mohammadnezhad and coworkers.[48] Beyond precision, the doctor blade method is also noted for its high scalability, enabling continuous and low-cost production. This makes it particularly suitable for transitioning from lab-scale prototypes to industrial-scale manufacturing. For example, Roy and coworkers reported successful use of doctor blade coating for large-area perovskite solar modules due to its roll-to-roll compatibility and ability to maintain consistent film characteristics across surfaces exceeding 10×10 cm^2.[49] One significant drawback is the use of solvents, which can be hazardous and environmentally unfriendly, as noted in the study on nanocomposite TiO_2-WO_3 films.[50] Another limitation is that the technique is mainly applicable to flat or slightly curved surfaces, restricting its use in more complex geometries. Additionally, some applications require additional post-treatment processes, increasing production complexity and cost, as illustrated in the research on vanadium pentoxide films for ECDs.[51]

Polymer-based ECDs fabricated using the doctor blade technique exhibited high CE (1872.8 cm^2/C at 600 nm) and low power consumption (102 μW cm^{-2} for colouration and 11 μW cm^{-2} for bleaching), suitable for large-scale smart window applications.[52] Additionally, a study using the doctor blade method to prepare a TiO_2 EC electrode with an electrospun polyacrylonitrile (PAN) nanofiber membrane gel electrolyte achieved a ΔT of 33.40% in the visible region, 93% of the 35.91% achieved with liquid electrolyte-based ECDs. In contrast, ECDs with conventional gel electrolytes showed a much lower ΔT of just 4.22%, indicating their reduced effectiveness in modulating light transmission.[53] These examples highlight the versatility and effectiveness of the doctor blade technique in producing high-performance ECDs, demonstrating its potential in various applications.

3.1.5 Screen printing

It has emerged as the most widely used technique for producing ECDs due to its scalability (devices number per time), cost-effectiveness, and ability to create robust, patterned films.[54] This method supports high-volume manufacturing, with studies reporting a manufacturing yield of approximately 99.8%, making it highly efficient and reliable for mass production.[55] For example, roll-to-roll screen printing of ECDs has demonstrated yields exceeding 93% across batches of 1500, while pilot-scale industrial lines achieve throughputs of up to 30 meters per minute, confirming the scalability of the process for flexible displays.[11,56] Screen printing accommodates various substrates, including flexible and curved surfaces, unlike spin coating, which is limited to flat, rigid substrates.[57] The thickness of screen-printed layers typically ranges from a few micrometers to tens of micrometers, depending on the specific application and materials used. Various factors influence the thickness of the screen-printed layers, including the viscosity of the ink, the mesh size of the screen, the squeegee pressure, and the speed of the printing process.[56,58]

However, screen printing does have its challenges. Unlike inkjet and spray coating, where the solution can be in liquid form, screen printing requires more viscous inks. This higher viscosity prevents the ink from spontaneously dripping through the mesh, ensuring controlled and precise application. These inks typically need to have a viscosity range of 1000 to 20000 mPa·s to ensure they flow correctly through the mesh while maintaining the integrity of the printed pattern.[9,59] Developing such inks can add complexity to the process, but the benefits in terms of scalability and cost efficiency often outweigh these challenges. According to the literature, nanocellulose is often used to increase the viscosity of carbon inks, making them suitable for screen printing with viscosities ranging from 1000 to 5000 mPa·s using a concentration of about 4%.[60] WO_3 inks have their viscosity adjusted to between 10000 and 20000 mPa·s using specific nitrocellulose 20% w/w to ensure suitability for screen printing.[61] Polyvinyl alcohol (PVA) is another common additive used to improve the dynamic viscosity of inks. In the development of screen-printable EC polymer inks, researchers controlled the viscosity within the range of 1000 to 5000 mPa·s by adjusting the polymer concentration between 1.1% and 6.5% in weight.[62] Additionally, the use of cellulose nanofibrils combined with hydroxypropyl methylcellulose (HPMC) has been reported to achieve a viscosity range of 3000 to 10000 mPa·s for silver nanowire inks when employed between 3% to 8% in weight.[63] Finally, developing the proper viscosity for screen printing inks using biocompatible and green additives like Agar Agar, collagen, and Starch significantly enhances their suitability. These compounds can be solubilized in water, eliminating the need for organic solvents and making them more industrially viable. Specifically, Gunter Hübner and coworkers reported in their

work that Agar Agar-based inks achieve viscosities of 2500 to 38000 mPa·s at 5% to 15% w/w in water.[64] The group of Jiya Jose at al.[65] found out viscosity between 5000 and 15000 mPa·s at 5% to 10% w/w of Starch concentration while the group of Shikha and coworkers[66] stated values from 3000 to 8000 mPa·s at 0.5% to 2% of collagen concentration.

These advantages make screen printing a preferred method for ECD fabrication, but to fully appreciate its effectiveness, it is important to understand how the process works and why specific ink properties are essential for its success. Central to the screen printing process is the use of a stencil or template that selectively blocks areas of the mesh screen, allowing ink to pass through only the desired regions with a specific design. A squeegee then applies pressure, forcing the ink through the open mesh areas onto the substrate below, Figure 3.5.[10]

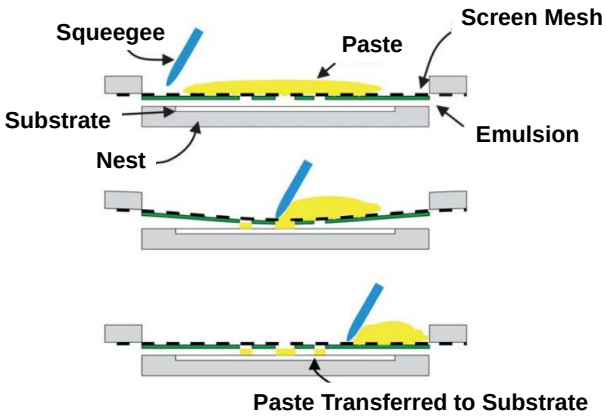


Figure 3.5. Diagram of the screen printing process.[67]

One of the key reasons screen printing is favoured in the production of ECDs is its ability to apply thick layers of ink uniformly, which is essential for the functionality of these devices, as shown in the work of Payman et at. where screen printed layers of EC PEDOT:PSS (polystyrene sulfonate) thick 20 µm reported consistent performance across the display.[68] The inks used in screen printing must possess thixotropic properties, meaning they should have a gel-like consistency that becomes fluid when a shear stress is applied. This property allows the inks to achieve viscosities in the range of 1000 to 10000 mPa·s during application, ensuring they can be easily applied but will not run or bleed once printed, maintaining the precision of the printed patterns.[60,69]

In the field of ECDs several studies have highlighted the effectiveness of screen printing for the deposition of thin films of EC materials. For instance, Andersson and coworkers demonstrated the production of flexible active matrix addressed displays using screen printing, showing high electrical performance with a sheet resistance of 50 Ω/sq and flexibility, maintaining functionality after 1000 bending cycles at a bending radius of 5 mm.[70] Another

study by Guodong and coworkers reported the creation of fully screen-printed ECD which exhibited excellent electrical characteristics, including an elevated CE of 140.63 cm^2/C and fast response time of 1 to 2 seconds (modulating 77%-coloured/bleached).[71] Wei and coworkers demonstrated screen-printed displays on textiles with a 3 x 3 matrix pixel consisting of nine 10×10 mm^2 PEDOT:PSS electrodes, reporting colour change of each electrode within 5 seconds.[72]

These examples underscore the significant advancements achieved through screen printing in the fabrication of ECDs, highlighting its scalability, patterning capability, and suitability for flexible devices. As introduced in the previous section, doctor blade coating also represents a widely used technique in the field, particularly valued for its simplicity, precise thickness control, and ability to produce uniform films. Given their complementary advantages and widespread adoption in ECDs research, both screen printing and doctor blade coating will be employed in this thesis work for the preparation of EC layers. These two techniques have been selected not only for their relevance in the literature but also for their practicality and ease of implementation in a research setting.

3.2 Ink formulation

Ink formulation refers to the process of designing and creating a specific composition of ink, tailored to meet particular requirements for printing. The ink comprises a carefully balanced mixture of solvents, binders, and additives, each playing a central role in the ink's performance and behaviour.[73] Solvents are crucial for dissolving the binders and facilitating the ink's flow through the screen mesh. Binders act as the adhesive component, ensuring the ink adheres properly to the substrate and providing durability and resistance to wear. Additives are incorporated to modify and enhance the ink's properties, such as controlling the drying time, improving adhesion, increasing the stability and adjusting the ink's flow characteristics.

Screen printing inks exhibit non-Newtonian behaviour, which significantly influences their application and performance characteristics. Unlike Newtonian fluids, non-Newtonian fluids possess a viscosity that varies with the rate of shear strain, Figure 3.6a.[74] This property implies that the inks' flow properties change under different conditions of shear stress, thereby affecting the quality and consistency of the printed image. A non-Newtonian behaviour observed in screen printing inks is shear-thinning, also known as pseudoplasticity or thixotropy. Shear-thinning is characterized by a decrease in viscosity with increasing shear rate. This property is advantageous in the screen printing process, as it enables the ink to flow more easily through the mesh of the screen when subjected to force, thus ensuring uniform coverage and reducing

the likelihood of clogging. Once the shear force is removed, the ink rapidly reverts to a higher viscosity, which helps in preventing excessive spreading and maintaining the sharpness of the print edges, Figure 3.6b.[75] The non-Newtonian nature of screen printing inks is crucial in determining print quality. Proper control of viscosity and flow properties ensures that the ink deposits evenly and adheres effectively to the substrate, resulting in sharp, high-quality images.

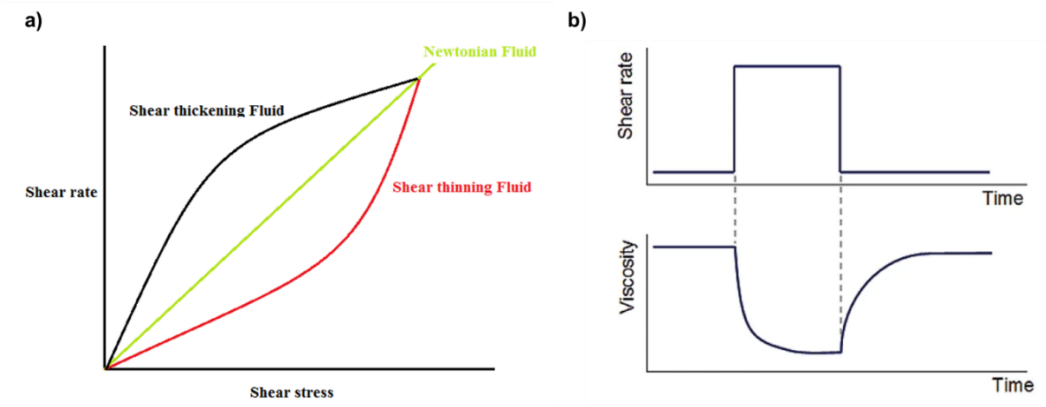


Figure 3.6. a) Relationship between shear rate and shear stress for different types of fluids: Newtonian fluid (green), shear-thickening fluid (black), and shear-thinning fluid (red).[74] b) Shear-thinning behaviour of a non-Newtonian fluid, showing a decrease in viscosity with increased shear rate and subsequent recovery when the shear rate returns to baseline.

Screen printing is widely used for depositing EC inks due to its capability to produce uniform and high-quality films. However, the development of organic EC inks suitable for screen printing faces challenges. These challenges arise because such compounds are generally soluble in organic solvents that, while useful for research, pose significant risks for industrial applications due to their harmful effects. A notable example from the literature involves creating a screen-printable ink based on poly(3,4-propylenedioxythiophene) bis(ethylhexyloxy), a magenta polymer, with poly(vinylidene fluoride-co-hexafluoropropylene) as a binder. The polymer dispersion for this ink is prepared in dichloromethane, a solvent well-known for its efficacy in dissolving polythiophenes, but also classified among CMR substances (carcinogenic, mutagenic, or toxic for reproduction).[76] Further illustrating the solvent-related constraints, Mortimer and coworkers demonstrated that EC polythiophene-based polymers, such as poly(1,3,5-phenylene), poly(triphenylamine), poly(3-hexylthiophene), poly(3,4-(ethylenedioxy)thiophene-didodecyloxybenzene), and poly(dibutyl-3,4-(propylenedioxy)thiophene), can be solubilized in tetrahydrofuran (THF). Although THF is effective as a carrier for deposition techniques like spin coating, it too presents hazards due to its flammability and potential health effects, thereby complicating the formulation of safe and scalable organic EC inks.[77]

Expanding on these solvent-related concerns, several studies have explored the use of poly(3-hexylthiophene) (P3HT), a widely investigated conjugated polymer for EC applications, in chloroform-based formulations. Chloroform is a powerful solvent for P3HT, enabling excellent solubility and thin-film formation, but is also a well-known suspected human carcinogen. In one of the earliest works, Cho and coworkers[78] used a P3HT ink with a concentration of approximately 3 mg/mL in chloroform for printed ion-gel gate dielectrics in polymer thin-film transistors. The inks exhibited excellent printability and film continuity, yet the toxic nature of chloroform posed limitations for commercial applications. Further supporting this, Song and coworkers[79] prepared a screen-printable ink by dissolving P3HT in chloroform at 1 mg/mL to fabricate high-resolution flexible electronic devices. Their work demonstrated the utility of chloroform in ensuring good molecular ordering and consistent electrical performance, but again highlighted the limitations imposed by solvent safety concerns. More recently, Padilla and coworkers compared EC nanoparticle films of P3HT processed from chloroform and THF–water mixtures. Films processed from chloroform exhibited superior switching performance and optical contrast. However, despite the enhanced EC behaviour, the toxicity of chloroform continued to be a limiting factor for sustainable deployment.

These concerns are present even in recent works. For instance, Wang and coworkers developed a class of donor–acceptor-type EC polymers capable of switching from fully transparent to deep black, achieving an $\Delta T>65\%$. Nevertheless, the polymer inks were formulated in chloroform and chlorobenzene. This persistent reliance on hazardous solvents underscores a fundamental dilemma in the field, even state-of-the-art materials often depend on carriers that impede the transition from laboratory-scale innovation to environmentally responsible industrial production. These environmental and health concerns are not isolated cases. Toxicity, flammability, and disposal issues associated with organic solvents are pervasive across the ink formulation landscape.[80] Consequently, there is a growing push to develop water-based inks, as water is non-toxic and environmentally benign. However, this transition is not straightforward. Many EC materials are inherently insoluble in water and require halogenated solvents for processing.[81] Even alternative non-halogenated solvents like toluene, hexanes, and THF still pose flammability and toxicity hazards.[82] To overcome this, researchers have explored strategies to provide water solubility to EC polymers, such as incorporating polar functional groups (*e.g.*, carboxylates, sulfonates, ammonium moieties) or leveraging redox-induced charge states. When direct solubility is not achievable, dispersible formulations can be created by blending hydrophobic materials with water-soluble counterparts.[83,84]

PEDOT is an example of this successful development, wherein PSS was added during synthesis to enhance its solubility.[85] PSS is a water-dispersible polyelectrolyte and a polymer surfactant, acting as a dopant for PEDOT due to its $^{-}SO_3H$ functional group, which serves as the hydrophilic component. When combined, PEDOT and PSS form a composite material known as PEDOT:PSS, characterized by an electrostatic interaction between the positively charged PEDOT cation and the negatively charged PSS anion, Figure 3.7.[86] This complex comprises both positively charged conjugated PEDOT and negatively charged saturated PSS. PEDOT:PSS is widely regarded as the most successful commercially available aqueous dispersion, boasting high water dispersibility, excellent miscibility, and good transparency.

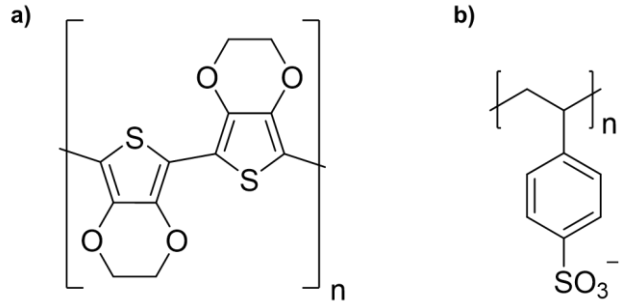


Figure 3.7. Chemical structure of a) PEDOT and b) PSS.

Nevertheless, incorporating these functional groups can significantly impact the electronic characteristics of the molecules and their aggregation behaviour. This alteration in solubility not only affects the materials' hydrophilic nature but also influences their absorption attributes and redox potentials. Consequently, it is crucial to possess a thorough comprehension of how water solubility influences the optoelectronic properties of organic EC materials.

3.3 Aim of the project

The objective of this project is to develop a DA-based ink formulation with tailored rheological properties suitable for doctor blade and screen printing processes. Building upon the liquid EC solution described in Chapter 2, the formulation must be transformed into a viscous, spreadable system capable of controlled deposition and uniform film formation. A crucial requirement is that the formulation keeps its electrochemical functionality, specifically, DA's ability to reduce the ITO electrode, which is responsible for the colour change in the *i*-ECD. To this end, a set of biocompatible and water-soluble binders, Agar Agar, Corn Starch, Polyethylene Glycol (PEG), and Porcine Skin collagen, were selected based on their non-toxic nature, compatibility with the DA–PBS matrix, and chemical inertness with respect to DA oxidation. These materials were identified through a preliminary screening process focused on safety, environmental

sustainability, and formulation stability, with the goal of enabling scalable, cost-effective, and substrate-independent manufacturing of DA-based *i*-ECDs.

RESULT AND DISCUSSION

3.4 DA ink formulation

The selected binders play a critical role in tuning the ink's rheological behaviour by increasing dynamic viscosity and introducing thixotropic properties, both of which are essential for reproducible printing performance, Figure 3.8. Each binder contributes through a distinct mechanism. Polymeric gelation (*e.g.*, Agar Agar), hydrogen bonding (*e.g.*, PEG), or polymer chain entanglement (*e.g.*, Starch and collagen). These interactions, which will be discussed in the following sections, transform the initially low-viscosity DA solution into a stable, gel-like system capable of shear-thinning during deposition and rapid viscosity recovery post-application. This thixotropic behaviour ensures smooth ink flow through the screen mesh or under the doctor blade, while promoting high-resolution patterning, minimising smudging, and enabling uniform film formation.[87] Additionally, these binders support substrate adhesion and film integrity, further enhancing print fidelity and device reliability.[88] The resulting ink formulation meets key manufacturing criteria such as scalability, print precision, and environmental compliance, making it suitable for the production of advanced *i*-ECDs.

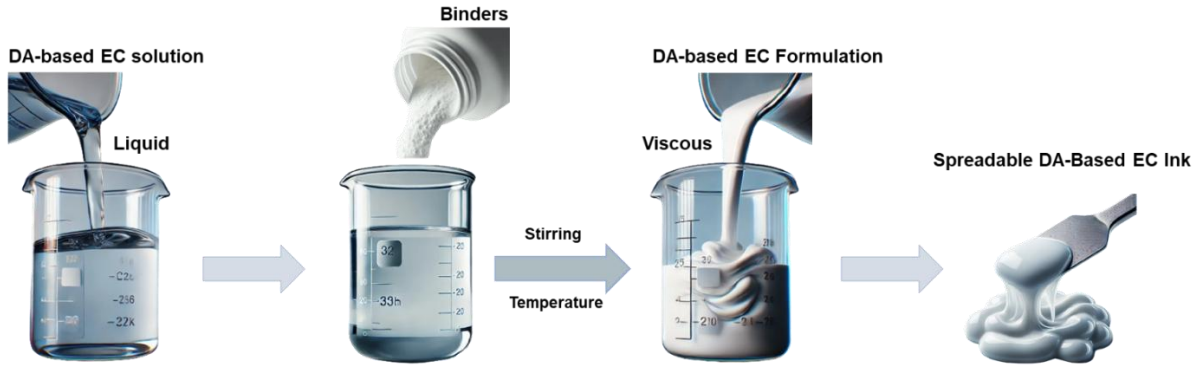


Figure 3.8. Illustrative diagram showing the steps required for the transformation of DA-based EC formulation from liquid to viscous, making it spreadable.

3.4.1 Agar Agar

Agar Agar, a natural polysaccharide extracted from red algae, is composed primarily of agarose and agaropectin. These two components provide a unique structural framework. Agarose

consists of linear chains of repeating galactose units, while agaropectin contains branched regions with sulfate groups and other side chains, Figure 3.9a,b.[89] This molecular architecture imparts desirable gelling and film-forming properties to the material.

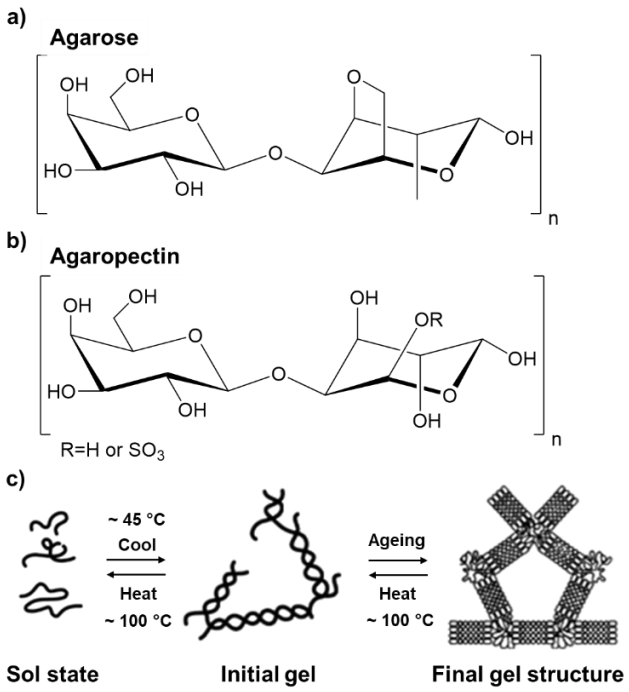


Figure 3.9. Molecular structure of a) Agarose and b) Agaropectin. c) Gelling mechanism of Agar Agar.[90]

When dissolved in hot water, the agarose chains hydrate and uncoil, producing a viscous solution suitable for ink formulation. Upon cooling, hydrogen bonds and hydrophobic interactions facilitate the formation of a three-dimensional gel network, entrapping water molecules and increasing the elasticity and mechanical stability of the resulting film, Figure 3.9c.[91] This process ensures good ink retention on the substrate and facilitates uniform layer deposition. However, the major limitation of Agar Agar lies in its relatively high gelation temperature, typically in the range of 35–45 °C.[92] This property can interfere with room-temperature printing processes, as the ink may prematurely solidify or become unprintable before application. As a result, while Agar Agar offers excellent rheological control and film-forming behaviour, its thermal sensitivity demands careful process control or modification of formulation conditions, potentially including the use of gelling modifiers or alternative binders.

3.4.2 Starch

To address some of the challenges posed by Agar Agar, Starch was considered as an alternative binder. This polysaccharide, abundantly found in plants, offers a more flexible gelation behaviour that is advantageous for screen printing under ambient conditions. Unlike Agar

Agar, Starch does not form a firm gel network at room temperature, enabling higher formulation viscosities while maintaining printability. Starch is composed of two main constituents. Amylose, which consists of mostly linear α-1,4-linked glucose units, and amylopectin, a highly branched polymer with additional α-1,6 linkages, Figure 3.10a,b.[93,94] These two components interact differently with water, affecting the material's hydration, swelling, and thickening properties.

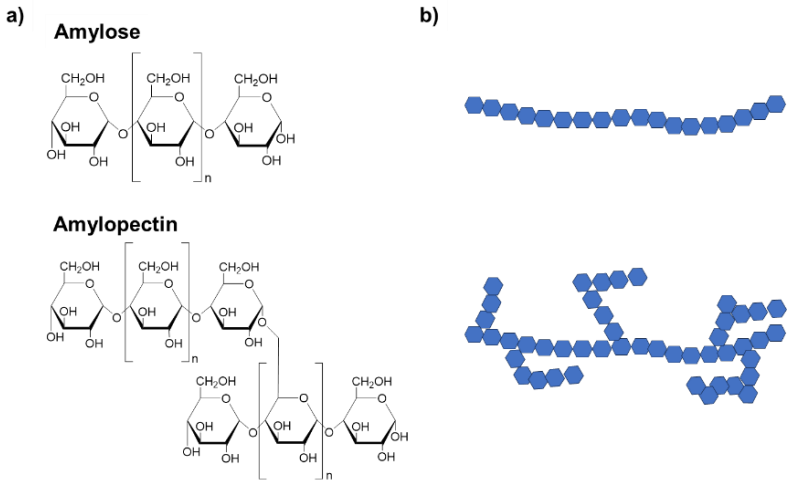


Figure 3.10. a) Molecular structure of Amylose and Amylopectin. b) Corresponding geometry representation showcasing the arrangement of repetitive unit and bonds within the polymer.

Upon heating in water, the Starch granules absorb water, swell, and gradually release amylose and amylopectin into the medium. This leads to a significant increase in viscosity due to polymer entanglement and intermolecular hydrogen bonding.[95] While Starch gelation does occur, it is generally partial and reversible, unlike the rigid, irreversible network formed by Agar Agar. This reversibility grants greater control over viscosity and shear behaviour, allowing for consistent ink flow and levelling during screen printing. A notable drawback of Starch-based formulations, however, is their visual appearance. While Agar Agar gels tend to remain transparent or slightly translucent, Starch-based films often appear opaque or white. This opacity can interfere with optical measurements such as transmittance in ECDs, complicating the monitoring of switching behaviour. On the other hand, this characteristic may prove beneficial by eliminating the need for a separate white backing layer in certain device architectures, thereby simplifying the manufacturing process.

3.4.3 PEG

Polyethylene Glycol (PEG), particularly with a molecular weight of 20000 g/mol, was explored as a synthetic binder that offers tunable viscosity and high solubility in water.[96] PEG is

composed of repeating ethylene glycol units, forming linear chains that can vary in length based on molecular weight requirements. The structure of PEG promotes strong intermolecular interactions when dissolved in water, resulting in entanglement and a corresponding increase in solution viscosity, Figure 3.11a,b.[97]

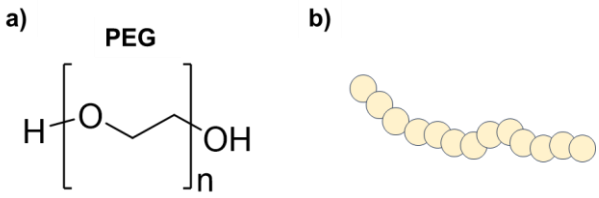


Figure 3.11. a) Molecular structure of Polyethylene Glycol (PEG) b) Corresponding arrangement of repetitive unit and bonds within the polymer.

One of the key advantages of PEG is its stability and compatibility with a wide range of ink additives and functional materials. Its rheological properties can be finely tuned by adjusting the molecular weight and concentration, allowing precise control over ink flow, film thickness, and printing resolution. However, the use of PEG also introduces challenges. To achieve the high viscosities needed for screen printing, relatively large amounts of PEG must be incorporated. This can dilute the concentration of active EC materials within the ink formulation, potentially reducing optical contrast and slowing switching kinetics in the final ECD. Therefore, a balance must be struck between achieving the desired rheological profile and maintaining functional performance.

3.4.4 Porcine skin

The final binder evaluated in this study is collagen derived from Porcine Skin, a biopolymer widely used in biomedical and cosmetic applications due to its natural abundance, biocompatibility, and film-forming ability.[98] Collagen is composed of repeating sequences of three amino acids, glycine, proline, and hydroxyproline, arranged into a characteristic triple-helix structure, Figure 3.12.[99]

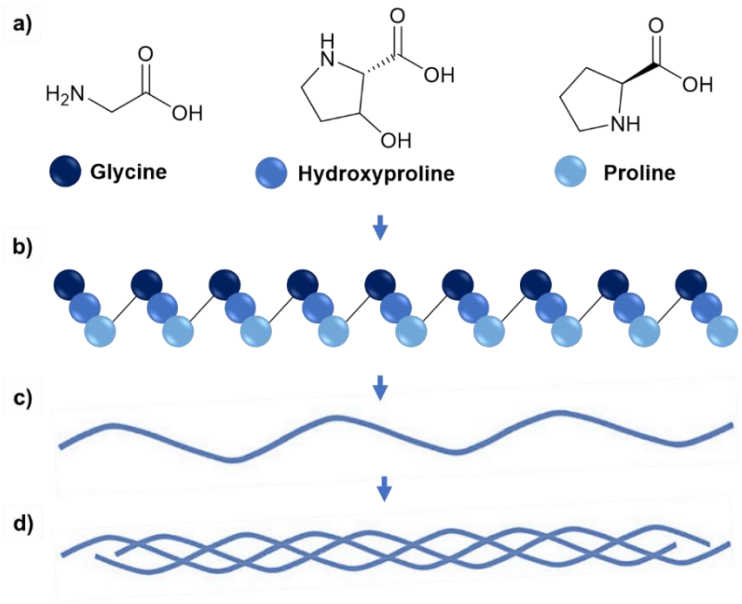


Figure 3.12. a) Molecular structure of the three amino acid Glycine, Hydroxyproline and Proline b) Amino acid sequence. c) Single chain of amino acid sequences. d) Collagen triple helix.

When dispersed in aqueous solution, collagen undergoes partial denaturation and swelling, allowing its molecules to interact via hydrogen bonding and hydrophobic contacts. This leads to the formation of a viscoelastic gel network, capable of entrapping solvent molecules and enhancing the viscosity of the system. This behaviour is particularly useful in printing, where precise control of ink spreading and layer formation is crucial. In terms of functionality, collagen shares similarities with Agar Agar in its ability to form structured gels, but its behaviour under ambient conditions may offer more flexibility for practical applications. Additionally, due to its protein structure, collagen may interact uniquely with substrates or active components, which could improve both adhesion and overall stability.

3.5 Doctor blade ink formulation and *i*-ECD testing

The doctor blade technique was selected as the primary deposition method owing to its simplicity, ease of implementation, and effectiveness in the early stages of ink formulation development. This method offers precise control over film thickness by adjusting the blade height relative to the substrate, which is particularly advantageous when targeting specific thickness values. In the present study, a bi-adhesive frame with a height of 220 µm was employed to define the active area. The doctor blade enabled accurate filling of this cavity and facilitated reliable sealing, either manually or via a laminator, thus supporting the fabrication of the *i*-ECD.

Afterwards, their testing was conducted following the same methodology described in Chapter 2 to ensure consistency in all investigated parameters, including switching time, ΔT, charge consumption, and CE. This approach guarantees comparability across experiments and supports a coherent analysis throughout the manuscript.

3.5.1 P*reliminary assessment and viscosity optimization*

Before initiating the formulation development, a preliminary review of the scientific literature was carried out to gather information on the typical concentration ranges of polymeric binders used in aqueous formulations for deposition techniques such as doctor blade and screen printing. Studies provided useful benchmarks, highlighting common practices in selecting binder content to achieve desirable film-forming and rheological properties.[100–104] These references served as a starting point for estimating the lower and upper concentration limits, offering initial guidance on formulation design. Nevertheless, due to the diverse chemical nature and rheological behaviour of the binders under consideration, as well as the specific flow and spreading requirements of the target deposition process, a systematic experimental screening was deemed necessary to determine the most suitable binder concentrations for the application at hand.

The primary objective of this screening was to determine the optimal viscosity window that ensures adequate rheological behaviour, particularly in terms of flowability and spreadability. Viscosity was identified as the main parameter governing the success of film formation via doctor blade, as it directly impacts the ability of the formulation to homogeneously fill the biadhesive frames without retraction or discontinuities. To this end, dynamic viscosity measurements were performed using a rotational viscometer across a series of formulations containing increasing binder concentrations (from 10 g/L up to 200 g/L). These measurements are reported in Figure 3.13. The results indicate that PEG, although requiring significantly higher concentrations to reach similar viscosities, maintains fluidity due to its lack of three-dimensional network formation. In contrast, Agar Agar and Starch rapidly increase in viscosity as concentration rises, attributed to the formation of gel-like structures that impede solvent mobility. Notably, Agar Agar was measured at 50 °C due to its gelling point, typically in the range of 35–45 °C, which can hinder its ability to flow and spread uniformly if processed below this threshold.[105] Porcine Skin exhibited intermediate behaviour, characterized by delayed gelation and moderate viscosity enhancement. The target viscosity range for optimal blade casting was found to lie between 1000 and 10000 mPa·s. Within this window, formulations

demonstrated suitable flow under low shear conditions, enabling uniform layer formation while avoiding defects such as edge thickening, surface irregularities, or entrapped air.

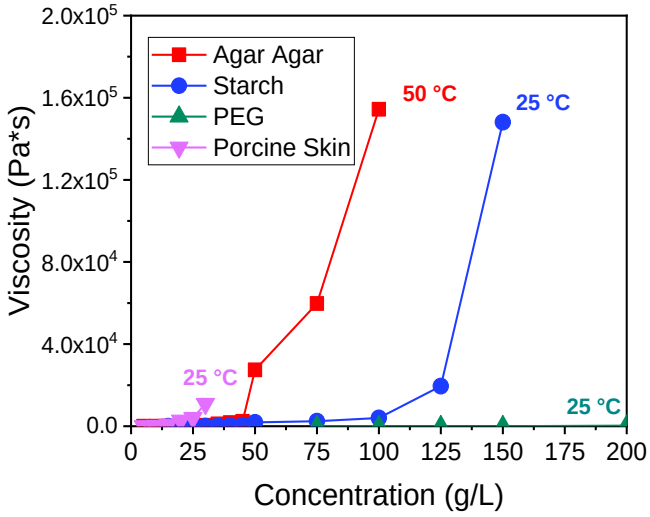


Figure 3.13. Dynamic viscosity measured with a rotational viscosimeter as function of concentration of Agar Agar, Starch, PEG and Porcine Skin.

3.5.2 Preparation and deposition of the DA Ink

Based on the viscosity data obtained, formulations corresponding to concentrations falling within the identified optimal range were selected for further evaluation. The final selection of binder concentrations was as follows, Agar Agar at 10 g/L, Starch at 15 g/L, PEG at 200 g/L, and Porcine Skin at 25 g/L (Table 3.1). These concentrations represented the best compromise between achieving sufficient viscosity for structural integrity and maintaining adequate fluidity to ensure uniform film formation. As shown in Figure 3.14, all selected formulations appear transparent to visible light when stored in vials, with the exception of the Starch-based formulation, which exhibits a distinctly white and opaque appearance.

	Concentration in PBS (g/L)
Agar Agar	10
Starch	15
PEG	200
Porcine Skin	25

Table 3.1. Concentration in PBS of the binders used for the formulation development.

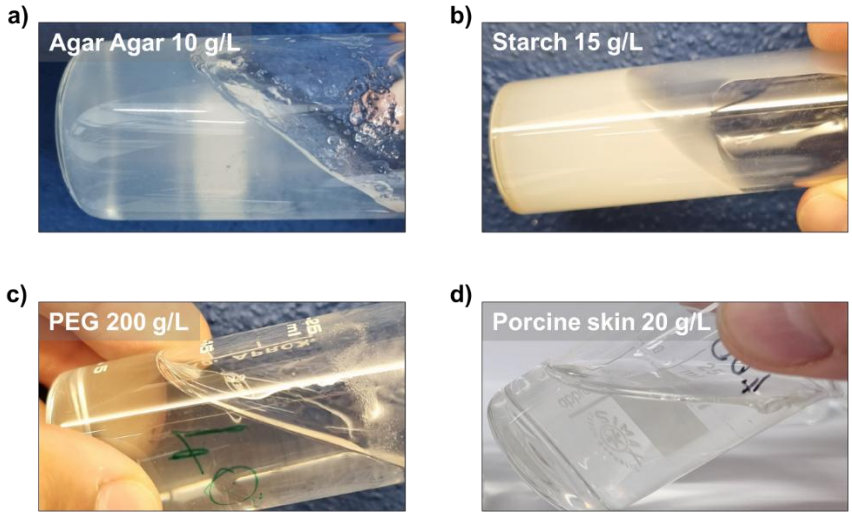


Figure 3.14. Pictures showcasing the formulation with the optimal binder concentrations in PBS for doctor blade casting, featuring Agar Agar at 10 g/L, Starch at 15 g/L, PEG at 200 g/L, and Porcine Skin at 25 g/L.

Following formulation selection, each sample was prepared by gradually dissolving the appropriate amount of binder into a preheated PBS solution. The temperature was maintained at 100 °C to ensure efficient solubilization, and mixing was conducted at 700 rpm using a magnetic stirring bar. The dissolution process was monitored visually, and formulations were considered fully solubilized when no undissolved particles remained. On average, the complete dissolution process required approximately 30 minutes, although this varied slightly depending on the binder. After cooling to room temperature, the formulations were applied using a doctor blade coating technique at a blade speed of 5 mm/s. During this procedure, the protective film covering the adhesive frames was left in place to prevent contamination or premature sealing. This film was only removed after the coating step to enable proper closure and integration of the *i*-ECD, as illustrated in Figure 3.15.

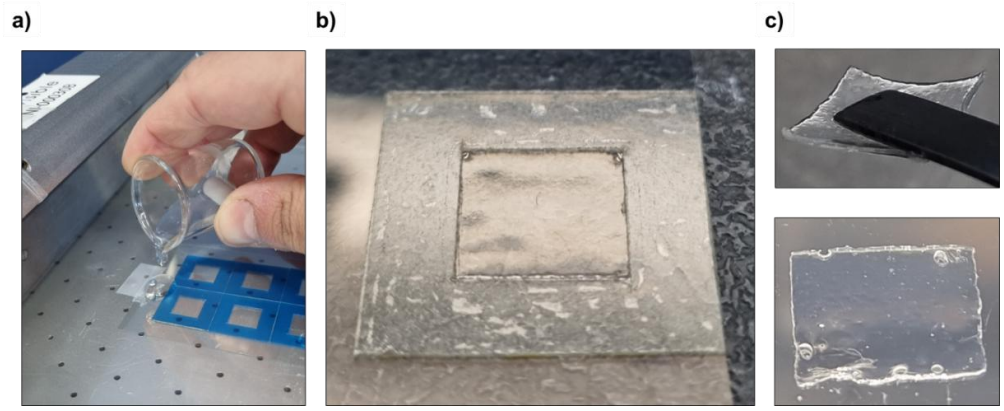


Figure 3.15. a) Pouring of the Agar Agar formulation in proximity of the biadhesive frames prior to doctor blade casting. b) Biadhesive square spacers entirely filled from the Agar Agar formulation after doctor blade casting c) Squared Agar Agar film formed after doctor blade casting and following gelation.

The coating procedure was conducted at room temperature for all formulations, with the exception of those containing Agar Agar, which required deposition at an elevated temperature of approximately 50 °C to maintain adequate fluidity. To assess the impact of processing temperature on coating quality, films cast from Agar Agar formulations at 50 °C and 70 °C were examined via optical microscopy, as shown in Figure 3.16. At 50 °C the formulation exhibits uniform spreading, forming a smooth, continuous film with minimal defects, Figure 3.16a. The viscosity at this temperature is sufficiently high to maintain controlled flow while still preventing premature gelation, resulting in good surface wettability and full coverage of the substrate. No significant air entrapment, film retraction, or edge discontinuities are visible, confirming the suitability of this processing temperature for doctor blade application. In contrast, the films processed at 70 °C show notable degradation in coating quality, Figure 3.16b. The higher temperature leads to a marked decrease in viscosity, which compromises the formulation's ability to wet the surface uniformly. As a result, irregular film morphology is observed, characterized by edge retraction, non-uniform thickness, and the presence of bubbles and voids, particularly in corner regions. These defects are attributed to the excessive fluidity of the solution, which causes poor anchoring to the substrate and facilitates air entrapment during spreading.

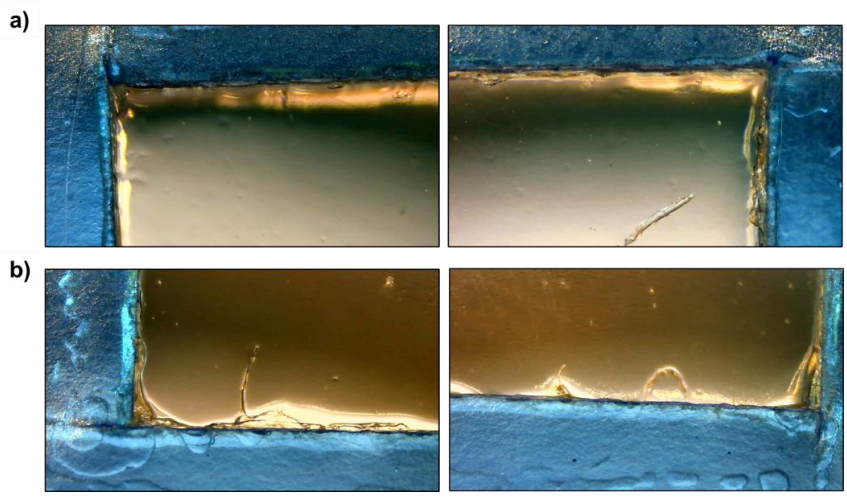


Figure 3.16. Optical microscopy images illustrative of films resulting from the doctor blade process of the Agar Agar formulation poured at a) 50 °C and b) 70 °C.

3.5.3 *Testing of the formulation in i-ECDs: casting, activation and charge consumption*

This paragraph discusses the manufacturing and comparison of EC properties, such as ΔT and charge consumption, acquired via activation of *i*-ECDs prepared employing the formulations developed. Specifically, the impact of different binders concentrations on the ΔT and final

contrast of the *i*-ECD was studied. To make this possible, the EC component DA+AntiOX was included in each formulation in the standard concentration of 10 mg of DA and 5 mg of antioxidant in 1 mL of PBS. Each formulation was then prepared following the previous protocol and adding, at *ca.* 60 °C, DA+AntiOX whose solubilization was facilitated by stirring. The formulations were then deposited at rt (50 °C for Agar Agar) over ITO electrodes through doctor blade, using the protocol explained in Figure 3.15. Subsequently, the *i*-ECDs were manually closed by placing a second ITO electrode over the deposited film and applying pressure on the adhesive frame to fully seal the display.

The first binder under examination was Agar Agar, from which five *i*-ECDs were manufactured using the DA+AntiOX formulation and a concentration of 10 g/L Agar Agar in PBS. Each *i*-ECD was then subjected to progressively increasing voltages (from 1.0 V to 3.0 V) to determine the threshold required for colour change, Figure 3.17a. The results consistently mirror those obtained with *i*-ECDs prepared with PBS. Voltages higher than 1.0 V are required to start the ITO reduction. At 1.5 V, the T@600nm is *ca.* 3%, with comparable results observed for higher voltages, as depicted in the *i*-ECD images. Moreover, variations in the concentration of Agar Agar in PBS do not yield significant changes in the colour change which by applying a constant 1.5 V on five *i*-ECDs prepared at increasing binder concentration, shows T@600 nm lower than 10%, Figure 3.17b. This outcome is confirmed by an intense black colour visible in the *i*-ECDs pictures acquired at the end of the process.

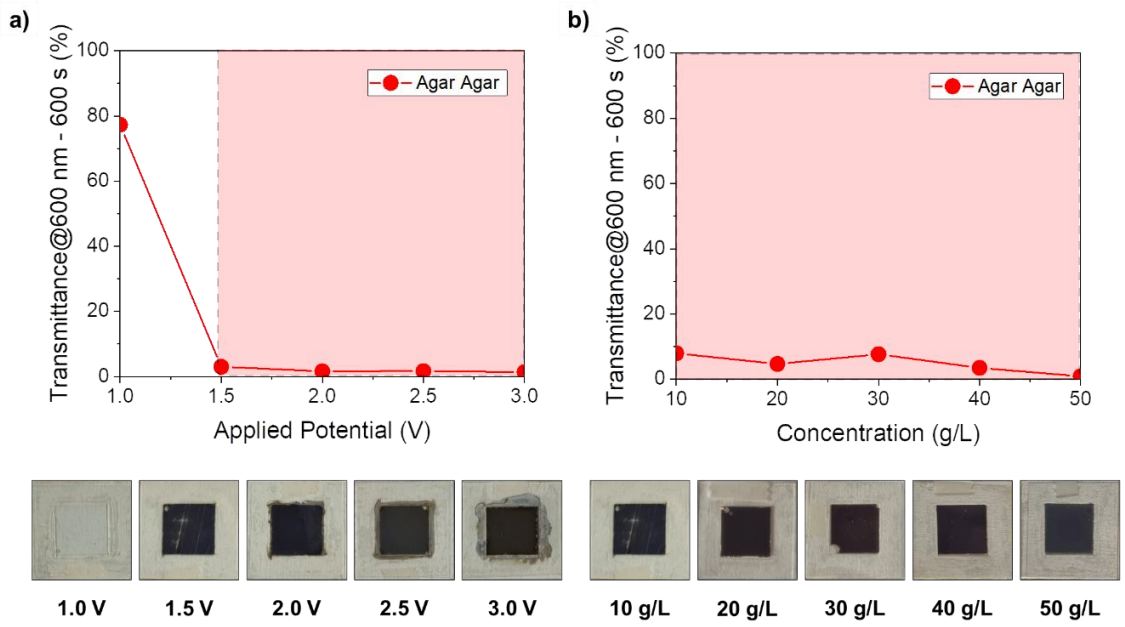


Figure 3.17. a) T@600 nm recorded after activation by applying a voltage ramp for 600 s on five *i*-ECDs DA+AntiOX based prepared with 10 g/L Agar Agar formulation and respective *i*-ECDs pictures. b) T@600 nm recorded after activation by applying 1.5 V for 600 s of five *i*-ECDs DA+AntiOX based prepared with Agar Agar formulation at growing binder concentration and respective *i*-ECDs pictures. The optimal operating parameters for an *i*-ECD in both graphs are indicated in the highlighted light red area.

Similarly, investigations using Starch as a binder yield comparable findings regarding activation thresholds, Figure 3.18a, and colour change performance across different binder concentrations, Figure 3.18b. The main distinction when using Starch as a binder is the initial appearance of the formulation, which is no longer transparent but whitish due to light scattering effects, Figure 3.14b. As a result, the initial T@600 nm decreases significantly (from approximately 80% to 40%), thereby limiting the maximum achievable ΔT after *i*-ECD activation. However, this does not compromise the overall performance, as the T@600 nm reaches values < 5% upon activation, yielding a deep black contrast comparable to that obtained using Agar Agar or PBS alone. Furthermore, the intrinsic whiteness of the Starch-based formulation reduces or eliminates the need to manually provide a white background to enhance visibility of the colour change. At higher applied voltages (≥ 2.0 V), faint brown halos appear around the active area, which are not present when agar or liquid PBS is used as binder. This effect is attributed to electrochemical or thermal degradation of Starch under high voltage conditions, leading to the formation of brownish by-products from the polysaccharide matrix.[106,107]

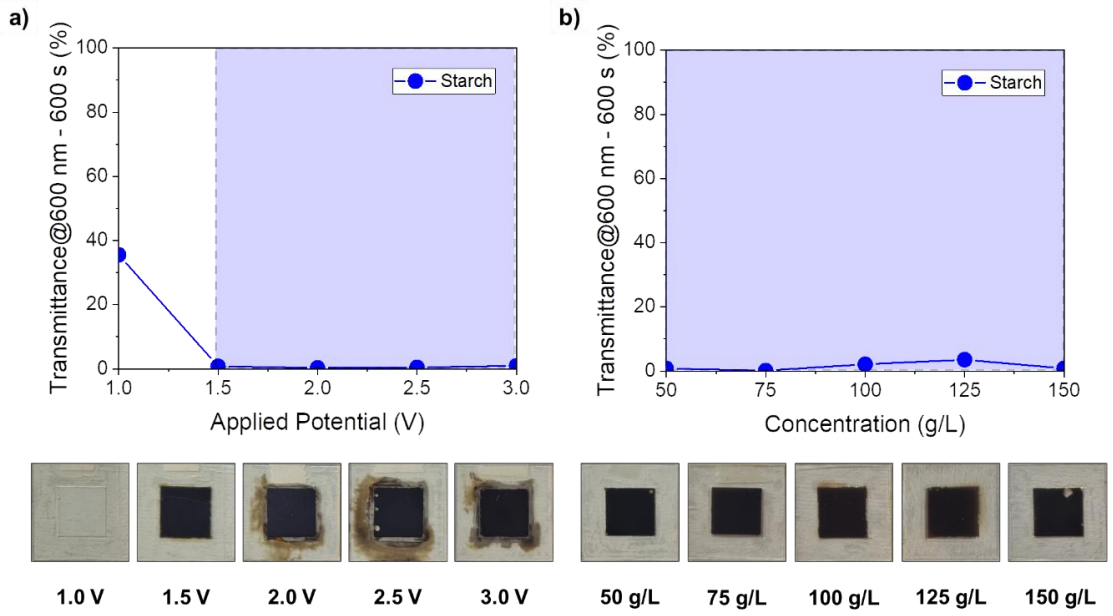


Figure 3.18. a) T@600 nm recorded after activation by applying a voltage ramp for 600 s on five *i*-ECDs DA+AntiOX based prepared with 15 g/L Starch formulation and respective *i*-ECDs pictures. b) T@600 nm recorded after activation by applying 1.5 V for 600 s of five *i*-ECDs DA+AntiOX based prepared with Starch formulation at growing binder concentration and respective *i*-ECDs pictures. The optimal operating parameters for an *i*-ECD in both graphs are indicated in the highlighted light blue area.

In contrast to formulations based on PBS, Agar Agar, or Starch, PEG-based systems exhibit notably higher minimum T@600 nm after activation. This is primarily due to the high PEG content, which impairs efficient ITO reduction. Even at the end of the activation process, T@600 nm typically remains in the range of 10–15%, depending on the applied voltage. The

use of PEG as a binder introduces specific challenges. While elevated PEG concentrations are necessary to achieve viscosities suitable for processing, they negatively affect electrochemical performance by slowing down the ITO reduction rate and limiting the optical contrast. At moderate PEG levels, a visible colour change is still observed, Figure 3.19a, but as PEG concentration increases further, the switching performance deteriorates significantly, as indicated by the higher T@600 nm values measured at the end of voltage application, Figure 3.19b. This reduction in performance is not only due to hindered electrochemical kinetics but also to a dilution effect. Although the DA concentration is kept constant during formulation, increasing the amount of PEG drastically lowers the relative proportion of DA in the mixture. For example, raising PEG content from 200 g/L to 1000 g/L reduces the DA-to-PEG ratio from 1:20 to 1:100. Consequently, each aliquot introduced into the *i*-ECD contains progressively less DA, eventually falling below the threshold needed to trigger effective ITO reduction. At this point, the EC reaction becomes incomplete or entirely absent, as confirmed by the lack of visible switching in *i*-ECDs formulated with 1000 g/L PEG. Moreover, the high PEG content simultaneously dilutes the PBS salts, leading to a marked decrease in ionic conductivity. This further slows down the redox kinetics by limiting ion transport.

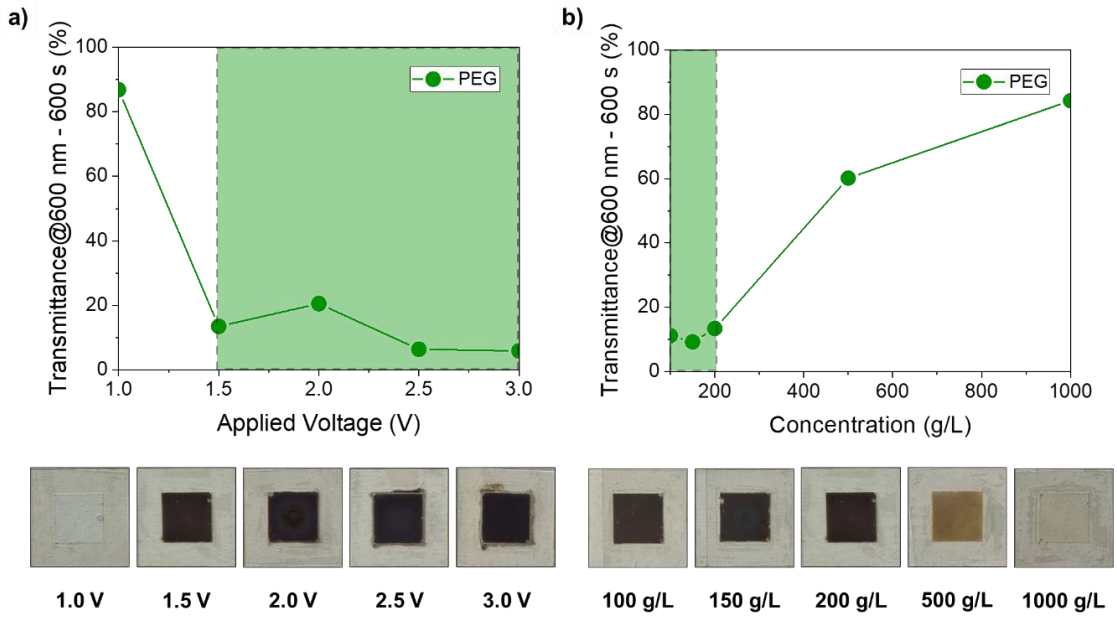


Figure 3.19. T@600 nm recorded after activation by applying a voltage ramp for 600 s on five *i*-ECDs DA+AntiOX based prepared with 200 g/L PEG formulation and respective *i*-ECDs pictures. b) T@600 nm recorded after activation by applying 1.5 V for 600 s of five *i*-ECDs DA+AntiOX based prepared with PEG formulation at growing binder concentration and respective *i*-ECDs pictures. The optimal operating parameters for an *i*-ECD in both graphs are indicated in the highlighted light green area.

Finally, Porcine Skin exhibits electrochemical behaviour comparable to that of Agar Agar, showing similar threshold voltages and efficient ITO reduction across a range of binder

concentrations, Figure 3.20. In all cases, T@600 nm consistently drops below 5% upon activation, confirming the formation of a strong optical contrast.

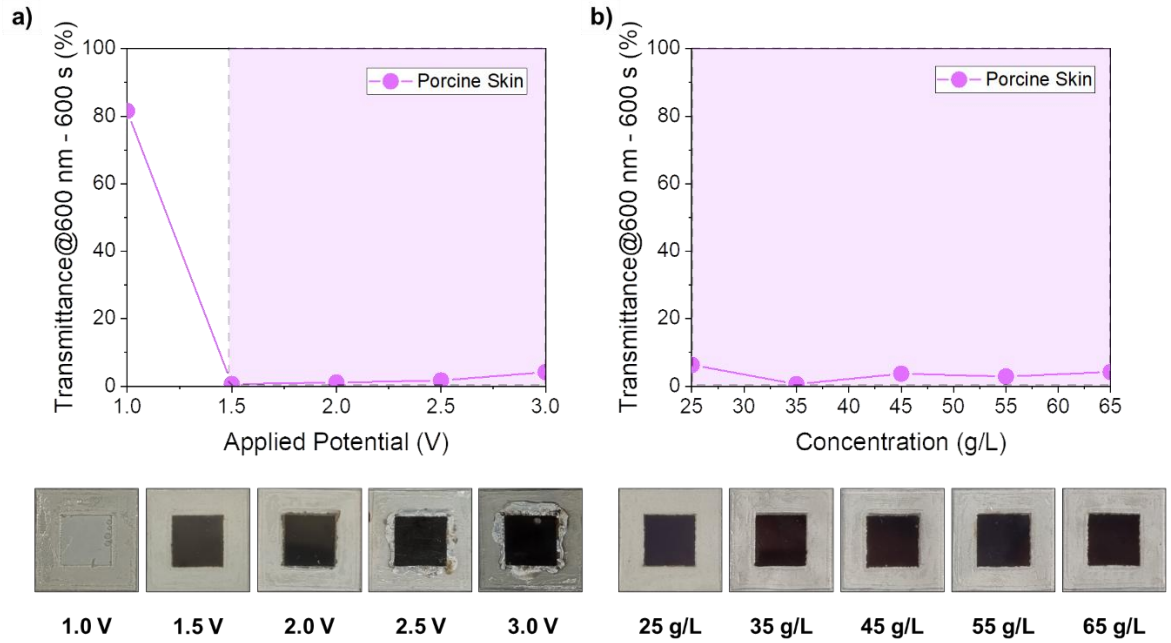


Figure 3.20. T@600 nm recorded after activation by applying a voltage ramp for 600 s on five *i*-ECDs DA+AntiOX based prepared with 25 g/L Porcine Skin formulation and respective *i*-ECDs pictures. b) T@600 nm recorded after activation by applying 1.5 V for 600 s of five *i*-ECDs DA+AntiOX based prepared with Porcine Skin formulation at growing binder concentration and respective *i*-ECDs pictures. The optimal operating parameters for an *i*-ECD in both graphs are indicated in the highlighted light purple area.

The analysis of the activations concludes with a comparison between the various formulations carried out by applying 1.5 V for 600 seconds to ten *i*-ECDs of each set prepared with DA+AntiOX + binder in PBS and evaluating ΔT, the charge consumed and the CE. The data obtained are shown in Figure 3.21a where the PBS was also inserted as a benchmark for comparison. The final T@600 nm and optical contrast achieved by the various *i*-ECDs after electrochemical activation show comparable values to those of the PBS-based reference system, especially in the cases of Agar Agar and Porcine Skin. Both of these binder-containing devices exhibited switching times nearly identical to PBS. Specifically, after 60 seconds of activation at 1.5 V, T@600 nm dropped to approximately 30% for PBS, while Agar Agar and Porcine Skin reached values of 37% and 32%, respectively. Although these differences are relatively minor, they can be attributed primarily to the presence of additional components in the formulations, the binders. These reduce the effective amount of DA introduced into the *i*-ECDs with each withdrawal from the stock solution, thereby influencing the EC behaviour. Furthermore, the formation of a polymeric network by the binders can hinder ion mobility, which in turn slows down the oxidation of DA, directly responsible of the ITO reduction. Starch-based *i*-ECDs also followed a similar switching pattern, reaching a final T@600 nm of

approximately 25% after 60 seconds at 1.5 V. Interestingly, despite achieving a lower transmittance value than PBS, Starch started from a lower initial T@600 nm (around 50%), which contribute to a more rapid approach to the darker state, although the final contrast remains comparable. In contrast, the PEG-based formulation exhibited slower switching dynamics. After the same activation period (60 seconds at 1.5 V), the T@600 nm remained higher, around 57%. The reasons behind this behaviour have been previously discussed in the section dedicated to PEG, highlighting the distinct impact of its physicochemical properties on the switching kinetics.

Despite the differences in kinetics and intermediate transmittance values, all *i*-ECDs, regardless of the binder used, converged to a final T@600 nm below 20% by the end of the full activation period. This substantial decrease in transmittance resulted in a pronounced black state and a strong visual contrast, which was difficult to distinguish by eye among the different formulations. As a result, average ΔT values across the binder-based groups ranged between 60% and 70%, highlighting the EC response achieved. These findings are illustrated in Figure 3.21b, which visually compares the *i*-ECDs post voltage activation. This translates into similar charge consumed and CE, whose values are reported in Table 3.2, confirming the comparable electrochemical performance of the various systems alongside their visual uniformity.

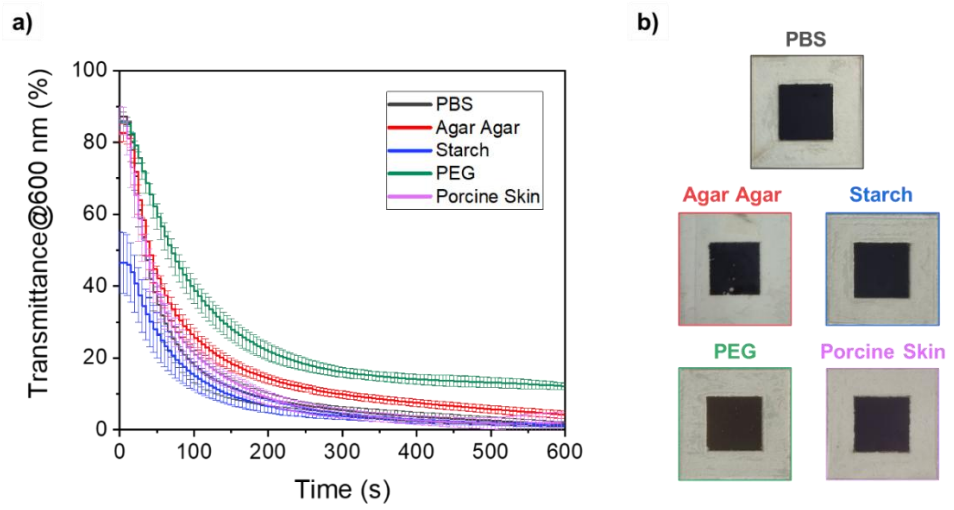


Figure 3.21. a) Average T@600 nm as function of a time for five series of ten *i*-ECDs prepared with DA+AntiOX and each binders, including PBS used as benchmark, activated with 1.5 V for 600 s. b) Pictures of one *i*-ECD for each series acquired at the end of the voltage application.

The charge consumed for Agar Agar, Starch and Porcine Skin are comparable hovering around 200 mC, consistent with the value obtained from PBS alone. Similarly, the CE ranges from 7 to 9 cm^2/C for these binders, in line with the PBS. Lower are the values obtained from the PEG, with a consumed charge of *ca.* 127 mC and a CE of less than 7, reflecting lower ΔT recorded.

	Charge consumption (mC)	CE (cm^2/C)
PBS	207.44 ± 10.07	8.48
Agar Agar	185.40 ± 6.35	6.97
Starch	188.27± 14.19	8.81
PEG	127.48 ± 11.00	6.75
Porcine Skin	207.21 ± 5.04	7.80

Table 3.2. Average charge consumption and CE for five sets of ten *i*-ECDs, each prepared with DA+AntiOX and a different binder. PBS is included as the benchmark.

3.5.4 i-ECDs stability

As with the PBS-based *i*-ECDs, the formulations with binders studied so far were tested for stability, which involved the ability of *i*-ECDs to change colour through applied potential several days after their manufacture. The study scrutinized the colour stability over 70 days post-manufacture of five *i*-ECDs prepared with formulations based on each binder containing DA+AntiOX. These were subjected to a potential of 1.5 V for 600 seconds and their T@600 nm was recorded at the end of the voltage application, Figure 3.22a. The most stable binder observed was Porcine Skin, retaining a T@600 nm of 46.9% after 70 days, followed by Starch at 55.1%. In opposite, over the same time-frame, Agar Agar and PEG exhibited values of 81.9% and 83.2%, respectively, consistent to the pristine *i*-ECDs, indicating that the voltage did not contribute to the reduction of ITO. Notably, PEG showed an increase in T@600 nm to 52.8% after 7 days, while Agar Agar showed 56.8% after 28 days. These contrast differences are clearly visible in Figure 3.22b. The drop in efficiency of these formulations is attributed to solvent loss from the polymer matrix, hindering ionic mobility and affecting ITO reduction.

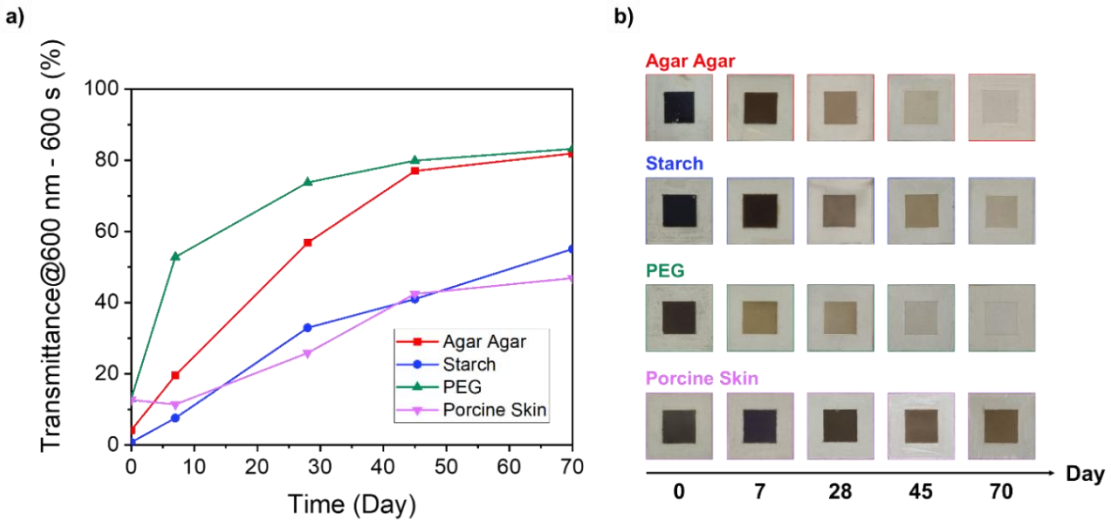


Figure 3.22. a) T@600 nm after the application of 1.5 V for 600 s as function of the time for DA+AntiOX based ECDs prepared with each binders. b) Pictures of the ECDs at the end of the activation process.

This hypothesis is supported by the data presented in Figure 3.23a, which compares five *i*-ECDs prepared with Agar Agar and five with Porcine Skin, stored either under standard laboratory conditions or in a 99% relative humidity environment. The results show that Agar-based devices maintained in high humidity reached a T@600 nm of just 20.7%, whereas those kept under standard conditions exhibited a much higher value of 81.9%. This highlights the detrimental effect of water loss on device performance. As water evaporates, ion mobility within the EC medium is reduced, slowing the redox reactions and resulting in a significantly lower ΔT. Over a period of 70 days, the T@600 nm of Agar Agar *i*-ECDs stored in humid conditions remained consistently below 20% (Figure 3.23b), demonstrating that high environmental moisture effectively preserves their EC response. In contrast, Porcine Skin *i*-ECDs displayed nearly identical transmittance values in both storage conditions, indicating a much lower sensitivity to solvent loss.

This marked difference in stability arises from the distinct water-retention properties of the two materials. Agar Agar gels are known to undergo syneresis, a process in which continued helix-to-helix aggregation gradually contracts the network and expels water to the surface, where it readily evaporates.[108] The resulting gel structure is porous and loosely packed, offering short diffusion paths for water and a low capacity for retention. As a consequence, Agar Agar formulations dry out quickly under ambient conditions, compromising ion transport and device functionality. In contrast, Porcine Skin, primarily composed of gelatin, forms a denser and more compact network of triple helices rich in polar functional groups. This structure strongly binds water molecules via hydrogen bonding, effectively confining them within the matrix and hindering evaporation.[109,110] Therefore, the reduced ΔT observed in Agar-based *i*-ECDs under

ambient conditions can be directly attributed to accelerated water loss, whereas the gelatin matrix in Porcine Skin devices preserves hydration and ion mobility over time, ensuring far greater stability and EC performance.

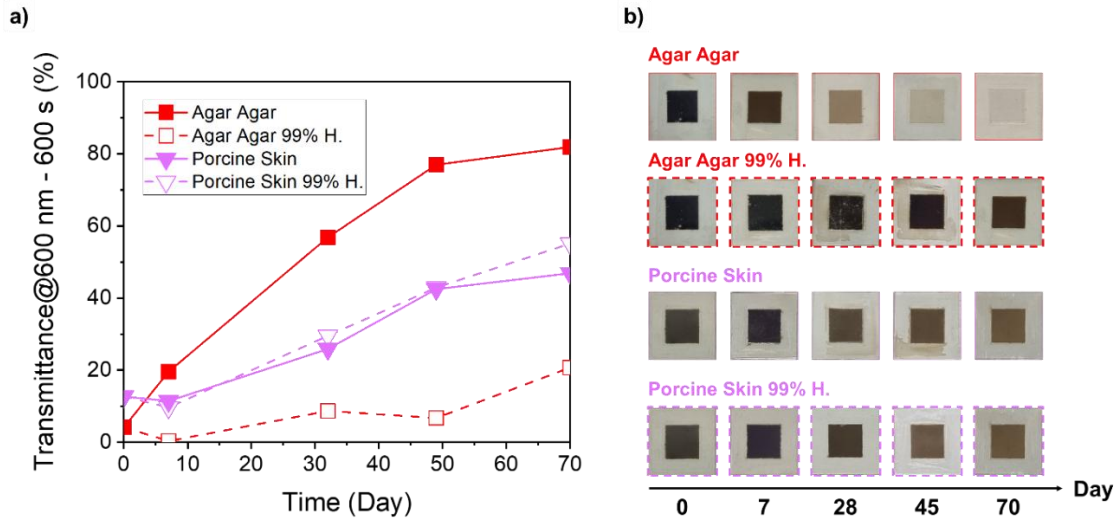


Figure 3.23. a) T@600 nm after the application of 1.5 V for 600 s as function of the time for DA+AntiOX based ECDs prepared with Agar Agar and Porcine Skin stored under standard and humid conditions. b) Pictures of the ECDs at the end of the activation process.

Finally, another critical aspect to consider, independent of the specific binder formulation, is the dehydration of the deposited EC film. As shown in Figure 3.24a, this process begins from the edges of the layer and progressively extends toward the center, leading to complete drying within less than 10 minutes. The high surface-to-thickness ratio of the film accelerates water evaporation, making the system particularly vulnerable to solvent loss immediately after deposition. This dehydration has direct consequences on the functionality of the *i*-ECDs. The loss of water reduces ion mobility within the electrolyte matrix, which in turn disrupts the electrochemical switching mechanism. Without sufficient liquid content, electrolyte ions cannot move freely during voltage application, preventing the redox reactions required for *i*-ECD activation. In the context of Figure 3.24b, is evident that in regions where dehydration has occurred, the *i*-ECDs fail to switch colour entirely. The absence of DA oxidation in these zones also means that no reduction of the ITO electrode takes place, halting the entire EC cycle. This underlines the importance of immediate encapsulation following doctor blade deposition. Delays in sealing allow rapid solvent loss, irreversibly compromising the device's switching capability. Ensuring a controlled humidity environment or using sealing strategies immediately after deposition is therefore essential to preserving the electrochemical activity and long-term performance of the *i*-ECDs.

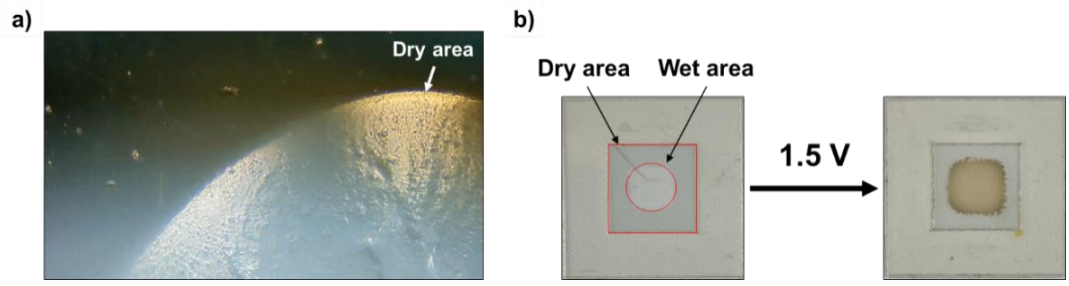


Figure 3.24. a) Agar Agar film viewed under an optical microscope showing a dry central area shortly after blade casting. b) ECD prepared with Agar Agar formulation DA+AntiOX based activated with 1.5 V for 600 s.

3.6 Screen printing ink formulations and *i*-ECD production

To streamline the printing process, a concentrated Agar Agar formulation (20 g/L; ~500 mPa·s at 50 °C) was prepared by dissolving 200 mg of Agar Agar in 10 mL of PBS, following the established protocol. This concentration was selected to achieve the target viscosity range for screen printing (1000–10000 mPa·s),[88,111,112] ensuring proper transfer through the mesh. The formulation was applied onto the screen at approximately 50 °C to prevent premature gelation. However, due to the thermal inertia of the printing setup, including the screen, substrate, and squeegee, the formulation rapidly cools upon contact. This cooling results in a progressive increase in viscosity, which enhances mechanical adhesion to the substrate. As the squeegee exerts pressure during printing, the formulation is effectively pressed through the mesh and remains fixed in place over the substrate upon deposition.

Due to the vigorous stirring and viscosity reached during the preparation of the formulations, given by the elevated amount of Agar Agar, multiple air bubbles were trapped during the stirring. It was observed that their removal before the printing process is crucial to avoid inhomogeneity of the film over the substrate, Figure 3.25ab. Because the deposited films are a few microns thick, dehydration becomes significantly important compared to films deposited via doctor blade. Therefore, prompt closure of the *i*-ECD following screen printing is crucial to avoid solvent evaporation, which affects the performance of the display. Indeed, the procedure implemented with the prototype depicted in Figure 3.25b involved sealing the *i*-ECD immediately after depositing the EC film onto the ITO electrode. This sealing was achieved by placing a second ITO electrode on top of the film, ensuring careful handling to avoid excessive pressure that might lead to the electrodes coming into contact and causing a short circuit. Scotch tape was utilized for sealing since double-sided adhesive tapes of appropriate thickness were not available. Excessively thick tapes, such as the previously used NITTO double-sided tape (220 µm), would create unwanted air gaps within the *i*-ECD, thereby impeding its functionality.

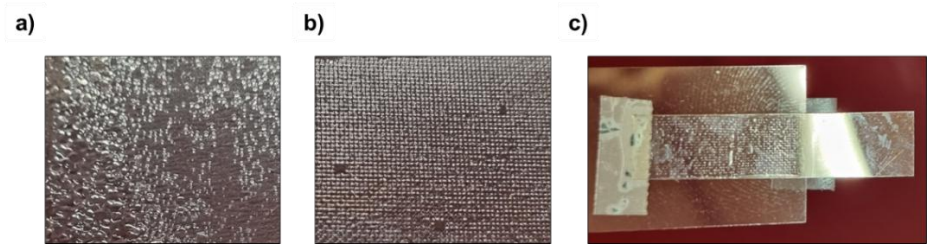


Figure 3.25. Pictures of the PET substrate after screen printing trials of the formulation based with Agar Agar a) before and b) after bubble remotion. c) ECD prototype with the Agar Agar formulation screen printed.

Following formulation preparation, the manufactured *i*-ECD was activated by applying 1.5 V for 600 seconds, resulting in the characteristic black colour indicative of ITO reduction, Figure 3.26. However, unlike *i*-ECDs manufactured using liquid solutions, which presented a homogenous and uniform black layer, the mesh spots of the employed screen for printing are visible on the electrode surface. Additionally, the deposited film displays empty areas, suggesting that further optimization steps of the formulation are required. Further, since Agar Agar-based formulations require temperatures above their jellying point (35–45 °C), it cannot be used at room temperature, which poses problems for its use on a large scale, in contrast to the reason for screen printing to be used.

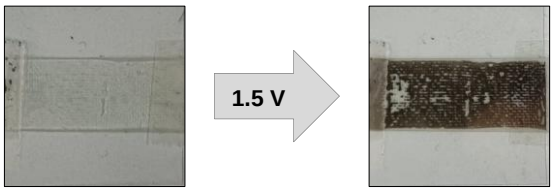


Figure 3.26. Activation with 1.5 V for 600 s of an ECD prototype prepared with a screen printed formulation of Agar Agar with DA+AntiOX.

3.7 Conclusions and outlook

This chapter examined the formulation and deposition of DA-based EC inks for use in inkjet-free *i*-ECDs, focusing on doctor blade coating and screen printing as scalable fabrication techniques. The doctor blade technique enabled the successful deposition of EC formulations with thicknesses precisely defined by 220 µm biadhesive frames, facilitating reproducible film morphology and sealing procedures. Through systematic viscosity optimization, four binders, Agar Agar, Starch, PEG, and Porcine Skin, were tested at various concentrations, with optimal viscosities (1000–10000 mPa·s) achieved at 10 g/L, 15 g/L, 200 g/L, and 25 g/L, respectively. All formulations, when loaded with 10 mg/mL DA and 5 mg/mL antioxidant in PBS, yielded functional *i*-ECDs with effective EC performance. Specifically, upon applying 1.5 V for 600 s, all *i*-ECDs achieved T@600 nm below 20%, with ΔT values ranging from 60% to 70%,

confirming effective ITO reduction and deep black contrast. Charge consumption was comparable for Agar Agar (185.4 ± 6.35 mC), Starch (188.3 ± 14.2 mC), and Porcine Skin (207.2 ± 5.0 mC), aligning closely with the PBS benchmark (207.4 ± 10.1 mC). Corresponding CE also remained high, between 6.97 and 8.81 cm^2/C. PEG-based formulations, while reaching the target viscosity only at high concentrations (≥200 g/L), demonstrated inferior electrochemical performance. These systems exhibited slower switching, higher residual T@600 nm (10–15%), and lower CE (6.75 cm^2/C), due to binder dilution effects and reduced ionic mobility.

From a processing standpoint, Agar Agar required deposition at 50 °C to avoid premature gelation, but above 70 °C, film homogeneity deteriorated due to over-fluidity. Screen printing trials with Agar Agar (20 g/L) produced functional *i*-ECDs, yet bubble trapping and mesh artifacts led to poor uniformity, indicating that additional rheological tuning is required to make the formulation compatible with industrial-scale screen printing. Long-term stability tests revealed Porcine Skin to be the most robust binder, maintaining T@600 nm as low as 46.9% after 70 days, even under ambient conditions. In contrast, Agar Agar and PEG showed significant performance degradation due to water loss, with final T@600 nm values of 81.9% and 83.2%, respectively. Indeed, *i*-ECDs stored in 99% relative humidity retained their switching ability, particularly those based on Agar Agar, underscoring the critical role of moisture in maintaining ion mobility. The distinct syneresis behaviour of Agar Agar and the dense hydrogen-bonding network in gelatin (Porcine Skin) explain the observed differences in water retention and stability. Finally, the high surface-to-thickness ratio of deposited films (~220 µm thick) caused rapid dehydration within 10 minutes post-casting, stressing the need for immediate sealing to preserve electrochemical functionality.

Future efforts should concentrate on refining screen-printable ink formulations capable of operating at room temperature. For this, the rheological behaviour of biopolymeric binders must be fine-tuned to balance thixotropy, viscosity, and water retention.[113] Alternatives to Agar Agar, such as blends of Starch or collagen with plasticizers, could enable effective screen printing without thermal requirements.[114] Exploring crosslinkable or semi-interpenetrating polymer networks may also provide enhanced mechanical stability and water retention. Additionally, high-throughput rheological profiling and mesh-specific ink optimization will be essential for upscaling. Moreover, adopting encapsulation strategies, such as barrier coatings or humidity-controlled roll-to-roll lamination, could significantly improve display longevity.[115] Integrating advanced polymer electrolytes or hydrogel matrices with tailored ionic conductivity and low evaporation rates presents another promising direction. In conclusion, the results establish a solid foundation for sustainable, aqueous, and scalable EC

ink systems. With targeted optimization of formulation chemistry and deposition parameters, doctor blade and screen printing can be harnessed for the cost-effective fabrication of flexible, patterned *i*-ECDs suitable for integration into smart labels, displays, and adaptive surfaces.

REFERENCES

[1] C. Gu, A.-B. Jia, Y.-M. Zhang, S. X.-A. Zhang, *Chem Rev* **2022**, *122*, 14679–14721.

[2] A. Cannavale, U. Ayr, F. Fiorito, F. Martellotta, *Energies* **2020**, *13*, 1449.

[3] H. Fan, W. Wei, C. Hou, Q. Zhang, Y. Li, K. Li, H. Wang, *J. Mater. Chem. C* **2023**, *11*, 7183–7210.

[4] Q. Lei, Y. Wang, W. Dong, H. Sun, J. Lv, H. Li, *Journal of Electroanalytical Chemistry* **2019**, *839*, 108–115.

[5] S. Guan, W. Wang, B. Li, J. Zheng, C. Xu, *J. Mater. Chem. C* **2019**, *7*, 7520–7524.

[6] K. Tajima, T. Kubota, C. Y. Jeong, *Thin Solid Films* **2022**, *758*, 139412.

[7] A. Maho, S. Nayak, F. Gillissen, R. Cloots, A. Rougier, *Coatings* **2023**, *13*, 1879.

[8] N. Nang Dinh, N. Minh Quyen, D. N. Chung, M. Zikova, V.-V. Truong, *Solar Energy Materials and Solar Cells* **2011**, *95*, 618–623.

[9] J. Velasco, A. Ateka, I. R. De Larramendi, F. J. Del Campo, *Electrochimica Acta* **2024**, *493*, 144414.

[10] J. Suikkola, T. Björninen, M. Mosallaei, T. Kankkunen, P. Iso-Ketola, L. Ukkonen, J. Vanhala, M. Mäntysalo, *Sci Rep* **2016**, *6*, 25784.

[11] L. Hakola, E. Jansson, R. Futsch, T. Happonen, V. Thenot, G. Depres, A. Rougier, M. Smolander, *Int J Adv Manuf Technol* **2021**, *117*, 2921–2934.

[12] C. Friebe, M. D. Hager, A. Winter, U. S. Schubert, *Advanced Materials* **2012**, *24*, 332–345.

[13] S. Lin, Q. Wu, Y. Lu, *ChemElectroChem* **2024**, *11*, e202300776.

[14] J. Zeng, H. Li, Z. Wan, L. Ai, P. Liu, W. Deng, *Solar Energy Materials and Solar Cells* **2019**, *195*, 89–98.

[15] E. L. Howard, C. A. T. Laia, C. Pinheiro, A. J. Parola, *J Appl Electrochem* **2024**, *54*, 547–557.

[16] E. Poverenov, M. Li, A. Bitler, M. Bendikov, *Chem. Mater.* **2010**, *22*, 4019–4025.

[17] W. Fu, H. Chen, Y. Han, W. Wang, R. Zhang, J. Liu, *New J. Chem.* **2021**, *45*, 19082–19087.

[18] M. S. Bhuiyan, M. Paranthaman, K. Salama, *Supercond. Sci. Technol.* **2006**, *19*, R1–R21.

[19] M. Clausi, M. G. Santonicola, S. Laurenzi, *Composites Part A: Applied Science and Manufacturing* **2016**, *88*, 86–97.

[20] C.-C. Chang, C.-L. Pai, W.-C. Chen, S. A. Jenekhe, *Thin Solid Films* **2005**, *479*, 254–260.

[21] C. Glynn, C. O'Dwyer, *Advanced Materials Interfaces* **2017**, *4*, 1600610.

[22] S. R. Forrest, *Nature* **2004**, *428*, 911–918.

[23] A. Khan, M. A. Gaikwad, J. H. Kim, A. Kadam, *Tungsten* **2024**, DOI 10.1007/s42864-024-00269-x.

[24] X. Huang, J. Chen, H. Xie, F. Zhao, S. Fan, Y. Zhang, *Sci. China Mater.* **2022**, *65*, 2217–2226.

[25] G. H. Shim, M. G. Han, J. C. Sharp-Norton, S. E. Creager, S. H. Foulger, *J. Mater. Chem.* **2008**, *18*, 594–601.

[26] F. Aziz, A. F. Ismail, *Materials Science in Semiconductor Processing* **2015**, *39*, 416–425.

[27] M. Habibi, A. Rahimzadeh, I. Bennouna, M. Eslamian, *Coatings* **2017**, *7*, 42.

[28] J. Silvano, S. Hamtaei, P. Verding, B. Vermang, W. Deferme, *ACS Appl. Energy Mater.* **2023**, *6*, 7363–7376.

[29] H. Wang, M. Barrett, B. Duane, J. Gu, F. Zenhausern, *Materials Science and Engineering: B* **2018**, *228*, 167–174.

[30] A. Abdellah, B. Fabel, P. Lugli, G. Scarpa, *Organic Electronics* **2010**, *11*, 1031–1038.

[31] W. T. Neo, Q. Ye, S.-J. Chua, J. Xu, *J. Mater. Chem. C* **2016**, *4*, 7364–7376.

[32] C. Dawo, H. Chaturvedi, *Flex. Print. Electron.* **2023**, *8*, 013001.

[33] C.-W. Chang-Jian, E.-C. Cho, S.-C. Yen, B.-C. Ho, K.-C. Lee, J.-H. Huang, Y.-S. Hsiao, *Dyes and Pigments* **2018**, *148*, 465–473.

[34] J. H. Choi, G. Balamurugan, G. K. Pande, Y. S. Eom, H.-K. Kim, D. E. Cha, J. S. Park, *Thin Solid Films* **2022**, *743*, 139067.

[35] S. Zhang, J. Ren, S. Chen, Y. Luo, X. Bai, L. Ye, F. Yang, Y. Cao, *Journal of Electroanalytical Chemistry* **2020**, *870*, 114248.

[36] S. Hong, B. Park, C. Balamurugan, J. Lee, S. Kwon, *Heliyon* **2023**, *9*, e18209.

[37] R. Ramos-Hernández, F. D. Calvo, E. Pérez-Gutiérrez, M. J. Percino, *Thin Solid Films* **2023**, *771*, 139787.

[38] I. Mjejri, C. M. Doherty, M. Rubio-Martinez, G. L. Drisko, A. Rougier, *ACS Appl. Mater. Interfaces* **2017**, *9*, 39930–39934.

[39] A. Glasser, É. Cloutet, G. Hadziioannou, H. Kellay, *Chem. Mater.* **2019**, *31*, 6936–6944.

[40] R. R. Søndergaard, M. Hösel, F. C. Krebs, *Journal of Polymer Science Part B: Polymer Physics* **2013**, *51*, 16–34.

[41] H. Yang, P. Jiang, *Langmuir* **2010**, *26*, 13173–13182.

[42] R. Anastasio, E. E. L. Maassen, R. Cardinaels, G. W. M. Peters, L. C. A. van Breemen, *Polymer* **2018**, *150*, 84–94.

[43] H. Pourkheirollah, J. Keskinen, M. Mäntysalo, D. Lupo, *Journal of Power Sources* **2022**, *535*, 231475.

[44] R. Ramos-Hernández, F. D. Calvo, E. Pérez-Gutiérrez, M. J. Percino, *Thin Solid Films* **2023**, *771*, 139787.

[45] H.-C. Hsu, S.-H. Wu, Y.-L. Tung, C.-F. Shih, *Organic Electronics* **2022**, *101*, 106400.

[46] P. Polfer, Z. Fu, T. Breinlinger, A. Roosen, T. Kraft, *Journal of the American Ceramic Society* **2016**, *99*, 3233–3240.

[47] T. Tan, P.-K. Lee, N. Zettsu, K. Teshima, D. Y. W. Yu, *Journal of Power Sources* **2020**, *453*, 227874.

[48] T. Cygan, M. Petrus, J. Wozniak, S. Cygan, D. Teklińska, M. Kostecki, L. Jaworska, A. Olszyna, *Ceramics International* **2020**, *46*, 7170–7177.

[49] S. Valsalakumar, A. Roy, T. K. Mallick, J. Hinshelwood, S. Sundaram, *Energies* **2023**, *16*, 190.

[50] D. H. Ninh, T. T. Thao, N. N. Dinh, P. D. Long, *Communications in Physics* **2014**, *24*, 57–63.

[51] I. Mjejri, L. M. Manceriu, M. Gaudon, A. Rougier, F. Sediri, *Solid State Ionics* **2016**, *292*, 8–14.

[52] C. Park, J. M. Kim, Y. Kim, S. Bae, M. Do, S. Im, S. Yoo, J. H. Kim, *ACS Appl. Electron. Mater.* **2021**, *3*, 4781–4792.

[53] H. N. M. Sarangika, G. K. R. Senadeera, M. A. K. L. Dissanayake, *Ionics* **2024**, *30*, 1627–1638.

[54] F. C. Krebs, *Solar Energy Materials and Solar Cells* **2009**, *93*, 394–412.

[55] M. Aller-Pellitero, J. Fremeau, R. Villa, G. Guirado, B. Lakard, J.-Y. Hihn, F. J. del Campo, *Sensors and Actuators B: Chemical* **2019**, *290*, 591–597.

[56] J. Jensen, M. Hösel, A. L. Dyer, F. C. Krebs, *Advanced Functional Materials* **2015**, *25*, 2073–2090.

[57] P. Andersson Ersman, R. Lassnig, J. Strandberg, P. Dyreklev, *Advanced Engineering Materials* **2021**, *23*, 2000771.

[58] G. Liu, Z. Wang, J. Wang, H. Liu, Z. Li, *Journal of Colloid and Interface Science* **2024**, *655*, 493–507.

[59] R. Brooke, A. Fall, M. Borràs, D. B. Yilma, J. Edberg, S. Martinez-Crespiera, C. Aulin, V. Beni, *Flex. Print. Electron.* **2021**, *6*, 045011.

[60] R. Brooke, A. Fall, M. Borràs, D. B. Yilma, J. Edberg, S. Martinez-Crespiera, C. Aulin, V. Beni, *Flex. Print. Electron.* **2021**, *6*, 045011.

[61] J. Velasco, A. Ateka, I. R. De Larramendi, F. J. Del Campo, *Electrochimica Acta* **2024**, *493*, 144414.

[62] K. Guo, G. Zhang, Y. Long, H. Ning, Z. Xu, T. Qiu, D. Luo, M. Li, R. Yao, J. Peng, *Coatings* **2021**, *11*, 872.

[63] F. Hoeng, A. Denneulin, N. Reverdy-Bruas, G. Krosnicki, J. Bras, *Applied Surface Science* **2017**, *394*, 160–168.

[64] G. Hübner, M. Krebes, L. Cirstea, A. Kolesova, *Advances in Printing and Media Technology* **2022**, *48*, 156–170.

[65] J. Jose, A. Peter, K. Y. Thajudeen, M. D. L. Gomes Pereira, A. V P, S. G. Bhat, H. Michel, *Results in Engineering* **2024**, *22*, 102060.

[66] S. Chaudhary, E. Chakraborty, *Beni-Suef Univ J Basic Appl Sci* **2022**, *11*, 3.

[67] F.-D. Munteanu, A. M. Titoiu, J.-L. Marty, A. Vasilescu, *Sensors* **2018**, *18*, 901.

[68] P. Tehrani, L.-O. Hennerdal, A. L. Dyer, J. R. Reynolds, M. Berggren, *J. Mater. Chem.* **2009**, *19*, 1799–1802.

[69] H. Menon, R. Aiswarya, K. P. Surendran, *RSC Adv.* **2017**, *7*, 44076–44081.

[70] P. Andersson Ersman, K. Freitag, M. Nilsson, J. Åhlin, R. Brooke, N. Nordgren, C. Aulin, A. Fall, Y. Nevo, V. Beni, *Advanced Photonics Research* **2023**, *4*, 2200012.

[71] G. Liu, Z. Wang, J. Wang, H. Liu, Z. Li, *Journal of Colloid and Interface Science* **2024**, *655*, 493–507.

[72] Y. Wei, X. Wang, R. Torah, J. Tudor, **n.d.**, DOI 10.1049/el.2017.0119.

[73] Y. Zhang, Y. Zhu, S. Zheng, L. Zhang, X. Shi, J. He, X. Chou, Z.-S. Wu, *Journal of Energy Chemistry* **2021**, *63*, 498–513.

[74] A. Sojoudi, S. C. Saha, *American Journal of Fluid Dynamics* **2012**, *2*, 117–121.

[75] J. W. Phair, M. Lundberg, A. Kaiser, *Rheol Acta* **2009**, *48*, 121–133.

[76] S. Santiago, M. Aller, F. J. del Campo, G. Guirado, *Electroanalysis* **2019**, *31*, 1664–1671.

[77] R. J. Mortimer, A. L. Dyer, J. R. Reynolds, *Displays* **2006**, *27*, 2–18.

[78] J. H. Cho, J. Lee, Y. Xia, B. Kim, Y. He, M. J. Renn, T. P. Lodge, C. Daniel Frisbie, *Nature Mater* **2008**, *7*, 900–906.

[79] D. Song, A. Mahajan, E. B. Secor, M. C. Hersam, L. F. Francis, C. D. Frisbie, *ACS Nano* **2017**, *11*, 7431–7439.

[80] M. Tobiszewski, J. Namieśnik, F. Pena-Pereira, *Green Chemistry* **2017**, *19*, 1034–1042.

[81] X. Shao, W. Li, Y. Kuai, Q. Huang, Y. Dong, C. Zhang, W.-Y. Wong, M. Ouyang, *Synthetic Metals* **2021**, *282*, 116953.

[82] F. P. Byrne, S. Jin, G. Paggiola, T. H. M. Petchey, J. H. Clark, T. J. Farmer, A. J. Hunt, C. Robert McElroy, J. Sherwood, *Sustainable Chemical Processes* **2016**, *4*, 7.

[83] T. A. Welsh, E. R. Draper, *RSC Advances* **2021**, *11*, 5245–5264.

[84] E. S. Nurazizah, A. Aprilia, R. Risdiana, L. Safriani, *Polymers* **2023**, *15*, 2725.

[85] T. Horii, H. Hikawa, Y. Mochizuki, H. Okuzaki, *Trans. Mat. Res. Soc. Japan* **2012**, *37*, 515–518.

[86] Z. Wang, R. Liu, *Materials Today Electronics* **2023**, *4*, 100036.

[87] C. Mao, Y. Tian, X. Zhou, J. Bai, S. Ma, H. Wang, *Colloids and Surfaces A: Physicochemical and Engineering Aspects* **2024**, *682*, 132982.

[88] H.-W. Lin, C.-P. Chang, W.-H. Hwu, M.-D. Ger, *Journal of Materials Processing Technology* **2008**, *197*, 284–291.

[89] Y. Pandya, M. Bakshi, A. Sharma, **2022**, *11*, 1151–1157.

[90] H. P. S. Abdul Khalil, Y. Y. Tye, C. K. Saurabh, C. P. Leh, T. K. Lai, E. W. N. Chong, M. R. Nurul Fazita, J. Mohd Hafiidz, A. Banerjee, M. I. Syakir, *Express Polym. Lett.* **2017**, *11*, 244–265.

[91] B. Dai, S. Matsukawa, *Food Hydrocolloids* **2012**, *26*, 181–186.

[92] M. Lahaye, C. Rochas, *Hydrobiologia* **1991**, *221*, 137–148.

[93] M. J. Miles, V. J. Morris, P. D. Orford, S. G. Ring, *Carbohydrate Research* **1985**, *135*, 271–281.

[94] H. Fredriksson, J. Silverio, R. Andersson, A.-C. Eliasson, P. Åman, *Carbohydrate Polymers* **1998**, *35*, 119–134.

[95] M. Tako, Y. Tamaki, T. Teruya, Y. Takeda, *Food and Nutrition Sciences* **2014**, *2014*, DOI 10.4236/fns.2014.53035.

[96] S. Kirinčič, C. Klofutar, *Fluid Phase Equilibria* **1999**, *155*, 311–325.

[97] J. Tóthová, M. Timko, P. Kopčanský, V. Lisý, *Int J Thermophys* **2014**, *35*, 2150–2157.

[98] I. F. Gorlov, E. I. Titov, G. V. Semenov, M. I. Slozhenkina, A. Y. Sokolov, R. S. Omarov, A. I. Goncharov, E. Y. Zlobina, E. V. Litvinova, E. V. Karpenko, *International Journal of Food Properties* **2018**, *21*, 1031–1042.

[99] A. Sobczak-Kupiec, A. Drabczyk, W. Florkiewicz, M. Głąb, S. Kudłacik-Kramarczyk, D. Słota, A. Tomala, B. Tyliszczak, *Materials* **2021**, *14*, 2096.

[100] D. K. S. Sira, *Psychology and Education Journal* **2021**, *58*, 178–188.

[101] R. Mohammadinejad, A. Kumar, M. Ranjbar-Mohammadi, M. Ashrafizadeh, S. S. Han, G. Khang, Z. Roveimiab, *Polymers* **2020**, *12*, 176.

[102] T.-C. Ho, C.-C. Chang, H.-P. Chan, T.-W. Chung, C.-W. Shu, K.-P. Chuang, T.-H. Duh, M.-H. Yang, Y.-C. Tyan, *Molecules* **2022**, *27*, 2902.

[103] H. Jiang, X. Yang, H. Wang, *RSC Adv.* **2024**, *14*, 32506–32516.

[104] M. Bertasa, A. Dodero, M. Alloisio, S. Vicini, C. Riedo, A. Sansonetti, D. Scalarone, M. Castellano, *European Polymer Journal* **2020**, *123*, 109442.

[105] K. A. Ross, L. J. Pyrak-Nolte, O. H. Campanella, *Food Hydrocolloids* **2006**, *20*, 79–87.

[106] X. Li, Z.-H. Zhang, X. Qi, L. Li, J. Zhu, C. S. Brennan, J.-K. Yan, *Comprehensive Reviews in Food Science and Food Safety* **2021**, *20*, 4367–4389.

[107] L. J. Andrew, E. Lizundia, M. J. MacLachlan, *Advanced Materials* **2025**, *37*, 2401560.

[108] D. C. D. Roux, F. Caton, I. Jeacomine, G. Maîtrejean, M. Rinaudo, *Polymers* **2024**, *16*, 811.

[109] Y. F. Zuev, S. R. Derkach, I. V. Lunev, A. A. Nikiforova, M. A. Klimovitskaya, L. R. Bogdanova, P. V. Skvortsova, R. K. Kurbanov, M. A. Kazantseva, O. S. Zueva, *International Journal of Molecular Sciences* **2024**, *25*, 11738.

[110] N. Riquelme, C. Savignones, A. López, R. N. Zúñiga, C. Arancibia, *Colloids and Interfaces* **2023**, *7*, 49.

[111] R. E. Sousa, J. Oliveira, A. Gören, D. Miranda, M. M. Silva, L. Hilliou, C. M. Costa, S. Lanceros-Mendez, *Electrochimica Acta* **2016**, *196*, 92–100.

[112] R. Bendoni, N. Sangiorgi, A. Sangiorgi, A. Sanson, *Solar Energy* **2015**, *122*, 497–507.

[113] H. Baptista, M. Dekker, P. Ferreira, C. Nunes, *Carbohydrate Polymers* **2025**, *367*, 124012.

[114] A. Willfahrt, E. Steiner, J. Hötzel, X. Crispin, *Appl. Phys. A* **2019**, *125*, 1–10.

[115] S. A. Starostin, M. Creatore, J. B. Bouwstra, M. C. M. van de Sanden, H. W. de Vries, *Plasma Processes and Polymers* **2015**, *12*, 545–554.

CHAPTER 4

SACRIFICIAL AGENTS IN POLYTHOPHENES-BASED ECDs

INTRODUCTION

4.1 Polythiophene polymers

In the late 1970s, conjugated polymers were classified as innovative materials poised to guide in a new era of electronic and optical devices. π-Conjugated polymers are characterized by a sequence of alternating single and double carbon-carbon bonds, resulting in each carbon atom having one π electron.[1] These carbon atoms are sp^2 hybridized and interact along the length of the polymer, causing electron delocalization throughout the chain.[2] This delocalization facilitates charge transport, giving the polymer conductive or semiconducting properties.[3,4] These polymers are highly valued for their potential applications in electronic, optical devices and sensors.[5–8]

Polythiophene (PT) polymers are an important representative class of conjugated polymers with unique electronic and optical properties.[9] Derived from thiophene monomers, PTs exhibit a recurring backbone structure composed of alternating carbon and sulphur atoms, Figure 4.1.[10]

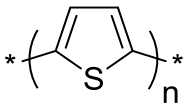


Figure 4.1. The monomer repeat unit of unsubstituted polythiophene.

PT and its derivatives are highly valued in device applications due to their stable doped and undoped states, ease of structural modification, and solution processability.[11,12] These attributes have made polythiophene a subject of extensive theoretical and experimental research.[13–15] Numerous studies have investigated the electronic structure of thiophenes using first-principles calculations, revealing how side-chain groups and dopants influence the polymer's electronic properties.[16–18] These studies show that the band gap can be adjusted from 3.0 to 1.0 eV depending on the dopant level or side-chain group used. Additionally, modifying the morphology and geometry of the oligomer chains can significantly impact the band gap and optical properties of polythiophene-based films.[19] This makes PTs and its derivatives particularly valuable in the field of organic electronics, where they are employed

in applications such as organic photovoltaics,[20] light-emitting diodes,[21] and field-effect transistors.[22]

Specifically, the work of Scharber and coworkers[23] shows that the PT bandgap can be finely tuned by incorporating various substitution groups onto the individual thiophene units within the polymer chain, Figure 4.2.

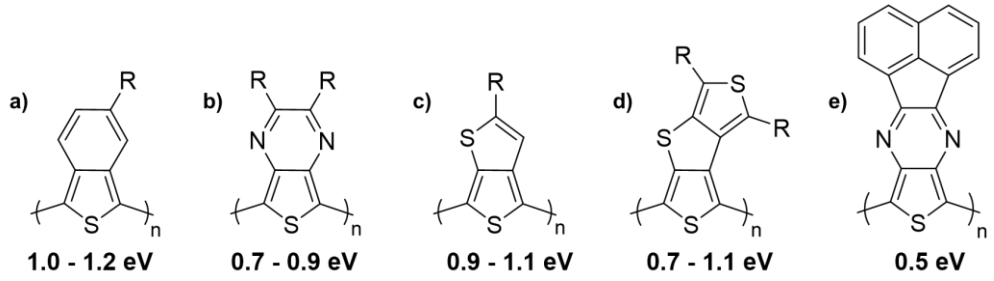


Figure 4.2. Polythiophene's bandgap tuning based on different substituent groups a) benzothiophene b) thienopyrazine c) thienothiophene d) dithienothiophene e) acenaphthothienopyrazine.[23]

The presence of these functional groups alters the electron distribution along the polymer backbone, affecting the energy levels of the molecular orbitals (HOMO-LUMO) and, consequently, the bandgap width. Moreover, these can introduce distinct torsion in the system, which could contribute to bandgap shift. For example, Ram S. Bhatta and coworkers estimated *ca.* 6 eV of bandgap increase in P3HT for a torsion of 90° angle.[19] Another way to modify the bandgap of PTs is via the removal of electrons from the HOMO level to generate charge defects called polarons (radical cation, Figure 4.3b) and bipolarons, (radical di-cation Figure 4.3c).[24] These quasi-particles are localized charge carriers coupled with lattice distortions. Polarons consist of a single charge (hole) and its associated deformation, while bipolarons involve two such charges and a larger distortion. This process, also called doping, results in a positively charged polymer backbone which undergoes structural changes, such as bond length alternations, around the localized charge. This distortion helps to stabilize the charge by lowering the overall energy. Moreover, the formation of these charged species enhances the electrical conductivity of the polymer, increasing the ability of the polymer to transport charges.[25]

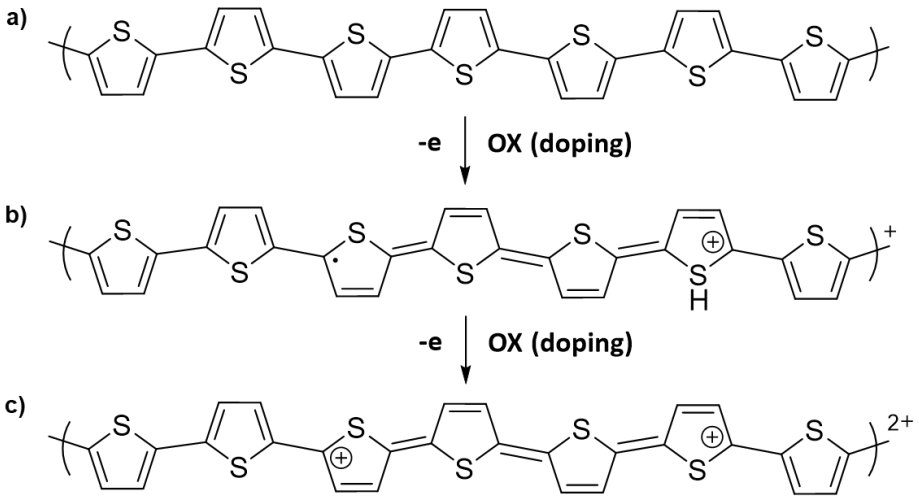


Figure 4.3. Diagram illustrative of the neutral and charged polythiophene rings. (a) neutral backbone, (b) polaron, and (c) bipolaron states.

This mechanism is a fundamental aspect of electrochromic (EC) polymers. In their neutral state, these polymers exhibit a specific optical absorption profile determined by their electronic structure and band gap, resulting in a characteristic colour in the visible spectrum. When an electrical potential is applied, the polymer undergoes oxidation (meaning it loses electrons) which leads to a change in its electronic configuration and a consequent narrowing of the band gap. This change causes a red-shift in the absorption spectrum, meaning the absorption maximum shifts toward lower energies, corresponding to longer wavelengths. Depending on the magnitude of the initial band gap and the specific molecular structure of the polymer, the oxidized form may continue to absorb within the visible range, producing a different visible colour. Alternatively, the absorption may shift beyond the visible spectrum and into the near-infrared region. In the latter case, since the oxidized polymer no longer absorbs significantly in the visible range, it appears colourless or bleached to eyes. This fall in absorption within the visible range, caused by the absorption band moving into the IR, is what leads to the loss of colour typically observed in the oxidized state. This EC behaviour, governed by the relationship between redox state and optical absorption, is illustrated in Figure 4.4.[26]

Electrochromic displays (ECDs) leverage the unique properties of PT polymer, with poly(3,4-ethylenedioxythiophene) polystyrene sulfonate (PEDOT:PSS) standing out as one of the most promising materials in this field.[27] The unique characteristics of PEDOT:PSS, such as high cycling stability (*ca.* 200000)[28], high coloration efficiency (CE) (109 cm^2/C at 670 nm)[29] with high ΔT (>50%)[30], and water solubility attributed to the presence of PSS, make it an ideal choice for EC applications.[31]

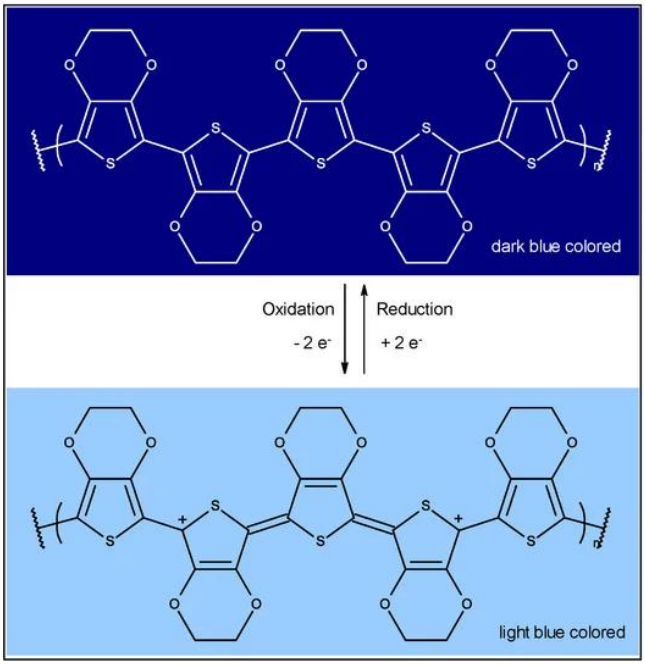


Figure 4.4. Picture of a PEDOT layer in the oxidized cationic state, light blue coloured and when reduced to the neutral state, dark blue coloured.[26]

Despite their well-documented EC properties and the broad range of applications explored in the literature, these polymers are inherently limited in contexts requiring permanent optical responses. Specifically, their reversible EC behaviour renders them unsuitable for use in applications such as anti-counterfeiting in cold-chain monitoring, where the visual indication of a single, irreversible event is essential. The ability of the material to switch back and forth between coloured states upon successive redox cycles contradicts the fundamental requirement of one-time, irreversible activation rendering the message unreliable.

4.2 Aim of the project

The objective of this project is to transform the reversible EC behaviour of PT polymers into an irreversible process. This transformation is achieved through the introduction of a sacrificial agent, namely a reactive compound capable of chemically reacting with the oxidized form of the polymer, thereby generating a different species that inhibits the polymer from reverting to its neutral state. Such an approach is intended to lock the colour change after a single redox event, thereby enabling the fabrication of PT-based *i*-ECDs that operate as one-time, tamper-proof indicators for applications including anti-counterfeiting and cold-chain monitoring. As previously discussed, the oxidation of PT polymers involves the removal of electrons, leading to the formation of delocalized positive charges (polarons or bipolarons) along the polymer backbone. It is hypothesized that these electron-deficient sites can be selectively targeted by

nucleophilic sacrificial agents, such as alcohols or amines, introduced into the electrochemical environment. Through nucleophilic addition, these molecules may covalently bind to the oxidized polymer, disrupting the π-conjugation or changing the backbone structure in a way that inhibits subsequent reduction. This chemical "locking" mechanism would prevent the polymer from reverting to its original coloured (neutral) state, thereby making the optical transition irreversible.

To establish a baseline, the chapter begins with the fabrication and characterization of conventional reversible ECDs based on PT. The deposition method is detailed, followed by electro-optical characterization of the displays, including measurements of ΔT between coloured and bleached states, switching time, charge consumption, and CE, averaged over a set of ECDs. Following this, a stability assessment of the PT polymer in solution was conducted using cyclic voltammetry (CV), during which an unexpected solubilization of the oxidized polymer into the electrolyte was observed. This behaviour suggested an alternative route for irreversible decolouration, the physical removal of the oxidized polymer from the electrode surface. Although this effect demonstrated promise in solution, its translation into the solid-state ECD configuration did not yield satisfactory or reproducible results. Consequently, the final section of the project focuses on the chemical locking strategy via agents. This is investigated through CV experiments in solution, where alcohols and ammines are introduced into the electrolyte during the electrochemical cycling. Changes in redox peak intensity, position, and shape, as well as any irreversible alterations in the polymer's colour, are monitored to evaluate the feasibility of this irreversible switching approach. Together, these investigations aim to demonstrate a proof-of-concept for turning a classically reversible PT-based EC material into a one-time-use, irreversible optical indicator.

RESULT AND DISCUSSION

4.3 Manufacturing and characterization of polythiophenes-based ECDs

For the study of the sacrificial agent-induced irreversibility, we went through the characterisation of a series of PTs produced in the lab, and from the collected data we decided to focus on the use of PURPLE, a purple coloured PT polymer comprising branched alkoxy chains as substituents in position 3 and 4 of its monomers. The reason why we selected alkoxy chains as substituents for our study is rooted in the understanding that the addition of substituents to the pristine PT polymer leads to modifications in its bandgap.[32] In this context, the good EC performances observed with alkoxy chains, particularly in terms of ΔT and

REDOX switching time, can be attributed to the lowering of the polymer bandgap, effect facilitated by the electron donor moiety of the methyl group in position 1 in the alkyl chain, Figure 4.5a. This reduction enables efficient charge transfer processes, which are central for achieving desirable EC properties. Hence, the selection of this structure was a strategic choice to enhance the EC behaviour of the polymer.

The PURPLE polymer is obtained via oxidative polymerization of the thiophene monomer, synthesis is inspired by and optimized based on the work carried out by D. Hebert and coworkers,[33] using $AlCl_3$ as the oxidant. This molecule oxidizes the monomer to a radical cation, which couples with another radical cation or neutral monomer to form dimers and longer chains. Polymer growth proceeds through successive oxidative coupling steps until termination occurs by recombination of radical cations or by overoxidation, which deactivates the chain ends.[33,34] After synthesis, the polymer, whose chemical structure is presented in Figure 4.5a, the EC solution was straightforwardly prepared by polymer solubilization in $CHCl_3$ aided by sonication for 30 minutes at 40 °C. This produced the PURPLE polymer solution reported in Figure 4.5b ready to be deposited.

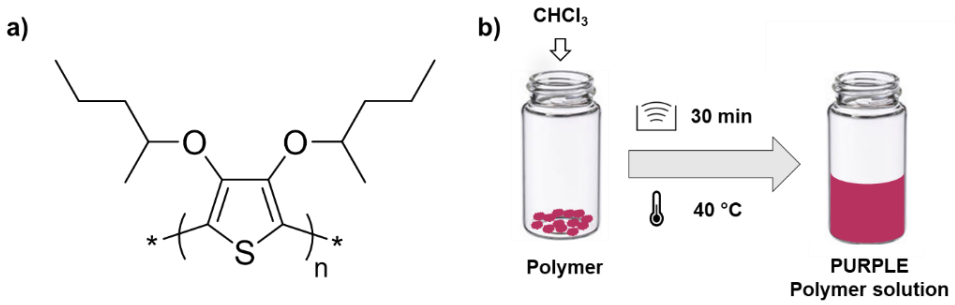


Figure 4.5. a) Graphic representation of the functionalized EC PURPLE polythiophene polymer. b) Schematic representation of the preparation process for the EC polymer solution which involved solubilization in $CHCl_3$ for 30 minutes at 40 °C.

The deposition of the EC film was performed through a spray coating, technique which allows the formation of a uniform and homogeneous layer.[35] The complete process, schematized in Figure 4.6a, starts with the (1) Mask adhesion on the PET-ITO surface allowing the polymer deposition only in precise and selected areas. The mask design depicts a squared frame of 3 cm^2 which will act as counter electrode (C.E.), and a 1 cm^2 square as working electrode (W.E.), which will be the characterization area. The rationale behind this specific design is to obtain the best geometry to minimize the distance between the two polymer areas avoiding overlap. By reducing this distance between the electrodes, the response time and energy efficiency are improved as it shortens the diffusion ion path in the electrolyte, necessary for balancing the polymer's polarons and preserving neutrality. At this stage, the PET-ITO substrate was affixed

over the spray coater plate, Figure 4.6b, which was warmed up to 60 °C to promote the $CHCl_3$ evaporation. Thus, 3 mL of the PURPLE solution, formerly prepared, were poured inside the gravity feed cup (2) Sprayed over the entire surface. The masks were then removed and the (3) Biadhesive spacer placed over the W.E., where a small square was sprayed. Thus, followed the (4) Electrolyte deposition, the placement of the other electrode on top of the W.E. and the display closure. The ECD was then ready when two stripes of copper tape, optional, were connected to both electrodes and the electrolyte (5) UV cured with 366 nm for 5 minutes. This process allows the electrolyte to gellify avoiding potential leakage and reducing the polymer solubility within the electrolyte solution. Essentially, the entire display is made up of six layers, two PET-ITO electrodes, two EC films, the biadhesive spacer and the electrolyte formulation. The electrolyte, developed by Ynvisible, contains Li^+/ClO_4^- ions dissolved in polyethylene carbonate (PEC), along with a photopolymer and a photoinitiator enabling UV-induced photopolymerization.

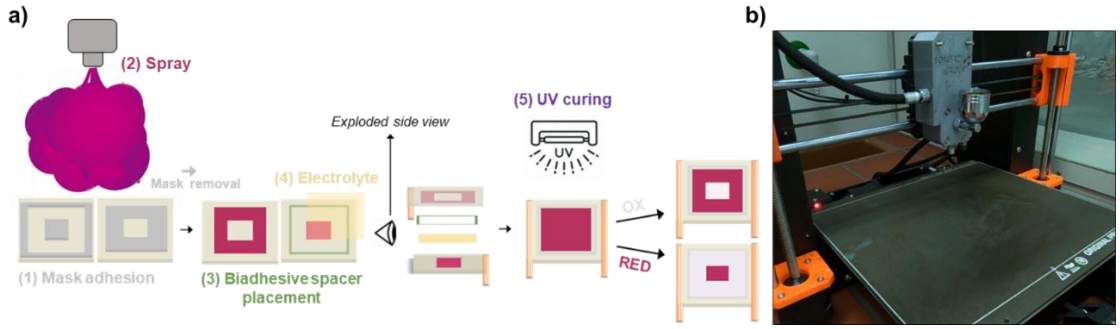


Figure 4.6. a) ECD manufacturing steps carried out through a spray coating technique which include (1) Mask adhesion, (2) Spray, (3) Biadhesive spacer, (4) Electrolyte deposition and (5) UV curing. b) Image of a Prusa 3D printer in-house modified in a spray coater machine employed for the polymer spray.

When an electric potential is applied to the ECD, its polarity, which governs the redox state of the EC polymer, is always defined with respect to the W.E., the small square at the center of the ECD used as the reference for all characterizations (Figure 4.7). A positive potential applied to the W.E. (+1.5 V) oxidizes the polymer, rendering it colourless (1). Conversely, applying a negative potential to the W.E. (-1.5 V) reduces the polymer, producing its coloured state (3). In the neutral condition (0.0 V), no external potential is applied, and the polymer adopts its most thermodynamically stable state, corresponding to the state with the lowest free energy, whose optical absorption, and thus colour, is essentially the same as in the reduced state (2). For clarity, in what follows we will refer to the state at -1.5 V as “reduced,” even though from a strict electrochemical standpoint it corresponds to the neutral state rather than a true n-doped reduction.

At +1.5 V the polymer is p-doped (oxidized), electrons are removed from the π-conjugated backbone, creating polaron/bipolaron states inside the bandgap. These gap states drain oscillator strength from the neutral π→π* transition in the visible and shift absorption toward polaronic bands in the near-IR, so the film bleaches. Sweeping back to -1.5 V simply dedopes the chain, polarons disappear and the neutral state is restored, bringing back the original π→π* band and thus the same colour as the neutral film. Achieving a true n-doped (reduced) state would require substantially more negative potentials to populate the LUMO and is often unstable in ambient conditions. Consequently, within ±1.5 V the polymer switches oxidized (bleached) ↔ neutral (coloured) without ever reaching a distinct reduced state.

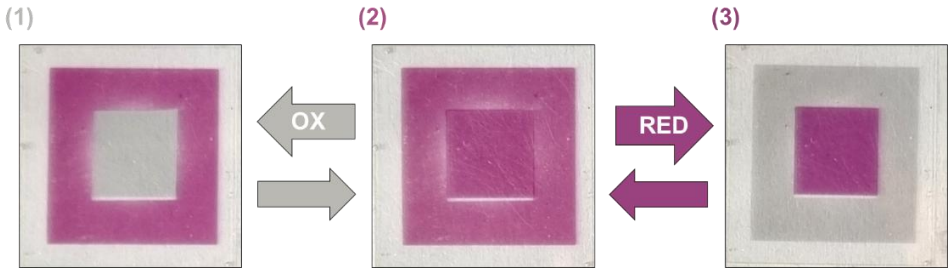


Figure 4.7. Picture of the PURPLE ECD in its neutral, oxidized (+1.5 V), and reduced (-1.5 V) states.

The characterization of the PURPLE ECD started with a spectroscopic analysis where the absorption of the oxidized and reduction state where measured. Thus, the absorption spectrum of the OX (+1.5 V, grey line) and RED (-1.5 V, purple line) state of the W.E. were measured, Figure 4.8a. The EC polymer exhibited a dominant absorption band centered at 540 nm and a secondary band at approximately 590 nm. These absorptions fall within the green–yellow region of the spectrum, thereby reducing light transmittance in this range. As a result, the polymer exhibits a macroscopic purple/pink coloration.

Subsequently, the ECD was electrochemically characterized by CV. The voltammogram in Figure 4.8b reveals a main oxidation peak at approximately +0.6 V, accompanied by a secondary shoulder at lower potentials, around +0.2 V. The presence of two distinct anodic features reflects two successive oxidation processes of the polymer. Specifically, the first signal at lower potential can be ascribed to the formation of polaronic species, whereas the second, at higher potential, corresponds to the subsequent generation of bipolaronic species along the polymer backbone. These two redox stages are characteristic of the doping mechanism in conducting and EC polymers, where gradual changes in the oxidation state are accompanied by the insertion or extraction of counter-ions from the electrolyte. This process directly governs the optical response of the ECD, since the different oxidation levels give rise to distinct chromatic transitions (neutral state → intermediate polaronic coloration → fully oxidized

bipolaronic state). On the reverse scan, two cathodic peaks appear at negative potentials. Specifically, a dominant reduction signal centered near -0.25 V and a second peak at more negative potential, around -1.1 V. These features are consistent with a two-step dedoping process of the previously oxidized polymer. The less negative peak corresponds to the bipolaron → polaron transition, while the more negative peak reflects the subsequent polaron → neutral transition.

Finally, it is worth noting that the electrochemical features appear relatively broad rather than sharp. This broadening can be attributed not only to the intrinsic polydispersity (PD) of the polymer, which gives rise to a distribution of redox-active sites, but also to limitations in ion transport within the polymer matrix. During the redox process, counterions must diffuse in and out of the film to maintain charge neutrality, and this process becomes increasingly hindered in thicker films, leading to a further widening of the electrochemical response.[36,37]

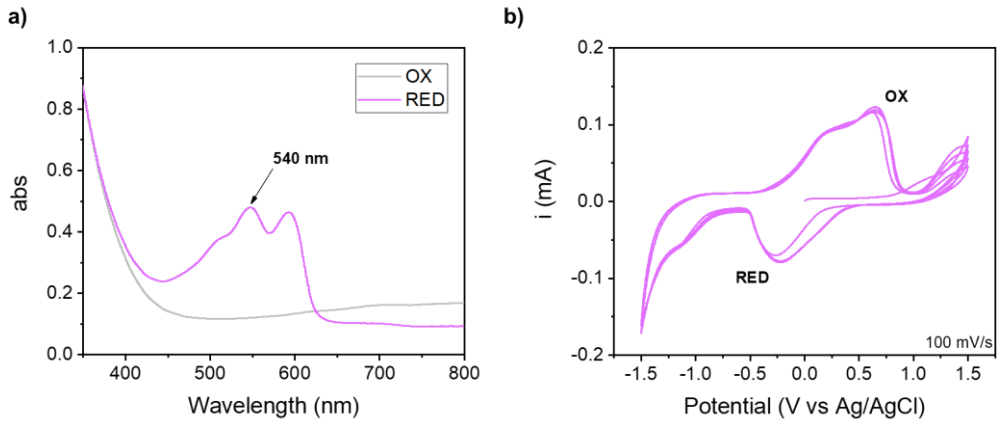


Figure 4.8. a) Absorbance in the visible spectrum as a function of the wavelength for the PURPLE ECD after OX at +1.5 V for 60 s (grey line) and RED at -1.5 V for 60 s (purple line). b) Voltammogram of the PURPLE ECD between ±1.5 V at 100 mV/s as scan rate.

After determining the polymer's peak absorption wavelength (λ=540 nm), we proceeded to analyse the time required for oxidation and reduction processes to occur, as well as the amount of charge consumed per switch and the CE. For reproducibility and to achieve a reliable analysis, five PURPLE ECDs were prepared and subjected to a voltage protocol of ±1.5 V for 30 cycles of 5 seconds and 5 cycles of 1 minute during which the transmission of the device at 540 nm (T@540 nm) of the ECD's W.E. was measured, Figure 4.9a,b. The initial short cycles (5 seconds) act as a conditioning phase for the ECD. During these early cycles, the ΔT does not immediately reach its maximum because several activation processes must take place. First, ions from the electrolyte (such as ClO_4^-) progressively penetrate and distribute within the polymer matrix, gradually neutralizing the holes generated along the polymer backbone during oxidation. At the same time, the polymer undergoes molecular and structural reorganization,

adapting to repeated ion insertion and extraction, which reduces kinetic barriers and enables deeper, more uniform doping. In parallel, the electrode–electrolyte interfaces stabilize, surface traps are reduced, and wetting of the active layer improves, all of which enhance charge transfer.[38–40]

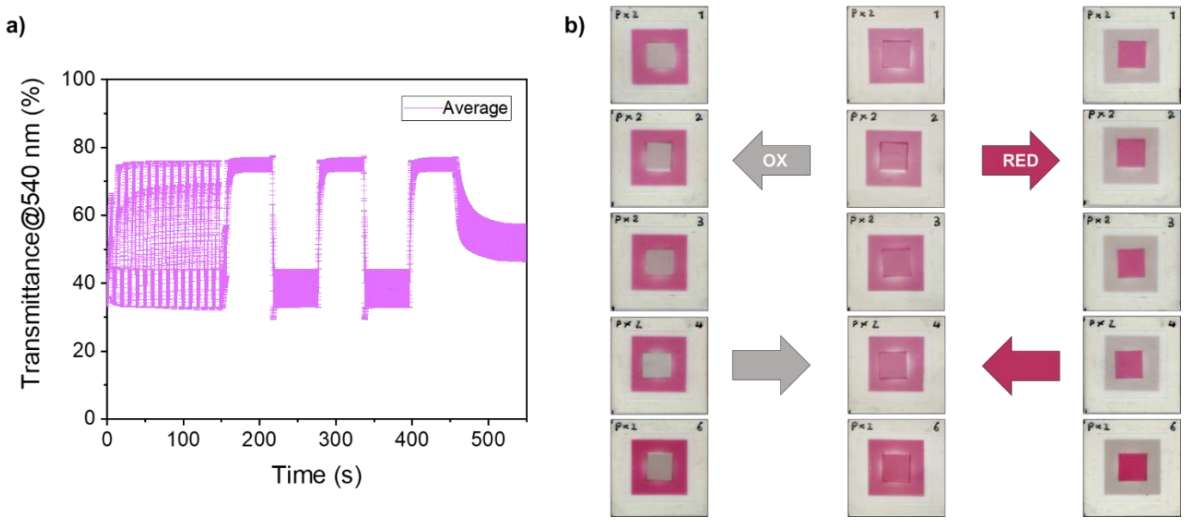


Figure 4.9. a) Average T@540 nm as a function of time of five PURPLE ECDs during the application of ±1.5 V for 30 cycles of 5 s and 5 cycles of 60 s. b) Pictures of the five PURPLE ECDs in their neutral, OX (+1.5 V) and RED (-1.5 V) state.

As cycling proceeds, more polymer chains become electrochemically accessible and fully oxidized, leading to progressively larger ΔT values. Eventually, the system reaches a saturation regime in which the entire polymer is participating reversibly in the redox process, and ΔT stabilizes at its maximum steady-state value. At this stage, longer cycles of 60 seconds are applied to provide sufficient time for the polymer to complete its oxidation and thereby reach the maximum attainable ΔT. This ensures that the switching process is not limited by kinetic factors but instead reflects the full electrochemical capacity of the material. The values reported in Table 4.1 below, are calculated under these conditions, and the table presents the individual data for each ECD together with the corresponding averages and standard deviations (SDT).

The data consistently show that EC polymers switch to their coloured or neutral state more rapidly during reduction than oxidation. This asymmetry arises from differences in electrochemical kinetics and charge transport during redox transitions.[40] Reduction proceeds quickly because small cations (*e.g.*, Li^+) readily migrate into the polymer matrix alongside electron injection, a process facilitated by their high mobility in the electrolyte and the thermodynamically favourable formation of polaronic carriers along the conjugated backbone. In contrast, oxidation is slower, as it requires electron withdrawal and cation extraction. The low conductivity of the undoped polymer hampers the onset of oxidation, while ions embedded during reduction may become electrostatically trapped or chemically bound, hindering their

release. Additional structural rearrangements and mechanical strain during oxidation can further restrict ion transport and charge propagation.[41] These effects are particularly evident in PEDOT:PSS systems, where oxidation often emerges as the rate-limiting step of the switching cycle.[42]

PURPLE ECD	ΔT@540 nm (%)	$t_{OX,90\%}$ (s)	$t_{RED,90\%}$ (s)	Charge (mC)	CE (cm^2/C)
1	33.49	2.20	0.86	1.50	167.61
2	33.52	1.50	0.61	1.50	167.75
3	34.15	1.51	0.56	1.70	148.05
4	38.12	6.81	2.54	1.70	147.90
6	43.06	3.20	1.03	2.10	119.75
Average	**36.47 ± 4.16**	**3.04 ± 2.22**	**1.12 ± 0.82**	**1.70 ± 0.24**	**150.21 ± 19.67**

Table 4.1. Data registered through characterization for each single PURPLE ECD and their average with standard deviation. From left to right, ΔT@540 nm, OX and RED time to reach 90% of the ΔT, charge consumption for 60 s of switch from RED to OX and CE.

The average charge consumption for an ECD during a 60-second RED→OX switching cycle was 1.70 ± 0.24 mC, determined by integrating the current response over the cycle. The corresponding average CE was 150.21 ± 19.67 cm^2/C. These values are consistent with literature reports, such as the flexible ECDs developed by Moreira and coworkers (124.00 ± 3.00 cm^2/C)[43] and the inkjet-printed ECDs on glass/ITO fabricated by Pietsch et al. (99.00 ± 6.0 cm^2/C).[44] In addition to charge and CE characterization, the testing protocol also included cycling stability analysis, which evaluates the colour deviation (ΔE) between the oxidized and reduced states over repeated redox transitions. This measurement was carried out by periodically inverting the applied voltage polarity between ±1.5 V with a dwell time of 5 seconds per state, as illustrated in Figure 4.10a.

To evaluate long-term colour stability, four ECDs were placed inside a cycling chamber illuminated with white light, equipped with a colour checker, and monitored by a perpendicularly positioned camera, Figure 4.10b. The voltage cycling protocol was simultaneously applied to all samples for 12000 cycles, with images recorded at intervals of 500 cycles. From these images, the L, a, and b* coordinates of the CIELAB colour space were extracted for both RED and OX states. This space provides a standardized and perceptually uniform description of colour, where L* denotes brightness, while a* and b* define chromaticity along the green–red and blue–yellow axes, respectively. The coordinates were

obtained using proprietary software developed by Ynvisible, which converts RGB values into CIELAB and enables the subsequent calculation of the colour difference ΔE (CIE 1976, Lab*) through established mathematical formulations.[45] Upon ΔE examination, ECDs n°1, n°2 and n°4 experience an important drop in the initial cycles, starting from *ca.* 20 and reaching saturation with a minimum value of 5 after 6000 cycles. ECD n°6 follows a similar pattern, maintaining a consistently higher ΔE until roughly 8000 cycles, after which it undergoes a rapid decline and stabilizes at values around 10 for the rest of the analysis. Upon analysis of the ΔE evolution, distinct behaviours were observed among the six tested displays. ECD n°1, n°2, and n°4 exhibited a pronounced decrease during the initial cycles, with ΔE values dropping from approximately 20 to a minimum of 5 after ~6000 cycles, where they remained stable. A comparable trend was observed for ECD n°6, although this device maintained higher ΔE values throughout the first 8000 cycles before undergoing a sharp decline and stabilizing around 10 for the remainder of the test. Such divergence in cycling durability, despite similar initial optical contrast, can be attributed to three recurrent degradation phenomena reported in the literature. First, non-uniformities in film thickness and morphology produce local regions with higher current density, where the polymer undergoes over-oxidation more rapidly, leading to early loss of electroactivity.[46] Second, electrolyte-related effects, such as trace water or oxygen, introduce parasitic side reactions that irreversibly trap charges or promote electrode corrosion, which manifests as a progressive decline in ΔE with cycling.[47] Third, charge imbalance between the working and counter electrodes can drive the active film beyond its electrochemically stable potential window, thereby accelerating polymer degradation.[48]

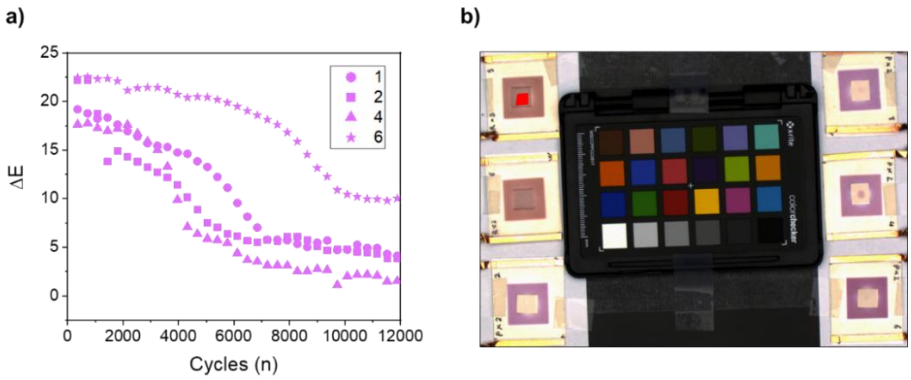


Figure 4.10. ΔE as a function of the REDOX cycles performed on four PURPLE ECDs. A cycle last 10 s and consists in the application of +1.5 V (OX) for 5 s and -1.5 V (RED) for 5 s. b) Picture of the cycling chamber with the ECDs (acquired during OX) and the colour checker. The ECD n°3 got damaged before the analysis. The red ECDs in the top left corner were not included in the study.

4.4 Harnessing sacrificial agents to promote irreversible EC transformations

After confirming the reversible EC behaviour of the polymer, experiments were initiated to explore whether its oxidation state could be permanently fixed, thereby making the colour change irreversible. Preliminary investigations were performed using CV, as the analysis of voltammograms enables monitoring of the evolution of redox peaks as a function of applied potential. This approach allows comparison of the polymer's oxidation and reduction processes both before and after the introduction of a sacrificial nucleophile (*e.g.*, alcohols or amines), which can react with the positive charges generated during oxidation. If the oxidized state of the polymer react with the sacrificial agent, its oxidation state will be locked, resulting in the disappearance of the corresponding redox peaks in the voltammogram.

4.4.1 Irreversibility test - polythiophenes decolouration in solution

Initially, CV measurements were performed in solution using a three-electrode setup with $LiClO_4$ in PEC, rather than on complete ECDs (Figure 4.11a). While tests on fully assembled ECDs are presented later in this chapter, the solution-based configuration was first adopted to accelerate the analysis. This approach avoided the time-consuming fabrication steps and required only polymer deposition onto a single PET–ITO W.E. with an active area of 1 cm^2, which corresponds exactly to the electrode area employed in the ECDs. The same solvent and ionic salt used in the display were also employed here, ensuring relevant conditions. Importantly, this open setup enabled straightforward testing of sacrificial agents by directly adding the compound into the electrolyte solution during CV, allowing immediate comparison of redox behaviour before and after this addition. In contrast, incorporating such agents into ECDs requires integration during fabrication, which is considerably more time-consuming.

In this setup, the polymer deposited onto ITO used as the W.E. was subjected to potentials ranging from 0 to +1.5 V for 10 cycles at a scan rate of 100 mV/s. The voltammogram in Figure 4.11b exhibits a broad oxidation peak at approximately +0.8 V, associated with the bleaching of the polymer, and a subsequent reduction peak at around +0.3 V, corresponding to the coloured state. The presence of both peaks confirms that the EC switching is reversible. However, the peak-to-peak separation ($\Delta Ep \approx 0.5$ V) is significantly larger than the theoretical value of 59 mV expected for a one-electron Nernstian reversible process at 25 °C,[49] indicating that the system is quasi-reversible, as typically observed for polymeric EC films due to ion diffusion and structural reorganization.[50] In addition, a progressive decrease in peak intensity is observed over successive cycles. This behaviour arises because a fraction of the EC polymer is gradually lost from the ITO electrode into the electrolyte upon oxidation. Such dissolution

processes are well-reported for conducting and EC polymers, where oxidation increases polymer chain polarity, reduces interchain interactions, and facilitates detachment or solubilization in the electrolyte.[51] As a result, active material is irreversibly removed from the electrode surface cycle by cycle, leading to a reduction in EC response.

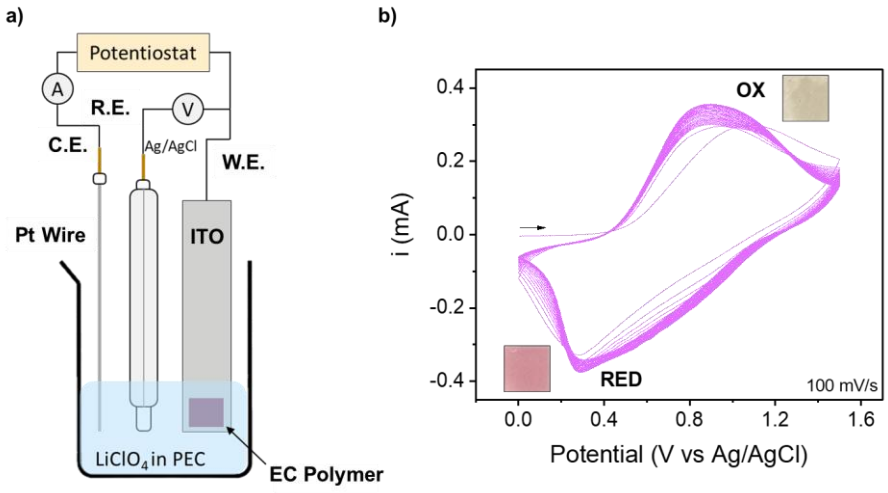


Figure 4.11. a) Diagram of the experimental three-electrodes setup employed for the CV in PEC:$LiClO_4$. The PURPLE polymer is deposited on the ITO employed as W.E. A Pt wire was used as C.E. and the aqueous Ag/AgCl utilized as RE. b) Voltammogram of the PURPLE polymer obtained through CV carried out between 0 and +1.5 V at a scan rate of 100 mV/s for 10 cycles.

To confirm that the polymer was dissolved, the experiment was repeated with a freshly deposited polymer square on the ITO W.E. First, 10 CV cycles were performed between 0 and +1.5 V. After this step, a constant oxidative potential of +1.5 V was applied for 600 seconds to ensure complete oxidation of the polymer. Finally, 10 additional CV cycles were carried out under the same conditions as the initial set. The resulting voltammogram (Figure 4.12a) shows a progressive decrease of the polymer's redox peaks over successive cycles, consistent with the previous observations. Moreover, the voltammogram recorded after the oxidation step, (Figure 4.12b) clearly shows the absence, or at least a strong attenuation, of both oxidation and reduction peaks, confirming the dissolution of the polymer.

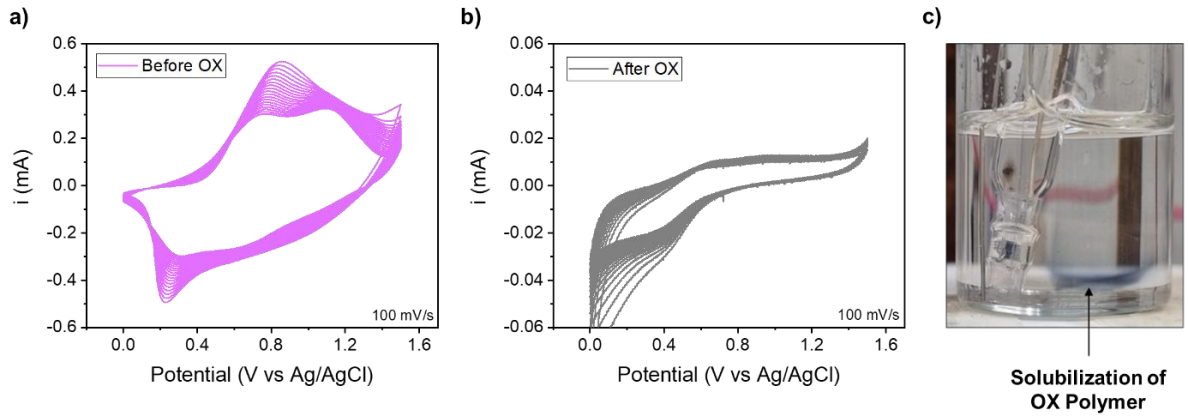


Figure 4.12. a) Voltammogram of the PURPLE polymer obtained through CV with a three-electrodes setup carried out between 0 and +1.5 V at a scan rate of 100 mV/s for 10 cycles a) before and b) after the application of a fixed OX potential of +1.5 V for 600 s. c) Picture of the experimental setup displaying the grey/black polymer which after OX is permanently lost from the PET-ITO electrode and solubilized in the electrolyte solution.

This conclusion is further supported by spectroscopic analysis (Figure 4.13a). The absorption spectra of the polymer were compared in three states: the pristine as-deposited layer (black line), after the initial CV cycles followed by long oxidation at +1.5 V for 600 seconds (red line), and after a subsequent reduction at -1.5 V for 600 seconds, intended to restore all possible polymer colours. A direct comparison of the spectra reveals that, after reduction, it was not possible to recover the absorption profile characteristic of the pristine polymer. If the amount of polymer on the electrode had remained unchanged, the colour should have been fully restored due to the intrinsic reversibility of the EC response, as demonstrated in the previous chapter. Therefore, the only consistent explanation is that part of the polymer was lost into the electrolyte, a conclusion further supported by the photographic documentation in Figure 4.13b, which shows a strong contrast in colour intensity between the vivid purple of the pristine layer and the much weaker coloration observed after oxidation and subsequent reduction.

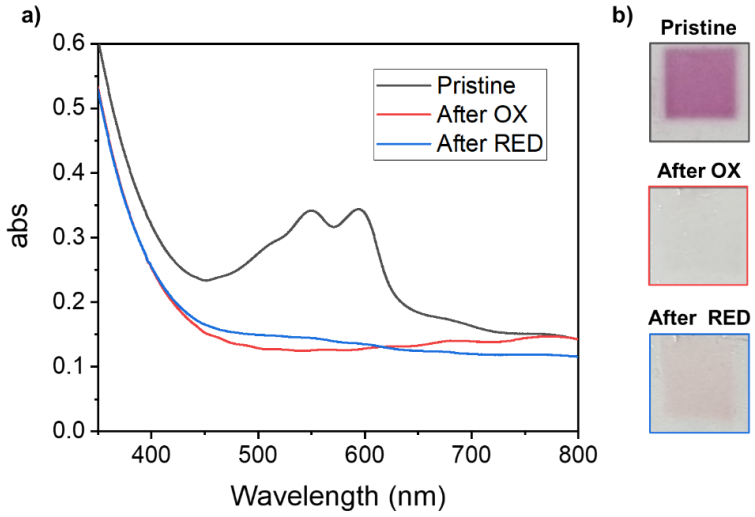


Figure 4.13. a) Absorbance in the visible spectrum as a function of the wavelength for the PURPLE polymer on PET-ITO, pristine, and after a REDOX cycle: OX (+1.5 V, 600 s), RED (-1.5 V, 600 s) carried out in a three-electrodes setup. b) Pictures of the PURPLE polymer on the ITO pristine, after OX and after RED.

Building on the previous results, the next objective was to translate the observations obtained in solution to conditions more closely resembling those of an ECD. For this reason, the subsequent experiments were carried out still in electrolyte solution but using two ITO electrodes together with a R.E. (Ag/AgCl). The use of ITO as both W.E. and C.E. allows us to mimic the electrode configuration employed in ECDs, which operate in a two-electrode system. At this stage, the three-electrode setup was maintained to ensure precise control of the applied potentials, while simultaneously replacing the Pt C.E. with ITO to reproduce the geometry of the display. In later experiments, the R.E. will also be removed, still within the solution environment, in order to further approximate the actual two-electrode configuration of the ECD before finally moving to fully assembled displays.

For this purpose, the PURPLE polymer was sprayed over the W.E., covering the standard active area of 1 cm^2. Its absorbance in the visible spectrum was recorded (Figure 4.14a, dashed purple line). The electrode was then subjected to five consecutive electrochemical cycles, each consisting of oxidation and reduction steps at ±1.5 V for 600 seconds. After every cycle, the absorbance of the polymer was measured. This procedure was designed to verify whether, by replacing the Pt as C.E. (employed in a three-electrode configuration) with ITO, the system could still induce polymer solubilization, thereby assessing the feasibility of translating this process to an ECD configuration. The results presented in Figure 4.14a show a progressive decrease in absorbance after each cycle, confirming the gradual dissolution of the polymer from the electrode surface, consistent with earlier observations. This trend is further supported by the electrochemical data in Figure 4.14b, which display a steady reduction in the oxidation

current and charge consumption over successive cycles. Such a decrease reflects the lower amount of polymer remaining on the electrode, since with each cycle less material is available to undergo oxidation and subsequent reduction.

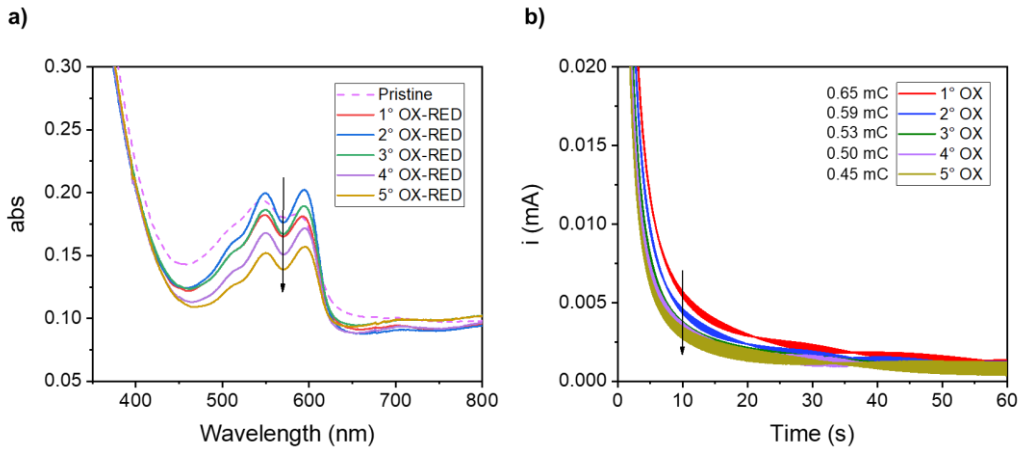


Figure 4.14. a) Visible absorbance spectra of the PURPLE polymer on ITO, recorded in a three-electrode setup (ITO as W.E. and C.E., Ag/AgCl as R.E.). Data are shown for the pristine film and after each of the five redox cycles, consisting of oxidation (+1.5 V, 600 s) and reduction (-1.5 V, 600 s). b) Current as a function of a time during each OX cycle (+1.5 V, 600 s) and related charge consumed for each cycle.

Nevertheless, although polymer solubilization in the electrolyte also occurs when employing the two-ITO electrode configuration (ITO–ITO), the extent of polymer loss from the W.E. surface differs significantly compared to the setup where a Pt wire is used as C.E. (ITO–Pt). This effect is illustrated in Figure 4.15a, which compares the absorbance spectra of the polymer films in the two configurations before and after one oxidation–reduction cycle. Before the potential application, the spectra nearly overlap, as both electrodes were coated with comparable amounts of polymer by spraying the same area of 1 cm^2. However, after a single cycle, a marked divergence is observed. The absorbance values obtained with the ITO–Pt configuration (red dashed line) are considerably lower than those recorded with the ITO–ITO configuration (blue dashed line). This discrepancy indicates that, in the presence of Pt as C.E., the polymer undergoes a more pronounced solubilization following the oxidation–reduction cycle. The effect can be attributed to the much higher electrical conductivity of platinum compared to ITO, which is greater by approximately two orders of magnitude, enabling a more extensive oxidation of the polymer.[52,53] This interpretation is further supported by the electrochemical data, which reveal that oxidation currents and charge consumption are over seven times higher in the ITO–Pt configuration compared to ITO–ITO. This is because the consumed charge directly reflects the number of electrons exchanged during polymer oxidation. Higher values thus indicate that a greater fraction of the polymer is oxidized, accounting for the more pronounced material loss observed with the Pt C.E.

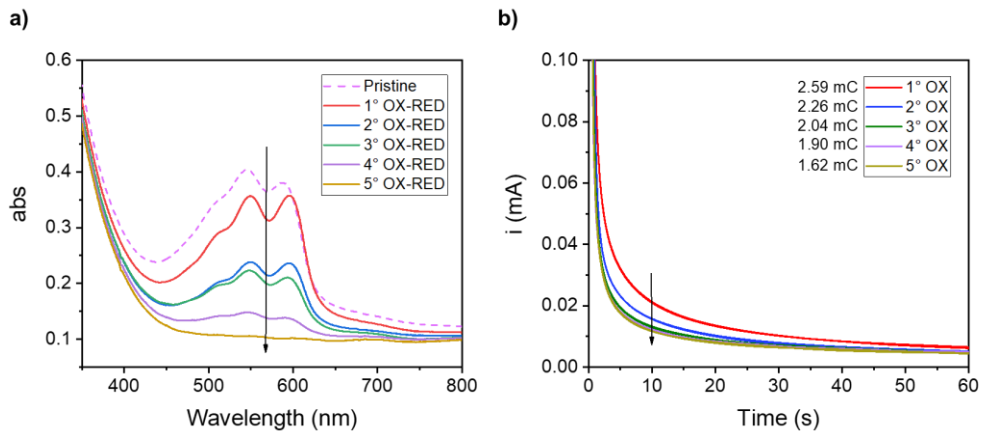


Figure 4.15. a) Absorbance in the visible spectrum as a function of the wavelength for the PURPLE polymer on ITO, in a three-electrodes setup (ITO as W.E. and C.E., Ag/AgCl as R.E. – blue traces) and (ITO as W.E., Pt as C.E., Ag/AgCl as RE – red traces) before and after OX (+1.5 V, 600 s) and RED (-1.5 V, 600 s). b) Current as a function of a time during the OX (+1.5 V) for both electrode configuration.

Consequently, after one oxidation–reduction cycle, the PURPLE polymer in the ITO–ITO setup experiences a reduction in intensity but remains distinctly visible (Figure 4.16a), whereas in the ITO–Pt setup, it nearly disappears (Figure 4.16b). This unexpected behaviour was initially discovered serendipitously, as the original experimental design aimed at characterizing the polymer prior to the addition of a sacrificial agent, in order to establish a reliable baseline for subsequent comparison. Instead, the observation of spontaneous polymer dissolution under oxidative conditions revealed an unforeseen phenomenon, the irreversible loss of colour. Strictly speaking, this process does not correspond to a true chromatic transformation of the polymer, but rather to the physical removal of the coloured material from the electrode surface. Nevertheless, the outcome exhibits as a visible and permanent change in contrast, which from a functional perspective is equivalent to an irreversible colour transition. The results obtained in solution thus represent a preliminary step, providing a basis for transferring the investigation from solution toward ECDs. The following chapters address this transition, focusing on how such behaviour manifests within display architectures and how it can be evaluated in terms of stability and long-term performance.

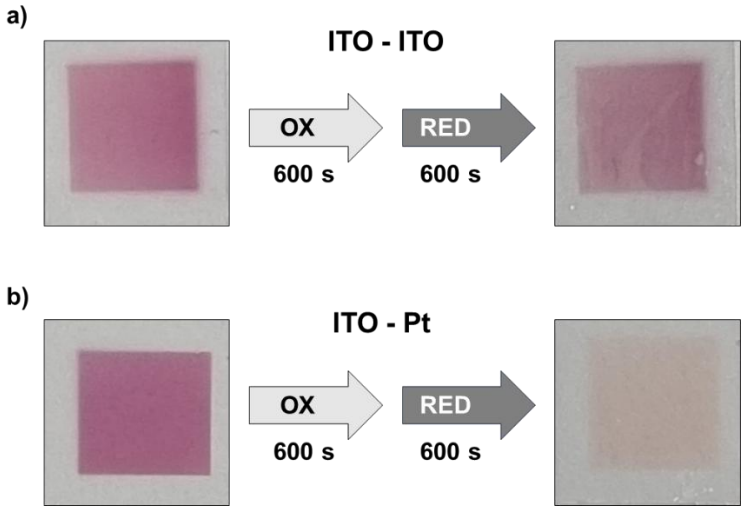


Figure 4.16. Picture of the PURPLE polymer on ITO before and after the OX (+1.5 V, 600 s) and RED (-1.5 V, 600 s) for a) three (ITO as W.E., ITO as C.E., Ag/AgCl as R.E.) and b) three (ITO as W.E., Pt as C.E., Ag/AgCl as R.E.) electrodes setup.

4.4.2 Irreversibility test - polythiophenes decolouration in i-ECDs

Building on the observations obtained in solution, the next objective was to assess whether the same decolouration behaviour could also be induced under display conditions. To this end, an ECD was fabricated following the standard protocol described previously, with the sole modification being the use of the same electrolyte adopted in the solution experiments, thereby ensuring direct comparability between the two configurations. In standard ECDs, the electrolyte is typically formulated with a photocurable monomer and a photoinitiator. Upon UV exposure, the mixture undergoes polymerization, yielding a crosslinked polymer network that plays a fundamental role in stabilizing the EC layer. The resulting matrix significantly increases the viscosity of the medium and effectively suppresses dissolution of the EC polymer into the electrolyte. This stabilization arises from the dense crosslinked structure, which restricts polymer chain mobility and limits solvation, thereby confining the active material to the electrode surface. In the present case, however, a liquid electrolyte was employed, consisting solely of PEC with $LiClO_4$ as solvent and salt, identical to that used in the solution experiments. The reduced viscosity of this medium allows the EC polymer to progressively dissolve during successive oxidation cycles, reproducing the behaviour already observed in solution.

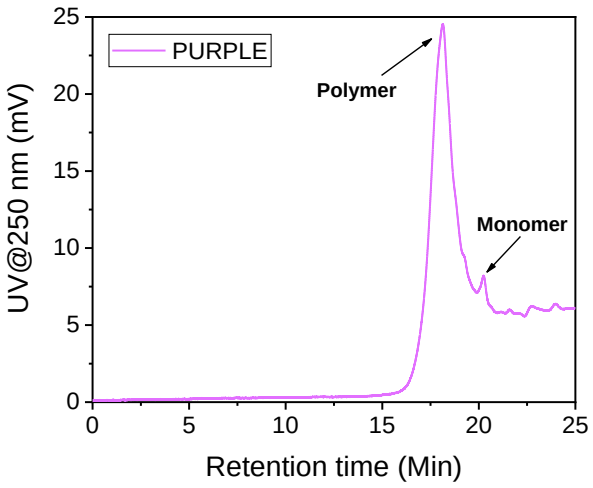


Figure 4.17. GPC analysis of the PURPLE polymer in $CHCl_3$.

To further rationalize the dissolution behaviour, gel permeation chromatography (GPC) was performed to determine the chain length of the synthesized material. The chromatogram (Figure 4.17) displays a minor peak attributable to the monomer (Mp = 304 g/mol), consistent with its theoretical molecular weight (256.4 g/mol), and a main peak corresponding to the polymer (Mp = 2434 g/mol). This value indicates an average chain length of approximately ten repeat units, with a distribution ranging between 8 and 20 units when considering the polydispersity index (PD = 1.38), the number-average molecular weight (Mn = 2144 g/mol), and the weighted average over longer chains (Mz+1 = 5392 g/mol) (Table 4.2). The markedly low molecular weight of this polymer provides a direct explanation for its ease of solubilization within the electrolyte. For comparison, EC dioxythiophene derivatives reported in literature exhibit considerably higher molecular weights, with GPC-determined Mn values in the range of 33000–47000 g/mol.[54] Similarly, PEDOT:PSS systems has been reported with Mn values of 33000–58000 g/mol, depending on the polymerization method.[55] When contrasted with these references, the present material lies more than an order of magnitude lower in molecular weight, a factor that strongly favours dissolution during repeated electrochemical cycling.

Peak	**Mp**	**Mn**	**Mz+q**	**PD**
Polymer	2434	2144	5392	1.38
Monomer	304	308	316	1.00

Table 4.2. Table reporting the average molecular weight of the peak (Mp), average molecular weight (Mn), weighted average over long polymer chains (Mz+1) and their polydispersity (PD) for the PURPLE polymer and its monomeric unit.

To directly compare the two electrolyte systems, both a standard PURPLE ECD, prepared with the Ynvisible electrolyte, and a modified PURPLE ECD, employing only PEC with $LiClO_4$, were subjected to the same cycling protocol previously used to evaluate reversibility in Figure 4.9. During this test, T@540 nm was monitored as a function of cycle number. The displays prepared with the Ynvisible electrolyte exhibited a stable ΔT across multiple cycles, confirming the polymer's retention at the electrode surface and its electrochemical reversibility (Figure 4.18a). In contrast, the ECD incorporating the modified electrolyte displayed a progressive decrease in T@540 nm over successive cycles, consistent with gradual polymer loss into the electrolyte (Figure 4.18b). Photographs of the ECDs in their neutral state after testing further illustrate this divergence, showing a clear visual difference between the two configurations (Figure 4.18c). The results corroborate the observations described earlier and provide further evidence of the correlation between electrolyte composition and polymer stability. It should be noted, however, that while this approach induces an irreversible change in appearance through dissolution of the polymer, the ECD does not become fully unresponsive to applied potentials. Although the extent of colour modulation diminishes as material is lost, a residual switching capability is maintained. Consequently, this method provides a pathway to irreversible visual change, but it does not yield a truly permanent and irreversible ECD.

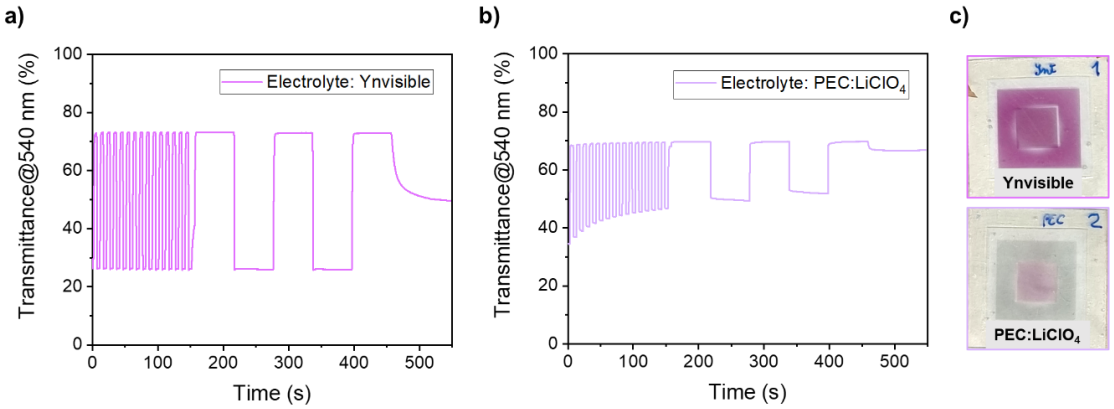


Figure 4.18. T@540 nm as a function of time during the application of ±1.5 V for 30 cycles of 5 s and 5 cycles of 60 s for a) a PURPLE ECD made with Ynvisible electrolyte b) a PURPLE ECD made with PEC:$LiClO_4$ electrolyte. c) Pictures of the two ECDs in the neutral state after the cycling.

4.4.3 Use of sacrificial agents - study in solution

After all the tests carried out on polymer solubility, performed because this effect was discovered during the preliminary measurements, it was then time to investigate the use of sacrificial agents as a strategy to deliberately induce irreversible behaviour in EC polymers. Nucleophilic compounds such as alcohols and amines were selected for their potential to react

with the oxidized state of the polymer. CV in electrolyte solution was employed as a diagnostic tool to test this hypothesis, using a standard three-electrode configuration so far already used during our investigations (Figure 4.19). In principle, the pristine polymer is expected to display well-defined anodic and cathodic peaks of comparable intensity, consistent with a reversible redox process. If a sacrificial agent interacts with the oxidized form, the CV response should change. The anodic peak associated with oxidation would still appear, while the cathodic peak corresponding to reduction might become attenuated or even suppressed. Such an imbalance would suggest that part of the oxidized polymer is chemically consumed by the sacrificial agent and cannot return to its reduced state. Additional effects, such as peak broadening, potential shifts, or the appearance of new signals, could be hypothesized as indicators of reaction products with different or partial electroactivity. Overall, monitoring changes in peak symmetry and reversibility by CV provides a rational approach to evaluate whether sacrificial agents effectively drive the polymer into an irreversible state.

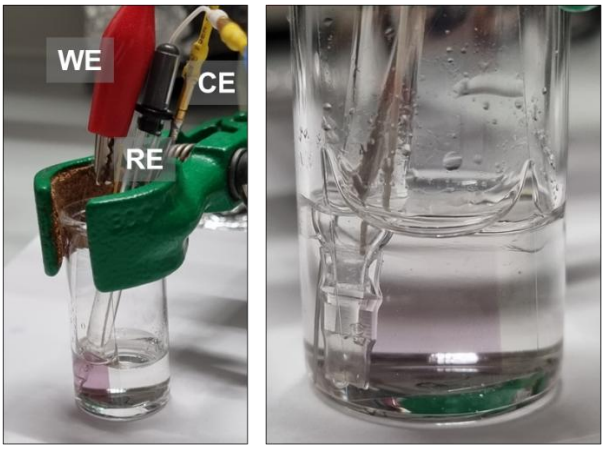


Figure 4.19. a) Picture of the three-electrodes setup (ITO as W.E., Pt as C.E., Ag/AgCl as R.E.) with the PURPLE polymer on the ITO.

4.4.3.1 Alcohols

The investigation initially focused on alcohols as sacrificial agents. Their selection was driven by their nucleophilic character, which allows them to interact with the positively charged sites formed along the polythiophene backbone during electrochemical oxidation. Through lone pair donation, alcohols can react with these charge carriers, thereby disrupting the normal redox reversibility of the polymer. Furthermore, the structural diversity of alcohols provides a valuable variable for modulating reactivity, enabling the assessment of how variations in chain length or functional substitution influence their effectiveness. On this basis, alcohols were

identified as suitable primary candidates for evaluating their ability to induce irreversible changes in the EC response.

To probe the steric and electronic factors governing these interactions, four representative alcohols were selected, namely ethanol, 2-propanol, phenol and 2-naphthol. Ethanol is a small primary alcohol that combines high nucleophilicity with minimal steric hindrance, favouring efficient interaction with electrophilic sites along the polymer backbone. In comparison, 2-propanol introduces increased steric bulk due to its secondary structure, potentially limiting access to reactive centres. Phenol is less nucleophilic owing to resonance delocalization of the hydroxyl lone pair, yet its aromatic ring can engage in π–π and acid–base interactions with conjugated systems. Finally, 2-naphthol possesses an extended aromatic framework that not only increases steric hindrance but also amplifies π–π stacking interactions, thereby modifying the potential binding mode with oxidized polythiophenes. The interaction between the oxidized polymer and the selected alcohols was investigated through CV, which served as a tool to monitor potential modifications of the redox response. All experiments were performed in a standard three-electrode configuration, employing ITO coated with the PURPLE polymer as the W.E., platinum as C.E., and Ag/AgCl as R.E., in PEC:$LiClO_4$ 0.1 M electrolyte. To establish the baseline behaviour, three voltammetric cycles were initially recorded between 0 and +1.5 V, confirming the characteristic oxidation and reduction peaks of the polymer. The alcohol was then introduced into the electrolyte, and the solution stirred at 400 rpm for one minute to ensure homogeneity. The electrochemical measurement was subsequently resumed, and seven additional cycles were performed to monitor possible variations in the redox features in the presence of the sacrificial agent.

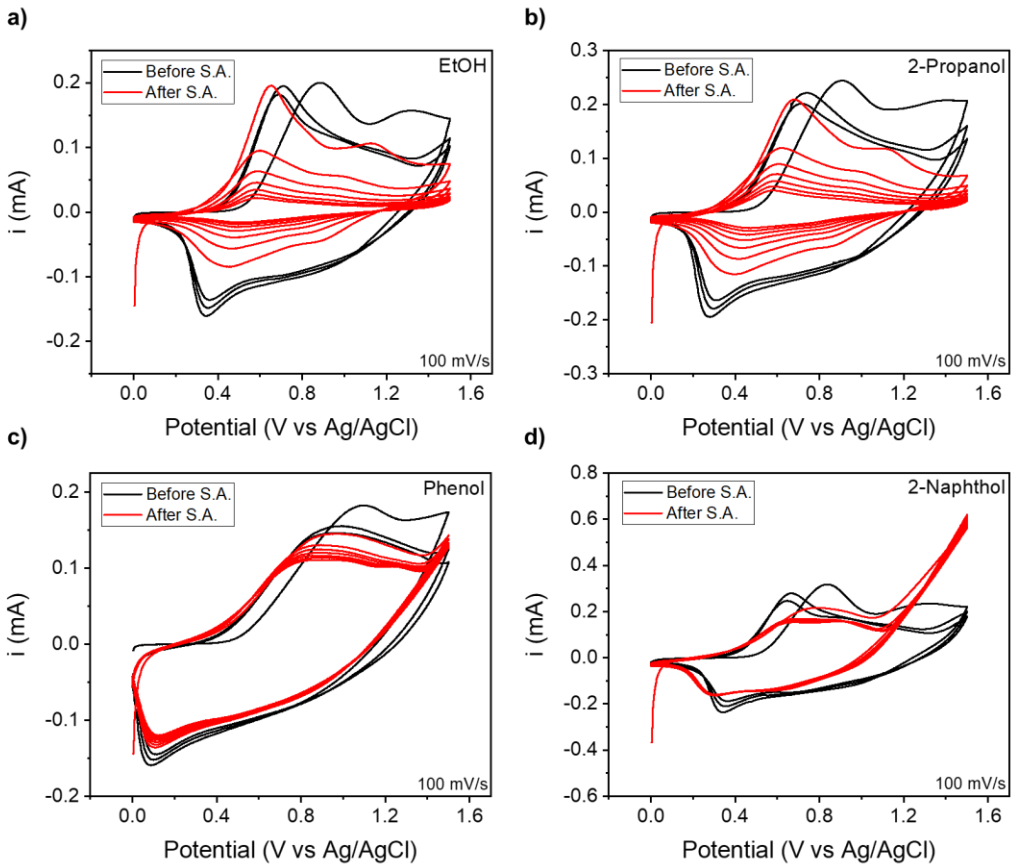


Figure 4.20. Cyclic voltammograms of the PURPLE polymer recorded between 0 and +1.5 V at a scan rate of 100 mV/s over 10 cycles (black: first 3 cycles before addition of the sacrificial agent, red: subsequent 7 cycles after addition). Sacrificial agents (S.A.) employed: a) 1 mL EtOH, b) 1 mL 2-propanol, c) 1 g phenol, and d) 1 g 2-naphthol.

Figure 4.20a,b shows that the addition of EtOH and 2-propanol leads to a progressive decrease in peak intensity, which can be attributed to the gradual solubilization of the polymer in solution, particularly in its oxidized form. This behaviour is consistent with literature reports indicating that small, aliphatic alcohols enhance the solubility of conjugated polymers by disrupting intermolecular interactions and stabilizing charged species through hydrogen bonding.[56,57] Their relatively low steric hindrance and high polarity favour penetration into the polymer matrix, thereby promoting detachment of short chains from the electrode surface. The decrease in electrochemical signals is therefore not the result of a chemical reaction with the polymer but rather a physical dissolution process, corroborated by the visible loss of the oxidized material (grey/black) observed during the experiment, in agreement with previous decolouration studies. Phenol, on the other hand, did not induce a significant decrease in the intensity of the redox peaks (Figure 4.20c), suggesting a limited ability to promote either solubilization or nucleophilic reaction with the oxidized polymer. By contrast, the behaviour of 2-naphthol was markedly different (Figure 4.20d). After its addition, both the oxidation and reduction peaks decreased considerably in intensity, consistent with the hypothesized

occurrence of a nucleophilic reaction with the oxidized polymer backbone. However, despite the clear changes observed in the voltammetric response, no corresponding visible colour change was detected in the polymer film, as evidenced by the picture in Figure 4.21. The photographic comparison highlights the distinct responses of the four alcohols. Ethanol and 2-propanol lead to a noticeably weaker PURPLE intensity, attributable to polymer loss from the electrode surface through enhanced solubility. By contrast, phenol and 2-naphthol preserve nearly the same colour intensity as the pristine film, confirming their limited impact on the macroscopic EC response.

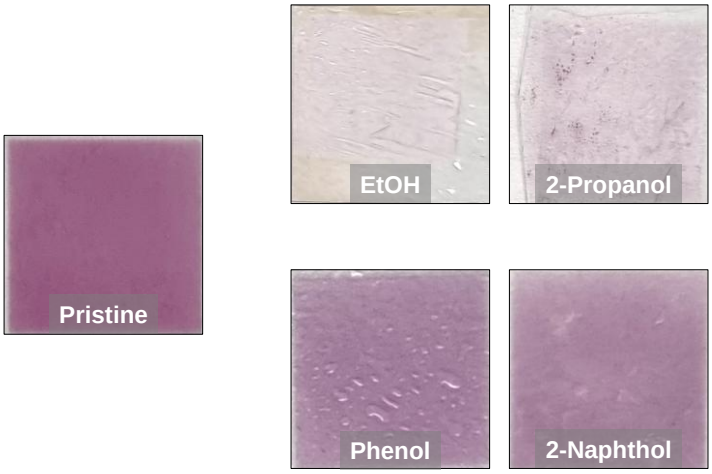


Figure 4.21. Pictures of the PURPLE polymer on the ITO pristine and after 10 cycles for each sacrificial agent.

4.4.3.2 Amines

Following the evaluation of alcohols, amines were investigated as an additional class of sacrificial agents. In particular, 3-ethylamine and tyrosine were selected as representative compounds. Amines are well known for their nucleophilic character, and it was hypothesized that they could interact with the oxidized form of the polymer in a manner analogous to alcohols, potentially leading to irreversible modification of the redox response. The same experimental configuration and protocol were employed, consisting of three initial CV cycles to establish the baseline behaviour of the polymer, followed by the introduction of the sacrificial agent into the electrolyte, stirring for one minute to ensure homogeneity, and seven subsequent cycles to evaluate the impact on the electrochemical response.

The results revealed that after the addition of 3-ethylamine, the reduction peaks rapidly disappeared, while the oxidation current initially increased and then progressively dropped to nearly zero over successive cycles (Figure 4.22a). This behaviour may indicate that 3-ethylamine interacts with the oxidized form of the polymer, potentially preventing its

subsequent reduction and thereby suppressing the reversibility of the redox process. The disappearance of the reduction peaks could be consistent with a nucleophilic addition of the sacrificial agent to the oxidized polymer backbone, although this cannot be confirmed unambiguously from voltammetry alone. In this scenario, the amine may donate electron density to the positively charged sites generated during oxidation, stabilizing them in a modified state that is no longer electrochemically reversible.

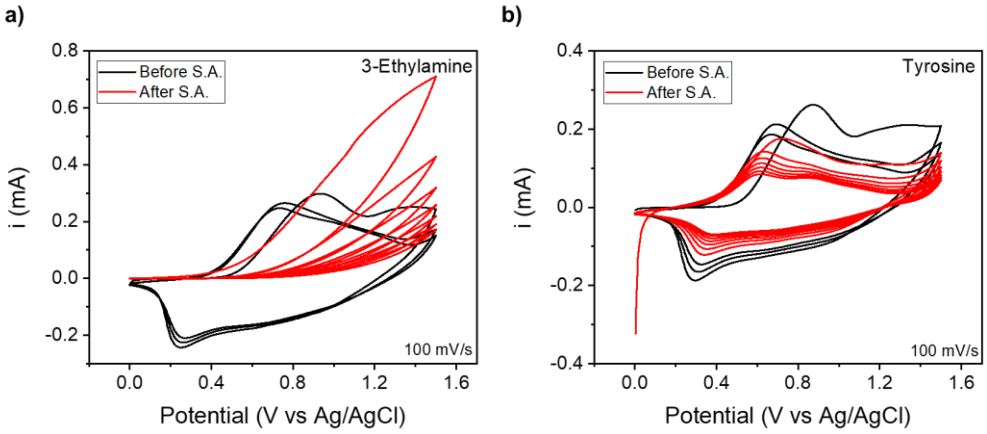


Figure 4.22. Cyclic voltammograms of the PURPLE polymer recorded between 0 and +1.5 V at a scan rate of 100 mV/s over 10 cycles (black: first 3 cycles before addition of the sacrificial agent, red: subsequent 7 cycles after addition). Sacrificial agents (S.A.) employed: a) 1 mL 3-ethylamine, b) 1 g tyrosine.

While such an effect could suggest the occurrence of nucleophilic addition, the photographic evidence in Figure 4.23 shows that the polymer did not undergo a visible colour change. This outcome may signify that no effective reaction took place, or alternatively, that a modification occurred but with an associated change in bandgap too small to manifest as a distinct colour variation. At present, this remains speculative, and further analyses would be required to confirm the mechanism. Conversely, the addition of tyrosine resulted in a gradual decrease in current peaks, mirroring the behaviour observed with EtOH (Figure 4.22b). This trend may be attributed to a slow dissolution process or to weaker interactions with the oxidized polymer, leading to progressive attenuation of the electrochemical response without clear evidence of a chemical reaction. This indicates polymer loss from the electrode surface via solubilization within the electrolyte solution, supported by the decrease in colour intensity of the PURPLE polymer observed in Figure 4.23.

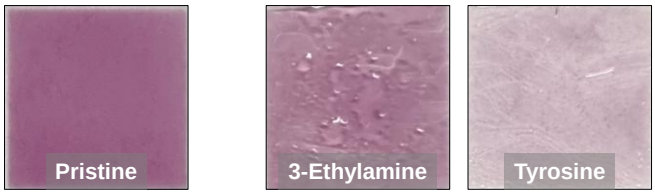


Figure 4.23. Pictures of the PURPLE polymer film pristine and after 10 cycles for each sacrificial agent.

4.4.3.3 Different nucleophilic compounds

Finally, in order to broaden the evaluation of potential nucleophilic compounds, NaOH and an aqueous solution of NH_3 (30% w/w) were investigated under the same experimental configuration and procedure. In the case of NaOH, the voltammograms displayed a progressive decrease in both oxidation and reduction peaks over consecutive cycles, without clear evidence of peak suppression or significant shifts (Figure 4.24a). This behaviour suggests that NaOH does not promote a specific reaction with the oxidized polymer, but rather contributes to a gradual attenuation of the current response, consistent with the stability trends observed in the earlier decolouration experiments.

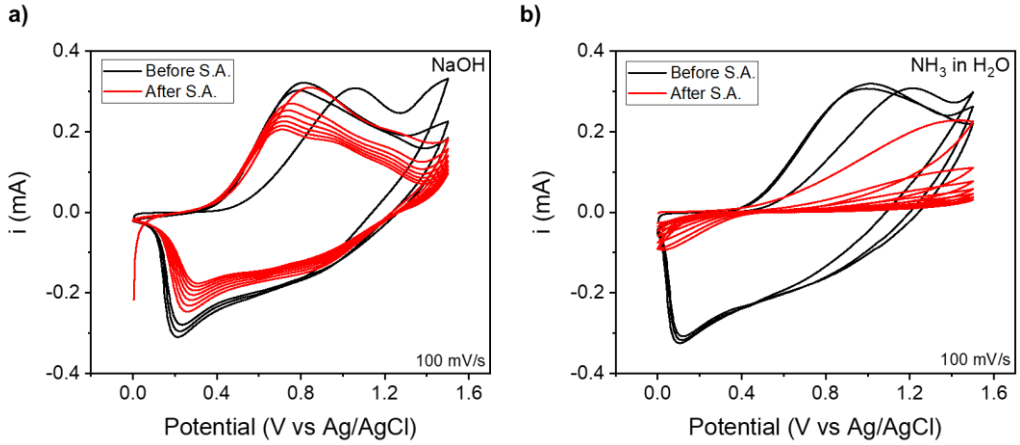


Figure 4.24. Cyclic voltammograms of the PURPLE polymer recorded between 0 and +1.5 V at a scan rate of 100 mV/s over 10 cycles (black: first 3 cycles before addition of the sacrificial agent, red: subsequent 7 cycles after addition). Sacrificial agents (S.A.) employed: a) 1 g NaOH, b) 1 mL of 25% v/w NH_3 in H_2O.

In contrast, the addition of aqueous NH_3 produced a markedly different response (Figure 4.24b). Here, the reduction peak rapidly disappeared, while the oxidation current initially remained detectable but progressively decreased over subsequent cycles. This trend resembles the behaviour observed with 3-ethylamine and could be interpreted as a possible interaction with the oxidized polymer. However, the data alone do not allow an unambiguous conclusion. The suppression of the reduction peak may indeed reflect a reaction mechanism, yet the overall decrease in current could equally be associated with changes in solution conductivity upon NH_3 addition, rather than a true nucleophilic process. As such, while the voltammetric profile points toward a potential interaction, the absence of clear optical evidence and the influence of electrolyte properties prevent a definitive assignment, underscoring the need for further investigation. These observations are further supported by visual inspection of the polymer films after CV testing (Figure 4.25). Compared to the pristine sample, the polymer exposed to NaOH retains a similar PURPLE intensity, indicating limited effect on the EC layer. Likewise, the film treated with NH_3 shows no substantial change in colour, reinforcing the conclusion

that, despite the electrochemical variations, neither compound produces a macroscopically visible alteration in the polymer's optical properties.

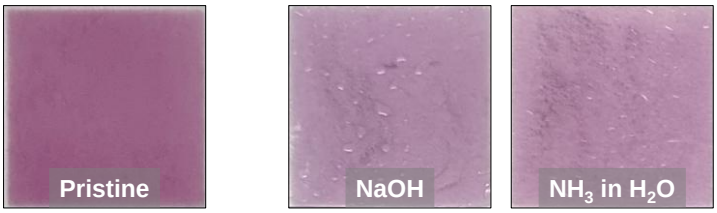


Figure 4.25. Pictures of the PURPLE polymer on the ITO pristine and after 10 cycles for each S.A. employed.

4.5 Conclusions

The experiments presented in this chapter were aimed at exploring strategies to induce irreversible colour changes in polythiophene-based EC polymers for application in ECDs. CV was first employed to evaluate the intrinsic reversibility of the material, establishing the characteristic oxidation and reduction peaks prior to the introduction of sacrificial agents. The underlying concept was that the disappearance or suppression of these peaks upon addition of a nucleophilic compound would provide evidence for a chemical reaction with the oxidized polymer. During these tests, however, an unanticipated decrease in redox peak intensity was observed even in the absence of sacrificial agents. This phenomenon was attributed to solubilization of the polymer into the electrolyte during the oxidation process, leading to irreversible loss of material from the electrode surface. Although initially regarded as a limitation, this effect was subsequently recognized as a possible pathway for achieving irreversible colour change, since polymer once dissolved cannot be restored. Indeed, CV analysis confirmed that oxidation promotes gradual dissolution, resulting in a permanent reduction in colour intensity.

Subsequent investigations examined the role of sacrificial agents, focusing on alcohols and amines. While changes in the voltammetric response were detected in several cases, no conclusive evidence of nucleophilic addition to the polymer backbone was obtained. Instead, the observed attenuation of colour intensity could largely be explained by enhanced polymer solubilization upon addition of certain compounds to the electrolyte. Although the sacrificial agent approach did not provide unambiguous proof of irreversible colour change via nucleophilic reactions, the solubilization pathway emerged as a promising alternative. The irreversible loss of polymer from the electrode represents a mechanism by which the EC behaviour of polythiophenes can be shifted from reversible to irreversible. Further studies will be required to understand, control, and optimize this process, with the ultimate goal of

identifying suitable conditions or additives to reliably exploit solubilization as a means of engineering irreversible ECDs.

REFERENCES

[1] H. Shirakawa, E. J. Louis, A. G. MacDiarmid, C. K. Chiang and A. J. Heeger, *J. Chem. Soc. Chem. Commun.*, 1977, **0**, 578–580.

[2] J. L. Brédas, G. B. Street, B. Thémans and J. M. André, *J. Chem. Phys.*, 1985, **83**, 1323–1329.

[3] A. J. Heeger, *Angew. Chem. Int. Ed.*, 2001, **40**, 2591–2611.

[4] X. Zhao and X. Zhan, *Chem. Soc. Rev.*, 2011, **40**, 3728.

[5] C. Li, M. Liu, N. G. Pschirer, M. Baumgarten and K. Müllen, *Chem. Rev.*, 2010, **110**, 6817–6855.

[6] D. Gao, J. Hollinger, A. A. Jahnke and D. S. Seferos, *J. Mater. Chem. A*, 2014, **2**, 6058–6063.

[7] C. Li and G. Shi, *ACS Appl. Mater. Interfaces*, 2013, **5**, 4503–4510.

[8] B. A. Deore, I. Yu and M. S. Freund, *J. Am. Chem. Soc.*, 2004, **126**, 52–53.

[9] H.-W. Tsai, K.-L. Hsueh, M.-H. Chen and C.-W. Hong, *Crystals*, 2021, **11**, 1292.

[10] T. P. Kaloni, P. K. Giesbrecht, G. Schreckenbach and M. S. Freund, *Chem. Mater.*, 2017, **29**, 10248–10283.

[11] A. Ramírez-Solís, B. Kirtman, R. Bernal-Jáquez and C. M. Zicovich-Wilson, *J. Chem. Phys.*, 2009, **130**, 164904.

[12] U. Mehmood, A. Al-Ahmed and I. A. Hussein, *Renew. Sustain. Energy Rev.*, 2016, **57**, 550–561.

[13] T. P. Kaloni, G. Schreckenbach and M. S. Freund, *J. Phys. Chem. C*, 2015, **119**, 3979–3989.

[14] T. P. Kaloni, G. Schreckenbach and M. S. Freund, *Sci. Rep.*, 2016, **6**, 36554.

[15] J. L. Bredas, R. Silbey, D. S. Boudreaux and R. R. Chance, *J. Am. Chem. Soc.*, 1983, **105**, 6555–6559.

[16] S. Radhakrishnan, R. Parthasarathi, V. Subramanian and N. Somanathan, *J. Chem. Phys.*, 2005, **123**, 164905.

[17] S. S. Zade and M. Bendikov, *J. Phys. Chem. C*, 2007, **111**, 10662–10672.

[18] A. Patra, Y. H. Wijsboom, G. Leitus and M. Bendikov, *Chem. Mater.*, 2011, **23**, 896–906.

[19] R. S. Bhatta and M. Tsige, *Polymer*, 2014, **55**, 2667–2672.

[20] U. Mehmood, A. Al-Ahmed and I. A. Hussein, *Renew. Sustain. Energy Rev.*, 2016, **57**, 550–561.

[21] I. F. Perepichka, D. F. Perepichka, H. Meng and F. Wudl, *Adv. Mater.*, 2005, **17**, 2281–2305.

[22] C. B. Nielsen and I. McCulloch, *Prog. Polym. Sci.*, 2013, **38**, 2053–2069.

[23] M. C. Scharber and N. S. Sariciftci, *Adv. Mater. Technol.*, 2021, **6**, 2000857.

[24] O. Bubnova, Z. U. Khan, H. Wang, S. Braun, D. R. Evans, M. Fabretto, P. Hojati-Talemi, D. Dagnelund, J.-B. Arlin, Y. H. Geerts, S. Desbief, D. W. Breiby, J. W. Andreasen, R. Lazzaroni, W. M. Chen, I. Zozoulenko, M. Fahlman, P. J. Murphy, M. Berggren and X. Crispin, *Nat. Mater.*, 2014, **13**, 190–194.

[25] J. Y. Fu, D. S. Liu and S. J. Xie, *Phys. E Low-Dimens. Syst. Nanostructures*, 2008, **40**, 915–919.

[26] C. Graßmann, M. Mann, L. Van Langenhove and A. Schwarz-Pfeiffer, *Sensors*, 2020, **20**, 5691.

[27] Z. Wang and R. Liu, *Mater. Today Electron.*, 2023, **4**, 100036.

[28] C. Faure, A. Guerfi, M. Dontigny, D. Clément, P. Hovington, U. Posset and K. Zaghib, *Electrochimica Acta*, 2016, **214**, 313–318.

[29] Z. Shao, A. Huang, C. Ming, J. Bell, P. Yu, Y.-Y. Sun, L. Jin, L. Ma, H. Luo, P. Jin and X. Cao, *Nat. Electron.*, 2022, **5**, 45–52.

[30] S. Zhao, X. Gao, L. Chen, W. Huang and Y. Liu, *Appl. Mater. Today*, 2022, **28**, 101543.

[31] M. Girtan, R. Mallet, M. Socol and A. Stanculescu, *Mater. Today Commun.*, 2020, **22**, 100735.

[32] S. Shao, J. Shi, I. Murtaza, P. Xu, Y. He, S. Ghosh, X. Zhu, I. F. Perepichka and H. Meng, *Polym. Chem.*, 2017, **8**, 769–784.

[33] D. D. Hebert, M. A. Naley, C. C. Cunningham, D. J. Sharp, E. E. Murphy, V. Stanton and J. A. Irvin, *Materials*, 2021, **14**, 6146.

[34] S. Geetha and D. C. Trivedi, *Synth. Met.*, 2005, **155**, 232–239.

[35] A. Maho, S. Nayak, F. Gillissen, R. Cloots and A. Rougier, *Coatings*, 2023, **13**, 1879.

[36] P. Ledwon, D. Ovsiannikova, T. Jarosz, S. Gogoc, P. Nitschke and W. Domagala, *Electrochimica Acta*, 2019, **307**, 525–535.

[37] T.-H. Le, Y. Kim and H. Yoon, *Polymers*, 2017, **9**, 150.

[38] X. Chen, H. Zhang, W. Li, Y. Xiao, X. Zhang and Y. Li, *Environ. Sci. Ecotechnology*, 2022, **10**, 100164.

[39] M. Gusatti, D. Aragão Ribeiro de Souza, M. Barozzi, R. Dell'Anna, E. Missale, L. Vanzetti, M. Bersani and M. Nalin, *ACS Appl. Mater. Interfaces*, 2024, **16**, 51253–51264.

[40] D. Levasseur, I. Mjejri, T. Rolland and A. Rougier, *Polymers*, 2019, **11**, 179.

[41] X. Wang, L. S. de Vasconcelos, K. Chen, K. Perera, J. Mei and K. Zhao, *ACS Appl. Mater. Interfaces*, 2020, **12**, 50889–50895.

[42] S.-H. Chiu, M. S. Widjajana, N.-A. Nor-Azman, F.-M. Allioux, R. Yu, L. Liu, N. Flores, Y. Wang, M. Asgharnejad-Laskoukalayeh, A. P. O'Mullane and K. Kalantar-Zadeh, *ACS Appl. Mater. Interfaces*, 2025, **17**, 43968–43978.

[43] T. Moreira, C. A. T. Laia, M. Zangoli, M. Antunes, F. Di Maria, S. De Monte, F. Liscio, A. J. Parola and G. Barbarella, *ACS Appl. Polym. Mater.*, 2020, **2**, 3301–3309.

[44] M. Pietsch, S. Schlisske, M. Held, N. Strobel, A. Wieczorek and G. Hernandez-Sosa, *J. Mater. Chem. C*, 2020, **8**, 16716–16724.

[45] Z. Wang, X. Wang, S. Cong, J. Chen, H. Sun, Z. Chen, G. Song, F. Geng, Q. Chen and Z. Zhao, *Nat. Commun.*, 2020, **11**, 302.

[46] P. M. Beaujuge and J. R. Reynolds, *Chem. Rev.*, 2010, **110**, 268–320.

[47] D. R. Rosseinsky and R. J. Mortimer, *Adv. Mater.*, 2001, **13**, 783–793.

[48] R. J. Mortimer, A. L. Dyer and J. R. Reynolds, *Displays*, 2006, **27**, 2–18.

[49] N. Elgrishi, K. J. Rountree, B. D. McCarthy, E. S. Rountree, T. T. Eisenhart and J. L. Dempsey, *J. Chem. Educ.*, 2018, **95**, 197–206.

[50] M. Deepa and S. Ahmad, *Eur. Polym. J.*, 2008, **44**, 3288–3299.

[51] S.-H. Hsiao and Z.-D. Ni, *Polymers*, 2025, **17**, 1152.

[52] X. Zhang, H. Xie, M. Fujii, H. Ago, K. Takahashi, T. Ikuta, H. Abe and T. Shimizu, *Appl. Phys. Lett.*, 2005, **86**, 171912.

[53] C. G. Granqvist and A. Hultåker, *Thin Solid Films*, 2002, **411**, 1–5.

[54] B. D. Reeves, C. R. G. Grenier, A. A. Argun, A. Cirpan, T. D. McCarley and J. R. Reynolds, *Macromolecules*, 2004, **37**, 7559–7569.

[55] J. Kim, C. Park, S. Im, H. Lee and J. H. Kim, *RSC Adv.*, 2019, **9**, 4028–4034.

[56] L. Tarachiwin, P. Kiattibutr, L. Ruangchuay, A. Sirivat and J. Schwank, *Synth. Met.*, 2002, **129**, 303–308.

[57] S. Zhou, T. Wu and J. Kan, *Eur. Polym. J.*, 2007, **43**, 395–402.

CHAPTER 5

CONCLUSION AND OUTLOOK

The work presented in this thesis demonstrates that irreversible EC systems can be designed and controlled by carefully tuning both the electrochemical processes and the material composition. The results obtained in Chapters 2, 3, and 4 show that different strategies can be used to achieve a permanent optical response, moving from fundamental understanding to practical device implementation.

The central outcome of this work, described in Chapter 2, is the development of DA-based *i*-ECDs. A key point that clearly emerged from the experimental results is that the colour change observed in these systems is not primarily due to the formation of PDA formed by DA oxidation, but rather to the electrochemical reduction of the ITO electrode. DA therefore acts as an oxidizing species that lowers the reduction potential of the ITO, enabling the transition of the display from a transparent to a black state. This mechanism was confirmed through a series of control experiments. In particular, when the devices were prepared without DA, using only PBS electrolyte, the reduction of ITO occurred only at significantly higher voltages. The threshold voltage for ITO reduction increased from approximately 1.25–1.35 V in the presence of DA to about 2.93 V in PBS alone, and even up to 3.7–3.8 V depending on the electrolyte composition. This clearly demonstrates that, although DA does not induce the colour change through the formation of PDA as initially hypothesized, it plays an important role in lowering the activation energy of the system and enabling the EC response at lower voltages. Additional experiments further support this interpretation. When a voltage ramp was applied, no colour change was observed below 1.0 V, while at 1.25 V a clear optical transition already occurs, with a transmittance T@600 nm of approximately 45.7% ($\Delta T \approx 35\%$). At voltages above 1.5 V, the devices consistently reach a fully dark state. In contrast, systems without DA only show a visible colour change at voltages above ~4 V, confirming that the reduction of ITO is the dominant mechanism, but requires much higher energy in the absence of a suitable redox mediator.

From a quantitative point of view, the DA-based *i*-ECDs show a strong optical modulation. Under standard conditions (1.5 V, 600 s), the T@600 nm decreases down to approximately 3%, indicating a nearly complete optical transition. At the same time, the charge required for full activation was measured to be 247.3 ± 22.2 mC, with a coloration efficiency of 6.02 cm^2/C. However, one of the most relevant findings of this work is that the system can be significantly optimized. By reducing the activation time to 60 seconds, T@600 nm of about 9% can still be

achieved, which is visually comparable to the fully switched state, while reducing the charge consumption to 54.9 ± 4.9 mC and increasing the CE to 17.65 cm^2/C. When the active area is further reduced to 0.25 cm^2, the required charge drops to approximately 15 mC, with a CE of 70.62 cm^2/C, highlighting the strong scalability of the system. From a kinetic perspective, the activation process is relatively fast, with most of the optical transition occurring within the first seconds after applying the voltage. This behaviour is consistent with a rapid onset of ITO reduction facilitated by DA oxidation, followed by a progressive increase in internal resistance that eventually stops the current flow. This self-limiting mechanism naturally leads to a stable and irreversible final state.

The reliability tests performed in this work confirm that the devices are stable under different conditions. The *i*-ECDs maintain their performance under bending, low temperature storage, and light exposure. Once activated, the optical state remains stable over time, which is essential for applications where a permanent visual signal is required. The study of DA derivatives further supports the proposed mechanism. Substituents that modify the oxidation potential of the molecule were shown to influence the threshold voltage for ITO reduction. For example, electron-donating groups lead to lower activation thresholds (*e.g.* OMeDA ~1.30 V), while electron-withdrawing groups increase the required voltage, confirming the direct link between molecular oxidation and ITO reduction. This provides a clear strategy for tuning device performance through molecular design.

Chapter 3 focuses on moving from a purely liquid system to something that can actually be processed at larger scale. By adding different gelling agents, such as Agar Agar, Starch, PEG, and Porcine skin-derived materials, the DA formulation was turned into inks with a controlled viscosity. This made it possible to deposit the material using techniques like doctor blade and, in a first step, also screen printing, going beyond simple lab-scale preparation. The viscosity of the formulation turned out to be a key parameter. On one side, increasing it improves film formation and makes the process more controllable. On the other side, it also limits ion mobility and can slow down the electrochemical response. Even with this limitation, the printed systems still showed an activation behaviour comparable to the liquid ones. In particular, the optical response and the charge consumption remained in the same order of magnitude as the standard DA-based devices. Some differences between the formulations were clearly visible. Agar Agar and Starch generally gave more homogeneous films and better mechanical stability. PEG, instead, was easier to process, but its high concentration required more attention, since it can dilute the active species and reduce ionic transport. The porcine skin-based formulation showed a good compromise, thanks to its ability to form stable gel-like networks. These results show that the system can be adapted to more scalable fabrication methods without losing its main

functionality. At the same time, they make it clear that there is a balance to find between viscosity, ion transport, and film quality, which will be important for achieving consistent and reliable devices.

Chapter 4 explores an alternative approach to irreversible electrochromism based on PT systems. In this case, permanent decolouration was not the initial objective, but rather an effect that was discovered during the characterization of the system in solution. During these preliminary experiments, carried out without any additives, it was observed that upon oxidation (*e.g.* +1.5 V for 600 s), the polymer undergoes a significant loss of colour due to partial or complete dissolution from the electrode surface. This behaviour results in a strong and irreversible optical change, as the oxidized polymer detaches from the electrode in a permanent way, leading to a loss of the active material and therefore of the colour. Based on this observation, a second strategy was explored using sacrificial nucleophilic agents, such as alcohols and amines, with the aim of reacting with the oxidized polymer and blocking its reduction. However, this approach proved to be significantly more complex. The results did not provide clear or consistent evidence of a controlled chemical locking mechanism, and the behaviour remained strongly dependent on experimental conditions.

Overall, the results of this thesis show that irreversible electrochromism can be achieved through different mechanisms, but also highlight the importance of understanding the underlying processes. In DA-based systems, the key factor is the ability of the molecule to lower the reduction potential of ITO, enabling activation at low voltages. This insight represents one of the most important contributions of this work. Looking forward, several directions can be considered. For DA-based systems, further work should focus on reducing the activation voltage and charge consumption while maintaining strong optical contrast (*e.g.* T@600 nm < 10%). This could be approached at different levels. On the molecular side, increasing the electron-donating character of the DA structure could help lower its oxidation potential, as already observed for example with OMeDA. In parallel, working on the electrode itself represents another effective strategy. Although the reduction threshold of ITO cannot be easily lowered without affecting its stability, it is possible to shift the onset of reduction by modifying the interfacial chemistry. In this work, it was shown that species present in the electrolyte can interact directly with the hydroxyl (–OH) groups on the ITO surface, through coordination, hydrogen bonding, and charge transfer effects. These interactions modify the local electronic structure of ITO, stabilizing reduced states and effectively lowering the voltage required for its reduction. For PT systems, a better understanding of the degradation mechanisms is needed in order to improve control and reproducibility. Combining different materials could also allow more complex and tunable irreversible responses. From a

technological point of view, the development of fully printable devices remains a key objective. Extending printing to all components of the device would enable large-scale production and integration into commercial applications.

Finally, the systems developed in this work show strong potential for applications beyond cold-chain monitoring. Their low energy consumption (down to ~15 mC), stable final state, and simple structure make them suitable for smart labels, tamper indicators, and low-cost sensing devices. In conclusion, this thesis demonstrates that irreversible EC systems can be developed in a controlled way and show clear potential for scalability, as confirmed by the successful transition from liquid formulation to a functional ink. At the same time, the identification of ITO reduction as the origin of the colour change, together with the role of DA in lowering the activation threshold, provides a solid basis for further development. However, the strong dependence on ITO, which is currently essential for device operation, may represent a limitation in terms of cost and sustainability for large-scale applications.

CHAPTER 6

EXPERIMENTAL SECTION

6.1 Instrumentation

Thin layer chromatography (TLC). The procedure was carried out using pre-coated aluminium sheets containing 0.20 mm Merck Millipore Silica gel 60 embedded with a fluorescent indicator F254. Visualization of the TLC plates occurred through exposure to ultraviolet light at either 254 nm or 366 nm wavelengths.

Column chromatography. The process was executed employing Merck Gerduran silica gel 60, characterized by a particle size ranging from 40 to 63 μm.

Preparative high-performance liquid chromatography (HPLC). The purification was accomplished using an Agilent 1260 Infinity Preparative LC System, which was outfitted with a reverse phase column (Varian Pursuit C18, 5 μm, 250 X 21.2 mm), 0.1% TFA in H_2O and ACN were used as eluents.

Melting points (Mp). The analysis was conducted using an MPA160 apparatus employing open capillary tubes with an average material loading of <0.5 mg. The melting temperature results were reported in degrees Celsius. Temperature measurements were achieved with a resolution of 0.1 °C and an accuracy described by ± (0.45+0.0045) °C. The typical accuracy was ±0.6 °C for temperatures below 200 °C and ±1.0 °C for temperatures equal to or above 200 °C. The reproducibility of temperature readings stood at 0.2 °C. The oven capabilities encompassed a temperature range from 50 °C to 260 °C, with ramp rates available at 0.5, 1.0, 2.0, 5.0, 10, and 20 °C per minute. Capillaries employed in the setup had dimensions spanning from 1.4 mm to 1.8 mm in outside diameter and a length of 100 mm.

Nuclear magnetic resonance (NMR). Characterizations were performed at the NMR centre of the University of Vienna (AT). All ^{1}H NMR and ^{13}C NMR spectra were recorded using a Bruker AV-600 spectrometer at 300K. The ^{19}F NMR was recorded using a Bruker AV-700 spectrometer at 300 K. Proton and carbon chemical shifts are reported in parts per million (ppm, δ scale) according to tetramethylsilane ($\delta_H = \delta_C = 0$ ppm) using the solve resual signal as internal reference ($CDCl_3$: δ_H= 7.26 ppm, δ_C= 77.16 ppm; D_2O: δ_H= 4.79 ppm, δ_C= 49.00 ppm). Fluorine chemical shifts are reported in ppm, referenced to the external standard fluorine signal

of $CFCl_3$ (δ_F= 0 ppm) Coupling constants (*J*) were given in Hz. Resonance multiplicity was described as *s* (singlet), *d* (doublet) and *m* (multiplet).

Mass spectrometry (HRMS). Analysis of the purified compounds was carried out by High Resolution Electrospray Ionization Mass Spectrometry. HRMS spectra (*m/z* 50-1900) were obtained on a maXis UHR ESI-Qq-TOF mass spectrometer (Bruker Daltonics, Bremen, Germany) in the positive ion mode by direct infusion. The sum formulas of the detected ions were determined using Bruker Compass DataAnalysis 4.1 based on the mass accuracy ($\Delta m/z \leq 5$ ppm) and isotopic pattern matching (SmartFormula algorithm).

Fourier-transform Infrared spectroscopy (FTIR). The spectra were captured using the ALPHA FTIR Routine Spectrometer, manufactured by Bruker Optics, operating in ATR mode with a diamond mono-crystal. This instrument is equipped with gold-coated optics, offering a resolution of 0.9 cm^{-1}, and covers a wavelength range spanning from 375 to 7500 cm^{-1}. Software, OPUS/Mentor.

Ultraviolet-Visible absorption spectroscopy (UV-Vis). UV/vis analyses were conducted utilizing an Agilent-Cary 5000 UV-Vis-NIR spectrophotometer, which was outfitted with a solid-state sample holder. The light source consisted of a combination of tungsten halogen visible and deuterium arc UV lights. The system boasted a maximum scanning speed of 2000 nm/min for UV-Vis and 8000 nm/min for NIR measurements. Employing a double-beam photometric setup, the spectrophotometer featured spectral bandwidths ranging from 0.01 to 5.00 nm for UV-Vis and 0.04 to 20 nm for NIR, while accommodating wavelengths spanning from 175 to 3300 nm. Software, Cary WinUV for UV-Vis-NIR Applications.

X-ray photoelectron spectroscopy (XPS). The elemental composition of the PET-ITO substrates was analysed in a ThermoScientific Nexsa spectrometer using monochromatic Al Kα radiation of energy 1486.6 eV. The samples were mounted onto a stainless-steel holder and introduced in the spectrometer. The elemental fingerprint of each sample was then recorded in three different areas using a spot size of 400 µm, a fixed pass energy of 50 eV and energy step size of 0.1 eV and 50 number of scans.

Scanning electron microscopy (SEM). SEM images were recorded with a Zeiss Supra 55 VP instrument (Carl Zeiss, Germany) with an acceleration voltage of 5 kV. The samples were sputtered with Au (Emitech K575X Peltier cooled) for 60 seconds at 60 mA prior to fixation

on an Al support. A set of samples was placed perpendicular to the detector to scan the surface, while another set was rotated 90° to obtain cross-sectional images useful for the evaluation of the thickness of the deposited polydopamine films.

Atomic force microscopy (AFM). The Veeco Nanoscope V multimode 8 instrument was employed for Atomic Force Microscopy (AFM) investigations, with analysis conducted in tapping mode at room temperature, utilizing a POINTPROBE-PLUS® Silicon-DPM-Sensor cantilever. The technical specifications include the material being silicon with a resistivity of 0.01 - 0.02 Ωcm, a thickness of 4.0±1 μm, length of 125±10 μm, and width of 30±7.5 μm. The cantilever exhibits a resonance frequency ranging from 204 to 497 kHz, a force constant between 10 and 130 N/m, and a tip height spanning 10 to 15 μm.

Solar lamp simulator. The measurement of the *i*-ECDs stability under solar irradiation was performed using a Quantum Design solar simulator, characterized by an output power equivalent to 1 sun (*i.e.*, 1000 W/m^2) and a uniform output beam of 51 × 51 mm^2. The lamp used is a high pressure 1000 W Xenon short arc. The full machine spectrum system starts from 250 nm to 2500 nm, and it comes with a 90° beam turner and Al-mirror. The *i*-ECDs is positioned perpendicularly to the beam at a working distance of 220 mm from the optical system and the irradiation lasted 8 hours.

Potentiostat. The Autolab PGSTAT204 features a basic potentiostat/galvanostat with a voltage range of -10 V to +10 V and a maximum current of ±0.4 A. The instrument's potential precision lies within ±0.2% and ±2 mV, while the current precision is ±0.2% and ±0.2% of the current range. The PGSTAT204 has a potential resolution of 3 μV (at gain 100) and a current resolution of 0.0003% of the current range. Software, NOVA version 2.1.

Dynamic 3-point bending tester. The mechanical durability analysis was performed using a custom-built three-point bending apparatus developed by Etteplan (Tampere, Finland). During testing, the *i*-ECD samples were securely clamped at their external edges to ensure stable positioning and uniform stress distribution throughout the bending process. The setup operated with a bending radius of 5 mm and a cyclic frequency of 1 Hz, allowing precise and repeatable deformation of the *i*-ECDs.

Temperature and humidity chamber for reliability. The reliability analysis was conducted using the ESPEC PL-1J Low Temperature & Humidity Chamber, which provides a controlled

environmental range from -40 to +100 °C and 20% to 98% relative humidity (RH). The system maintains exceptional stability, with temperature and humidity fluctuations limited to ±0.3 °C and ±2.5% RH, respectively. Temperature transitions occur at rates of 3.0 °C/min for heating and 2.0 °C/min for cooling, and the chamber supports an allowable heat load of 850 W.

Temperature chamber. The activation tests of the *i*-ECDs at different temperatures were conducted using a Binder Dynamic MK56 thermal chamber. This advanced chamber provides a precisely controlled thermal environment, with an operational temperature range extending from -40 °C to 180 °C and a temperature control precision of ±0.1 °C. Such a configuration allows for both accurate heating and cooling cycles

Self-built environment chamber. The experimental characterization of the Arduino-based smart label prototype was performed within a custom-designed 100 L testing chamber constructed using transparent plexiglass panels to allow visual inspection during operation. The chamber was equipped with an integrated ventilation system consisting of a controllable fan to ensure homogeneous air circulation, and a resistive heating element to precisely regulate the internal thermal environment. To monitor and record the environmental parameters, the setup included a digital temperature and relative humidity sensor, enabling tracking of the test conditions.

Rotational viscosimeter. Viscosity measurements were performed using a Sheen VISCOmaster VM2 rotational viscometer. The instrument provides a set of fixed rotational speeds covering the range from 0.3 to 200 rpm, allowing characterization across low- and high-shear conditions. It supports a broad measuring range from 100 to 13000000 cP (0.1–1300 Pa·s), making it suitable for both low-viscosity liquids and highly viscous formulations. The device offers an accuracy of ±1% of full scale, while the repeatability of measurements is 0.2%, ensuring reliability and reproducibility of the obtained data.

Doctor blade. The coating was applied using a Sheet Film Coater MSK-AFA-II-VC (MTI Corporation), which provides precise control over deposition parameters. The instrument features an adjustable stroke length from 10 to 550 mm, enabling both small-scale and larger-area coatings within the same platform. The traverse speed can be tuned between 5 and 100 mm/s, with a control accuracy of ±10 mm/s, allowing for fine optimization of coating uniformity and solvent leveling. The coater is equipped with a 250 mm-wide coating head,

which supports film thickness adjustment in the range of 0.01 to 5 mm, accommodating both ultra-thin layers and comparatively thick wet films depending on the application requirements.

Screen printing. Screen printing was conducted at room temperature using a screen-printing machine that was custom designed and assembled in-house by Ynvisible in Charneca (PT). A screen with a mesh density of 24T (24 threads per inch) was selected to achieve the desired film thickness and ink loading. During deposition, the ink was manually spread across the screen using a squeegee with a hardness of 70 durometer, ensuring uniform shear and consistent transfer through the mesh. The manual operation of the squeegee allowed better feedback and visual control over the print quality throughout the process.

Self-built spray coater machine. The reversible ECD layers were deposited by spray coating using a custom-built semi-automated system. A 3D-printed mount ensured that the airbrush remained fixed in a perpendicular position relative to the substrate throughout the process. The deposition was programmed via software, which set a constant spray height of 6 cm and defined a serpentine coating path for uniform coverage. The spray pressure was adjusted to 1 bar, and the substrate was heated to 60 °C during coating to accelerate solvent evaporation and promote the formation of a homogeneous film.

Cycling chamber. The cycling analysis of the reversible ECDs was performed inside a custom-made, fully white cycling chamber equipped with white illumination, a colour checker and a video camera (IDS Imaging UI-3590CP-C-HQ) positioned perpendicular to the device. Each captured frame contained an X-rite ColorChecker for colour reference. The images were first colour-corrected and subsequently converted from RGB to the CIE Lab* colour space using a Matlab script developed by Ynvisible Inc. Based on the calculated Lab* coordinates, the colour difference ΔE was then determined.

Desktop cutting plotter. All cutting operations of ITO and NITTO films, as well as the fabrication of labels for CHARISMA, cold-chain, and Prelonic design-specific applications, were carried out using a Silhouette Cameo® 4 desktop cutting plotter. The machine allows precise digital cutting of thin polymeric and flexible substrates through a computer-controlled blade system. All cutting paths were designed and executed using Silhouette Studio® software (version 4.x), which enables vector-based control of cutting speed, force, and blade depth.

3D printing machine. The fabrication of the milk carton prototype was carried out using a Prusa i3 3D printer, based on fused deposition modeling (FDM) technology. The printer features a 0.4 mm brass nozzle, a heated bed (up to 100 °C), and a build volume of approximately 250 × 210 × 200 mm. The printing process was controlled through PrusaSlicer software (version 2.x), which was used to prepare the 3D model. A PLA (polylactic acid) filament with a diameter of 1.75 mm was used as the printing material due to its ease of processing and good dimensional stability.

6.2 Chemicals and Materials

Chemicals and solvents. All chemicals were obtained from Sigma-Aldrich, TCI, and Alfa Aesar, and were employed without further purification, except for copper (0), which was finely ground to a uniform powder prior to use. Dopamine hydrochloride and sodium metabisulfite for the DA+AntiOX formulation were purchased from TCI and used as received. All solvents, including phosphate-buffered saline (PBS, pH 7.4), were obtained from Sigma-Aldrich, Merck, and Eurisotop. The electrolyte used in the reversible ECDs was kindly provided by Ynvisible Interactive Inc. This electrolyte is based on a polyethylene carbonate and photopolymer matrix, protected under patent, and employs $LiClO_4$ as the ionic conducting salt. Furthermore, the binders used in the formulations described in Chapter 3 were supplied by Merck.

***Materials*.** The PET-ITO (PET, 125 μm thick covered by ITO, 200 nm thick, 35–40 Ω/sq) and NITTO D9605 (220 μm thick) double-coated tape were provided by Ynvisible Interactive Inc. The copper tape was purchased from Digi-Key. The Arduino Nano (model A000005, equipped with an ATmega328P microcontroller running at 16 MHz, operating at 5 V with Mini-USB interface) and the temperature sensors were purchased from Amazon. The T-Sensor and the Super Capacitors for the smart label assembly were provided by Sunil Kumar Behera and Hamed Pourkheirollah respectively (ESR05 and ESR08 in the CHARISMA project). The PCB utilized for the "Tamperproof SMART LABEL" was bought from Silicon Austria Lab, while the flexible PCB for the event tickets was purchased from Prelonic Technologies. All UV-Vis measurements were performed using quartz cuvettes with a 1 cm optical path length. For spectroelectrochemical experiments, a BASi® quartz spectroelectrochemical cell (SEC-C) was used, featuring a 1 mm optical path length and an integrated three-electrode configuration comprising a platinum mesh working electrode, a platinum wire counter electrode, and an Ag/AgCl reference electrode. The cell was closed with a Teflon cap to prevent solvent evaporation and contamination during measurements. For the cyclic voltammetry (CV) in

solution, a glassy carbon electrode (3.0 mm diameter) was used as the working electrode, a platinum wire (thickness 0.5 mm) as the counter electrode, and an Ag/AgCl/KCl (saturated) reference electrode (outer diameter 4 mm).

6.3 Methods

Chapter 2

2.4 Preparation of the dopamine stock solution (**DA**). 10 mg of dopamine hydrochloride (DA) and 1 mL of PBS (phosphate saline buffer) pH 7.4 were added to a glass vial and the obtained solution (10 mg/mL) was sonicated for 1 minute at room temperature (150 W, 37 kHz) to favour complete dispersion.

2.4 Preparation DA stock solution with sodium metabisulfite antioxidant (**DA+AntiOX**). 10 mg of dopamine hydrochloride, 5 mg of sodium metabisulfite (1 : 1.28 molar ratio) and 1 mL of PBS (phosphate saline buffer) pH 7.4 were added to a glass vial and the obtained solution (10 mg/mL, with respect to the DA) was sonicated for 1 minute at room temperature (150 W, 37 kHz) to favour complete dispersion.

2.4 Manufacturing of the irreversible electrochromic display (*i*-ECD). The *i*-ECDs was manufactured following a vertical configuration. Two layers of conductive material, PET-ITO, were placed face to face settling an adhesive spacer in between. This adhesive spacer, square in shape and hollow in the centre, produces a tiny volume that was filled by injecting the dopamine-based solution. The total active area of the *i*-ECDs measure 1 cm^2.

2.4 *i*-ECD activation. By activation we mean the application of a potential difference across the *i*-ECD capable of producing the oxidation of DA and consequent reduction of ITO leading to a colour change from transparent to black. This was conducted by placing the *i*-ECD inside a spectrophotometer measuring the T@600 nm and applying 1.5 V across the *i*-ECD.

2.5 Effect of the pH. The PBS has a standard pH of 7.4. The variations were carried out by adding HCl and NaOH up to the desired pH. Four *i*-ECDs were prepared employing PBS at pH 1.5, 4.5, 9.8 and 12 with dopamine with a concentration of 10 g/L. Then each *i*-ECDs was connected to a potentiostat, placed inside a spectrophotometer, employing a solid-state sample holder, and subjected to 1.5 V for 600 seconds. The T@600 nm and one picture of each *i*-ECDs were recorded.

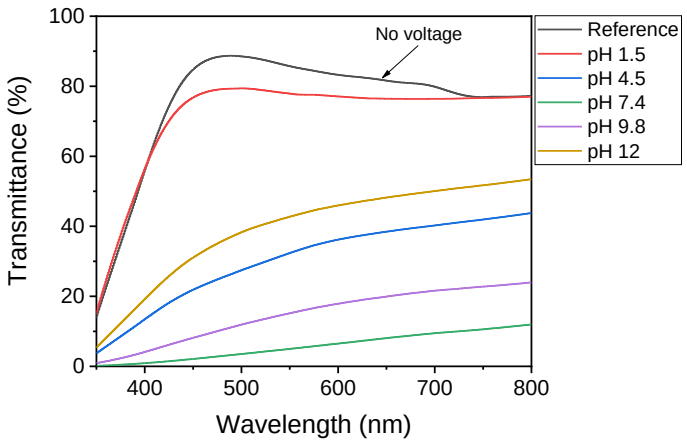


Figure 6.1. Transmittance spectra (350–800 nm) of five DA + PBS displays (without antioxidant) prepared with five different pH values, adjusted using NaOH or HCl, after applying 1.5 V for 600 s. The reference corresponds to the pH 7.4 display measured before the voltage application.

2.6.1 Study of the optimal concentration of DA for *i*-ECDs. Eight *i*-ECDs were prepared using growing concentrations of DA (0, 1, 5, 10, 25, 50, 75, 100 g/L in PBS pH 7.4). Through the use of a solid-state sample holder the *i*-ECDs containing different amounts of DA were placed into the spectrophotometer and connected to a potentiostat. Each sample was then subjected to 1.5 V for 600 seconds. T@600 nm was registered during the entire experiment. A picture of each *i*-ECDs was acquired at the end of the process.

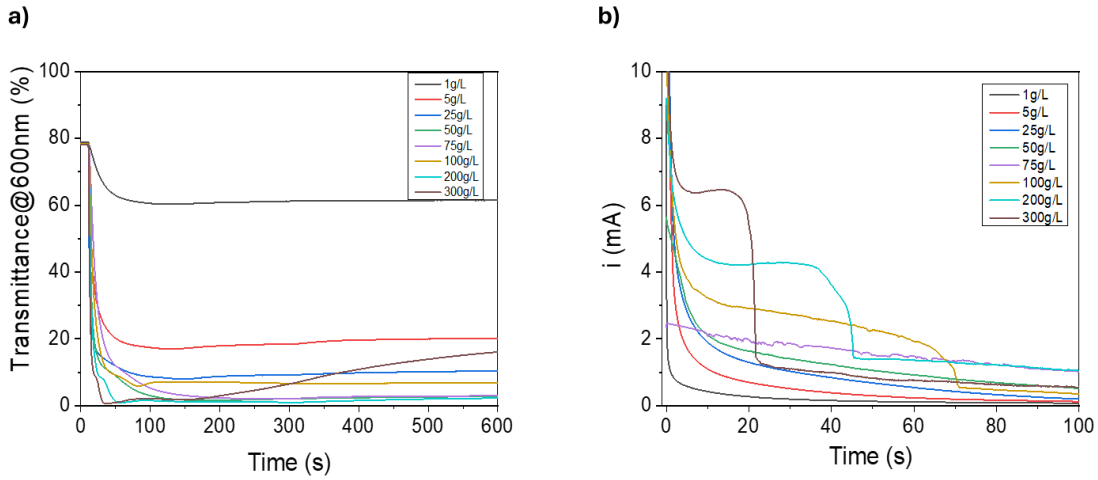


Figure 6.2. a) Transmittance at 600 nm as a function of time for eight displays in PBS (pH 7.4) containing increasing concentrations of DA (0–300 g/L), each activated for 600 s under an applied voltage of 1.5 V. b) Current recorded as a function of time during the activation of each display.

2.6.2 Determination the activation threshold voltage of the *i*-ECDs. Eleven DA based *i*-ECDs were settled on a solid-state sample holder subsequently inserted inside a spectrophotometer. After connected to a potentiostat they were subjected to a voltage ramp for 600 seconds (start: 0.50 V - end: 3.00 V, step: 0.25 V) registering T@600 nm for the entire

time. A picture of each *i*-ECDs was acquired at the end of the process. The same test was carried out for NO_2DA, ClDA, OMeDA and catechol to make comparison.

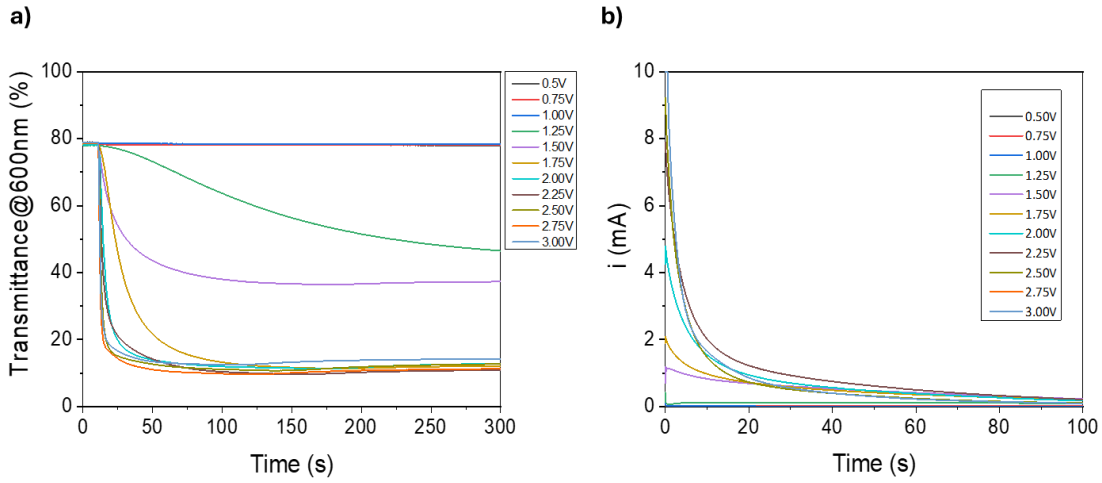


Figure 6.3. a) Transmittance at 600 nm as a function of time for eleven DA in PBS (pH 7.4) displays, each activated for 600 s under an applied voltage ramp ranging from 0.5 V to 3.0 V, with one distinct voltage assigned to each display. b) Current recorded as a function of time during the activation of each display at its respective applied voltage.

2.6.2 *i*-ECDs speed test. Two DA+AntiOX *i*-ECDs were prepared, connected to a potentiostat, placed inside a spectrophotometer, employing a solid-state sample holder, and subjected respectively to 1.5 V and 3.0 V for 180 seconds. A video during the activation process was recorded with a camera placed perpendicular to the *i*-ECDs. Thirteen frames were extracted from the recording at 0, 1, 3, 5, 10, 15, 20, 30, 45, 60, 90, 120 and 180 seconds to evaluate and compare the speed of colour change over time . The same analysis was carried out on the *i*-ECDs prepared with ClDA+AntiOX, OMeDA+AntiOX and catechol.

2.6.3 The importance of DA for the *i*-ECDs. Ten *i*-ECDs were prepared, five containing the DA+AntiOX, five employing only PBS at pH 7.4 (without dopamine). Each *i*-ECDs in each group was connected to a potentiostat, placed inside a spectrophotometer, employing a solid-state sample holder, and subjected to a voltage of 1.0 V, 2.0 V, 3.0 V, 4.0 V and 5.0 V for 600 seconds. The T@600 nm was recorded for each sample.

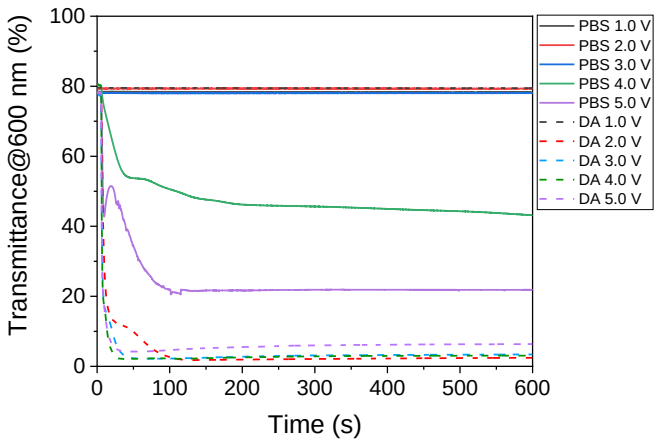


Figure 6.4. Transmittance at 600 nm as a function of time recorded during the activation of two sets of displays (five prepared in PBS pH 7.4 and five prepared with DA in PBS pH 7.4) under a 600-s voltage ramp ranging from 1.00 V to 5.00 V.

2.7 DA self-oxidation and i-ECDs stability. Two *i*-ECDs were prepared, one employing a DA+AntiOX solution and the other containing only DA. Both devices were stored without the application of any potential, and the transmittance at 600 nm (T@600 nm) was recorded every 24 hours for 28 days to monitor colour evolution due to DA self-oxidation. At the end of the test, a photograph of each *i*-ECD was taken. To further evaluate the impact of DA self-oxidation on device performance over time, a delayed-activation study was performed on eighteen *i*-ECDs, nine containing AntiOX and nine prepared without it. Each day for 10 consecutive days, one *i*-ECD from each group was connected to a potentiostat, placed inside a spectrophotometer using a solid-state sample holder, and subjected to 1.5 V for 600 seconds. During activation, the T@600 nm was continuously monitored and recorded. At the end of each activation, a photograph of the corresponding *i*-ECD was acquired.

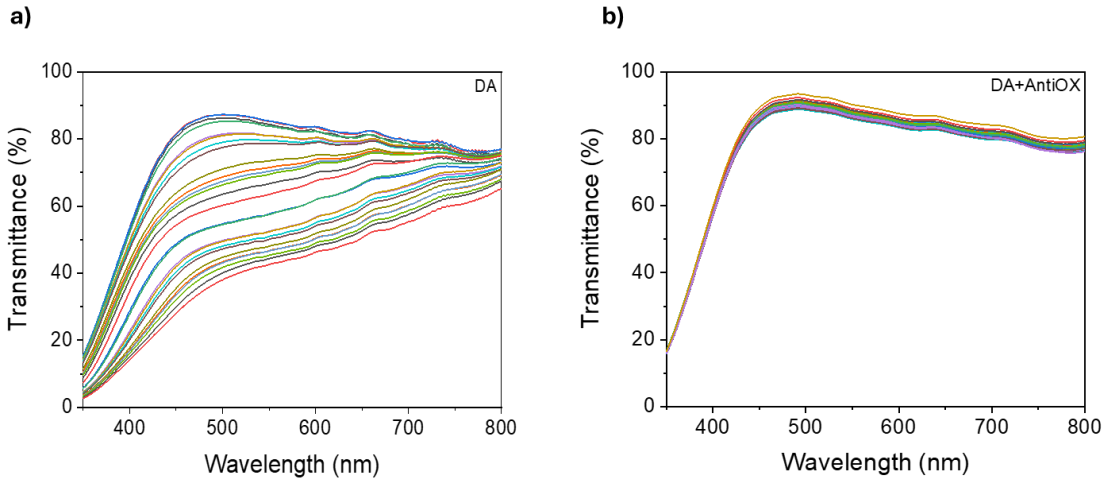


Figure 6.5. a) Transmittance spectra (350–800 nm) recorded daily over the course of one month for a display prepared with DA in PBS (pH 7.4). b) Transmittance spectra (350–800 nm) recorded daily over the course of one month for a display prepared with DA + AntiOX in PBS (pH 7.4).

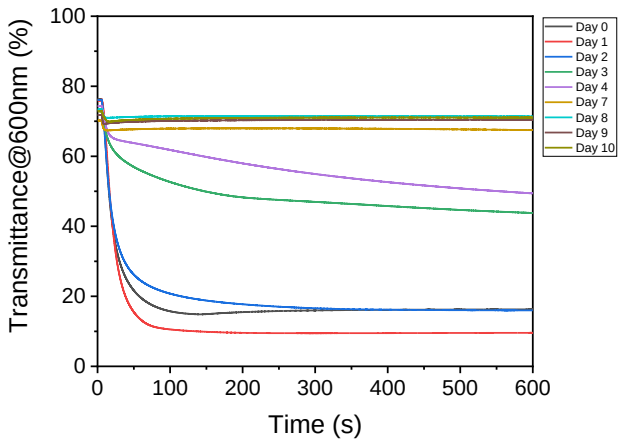


Figure 6.6. Transmittance at 600 nm as a function of time for ten DA+AntiOX displays, each activated for 600 s under an applied potential of 1.5 V, with one display activated per day over a period of ten consecutive days.

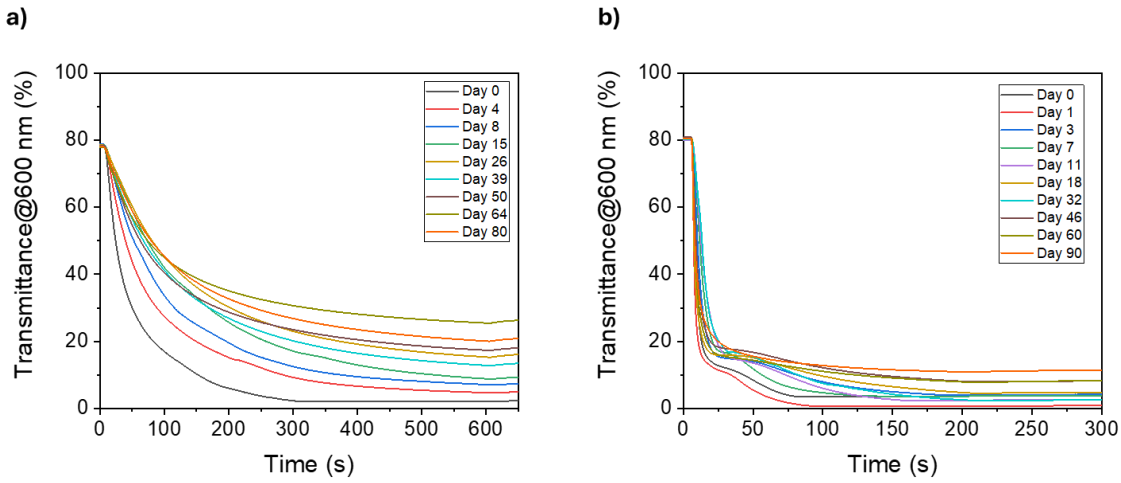


Figure 6.7. a) Transmittance at 600 nm as a function of time for ten DA+AntiOX displays, each activated for 600 s under an applied potential of 1.5 V, with one display activated approximately every 15 days over a study period of around three months. b) Transmittance at 600 nm as a function of time for ten DA+AntiOX displays, each activated for 600 s under an applied potential of 3.0 V, with one display activated approximately every 15 days over a study period of around three months.

2.9 Electrosynthesis in solution with salt-bridge. An electrochemical setup was designated by linking two containers via a salt bridge composed of Agar Agar and 3M KCl. Electrodes made of two layers of PET-ITO stripes were cut and connected to a potentiostat. One electrode, settled as W.E. was immersed in a solution of PBS pH 7.4 and DA 10 g/L in one container, while the CE was dipped in the other becker holding only the PBS pH 7.4. A potential of +1.5 V was applied to the electrochemical cell.

2.10 DA spectroelectrochemistry in solution. Spectroelectrochemistry in solution was performed using a three-electrode configuration. The W.E. consisted of a platinum grid, the

C.E. was a platinum wire, and the R.E. was an aqueous electrode of Ag/AgCl in KCl Sat. These electrodes were inserted into quartz cuvettes designed specifically for electrochemistry, with a narrowness of 1 mm, positioned at the point where absorbance was measured. Both a DA and DA+AntiOX solution in PBS pH 7.4 were introduced into the cuvette. A potential of +1.5 V was applied to the platinum grid to allow the oxidation of DA. The entire UV-Vis spectrum was monitored every minute to track the evolution of DA oxidation over time, both in the presence and absence of the antioxidant.

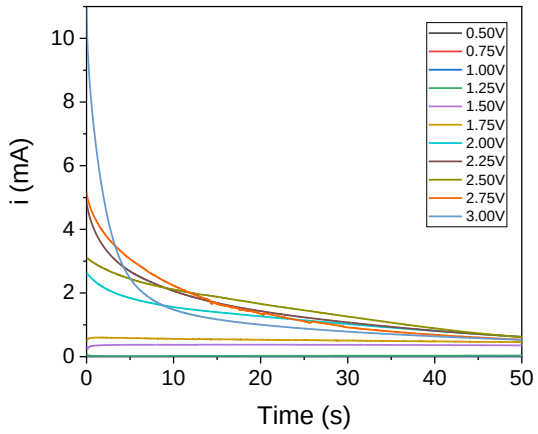


Figure 6.8. Current recorded as a function of time during the activation of each display prepared with catechol in PBS pH 7.4 at its respective applied voltage

2.11 DA cyclic voltammetry. CV was carried out employing a three-electrode system. The W.E. was a glassy carbon, the C.E. a Pt wire and the R.E. an aqueous Ag/AgCl electrode in KCl Sat. A solution containing DA in PBS at pH 7.4 was prepared. A potential ranging ±1.0 V was applied at a scan rate of 100 mV/s for 10 cycles.

2.12 *i*-ECD charge consumption and CE. Seven DA+AntiOX based *i*-ECDs were connected to a potentiostat, placed inside a spectrophotometer, employing a solid-state sample holder, and subjected to 1.5 V for 600 seconds. During the activation time, T@600 nm and current were recorded. The consumed charge was determined by integrating the current curve, followed by calculating the average value across the curves. The CE was calculated using the following equation:

$$CE = \frac{\mathrm{Log}\frac{T_{START}}{T_{END}}}{q} * A\ [cm^2/C]$$

Where T_{START} and T_{END} are the initial and final transmittance of the *i*-ECDs, q is the charge expressed in coulomb calculated thought the integration of the current registered during the *i*-

ECDs activation and A is the active *i*-ECDs area that is 1 cm^2. The value of the CE is expressed in cm^2/C.

2.13 Kinetic analysis. An *i*-ECD prepared with a DA+AntiOX solution in PBS at pH 7.4 was connected to a potentiostat, placed inside a spectrophotometer using a solid-state sample holder, and subjected to a potential of +1.5 V for 600 seconds. During the activation, the current response and the T@600 nm were recorded continuously and plotted as a function of time.

2.14 Proof of irreversibility. (1) An *i*-ECDs prepared with a DA+AntiOX solution in PBS pH 7.4 was connected to a potentiostat, placed inside a spectrophotometer, employing a solid-state sample holder, and subjected to +1.5 V for 5 seconds followed by -1.5 V for further 5 seconds. This process was repeated 30 times for a total of 150 seconds and immediately after also were applied +1.5 V for 60 seconds and -1.5 V for 60 seconds for 5 times for additional 300 seconds. T@600 nm was registered during the entire experiment. The process was carried out on a reversible ECD and data were compared. (2) The second experiment was carried out performing a CV between ±1.5 V for 10 cycles at 100 mV/s on a *i*-ECD prepared with DA+AntiOX in PBS pH 7.4. The same experiment was conducted on a reversible ECD and data were compared.

2.15 Role of the electrolyte. For the experiment, five *i*-ECDs were prepared by adding DA at a concentration of 10 g/L in PBS pH 7.4, along with four different 0.1 M electrolyte solutions: NaCl, Na_2HPO_4, KCl, and KH_2PO_4. Additionally, another set of five *i*-ECDs were prepared using PBS at pH 7.4 and the same electrolyte solutions but without the addition of DA. Each set of *i*-ECDs underwent linear sweep voltammetry, with the first series subjected to a voltage sweep from 0 to 3.0 V and the second series from 0 to 5.0 V with a scan rate of 100 mV/s.

2.16.1 *i*-ECDs Bendability study. The test was carried out by Etteplan (Finland). Four DA+AntiOX *i*-ECDs were subjected to 250, 500, 1000 and 4000 bends employing a self-built dynamic 3-point bending tester (bending radius 5 mm, frequency 1 Hz – 1 bend in 1 second). T@600 nm of each *i*-ECDs was recorded before and after the bending test. Afterwards, each *i*-ECDs was connected to a potentiostat and subjected to 1.5 V for 600 seconds. A picture of each *i*-ECDs was acquired at the end of the process.

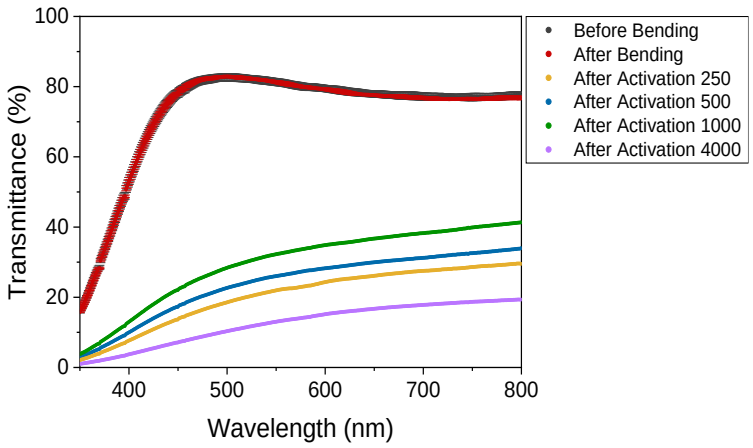


Figure 6.9. Transmittance spectra (350–800 nm) of the DA+AntiOX display, shown before bending, after 4000 bending cycles, and after activation under an applied voltage of 1.5 V for 600 s.

2.16.2 *i*-ECDs stability under storage at low temperature. The test was carried out by Etteplan (Finland). Fifteen DA+AntiOX *i*-ECDs were placed into an Espec Pr-1 humidity chamber, in which they were exposed to the environmental condition of 5 °C with relative humidity of 10% for 168 hours (7 days). T@600 nm was measured before and after the storage at 5°C. Afterwards, each *i*-ECDs was connected with a potentiostat and subjected to 1.5 V for 600 seconds. A picture of each *i*-ECDs was acquired at the end of the process.

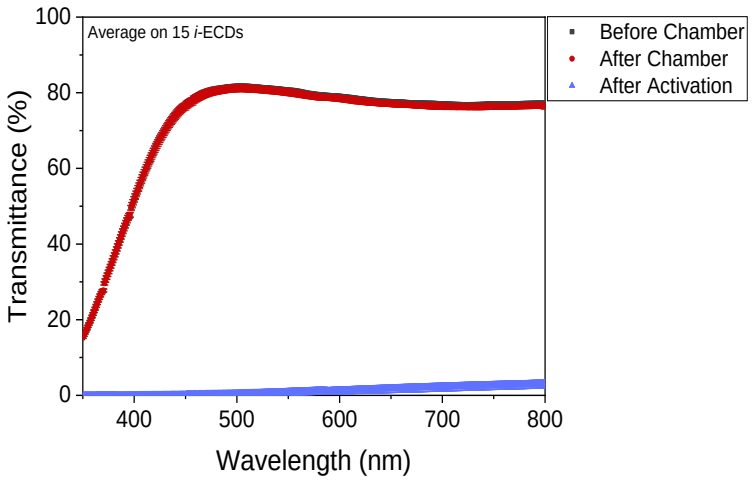


Figure 6.10. Transmittance spectra (350–800 nm) of the fifteen DA+AntiOX display, recorded before and after exposure at 5 °C and 10% RH for 168 h, and after activation at 1.5 V for 600 s.

2.16.3 *i*-ECDs activation - temperature tolerance. Twelve DA+AntiOX *i*-ECDs were prepared and placed inside a solid state sample holder in a temperature chamber equipped with two holes for the passage of an optical fiber suitable for recording T@600 nm. The *i*-ECDs were subjected to 1.5 V for 600 seconds while exposed to different temperature (-5 °C, 20 °C, 40 °C, 60 °C and 80 °C). A picture of each *i*-ECDs was acquired at the end of the process.

2.16.4 *i*-ECDs stability under solar light exposition. The analysis was carried out on five *i*-ECDs prepared with DA+AntiOX. T@600 nm was measured before and after exposure to the solar lamp simulator beam for 8 hours (equivalent to a real sun exposition), time selected based on a possible and/or accidental *i*-ECDs exposure to the sun. After irradiation, each *i*-ECDs was connected to a potentiostat, placed inside a spectrophotometer and subjected to 1.5 V for 600 seconds. T@600 nm was recorded once again after the applied voltage.

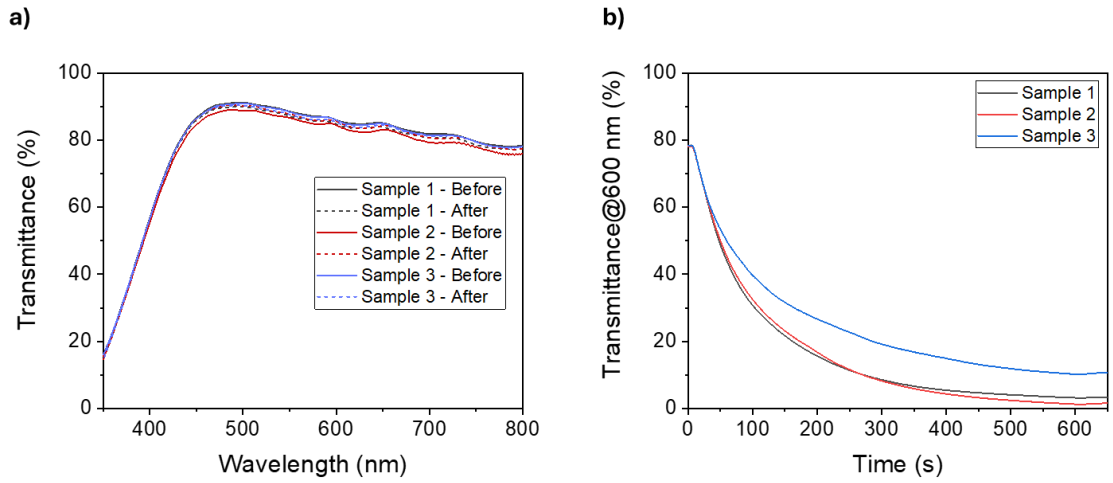


Figure 6.11. a) Transmittance spectra (350–800 nm) of three displays formulated with DA+AntiOX, recorded before and after 8 hours of exposure to sunlight (1000 W/m^2). b) Transmittance at 600 nm as a function of time for 3 DA + AntiOX displays activated with 1.5 V for 600 s.

2.17 DA functionalization. CV voltammogram of DA, ClDA, NO_2DA and OMeDA were recorded with solution of compound 10 g/L in PBS pH 7.4, except for NO_2DA where 1 g/L was employed. The system was a three-electrodes set-up (W.E. Glassy Carbon, C.E. Pt wire, R.E. Ag/AgCl KCl Sat.). The CV was carried within a voltage range of ±1.5 V for 10 cycles using a scan rate of 100 mV/s. The same equipment and procedure was employed for catechol.

2.17.1 Preparation methoxy-dopamine solution with sodium metabisulfite antioxidant (OMeDA+AntiOX). 10 mg of methoxy-dopamine, 5 mg of sodium metabisulfite and 1 mL of PBS (phosphate saline buffer) pH 7.4 were added to a glass vial and the obtained solution (10 mg/mL, with respect to the OMeDA) was sonicated for 1 minute at room temperature (150 W, 37 kHz) to favour complete dispersion.

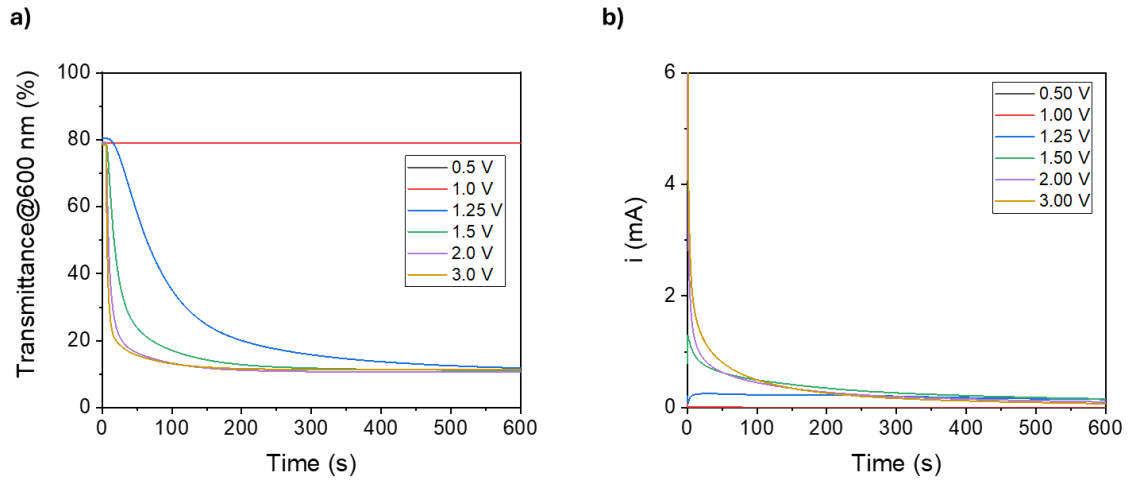


Figure 6.12. a) Transmittance at 600 nm as a function of time for six OMeDA in PBS pH 7.4 displays, each activated for 600 s under an applied voltage ramp ranging from 0.5 V to 3.0 V, with one distinct voltage assigned to each display. b) Current recorded as a function of time during the activation of each display at its respective applied voltage.

2.17.2 Preparation chloro-dopamine solution with sodium metabisulfite antioxidant (ClDA+AntiOX). 10 mg of chloro-dopamine, 5 mg of sodium metabisulfite and 1 mL of Phosphate buffer saline (PBS) pH 7.4 were added to a glass vial and the obtained solution (10 mg/mL, with respect to the ClDA) was sonicated for 1 minute at room temperature (150 W, 37 kHz) to favour complete dispersion.

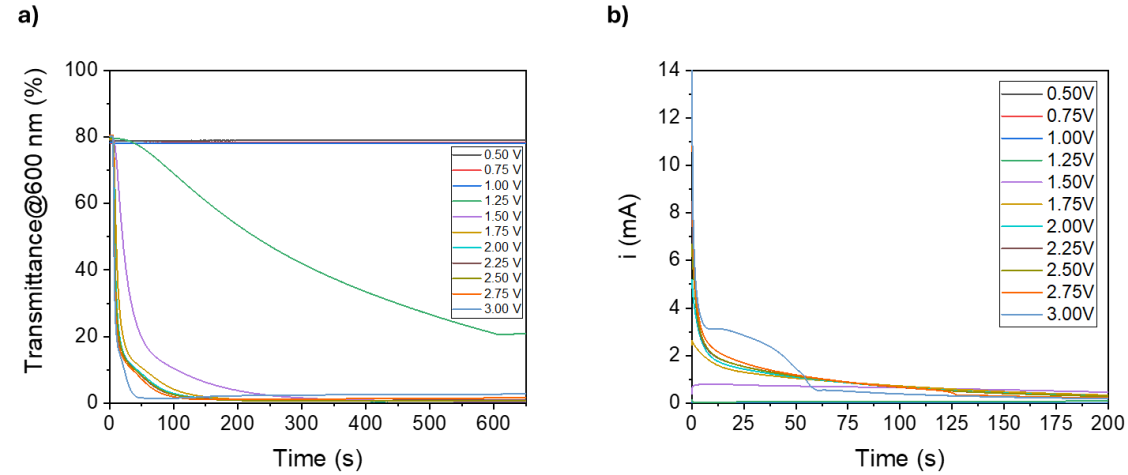


Figure 6.13. a) Transmittance at 600 nm as a function of time for eleven ClDA in PBS pH 7.4 displays, each activated for 600 s under an applied voltage ramp ranging from 0.5 V to 3.0 V, with one distinct voltage assigned to each display. b) Current recorded as a function of time during the activation of each display at its respective applied voltage.

2.17.3 Preparation of the nitro-dopamine solution (NO$_2$DA). 1 mg of nitro-dopamine and 1 mL of PBS (phosphate saline buffer) pH 7.4 were added to a glass vial and the obtained solution (1 mg/mL) was sonicated for 1 minute at room temperature (150 W, 37 kHz) to favour complete dispersion.

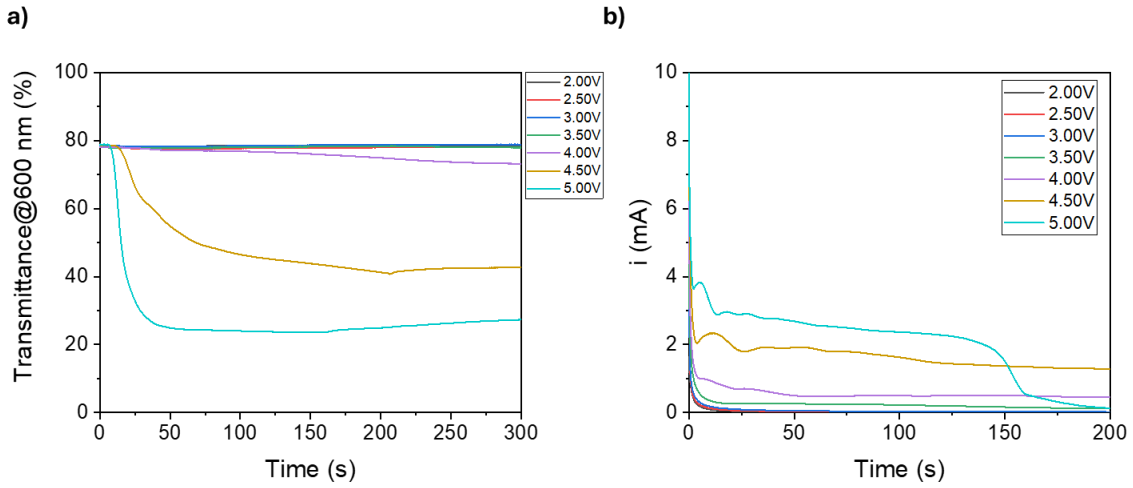


Figure 6.14. a) Transmittance at 600 nm as a function of time for eleven NO_2DA in PBS pH 7.4 displays, each activated for 600 s under an applied voltage ramp ranging from 2.0 V to 5.0 V, with one distinct voltage assigned to each display. b) Current recorded as a function of time during the activation of each display at its respective applied voltage.

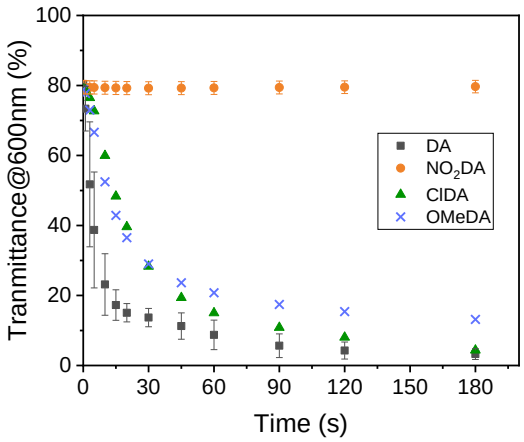


Figure 6.15. Average transmittance at 600 nm, recorded every 30 s, as a function of time for DA, NO_2DA, ClDA, and OMeDA displays during activation under an applied potential of 1.5 V.

2.19 Integration: CHARISMA smart label prototype for cold-chain applications. The prototype smart label was placed into an environmental chamber equipped with a thermometer able to precisely control the temperature (precision: 0.1 °C). Through the use of a heated resistance connected to a fan, the temperature inside the chamber was increased from 20 °C up to 30 °C. Once the threshold temperature, set to 26 °C, was reached, Arduino delivered as output to the *i*-ECDs the maximum value of voltage (4.35 V) for a pre-set period of 10 seconds.



Figure 6.16. Visualization of the bending analysis for the complete CHARISMA label after full assembly with all components.

2.20 Integration: SAL prototype for cold-chain . The cold-chain smart label prototype is manufactured in collaboration with Silicon Austria Labs (SAL). The device incorporates various printed electronic components, including an NFC antenna, a CPU, transistors, a temperature sensor, and convenient plug-and-play connectors designed for seamless integration with *i*-ECDs. The smart label is adaptable to temperature ranges easily customized using a smartphone app via NFC connectivity, essential to power the *i*-ECDs by enabling the flow of current.

2.20 Integration: Prelonic prototype for ticket events. The ticket events prototype is manufactured in collaboration with Prelonic. The device incorporates a printed NFC antenna with a diode and two conductive adhesive connectors for the *i*-ECD integration. The smart label works with an NFC reader able to provide enough voltage to activate the *i*-ECD.

Chapter 3

3.4.1 Preparation of Agar Agar formulation. 10 mg of Agar Agar was placed inside a vial and 1 mL of PBS pH 7.4 was poured inside. The suspension was stirred and heated to 90 °C for 5 minutes until complete dissolution of the compound. Afterwards, the solution was cooled down and at around 60 °C and DA+AntiOX was added. The formulation was employed for the doctor blade at 50 °C.

3.4.2 Preparation of porcine skin formulation. 25 mg of porcine skin was placed inside a vial and 1 mL of PBS pH 7.4 was poured inside. The suspension was stirred and heated to 90 °C for 5 minutes until complete dissolution of the compound. Afterwards, the solution was cooled down at room temperature and DA+AntiOX was added. The formulation was employed for the doctor blade at room temperature.

3.4.3 Preparation of corn Starch formulation. 15 mg of corn Starch was placed inside a vial and 1 mL of PBS pH 7.4 was poured inside. The suspension was stirred and heated to 90 °C for 5 minutes until complete dissolution of the compound. Afterwards, the solution was cooled down and at room temperature and DA+AntiOX was added. The formulation was employed for the doctor blade at room temperature.

3.4.4 Preparation of PEG formulation. 200 mg of PEG 20000 was placed inside a vial and 1 mL of PBS pH 7.4 was poured inside. The vial was closed to avoid evaporation. The suspension was stirred and heated to 90 °C for 30 minutes until complete dissolution of the compound. Afterwards, the solution was cooled down and at room temperature and DA+AntiOX was added. The formulation was employed for the doctor blade at room temperature.

3.5.1 Preliminary assessment and viscosity optimization After preparing the formulations, their dynamic viscosities were measured using a rotational viscometer. The measurements were conducted promptly following formulation preparation at room temperature, except for the Agar Agar formulation, which underwent measurement at 50°C. Utilizing the LV-3 spindle, speeds ranging from 0.5 to 50 rpm were employed for the viscosity assessments.

3.5.2 Preparation and Deposition of the DA Ink. The adhesive spacer was attached to the PET-ITO substrate by removing one of its plastic layer protection. The second protection was not removed but left on the surface as protection. The substrate was then placed and fixed on the casting machine to prevent unwanted movements. The formulation was poured near the adhesive spacers and the blade was activated at speed of 10 mm/s. Once the adhesive frames where filled, the formulation excess was removed, the second protective layer removed from the spacer and the *i*-ECDs closed placing another PET-ITO layer on top of it.

3.5.3 Testing of the formulation in *i*-ECDs: casting, activation and charge consumption. Twenty DA+AntiOX based *i*-ECDs, five for each formulation, were prepared using fixed concentrations of binders in PBS pH 7.4: Agar Agar (10 g/L), Starch (15 g/L), PEG (200 g/L)

and Porcine skin (25 g/L). Using a solid-state sample holder, the *i*-ECDs were placed into the spectrophotometer and connected to a potentiostat. Each series of five *i*-ECDs was subjected to a single voltage ramp condition of 600 seconds at one of the following potentials: 1.0, 1.5, 2.0, 2.5 or 3.0 V. The T@600 nm was recorded continuously throughout the entire experiment. A picture of each *i*-ECD was acquired at the end of the activation.

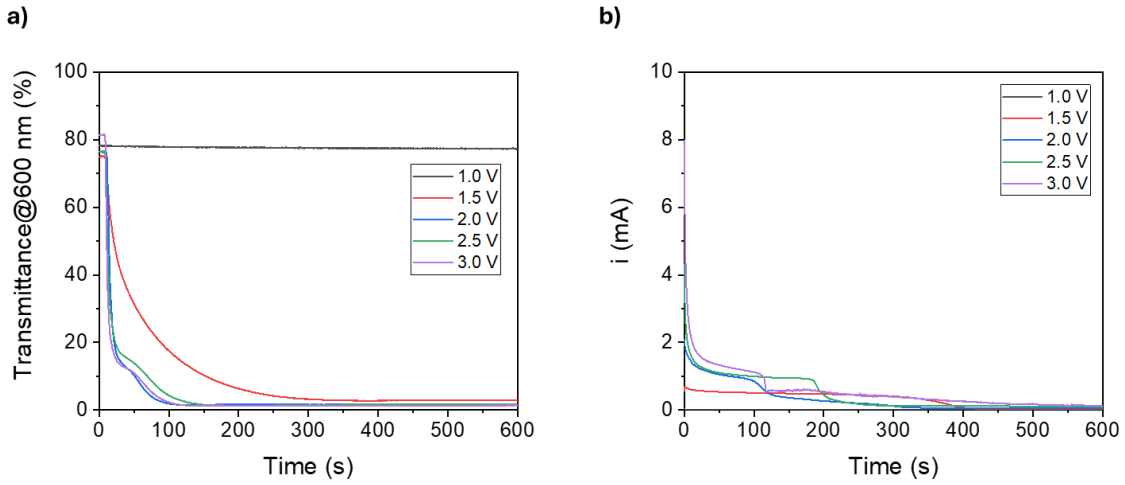


Figure 6.17. a) Transmittance at 600 nm as a function of time of five DA+AntiOX displays prepared with Agar Agar 10 g/L in PBS pH 7.4, each activated for 600 s under an applied voltage ramp ranging from 1.0 V to 3.0 V, with one distinct voltage assigned to each display. b) Current recorded as a function of time during the activation of each display at its respective applied voltage.

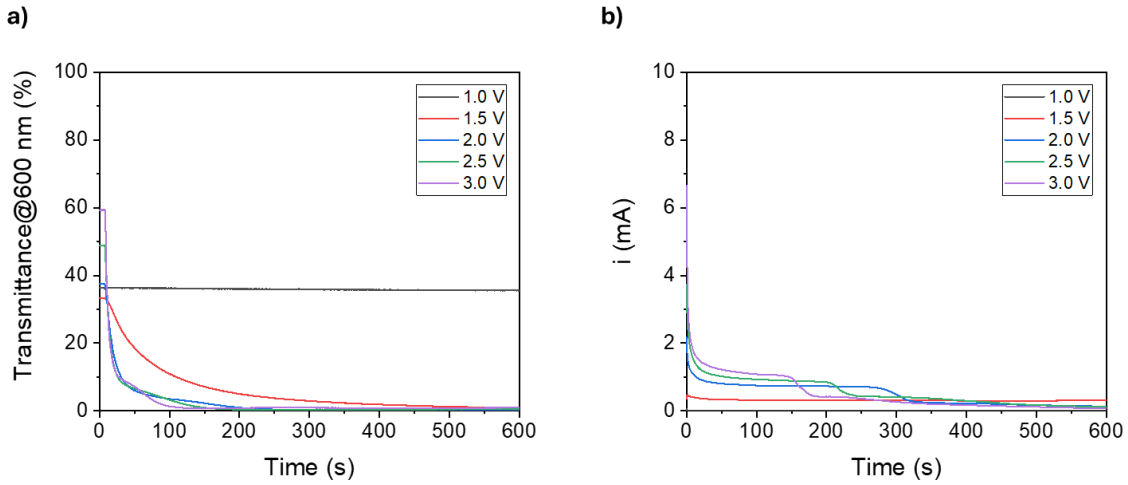


Figure 6.18. a) Transmittance at 600 nm as a function of time of five DA+AntiOX displays prepared with Starch 15 g/L in PBS pH 7.4, each activated for 600 s under an applied voltage ramp ranging from 1.0 V to 3.0 V, with one distinct voltage assigned to each display. b) Current recorded as a function of time during the activation of each display at its respective applied voltage.

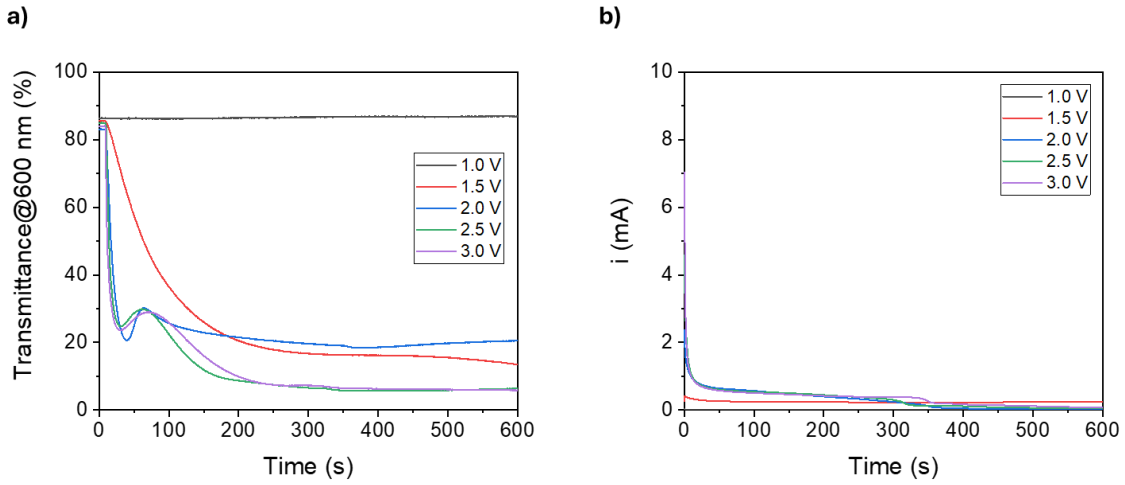


Figure 6.19. a) Transmittance at 600 nm as a function of time of five DA+AntiOX displays prepared with PEG 20000 200 g/L in PBS pH 7.4, each activated for 600 s under an applied voltage ramp ranging from 1.0 V to 3.0 V, with one distinct voltage assigned to each display. b) Current recorded as a function of time during the activation of each display at its respective applied voltage.

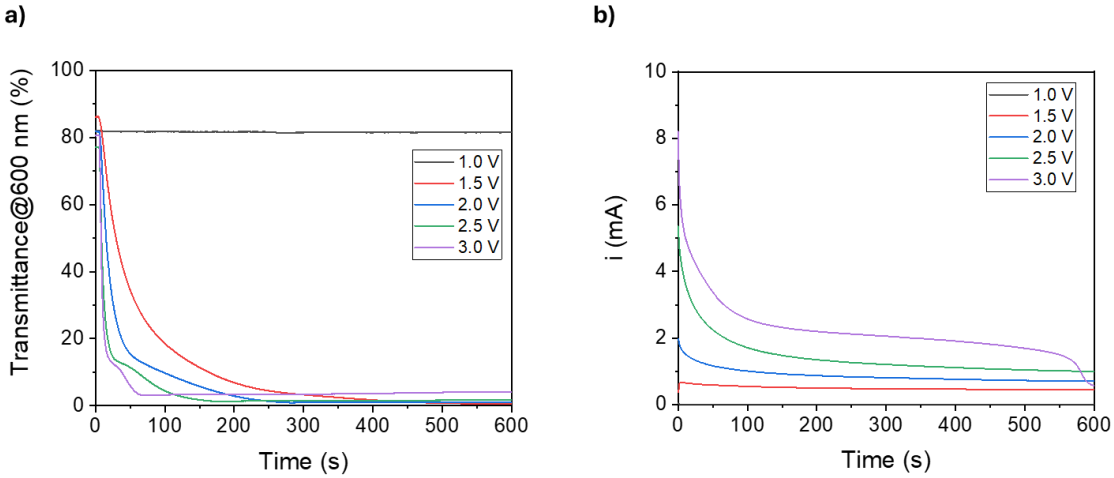


Figure 6.20. a) Transmittance at 600 nm as a function of time of five DA+AntiOX displays prepared with Porcine 25 g/L in PBS pH 7.4, each activated for 600 s under an applied voltage ramp ranging from 1.0 V to 3.0 V, with one distinct voltage assigned to each display. b) Current recorded as a function of time during the activation of each display at its respective applied voltage.

3.5.3 Testing of the formulation in *i*-ECDs: casting, activation and charge consumption.

Twenty DA+AntiOX based *i*-ECDs, five for each formulation, were prepared using growing concentrations of binders in PBS pH 7.4: Agar Agar (10, 20, 30, 40 and 50 g/L), Starch (50, 75, 100, 125, 150 g/L), PEG (100, 150, 200, 500, 1000 g/L) and Porcine skin (25, 35, 45, 55, 65 g/L). Through the use of a solid-state sample holder the *i*-ECDs were placed into the spectrophotometer and connected to a potentiostat. Each sample was then subjected to 1.5 V for 600 seconds. T@600 nm was registered during the entire experiment. A picture of each *i*-ECDs was acquired at the end of the process.

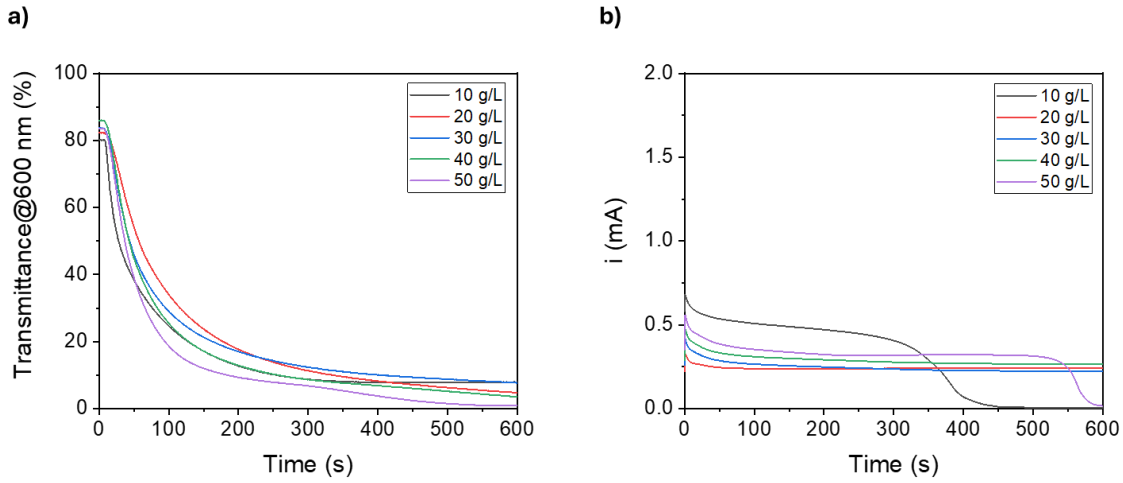


Figure 6.21. a) Transmittance at 600 nm as a function of time for five DA+AntiOX displays in PBS (pH 7.4) containing increasing concentrations of Agar Agar (10–50 g/L), each activated for 600 s under an applied voltage of 1.5 V. b) Current recorded as a function of time during the activation of each display.

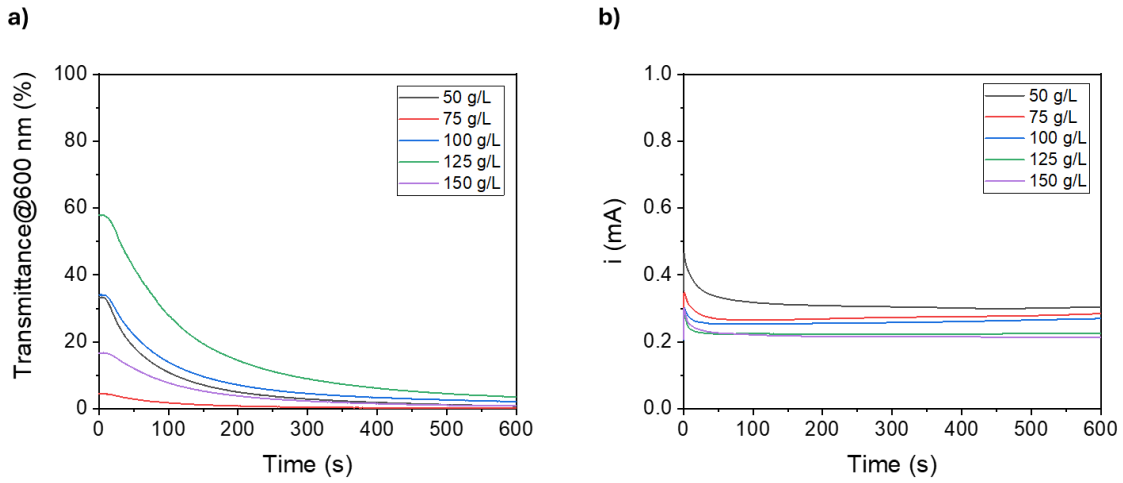


Figure 6.22. a) Transmittance at 600 nm as a function of time for five DA+AntiOX displays in PBS (pH 7.4) containing increasing concentrations of Starch (50–150 g/L), each activated for 600 s under an applied voltage of 1.5 V. b) Current recorded as a function of time during the activation of each display.

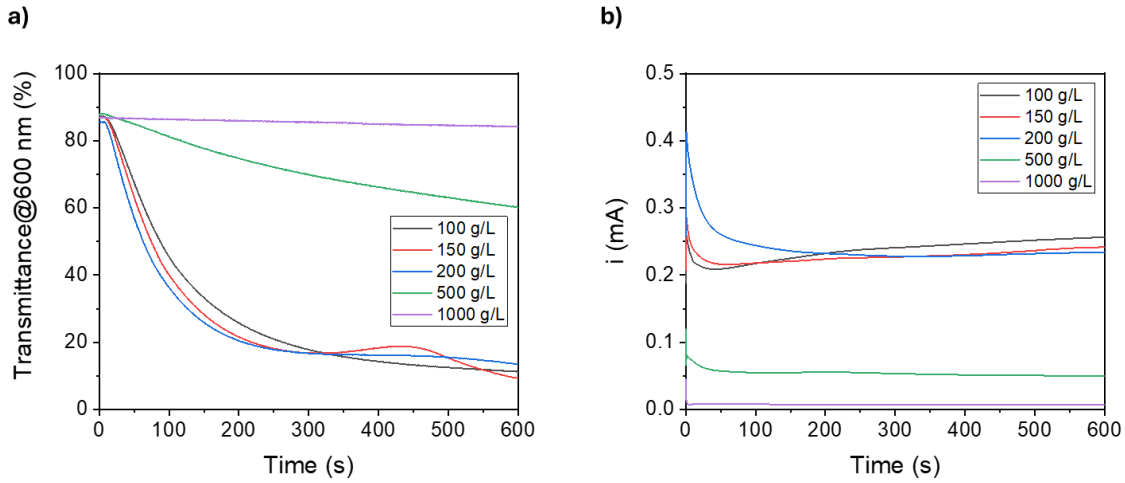


Figure 6.23. a) Transmittance at 600 nm as a function of time for five DA+AntiOX displays in PBS (pH 7.4) containing increasing concentrations of PEG (100–1000 g/L), each activated for 600 s under an applied voltage of 1.5 V. b) Current recorded as a function of time during the activation of each display.

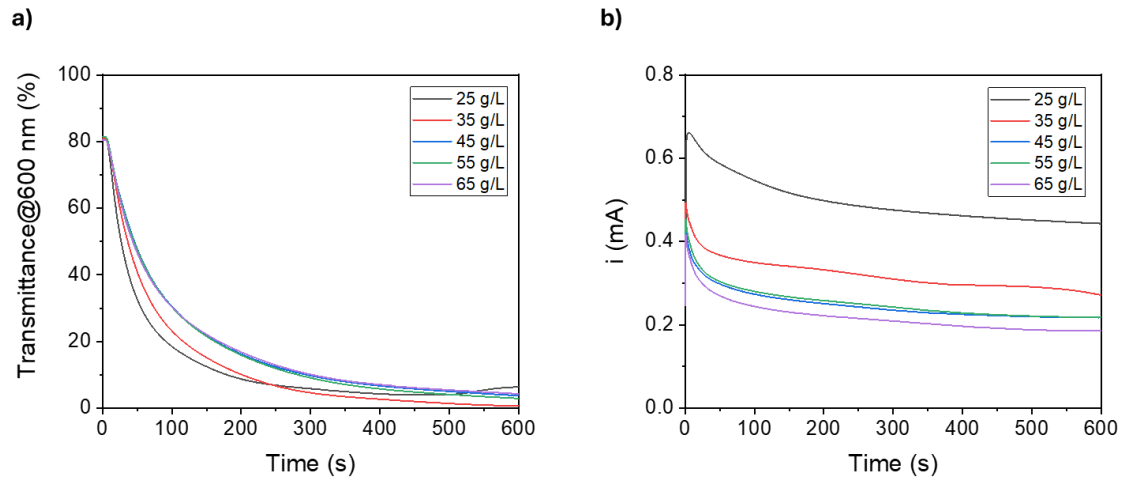


Figure 6.24. a) Transmittance at 600 nm as a function of time for five DA+AntiOX displays in PBS (pH 7.4) containing increasing concentrations of Porcine (25–65 g/L), each activated for 600 s under an applied voltage of 1.5 V. b) Current recorded as a function of time during the activation of each display.

3.5.3 Testing of the formulation in *i*-ECDs: casting, activation and charge consumption.

Ten DA+AntiOX based *i*-ECDs for each formulation were connected to a potentiostat, placed inside a spectrophotometer, employing a solid-state sample holder, and subjected to 1.5 V for 600 seconds. During the activation time, T@600 nm and current were recorded. The consumed charge was determined by integrating the current curve, followed by calculating the average value across the curves. The CE was calculated using the same described above in 2.12.

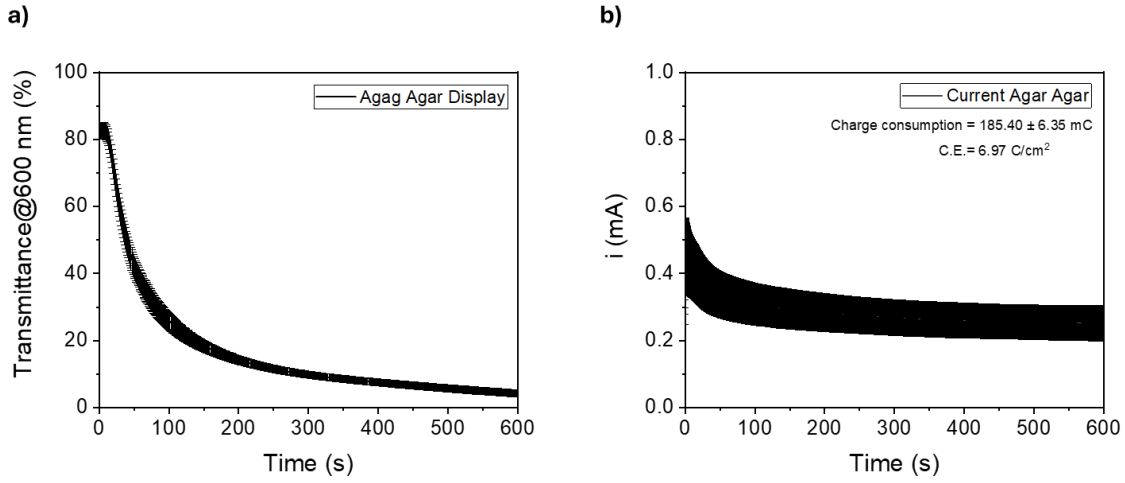


Figure 6.25. a) Average transmittance at 600 nm as a function of time for Agar Agar in PBS (pH 7.4) with DA+AntiOX, recorded during activation under an applied potential of 1.5 V. b) Average current as a function of time recorded during display activation, from which charge consumption and C.E. were calculated.

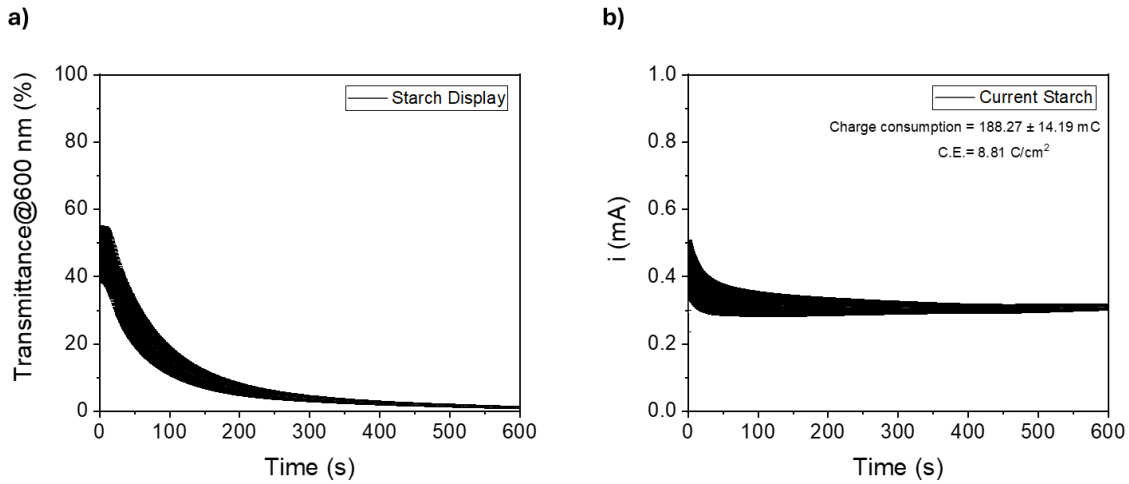


Figure 6.26. a) Average transmittance at 600 nm as a function of time for Starch in PBS (pH 7.4) with DA+AntiOX, recorded during activation under an applied potential of 1.5 V. b) Average current as a function of time recorded during display activation, from which charge consumption and C.E. were calculated.

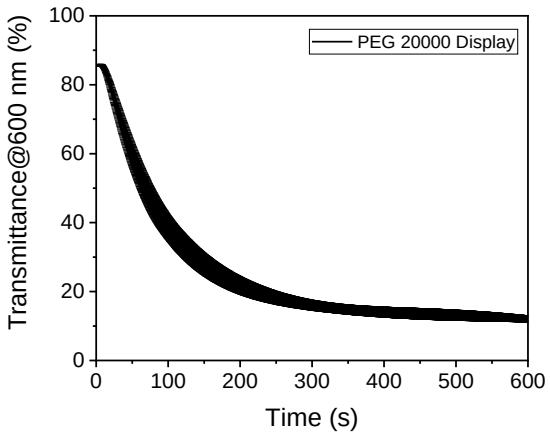


Figure 6.27. a) Average transmittance at 600 nm as a function of time for PEG 20000 in PBS (pH 7.4) with DA+AntiOX, recorded during activation under an applied potential of 1.5 V.

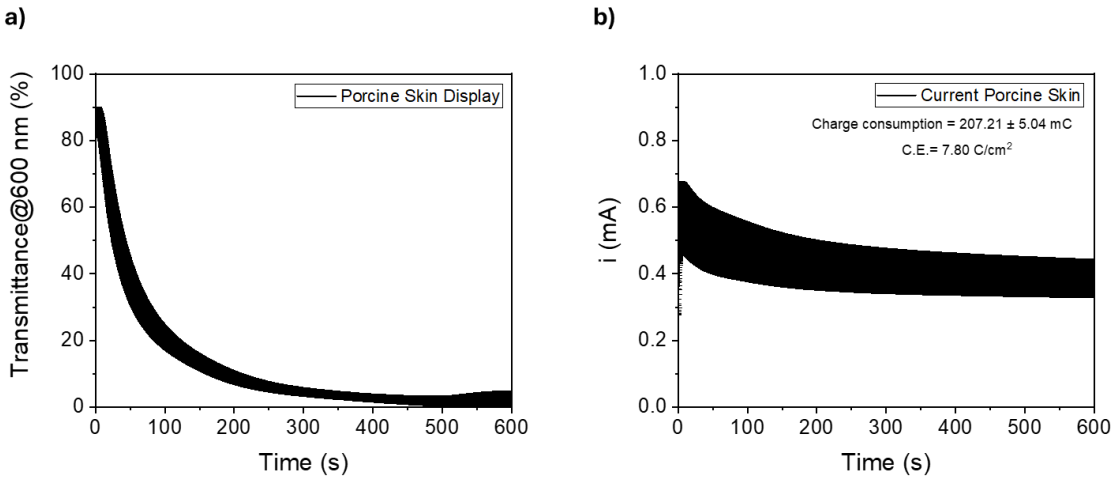


Figure 6.28. a) Average transmittance at 600 nm as a function of time for Porcine in PBS (pH 7.4) with DA+AntiOX, recorded during activation under an applied potential of 1.5 V. b) Average current as a function of time recor2ded during display activation, from which charge consumption and C.E. were calculated.

3.5.4 *i*-ECDs stability. Twenty DA+AntiOX based *i*-ECDs, five for each formulation, were manufactured and stored under atmospheric conditions. One *i*-ECD for each series was activated thought 1.5 V for 600 seconds at day 0, 7, 28, 45 and 70 after their preparation and T@600 nm was recorded at the end of the activation. One picture for each *i*-ECDs was acquired at the end of the measurement.

3.5.4 *i*-ECDs stability. Four series of five DA+AntiOX based *i*-ECDs were prepared of which two series employing Agar Agar and two series using porcine skin. Of those, one series prepared with Agar Agar and one prepared with Porcine Skin were stored under 99% H. while the other two series were stored in dry conditions. The *i*-ECDs were activated following a schedule starting from day 0, ending with day 70. During each activation, the *i*-ECDs were connected to a potentiostat, placed inside a spectrophotometer, employing a solid-state sample holder, and subjected to 1.5 V for 600 seconds. T@600 nm and a picture of each *i*-ECD was recorded.

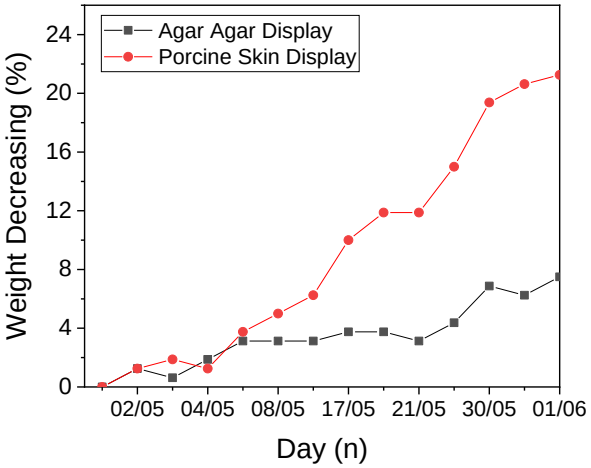


Figure 6.29. Weight decrease over time for two DA+AntiOX displays prepared with Agar Agar (10 g/L) and Porcine Skin (25 g/L) in PBS pH 7.4.

3.6 Screen printing ink formulations and ECD production. The trial was carried out by employing a formulation based on DA+AntiOX and Agar Agar 20 g/L in PBS pH 7.4. The formulation, once prepared and cooled to 50 °C was poured onto the screen and immediately printed over the PET-ITO making pressure with the squeegee. After printing, the ITO substrate was closed quickly by placing another ITO piece on top and sealing it using standard tape to make a prototype of *i*-ECD that was activated by applying 1.5 V for 600 seconds.

Chapter 4

4.4.1 Irreversibility test - polythiophenes decolouration in solution. CV was performed in PEC/$LiClO_4$ using a three-electrode configuration with PET–ITO as W.E. (1 cm^2), Pt wire as C.E. and Ag/AgCl as R.E. The polymer film was deposited only on the W.E. to avoid full ECD fabrication, and sacrificial agents, when tested, were directly introduced into the electrolyte. The potential was scanned between 0 and +1.5 V for 10 cycles at 100 mV/s. After the initial 10 cycles, a constant oxidative potential of +1.5 V was applied for 600 s to fully oxidize the film, followed by an additional set of 10 CV cycles under the same scan conditions. Current–potential profiles were recorded throughout the experiment.

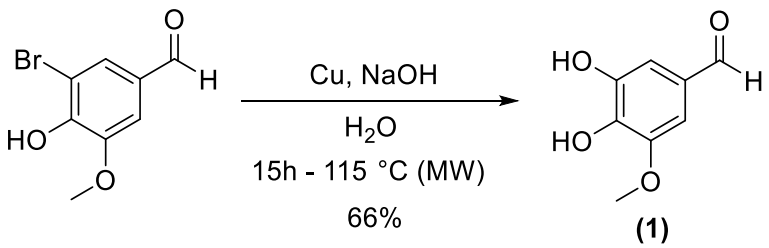
4.4.1 Irreversibility test - polythiophenes decolouration in solution. UV–Vis spectra of the polymer film on PET–ITO were recorded in three conditions: (i) pristine as-deposited state, (ii) after 10 CV cycles followed by oxidation at +1.5 V for 600 s, and (iii) after a subsequent reduction at -1.5 V for 600 s. The same optical setup and electrolyte used for CV were employed. The spectra acquired after oxidation and reduction were compared to the pristine

trace to assess the recovery of the absorption features. Photographic documentation of the electrode surface was also collected at each stage.

4.4.2 Irreversibility test - polythiophenes decolouration in *i*-ECDs. The experiment was conducted in PEC/$LiClO_4$ using ITO as both W.E. and C.E. and Ag/AgCl as R.E. The polymer-coated W.E. (1 cm^2) was immersed in the electrolyte, and five consecutive electrochemical cycles were applied by holding the potential at +1.5 V for 600 s followed by -1.5 V for 600 s. After each cycle, the UV–Vis absorbance spectrum of the polymer film was acquired without removing the electrodes from the cell. Simultaneously, the current profiles were recorded and the consumed charge was determined by integration.

4.4.3 Use of sacrificial agents - study in solution. The effect of sacrificial agents on the redox reversibility of the polymer was evaluated by CV in PEC:$LiClO_4$ (0.1 M) using a three-electrode configuration with polymer-coated PET–ITO (1 cm^2) as W.E., Pt wire as C.E. and Ag/AgCl as R.E. Three initial voltammetric cycles were recorded between 0 and +1.5 V at 100 mV/s to establish the baseline response. The sacrificial agent (EtOH, 2-propanol, phenol, 2-naphthol, 3-ethylamine, tyrosine, NaOH or aqueous NH_3) was then introduced into the electrolyte and the solution stirred for 1 minute at 400 rpm to ensure homogeneity. Seven additional CV cycles were subsequently recorded under the same potential window and scan rate. Photographs of the polymer film on the electrode were acquired before and after cycling for each tested compound.

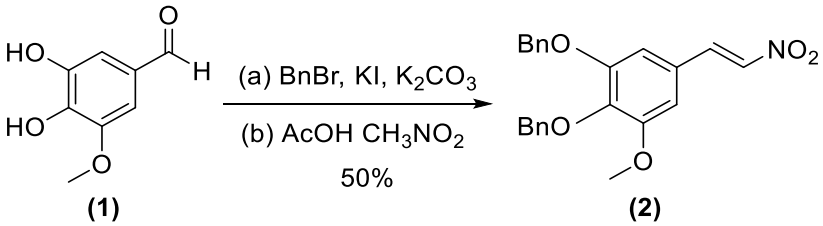
6.4 Synthetic procedures



Scheme S1: Synthetic scheme for the preparation of intermediate **(1)**

Synthesis of 3,4-dihydroxy-5-methoxybenzaldehyde (1). 5-Bromovanillin (0.445 g, 1.93 mmol) and NaOH (0.772 g, 19.20 mmol) were added to a microwave vial (10 mL – 20 mL size) with 15 mL of distilled H_2O. Subsequently, metallic Cu powder (0.0123 g, 0.19 mmol) was added, and the vial was sealed, sonicated for 2 minutes (rt, 150 W, 37 kHz) and stirred for 5 minutes

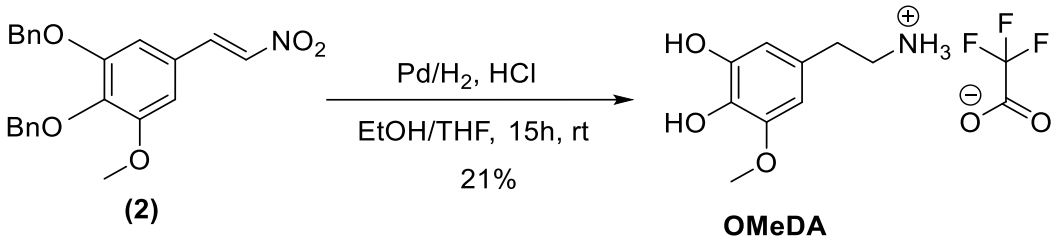
on a heating plate to help solubilize the NaOH pellets before starting the reaction. The reaction was introduced in a microwave reactor (Biotage® Initiator+) and heated for 15 hours at 115 °C. After this time, the vial was opened and Na_2HPO_4 (0.0275 g, 0.19 mmol) was added in a stoichiometric amount in respect to the Cu powder. Afterwards, the vial was again sealed, introduced in the microwave and heated at 115 °C for another hour. The obtained suspension was hence filtered with paper filter to remove the metallic copper. The microwave vial was then rinsed 3 times with distilled H_2O (150 mL) and the recovered solution was acidified with HCl until pH ≈ 3 to protonate hydroxy groups. The H_2O was then evaporated under reduced pressure (60 °C, 40 mBar). The resulting grey powder was then dissolved in ethyl acetate (250 mL) and sonicated for 5 minutes (rt, 150 W, 37 kHz). Then, the solution was dried over $MgSO_4$ and filtered. The solvent was again evaporated under reduced pressure (40 °C, 100 mbar), and the resulting crude purified with the "Biotage® Isolera™ Systems" using as eluent DCM/MeOH 95 : 5 (v/v) in "Biotage® Sfär Silica 60 µm 25 g" cartridge in order to give an off-white powder (0.214 g, 1.27 mmol, 66%). **Mp** 120 - 122 °C. **^{1}H NMR** (600 MHz, $CDCl_3$, δ): 9.79 (*s*, 1H), 7.14 (*d*, *J* = 1.7 Hz, 1H), 7.08 (*d*, *J* = 1.7 Hz, 1H), 5.99 (*s*, 1H), 5.49 (*s*, 1H), 3.96 (*s*, 3H). **^{13}C NMR** (150 MHz, $CDCl_3$, δ): 190.9, 147.2, 143.9, 138.3, 129.0, 113.0, 102.8, 56.4. **HRMS** m/z 191.0308 for $C_8H_8O_4$ ([M + Na], calculated m/z 191.0315). **IR** (cm^{-1}): 3490, 3092, 2922, 2850, 1657, 1593, 1511, 1468, 1344, 1295, 1193, 1137, 1086, 1004, 856, 714, 636.



Scheme S2: Synthetic scheme for the preparation of intermediate **(2)**

Synthesis of (E)-(((3-methoxy-5-(2-nitrovinyl)-1,2-phenylene)bis(oxy))bis(methylene))dibenzene (2). (a) A suspension of **1** (0.121 g, 0.720 mmol) and K_2CO_3 (0.498 g, 3.60 mmol) was placed into a round-bottom flask with 15 mL of DMF. The suspension was sonicated (rt, 150 W, 37 kHz) and degassed with Argon for 10 minutes. Afterwards, benzyl bromide (0.214 mL, 1.80 mmol) and KI (0.0359 g, 0.216 mmol) were added to the suspension. The reaction mixture was then sonicated (rt, 150 W, 37 kHz) and degassed with Argon once again for 10 minutes before heating at 80 °C for 4 hours. After this time, the reaction mixture was cooled down to room temperature. K_2CO_3 was removed by filtration and the filtered solution extracted with EtOAc (200 mL), washed with 1 N HCl and

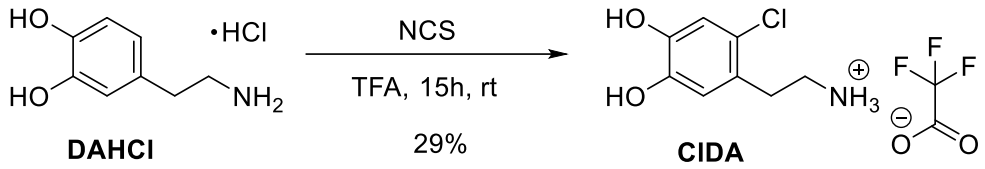
brine and finally dried over Na_2SO_4. (b) Filtration and solvent removal under reduced pressure afforded the benzylated intermediate (0.182 g), which was introduced without purification in a round-bottom flask with ammonium acetate (0.131 g, 1.70 mmol) and dissolved in 15 mL of acetic acid. Nitromethane (0.154 mL, 2.84 mmol) was then added to the reaction mixture, before refluxing at 140 °C for 5 hours under stirring. The reaction was then cooled down to room temperature and slowly added to 100 mL of distilled H_2O. The aqueous phase was extracted with ethyl acetate (3 x 100 mL). The combined organic phases were washed with brine and dried over Na_2SO_4. The solvent was then evaporated under reduced pressure and the crude product purified with the "Biotage® Isolera™ Systems" using as eluent 50/50 DCM/Heptane in "Biotage® Sfär Silica 60 µm 25 g" to give a yellow powder (0.101 g, 50%). **Mp** 124 - 126 °C. **^{1}H NMR** (600 MHz, $CDCl_3$, δ): 7.89 (*d*, *J* = 13.5 Hz, 1H), 7.47 (*d*, *J* = 13.5 Hz, 1H), 7.45- 7.27 (*m*, 10H), 6.79 (*d*, *J* = 1.9 Hz, 1H), 6.75 (*d*, *J* = 1.9 Hz, 1H), 5.12 (*s*, 4H), 3.88 (*s*, 3H). **^{13}C NMR** (150 MHz, $CDCl_3$, δ): 154.3, 153.1, 141.3, 139.3, 137.2, 136.3, 136.4, 128.7, 128.5, 128.3, 128.2, 128.1, 127.4, 125.3, 108.8, 106.6, 77.4, 77.2, 77.0, 76.7, 75,2, 71.4, 56.3. **HRMS** m/z 414.1304 for $C_{23}H_{21}O_5N$ ([M + Na], calculated m/z 414.1312). **IR** (cm^{-1}): 3108, 3028, 2936, 1630, 1581, 1498, 1423, 1310, 1246, 1125, 963, 819, 733, 694.



Scheme S3: Synthetic scheme for the preparation of **OMeDA**.

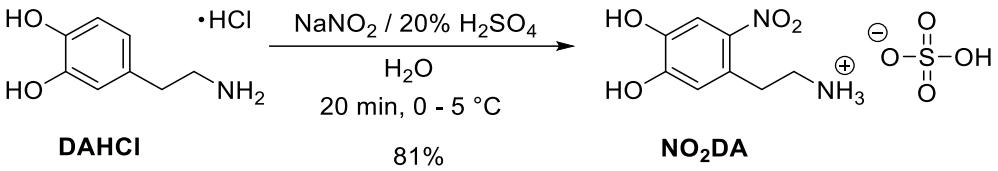
Synthesis of 5-(2-aminoethyl)-3-methoxybenzene-1,2-diol (OMeDA). 2 (0.235 g, 0.60 mmol) was added in a round-bottom flask to a 1 : 1 Ethanol/THF mixture (24 mL) and the solution degassed via a series of three freeze-pump-thaw cycles. Afterwards, HCl (0.223 mL, 6.42 mmol) and Pd/C 10% (0.234 g, 2.20 mmol) were added to the flask under Argon. The reaction mixture was once again degassed with three freeze-pump-thaw cycles and three vacuum/hydrogen cycles to establish a reducing atmosphere in the reaction flask. The reaction was stirred for 15 hours under hydrogen at room temperature with vigorous stirring. The mixture was then filtered over celite with ethanol (200 mL) to remove the Pd catalyst. Then, the solvent was removed under reduced pressure (40 °C, 50 mbar) to give a sticky brown crude. The purification was carried out with a preparative HPLC "Agilent 1260 Infinity liquid chromatograph system" employing a Varian Pursuit C18 column (5 µm, 250 X 21.2 mm) using H_2O and ACN as solvents and following this run protocol: 0 – 3' isocratic 100% H_2O - 0.1 %

TFA; 3' – 33' gradient from 100% H_2O to 100% ACN. In these conditions the product elutes at minute 8. The solvent was then removed by freeze drying to give **OMeDA** as a white powder (0.036 g, 0.01 mmol, 21%). **Mp** 176.3 °C – 177.8 °C. **^{1}H NMR** (600 MHz, D_2O, δ): 6.59 (*d*, *J* = 1.5 Hz, 1H), 6.52 (*d*, *J* = 1.5 Hz, 1H), 3.86 (*s*, 3H), 3.24 (*t*, 2H), 2.88 (*t*, 2H). **^{13}C NMR** (150 MHz, D_2O, δ): 148.7, 144.6, 132.0, 128.6, 109.7, 105.2, 56.2, 40.5, 32.4. **^{19}F NMR** (660 MHz, D_2O, δ): -75.6. **HRMS** m/z 184.0961 for $C_9H_{14}NO_3^+$ ([M + H]$^+$, calculated m/z 184.0968). **IR** (cm^{-1}): 3455, 3178, 1704, 1616, 1542, 1457, 1427, 1336, 1238, 1193, 1125, 1071, 839, 794, 722, 640.



Scheme S4: Synthetic scheme for the preparation of **ClDA**

Synthesis of 4-(2-aminoethyl)-5-chlorobenzene-1,2-diol (ClDA). In a round-bottom flask N-chlorosuccinamide (0.206 g, 1.54 mmol) was added to a stirred solution of DAHCl (0.271 g, 1.40 mmol) in 4 mL of TFA. The solution was stirred at room temperature for 15 hours during which its colour changes from transparent to orange during the first hour and to yellow by the end of the reaction time. Afterwards the solvent was removed by argon flushing to produce a pale-yellow oily crude, which was purified with a "Biotage® Isolera™ System" equipped with a "Biotage® Sfär Bio C18 Duo 300 Å 20 μm 12 g" cartridge, employing the solvent mixture H_2O/MeOH 99 : 1 (v/v) as eluent (flow 12 mL/min). The solvent was removed from the collected fractions via freeze-drying to give the product **ClDA** as a white powder (0.121 g, 0.40 mmol, 29%). **Mp** 146.9-148.9 °C. **^{1}H NMR** (600 MHz, D_2O, δ): 6.97 (1H, *s*), 6.84 (1H, *s*), 3.22 (2H, *t*, *J* = 7.34 Hz), 2.97 (2H, *t*, *J* = 7.34 Hz). **^{13}C NMR** (150 MHz, D_2O, δ): 144.1, 143.3, 125.8, 123.6, 117.9, 116.9, 39.2, 30.3. **HRMS**: m/z 188.0468 for $C_8H_{10}O_2NCl$ (M+nH, calculated m/z 188.0473). **IR** (cm^{-1}): 3255, 3058, 2947, 1660, 1618, 1595, 1542, 1509, 1433, 1351, 1283, 1133, 899, 837, 798, 722. **CHNX EA**: calc. for $C_8H_{10}O_2NCl$: C, 39.82; H, 3.68; Cl, 11.75; F, 18.89; N, 4.64; O, 21.22. Found: C, 39.13; H, 3.57; Cl, 11.33; F, 20.03; N, 4.48; O, 21.46.



Scheme S5: Synthetic scheme for the preparation of **NO_2DA**

Synthesis of 4-(2-aminoethyl)-5-nitrobenzene-1,2-diol (NO_2DA). In a round-bottom flask dopamine hydrochloride (DAHCl, 0.502 g, 2.65 mmol) and $NaNO_2$ (0.599 g, 8.68 mmol) were dissolved in 15 mL of distilled H_2O. The flask was placed into an ice bath, prepared with ice and H_2O, and H_2SO_4 (2.50 mL) was slowly added to the dopamine solution under vigorous stirring. After 15 minutes a yellow precipitate was formed on the bottom of the flask, which was then recovered via filtration onto paper and washed with cold distilled H_2O (50 mL) and MeOH (50 mL). The filtrate was dried under vacuum at 10 mBar for 1 hour to obtained **NO_2DA** as yellow powder (0.411 g, 2.07 mmol, 81%). **Mp** 190 °C dec. **^{1}H NMR** (600 MHz, D_2O, δ): 7.68 (1H, *s*), 6.89 (1H, *s*), 3.31 (2H, *t*, *J* = 7.45), 3.19 (2H, *t*, *J* = 7.45). **^{13}C NMR** (150 MHz, D_2O, δ): 150.7, 143.4, 140.3, 126.7, 118.6, 113.4, 39.7, 30.8. **HRMS**: m/z 199.0713 for $C_8H_{10}O_4N_2$ ($[M+H]^+$, calculated m/z 199.0713). **IR** (cm^{-1}): 3489, 3179, 3045, 2943, 1624, 1600, 1540, 1513, 1492, 1437, 1283, 1033, 622.

Appendix: ^{1}H, ^{13}C, AND HRMS SPECTRA

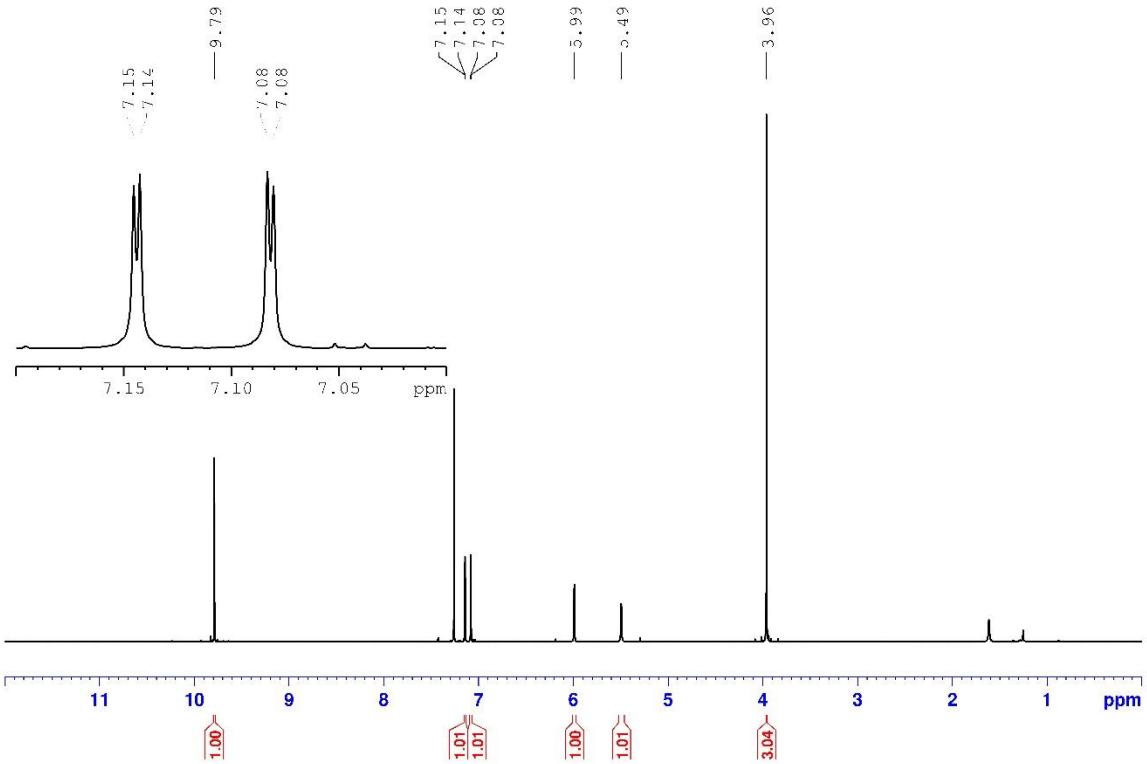


Figure A1: ^{1}H NMR spectrum of 1 in $CDCl_3$.

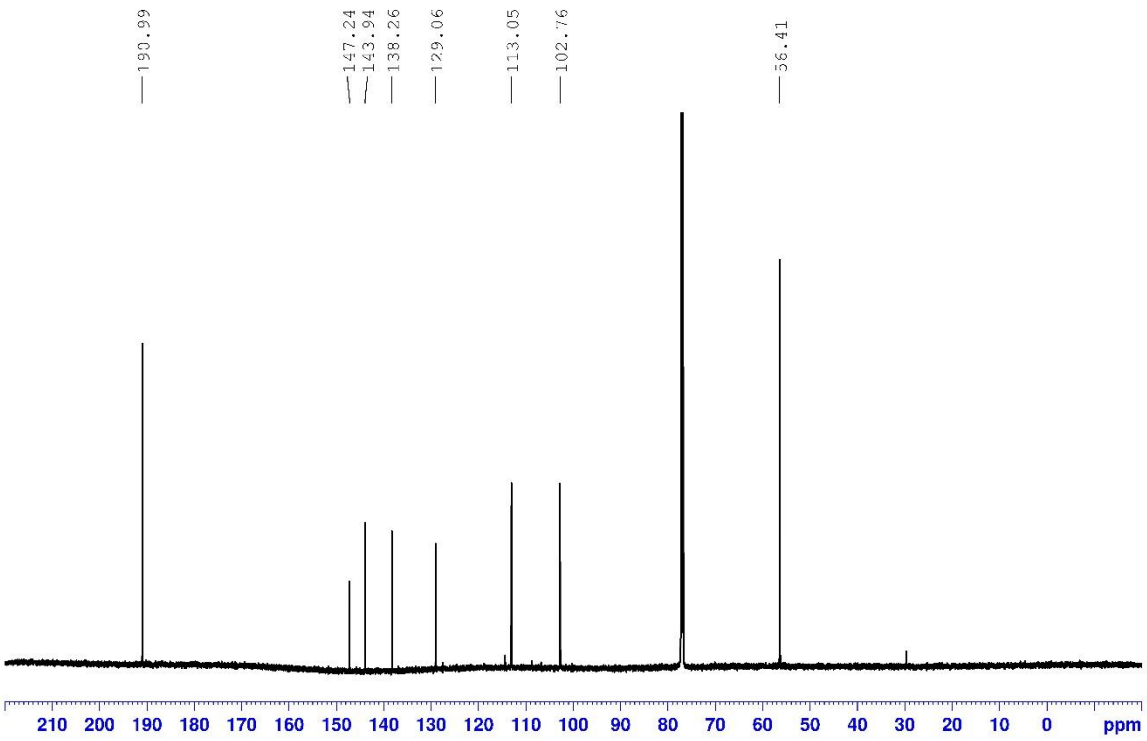


Figure A2: ^{13}C NMR spectrum of 1 in $CDCl_3$.

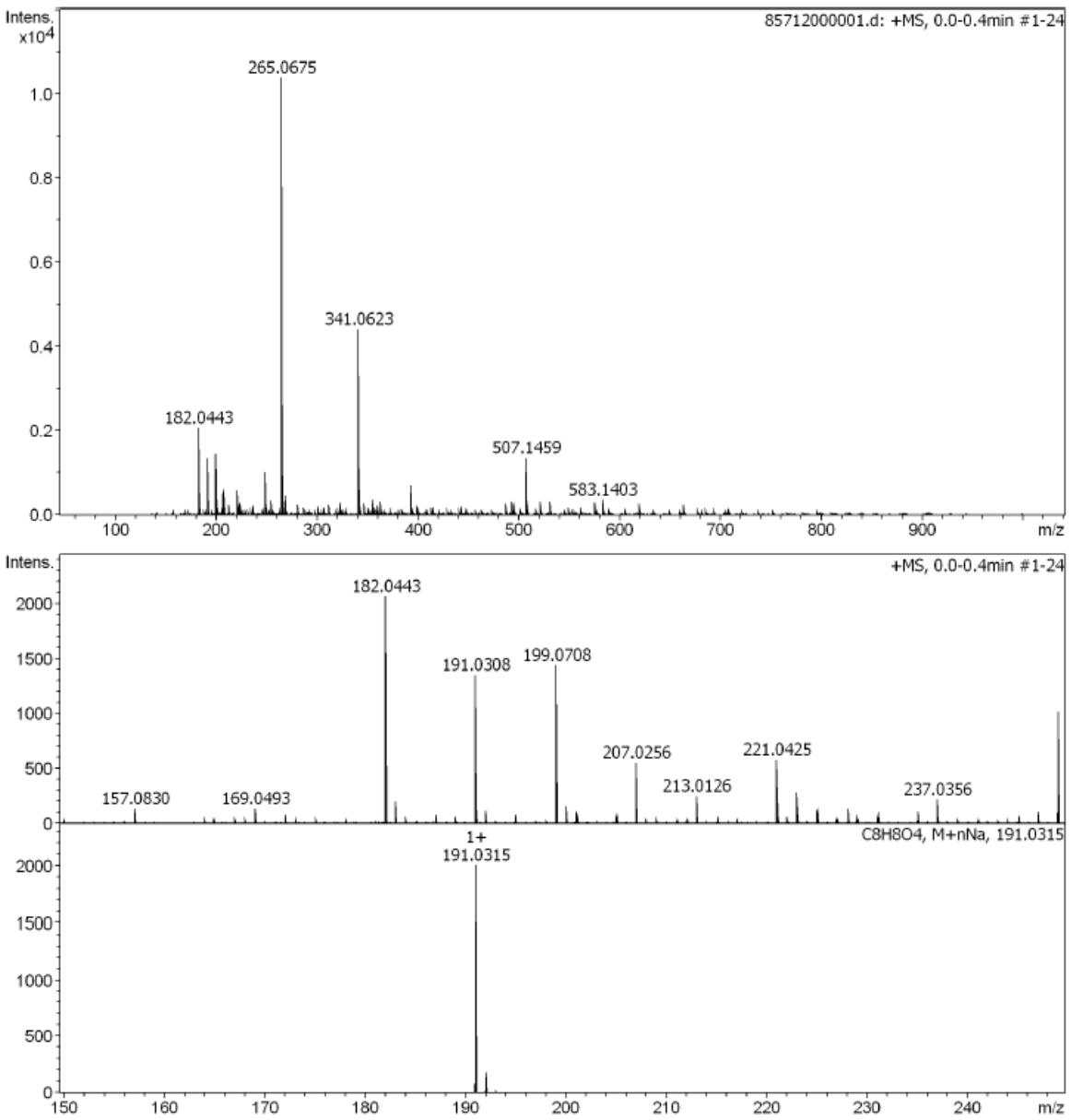


Figure A3: HRMS mass spectrum of 1.

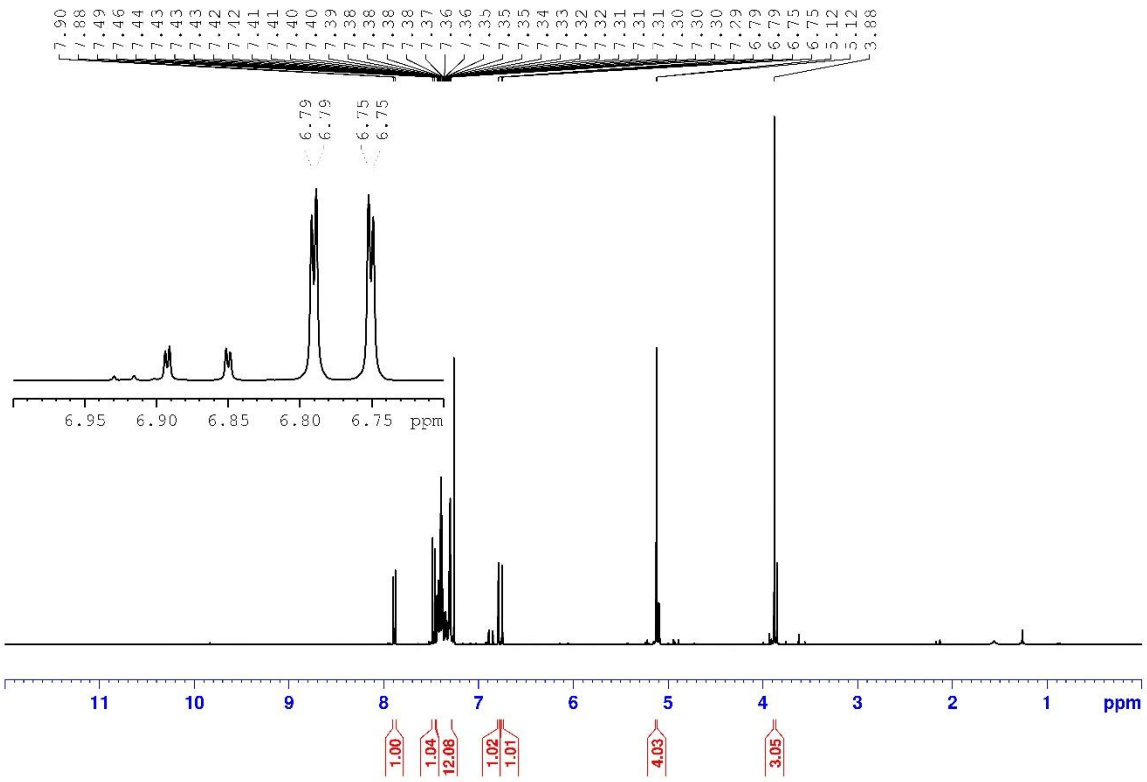


Figure A4: ^{1}H NMR spectrum of 2 in $CDCl_3$.

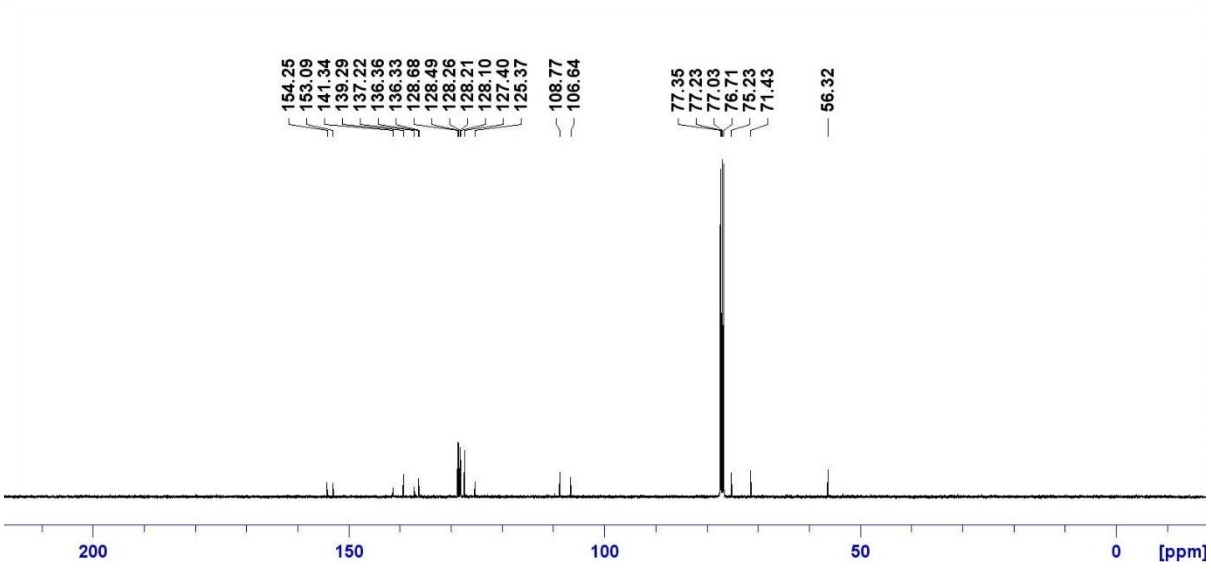


Figure A5: ^{13}C NMR spectrum of 2 in $CDCl_3$.

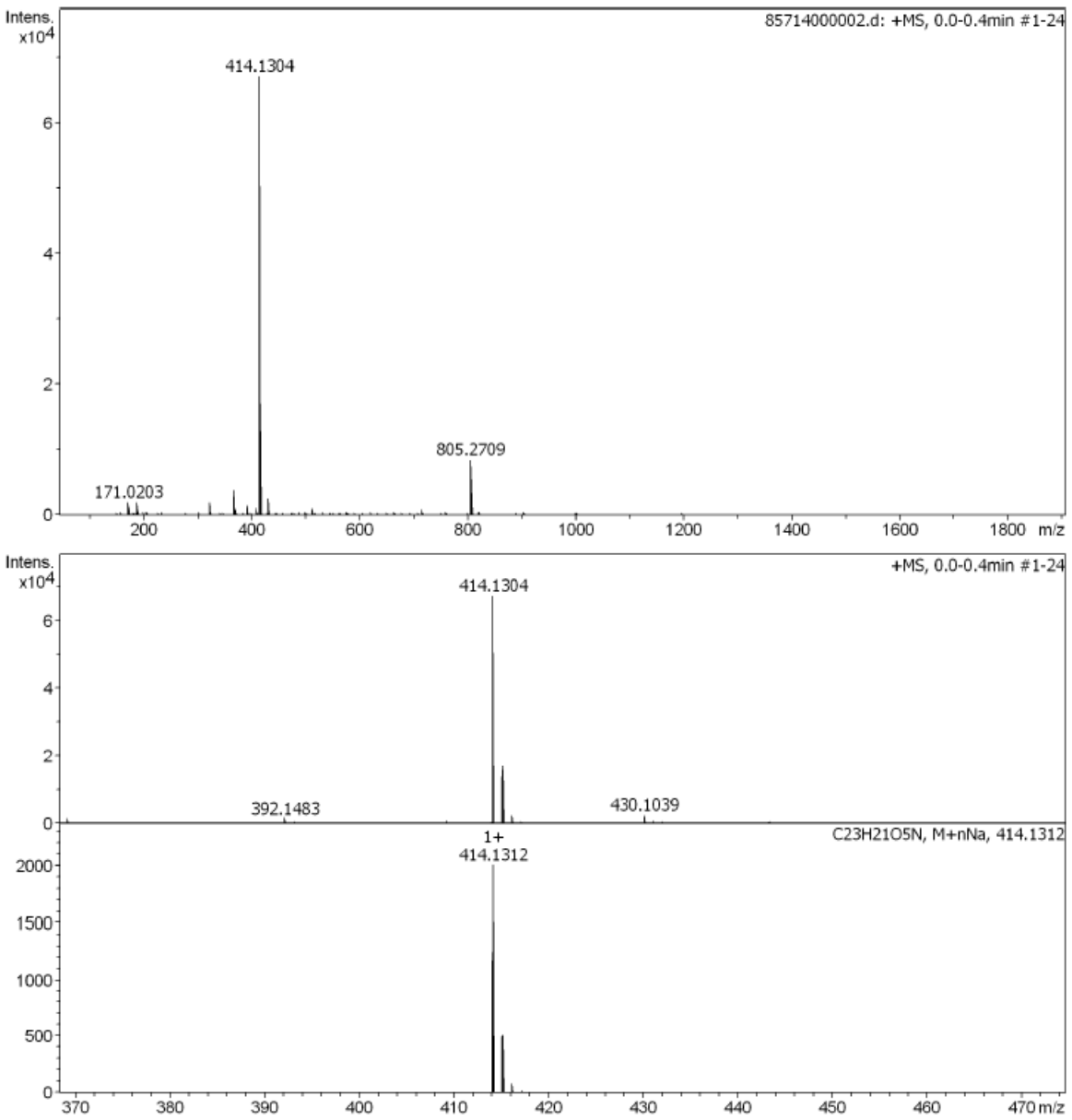


Figure A6: HRMS mass spectrum of 2.

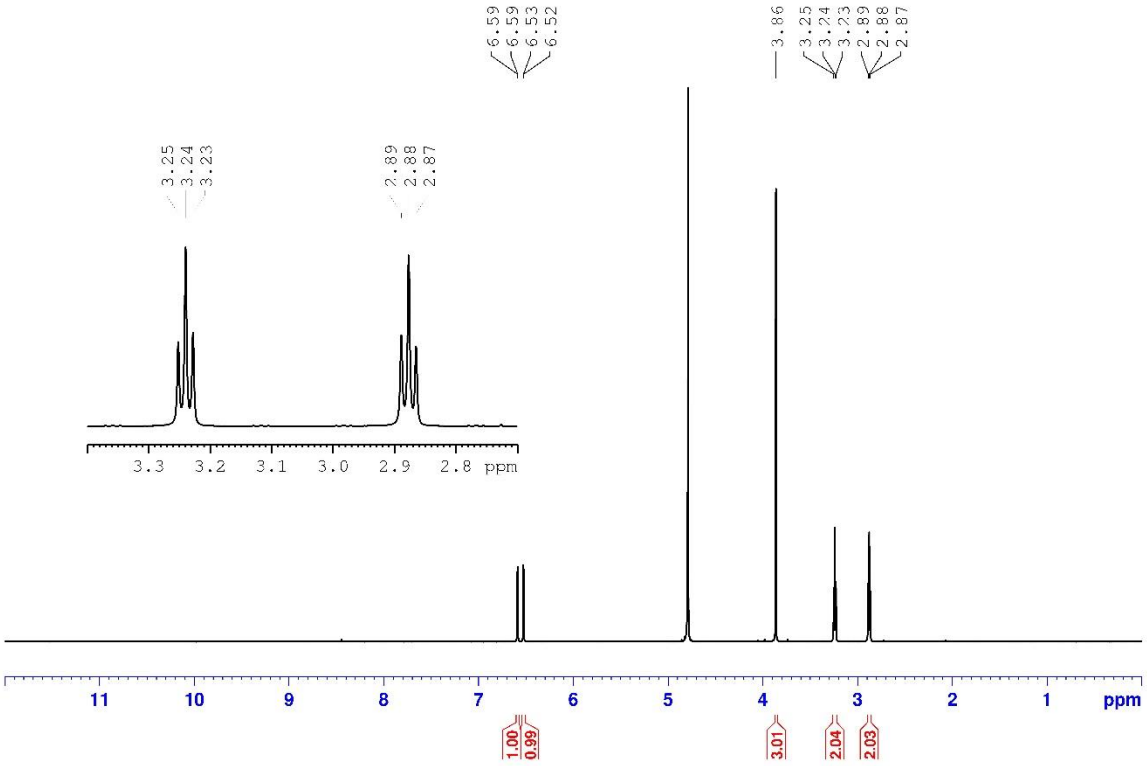


Figure A7: ^{1}H NMR spectrum of OMeDA in D_2O.

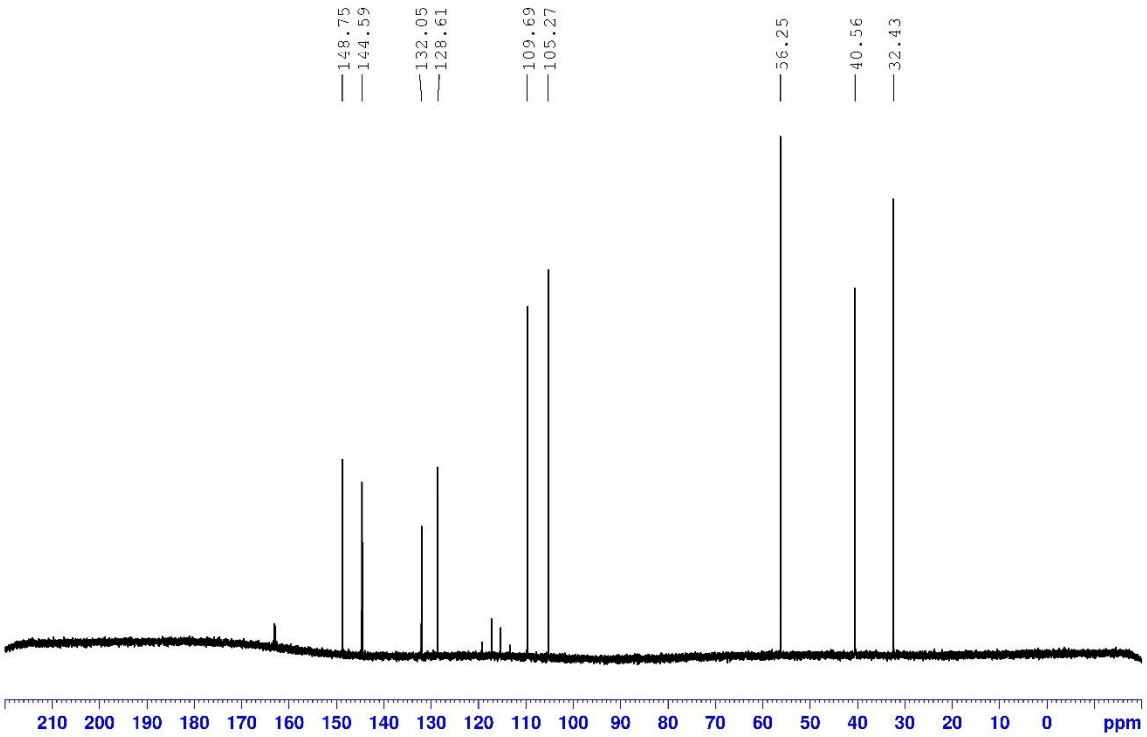


Figure A8: ^{13}C NMR spectrum of OMeDA in D_2O.

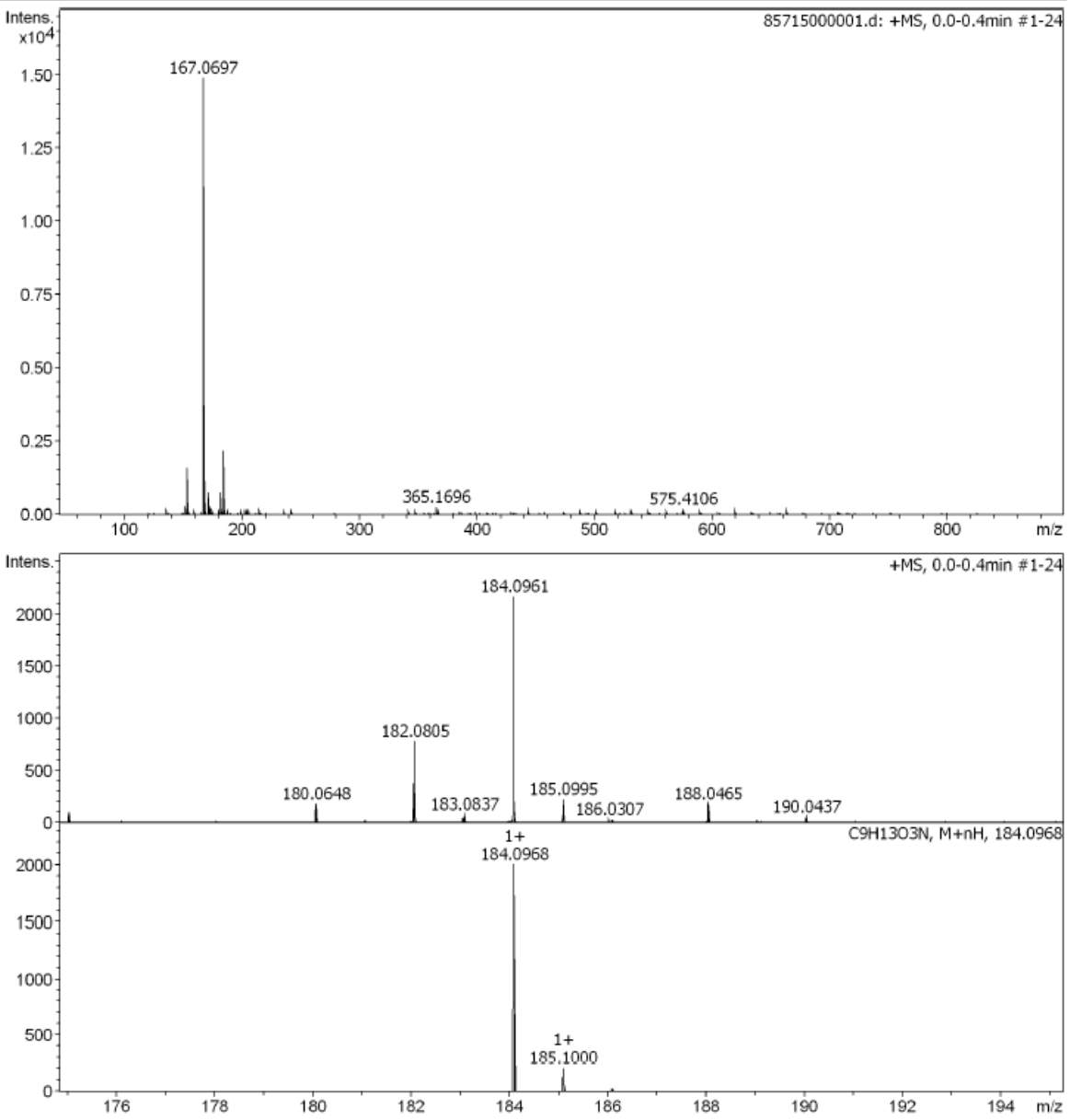


Figure A9: HRMS mass spectrum of OMeDA.

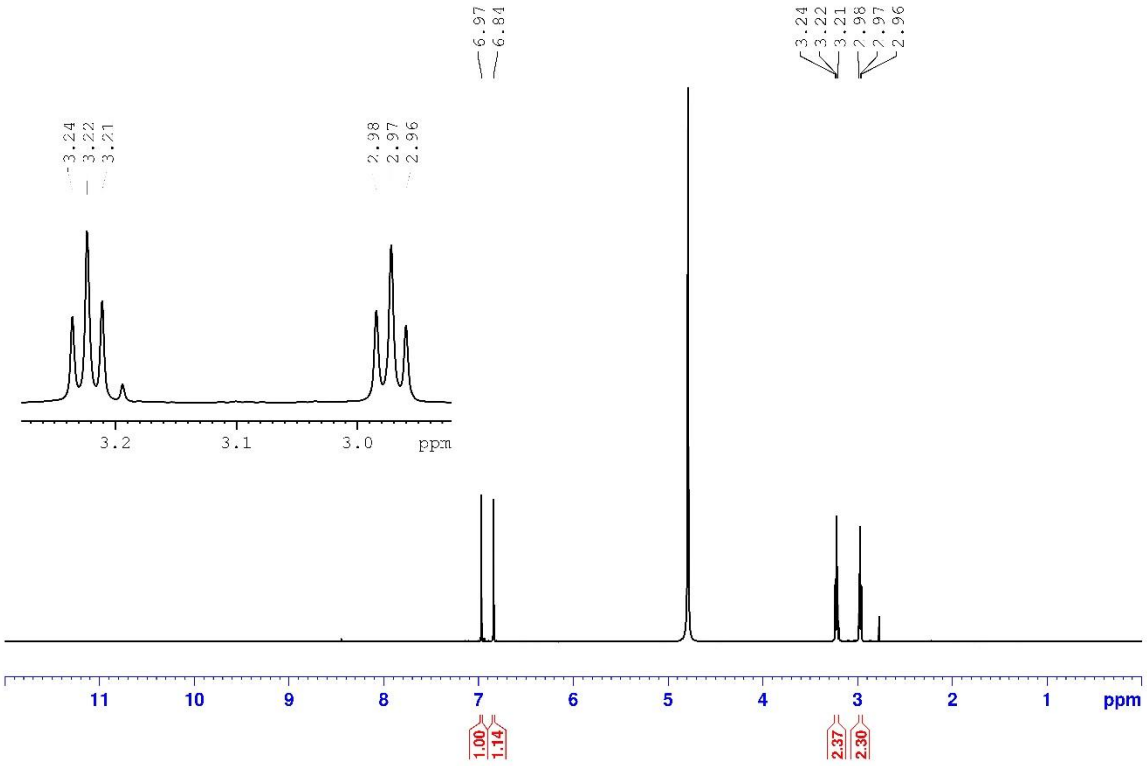


Figure A10: ^{1}H NMR spectrum of ClDA in D_2O.

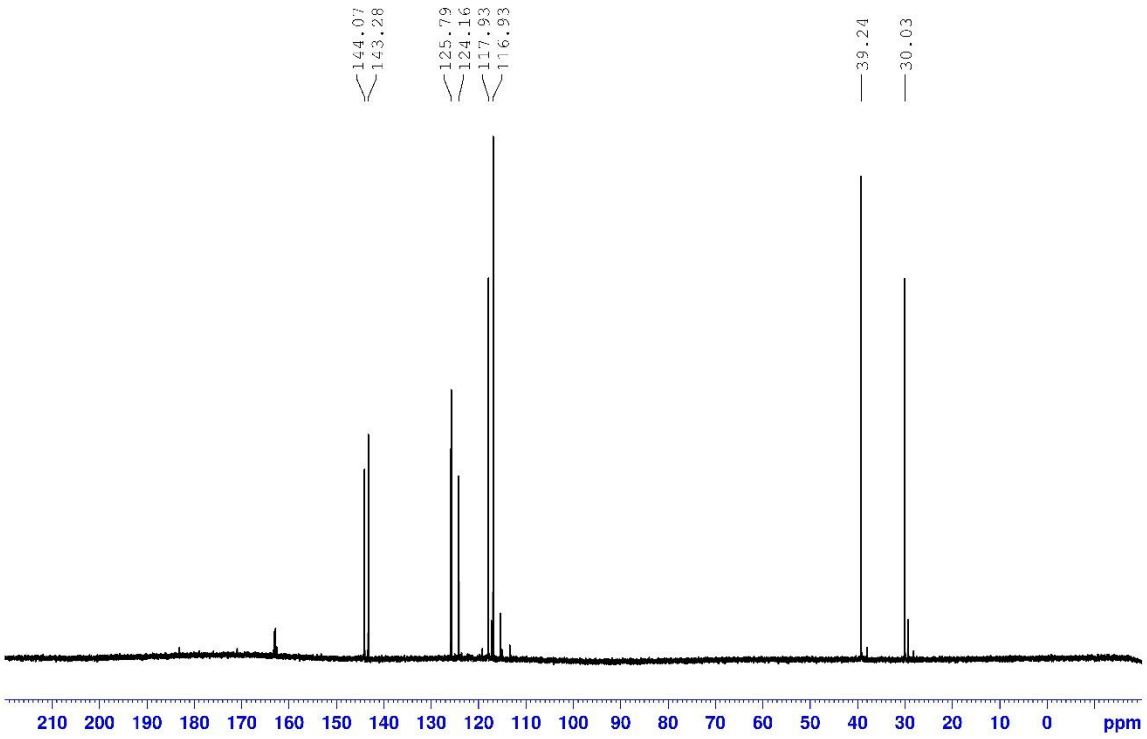


Figure A11: ^{13}C NMR spectrum of ClDA in D_2O.

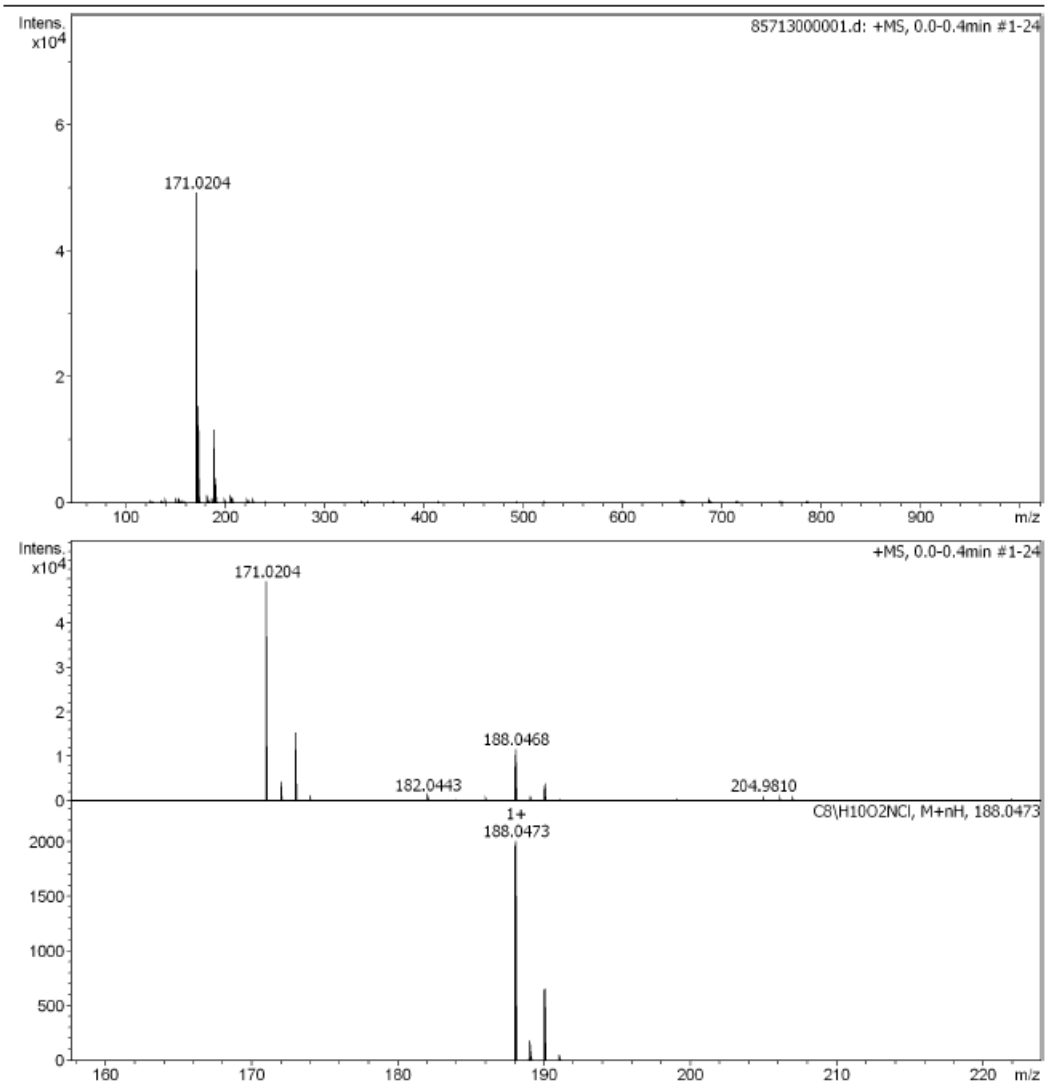


Figure A12: HRMS mass spectrum of ClDA.

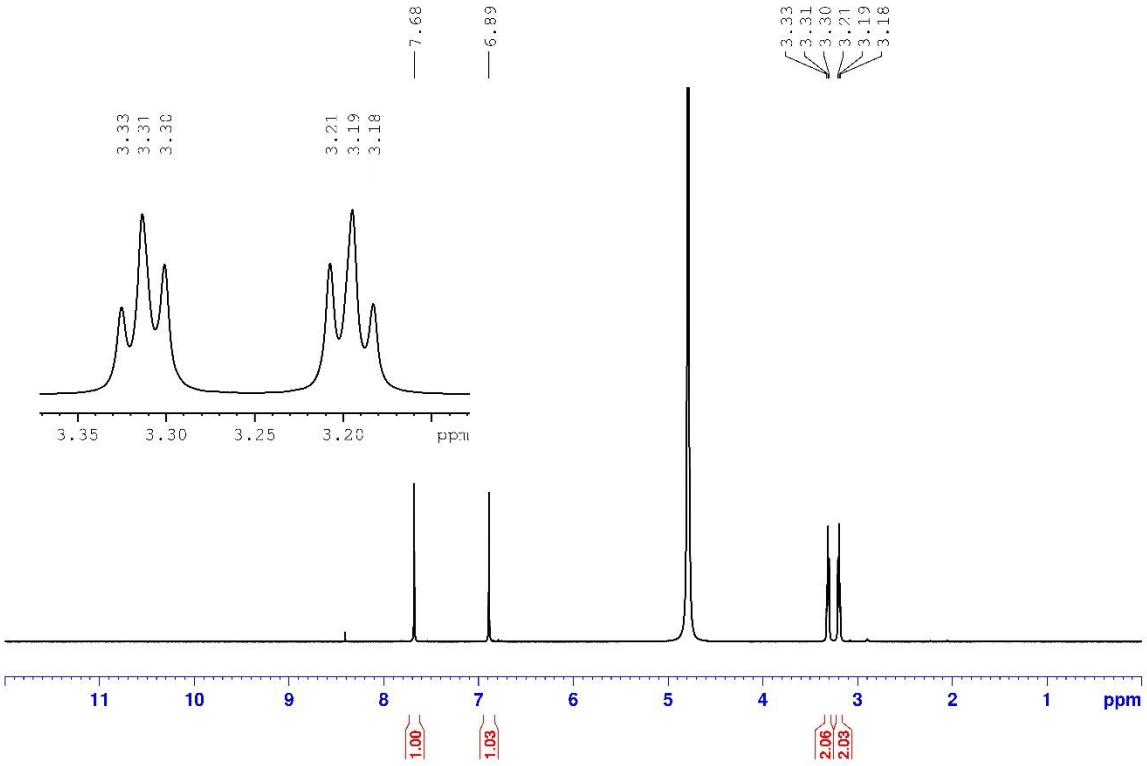


Figure A13: ^{1}H NMR spectrum of NO_2DA in D_2O.

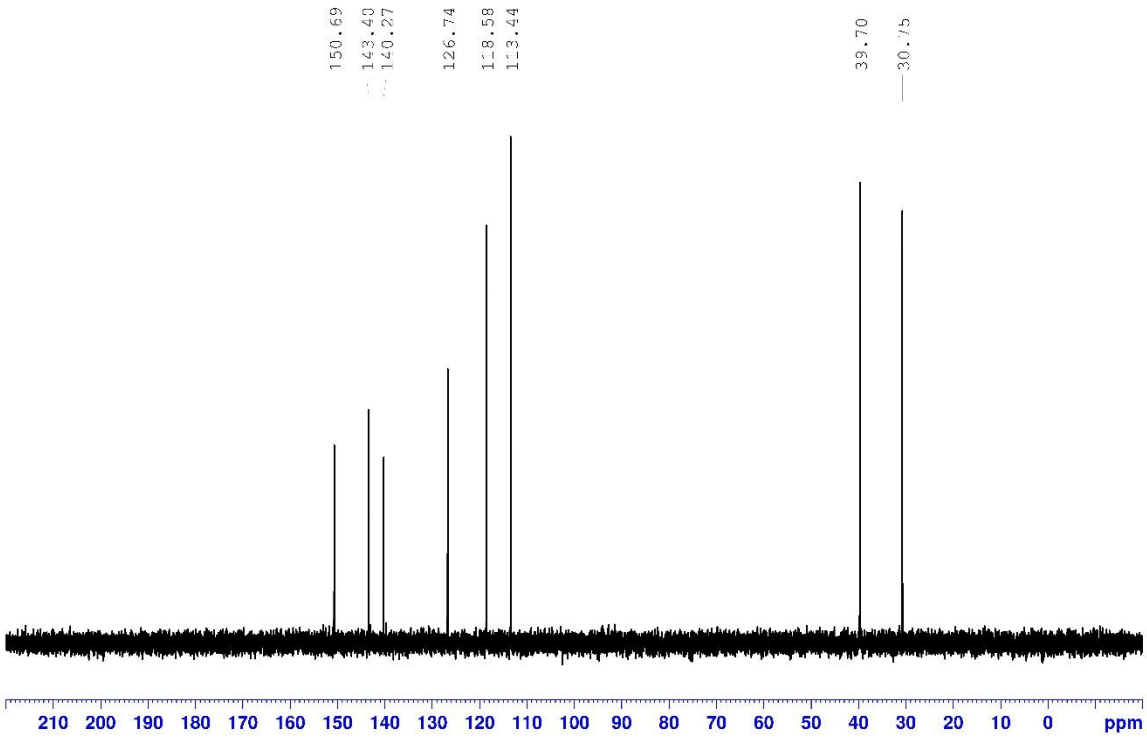


Figure A14: ^{13}C NMR spectrum of NO_2DA in D_2O.

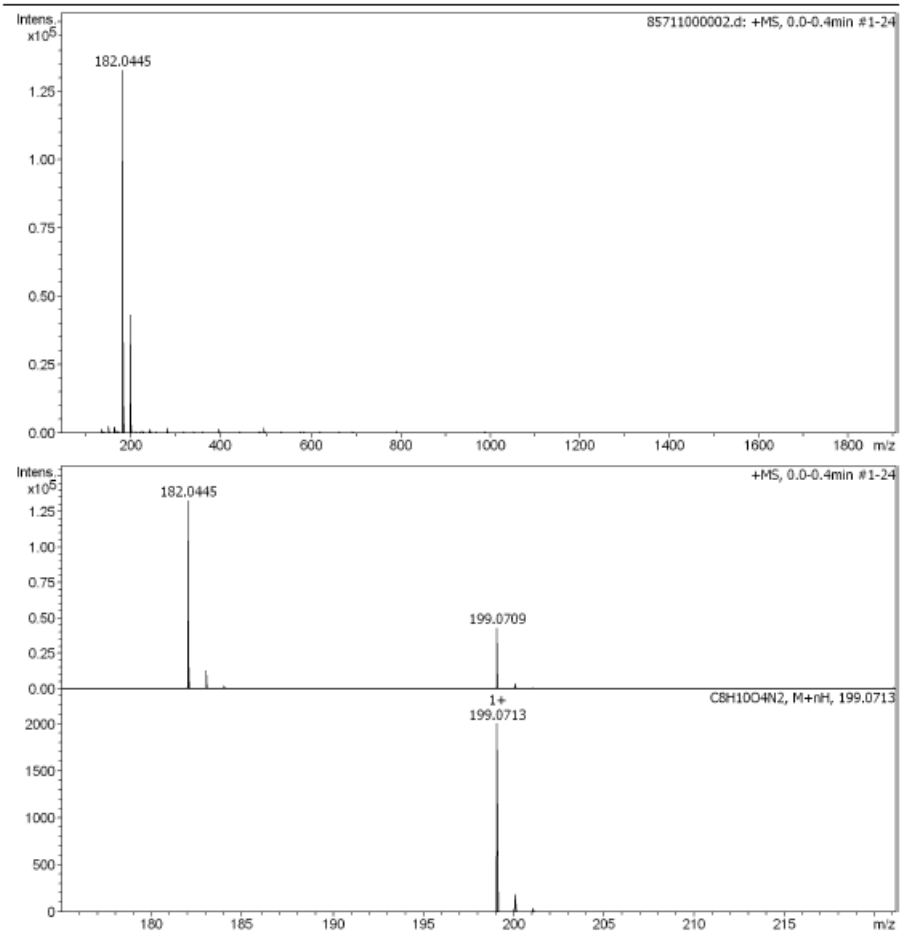


Figure A15: HRMS mass spectrum of NO_2DA.